Calhoun
Institutional Archive of the Naval Postgraduate School

Calhoun: The NPS Institutional Archive

DSpace Repository

Theses and Dissertations 1. Thesis and Dissertation Collection, all items

1966

Non-equilibrium condensation of carbon dioxide in supersonic nozzles.

Duff, Karl M.

http://hdl.handle.net/10945/9591

Downloaded from NPS Archive: Calhoun

DUDLEY KNOX LIBRARY

Calhoun is the Naval Postgraduate School's public access digital repository for research materials and institutional publications created by the NPS community. Calhoun is named for Professor of Mathematics Guy K. Calhoun, NPS's first appointed -- and published -- scholarly author.

Dudley Knox Library / Naval Postgraduate School
411 Dyer Road / 1 University Circle
Monterey, California USA 93943

http://www.nps.edu/library

NPS ARCHIVE
1966
DUFF, K.

NON-EQUILIBRIUM CONDENSATION OF
CARBON DIOXIDE IN SUPERSONIC NOZZLES

by

Karl M. Duff

Sc.D. Thesis January 1966

Department of Mechanical Engineering
MASSACHUSETTS INSTITUTE OF TECHNOLOGY

DUDLEY KNOX LIBRARY
NAVAL POSTGRADUATE SCHOOL
MONTEREY CA 93943-5101

NON-EQUILIBRIUM CONDENSATION OF CARBON DIOXIDE IN SUPERSONIC NOZZLES

by

Lt. Karl M. Duff, USN

S. B., Massachusetts Institute of Technology
(1957)

S. M., Massachusetts Institue of Technology
(1964)

Cambridge, Massachusetts

Submitted in Partial Fulfillment of
the Requirements for the Degree of

DOCTOR OF SCIENCE

in

MECHANICAL ENGINEERING

at the

MASSACHUSETTS INSTITUTE OF TECHNOLOGY

January 1966

NON-EQUILIBRIUM CONDENSATION OF CARBON DIOXIDE IN SUPERSONIC NOZZLES

by

Karl M. Duff

Submitted to the Department of Mechanical Engineering on January 10, 1966, in partial fulfillment of the requirements for the Degree of Doctor of Science.

ABSTRACT

Tests involving the condensation of CO_2 in three supersonic nozzles have been conducted. Data of streamwise pressure variation and local conditions at onset of condensation have been obtained and show that rate of expansion, as determined by nozzle geometry, has a significant influence on the supersaturation obtained prior to condensation.

Interferometric density measurements for non-condensing flow verified the applicability of 1-dimensional gas dynamics to the expansions, and the need for consideration of departure from perfect gas behavior of CO_2. Non-condensing density-pressure measurements and total pressure measurements substantiated the use of the Plank Equation of State in the low temperature region of testing.

Classical nucleation and drop growth theory, as applied in this study to nozzle flow, will predict the conditions of supersaturation at onset of condensation reasonably well, provided small corrections to the flat film liquid surface tension of CO_2 are applied. These corrections amount to increases of from 17% to 38%, depending upon values of thermal and mass accommodation coefficients which are also applied.

The applied theory does not successfully predict the experimental streamwise variation in pressure caused by condensation, nor the extent of effects of nozzle geometry noted experimentally. These failings are thought to indicate inadequacies in drop growth theory, or in its application.

Thesis Supervisor: ______________________________

Philip G. Hill

Title: Associate Professor of Mechanical Engineering

BIOGRAPHICAL NOTES

The author was born February 18, 1936 in Fort Worth, Texas and received his high school diploma from Edmonds High School, Edmonds, Washington in June, 1953. He entered M.I.T. that fall and received his Bachelor of Science Degree in Mechanical Engineering in June 1957. After graduating from M.I.T., he entered Naval Officer's Candidate School at Newport, Rhode Island in September, 1957 and was commissioned in January, 1958. He served for three years aboard the U.S.S. Brown(DD-546) in the Pacific Fleet, and obtained the positions of Engineering Officer and Senior Watch Officer prior to completing his duty aboard. In June, 1961 he returned to M.I.T. under the Navy's post-graduate school program and in September, 1964 obtained a Master of Science Degree in Naval Architecture and Marine Engineering.

The author is a member of Pi Tau Sigma, honorary Mechanical Engineering Fraternity, and the American Society of Naval Engineers. In June, 1964 he received the Brand Award from the Society for having stood first in his class, course XIII-A, the post-graduate curricula entered into in 1961.

He is married to the former Gretchen M. Raddatz of La Jolla, California, and presently has one daughter, age one year.

ACKNOWLEDGEMENTS

I am indebted to my thesis advisor, Professor Philip G. Hill, Associate Professor at M. I. T., who originally conceived of this project, and who contributed throughout with his timely thought, comment and guidance. His sincere interest and effort played a significant role in its accomplishment.

Professor Edward S. Taylor, Director of the Gas Turbine Laboratory at M. I. T., in which the work took place, was particularly helpful with his continuing interest and advice, as were the other members of the author's thesis committee; Professor Ronald F. Probstein and Associate Professor Peter Griffith of the Department of Mechanical Engineering at M. I. T., and Professor Jack L. Kerrebrock of the Department of Aeronautics and Astronautics at M. I. T.

This work was carried out with the day-to-day interest and advice of the members of the teaching and research staff of the Gas Turbine Laboratory. The technical assistance of Mr. Thorvald Christensen was particularly helpful. Mr. Michael Kremmer designed and constructed Nozzle II used in the experiments.

Mrs. Madelyn M. Euvrard has contributed much in the way of her secretarial and other services, ranging from coffee to beach parties, and the author feels he has greatly benefited from his membership in her "brood". The final manuscript was the joint effort of many, and, in the absence of any other inspiration, would always serve to remind the author of a lasting debt to his loving wife, Gretchen.

The programmed computations were carried out with the assistance of the M. I. T. Computation Center's IBM 7094 digital computer, with many valuable contributions by Mrs. Joan Kukolich.

TABLE OF CONTENTS

Page

Abstract i

Acknowledgements ii

Table of Contents iii

Nomenclature v

I. Introduction 1

II. Nozzle Flow Phenomena 3

- A. Isentropic Effects 3
- B. Wall and Boundary Layer Effects 3
- C. Test Vapor Considerations 5

III. Experimental Investigations 8

- A. Test Apparatus 8
- B. Test Nozzles 9
- C. Experimental Procedures 10
  - 1. Pressure-Density Measurements 10
  - 2. Stagnation Pressure Measurements 11
- D. Non-Condensing Measurements 11
  - 1. Real Gas Behavior 11
  - 2. Pressure-Density Measurements 14
  - 3. Normal Shock Total Pressure Measurements 15
  - 4. Influence of Equation of State Upon Isentropes 17
- E. Condensation Measurements 17
  - 1. Pressure Profiles and Local Conditions at Onset of Condensation 17
  - 2. Visual Observations 19

IV. Interpretation of Experimental Results 21

- A. Nucleation Theory 21
  - 1. General Form of Nucleation Rate Equation 21
  - 2. Evaluation of Classical Nucleation Rate Equation 23
- B. Drop Growth Theory 27
- C. Application of Nucleation and Drop Growth Equations 30
- D. Real Gas Effects 33
- E. Results of Application of Theory to Condensation of CO_2 35
  - 1. Comparison of Theory and Experimental Data 35
  - 2. Influence of Nucleation and Drop Growth Parameters on Theoretical Predictions 36
    - a) Onset of Condensation 37

TABLE OF CONTENTS Continued...

Page

b) Profile Shapes 38

c) Downstream Moisture Formation 39

3. Influence of Contamination 40

V. Summary of Findings and Conclusions 42

A. Experimental Findings 42

B. Application of Nucleation and Condensation Theory 42

VI. Suggestions for Further Study 45

Bibliography 48

Appendix A - Figures and Tables A1

Appendix B - Review of Nucleation Rate Equation Development B1

Appendix C - Review of Development of Drop Growth Equations C1

Appendix D - Modification of Foregoing Gas Dynamics, Nucleation and Drop Growth Equations for Departure from Perfect Gas During an Isentropic Expansion. D1

Appendix E - A Closed Form Solution to the Momentum Integral Boundary Layer Equation Including Approximate Effects of Streamwise Density Variation E1

Appendix F - Estimated Effect of Departure from 1-Dimensional Flow on Nozzle Throat Pressure Measurements F1

Appendix G - Discussion of Interferometry Application to Two-Dimensional Nozzle Flow G1

Appendix H - Programmed Computation Listings H1

Appendix I - Estimation of Experimental Error I1

NOMENCLATURE

A	Nozzle Flow Area
C_p	Specific Heat at Constant Pressure
C_v	Specific Heat at Constant Volume
g	Number of Molecules in a Droplet Cluster
g^*	Number of Molecules in a "Critical" Cluster
h	Specific Enthalpy
h_{fg}	Specific Enthalpy of Vaporization
H	Total Enthalpy
J	Number of Nuclei Produced per Unit Time per Unit Volume
k	Boltzman Constant
m	Molecular Weight
m'	"Effective" Molecular Weight
$\dot{m}$	Mass Flux, Particles/Unit Area-sec.
M	Mach Number
n	Number of Vapor Molecules/Unit Volume
n_i	Index of Refraction of a Vapor in State i
$N(g)$	Equilibrium Size Density Distribution of g-molecule Clusters
P, p	Static Pressure
P_o	Stagnation Pressure
P_o'	Stagnation Pressure behind a Normal Shock
P_∞, p_∞	Flat Film Equilibrium Vapor Pressure
P_D	Droplet Equilibrium Vapor Pressure
Q	Heat
r	Droplet Radius
r^*	Helmholtz "Critical" Radius
R	Gas Constant
R'	Effective Gas Constant

s	Entropy
S	Fringe Shift, Number of Fringes
t	Time
T	Static Temperature
T_o	Stagnation Temperature
T_D	Drop Temperature
T_R	Temperature of Molecules Reflected from a Droplet
u	Streamwise Velocity
U_{fd}	Internal Energy of a Droplet
v	Specific Volume
V	Total Volume
x	Streamwise Variation of Distance in Nozzle
y	Vertical Cross-Stream Variation of Distance in Nozzle
z	Horizontal Cross-Stream Variation of Distance in Nozzle
α	Thermal Accommodation Coefficient
γ	Ratio of Specific Heats
γ'	Effective Ratio of Specific Heats
δ	Boundary Layer Thickness
ε	Defined in Appendix B, page B2.
η	Quasi-Equilibrium Droplet Density Distribution
θ	Angle, Radians
λ	h_{fg}/C_pT
λ_o	Wave Length of Interferometer Light Source - 5461 a°
μ	Mass Fraction of Condensed Moisture
ξ	Condensation (Mass Accommodation) Coefficient
ρ	Local Density
ρ_o	Stagnation Density

ρ_L	Droplet (Cluster) Density
σ	Drop Surface Tension
σ_∞	Liquid Flat Film Surface Tension
τ	1/T
ϕ	Free Energy per Molecule (Subscripts; L = Liquid, V = Vapor)
Φ	Total Free Energy of g Molecules
l	Distance z Between Optical Glass Side Walls, Nozzle I

I. INTRODUCTION

In recent years, increasing attention has been given to the problem of homogeneous nucleation and condensation of supersaturated vapors.

Particular interest has arisen in connection with high temperature, low vapor pressure fluids, capable of high Carnot efficiencies in power plant application. The possible space application of systems employing alkali metals, and recent reports of experiments involving the flow of sodium and potassium through nozzles[43,54] underlines the need to understand the condensation behavior of these gases well enough to provide a basis for optimum turbine and cycle design.

Early investigations in cloud chambers showed that, after initial expansions and settling had removed dust particles and other nuclei, subsequent expansions into the saturated region would result in the spontaneous formation of a condensation cloud at some limiting expansion ratio. In the absence of other nucleation sites, it was concluded that such clouds were the result of homogeneous nucleation of the super-saturated vapor. Similar condensation occurs in vapors expanded in nozzles, where rates of expansion are generally much more rapid than those of cloud chambers.

Despite extensive literature on the subject, there exists little agreement as to the correct formulation of nucleation and drop growth rates, and within the theoretical framework there exist many other uncertainties regarding the fluid properties pertinent to numerical evaluation. Experimental work is relatively limited in terms of range of test conditions, and numbers of fluids tested. Although a variety of gases have been studied in cloud chamber expansions, applicable and informative studies of nozzle expansions are somewhat sparse outside of steam and airborne water vapor for which both cloud chamber and nozzle data is extensive.[7,62,63,66 & 67] This data as well as the cloud chamber data for several other vapors tends to substantiate

I. INTRODUCTION

In recent years, increasing attention has been given to the problem of homogeneous nucleation and condensation of supersaturated vapors.

Particular interest has arisen in connection with high temperature, low vapor pressure fluids, capable of high Carnot efficiencies in power plant application. The possible space application of systems employing alkali metals, and recent reports of experiments involving the flow of sodium and potassium through nozzles[43,54] underlines the need to understand the condensation behavior of these gases well enough to provide a basis for optimum turbine and cycle design.

Early investigations in cloud chambers showed that, after initial expansions and settling had removed dust particles and other nuclei, subsequent expansions into the saturated region would result in the spontaneous formation of a condensation cloud at some limiting expansion ratio. In the absence of other nucleation sites, it was concluded that such clouds were the result of homogeneous nucleation of the super-saturated vapor. Similar condensation occurs in vapors expanded in nozzles, where rates of expansion are generally much more rapid than those of cloud chambers.

Despite extensive literature on the subject, there exists little agreement as to the correct formulation of nucleation and drop growth rates, and within the theoretical framework there exist many other uncertainties regarding the fluid properties pertinent to numerical evaluation. Experimental work is relatively limited in terms of range of test conditions, and numbers of fluids tested. Although a variety of gases have been studied in cloud chamber expansions, applicable and informative studies of nozzle expansions are somewhat sparse outside of steam and airborne water vapor for which both cloud chamber and nozzle data is extensive.[7,62,63,66 & 67] This data as well as the cloud chamber data for several other vapors tends to substantiate

so-called "classical"[5,18,23] nucleation theory, as opposed to revised models of nucleation theory offered by more recent authors, as a better means of predicting condensation behavior. However, there is doubt regarding the extent to which cloud chamber data may be applied to the determination of nucleation rates, and too little data outside of water vapor has been obtained for flow in nozzles to allow a comprehensive test of theory over a variety of gases.

The purpose of this work has been to extend the limits of existing experimental data involving condensation in nozzles, through experimentation with CO_2, to study by means of a computational program the predictions of existing theory and make some judgments regarding the importance of the various physical parameters and uncertainties pertaining thereto, and to reduce these uncertainties to a point where a valid comparison of existing theory and experimental results can be made for CO_2.

II. NOZZLE FLOW PHENOMENA

Converging-diverging nozzles lend themselves particularly nicely to the study of condensation behavior of gases. Following are some of the aspects of gas behavior in nozzle flow and features which recommend it as a means of experimental study of condensation.

A. Isentropic Effects

It is general knowledge that for sufficiently high pressure ratios, an ideal gas will expand isentropically in a converging-diverging nozzle, becoming sonic at the point of minimum flow area and supersonic downstream, with continuously increasing velocities and decreasing pressures, densities and temperatures all along the expansion. A non-ideal gas behaves similarly, and depending upon the stagnation conditions, the extent of the expansion, and the properties of the vapor being tested, the isentrope may approach saturation conditions of pressure and temperature. As illustrated on the T-S diagram of Figure 1, it is possible for conditions to exist for certain gases when the opposite may be true and an isentropic expansion will result only in increasing the degree of superheat of the vapor (i.e. as with many of the FREONS). However, in most cases it is a simple matter to devise stagnation conditions which result in the rapid arrival of the gas to conditions of supersaturation during its isentropic expansion. For a supersonic nozzle a few inches in length expansion time is of the order 10^{-4} seconds.

B. Wall and Boundary Layer Effects

In all real gases there are departures from ideal non-viscous behavior which must be considered. Fortunately, in nozzle flow these effects are easily accounted for, provided fully developed flow does not occur. Viscous effects are accounted for by considering the nozzle flow to be an isentropic expansion contained between wall boundary layers. The boundary layers are greatly influenced by the shape of the pressure gradient and are generally

depressed to a very small mimimum value near the most critical point, the geometric throat. Further, viscous and recovery effects on the nozzle walls will keep the wall temperature close to stagnation value in the absence of very strong wall cooling or heating, and, at decreased downstream pressures, is adequate guarantee that there will be no condensation of liquid on the walls which could interfere with the mid-stream process.

In experimentation where nozzle size might be limited by mass flow or other restrictions, considerations of Reynold's Numbers and boundary layer thicknesses which may be expected in the throat region are important since large boundary layers in relation to nozzle size could invalidate the assumption of an isentropic region of flow. A means of estimating the boundary layer thickness in the throat region of a supersonic nozzle was devised (Appendix E) and showed good agreement with interferometric photos that the boundary layers involved in the CO_2 experiments of this investigation were about .006" at the nozzle throat. In all nozzles tested this was less than 11% of the throat width. Additional discussion of boundary layer treatment in this investigation is included later.

The isentropic region between boundary layers may be described by one-dimensional gas dynamics, and, by means of measurement of some vapor property (such as static pressure) along the nozzle, a complete time-history of the expansion may be obtained.

Condensation in a nozzle expansion has been shown by many investigations to have a large influence on the thermodynamic properties of the fluid. In particular, the static pressure records large variation from the non-condensing profile as a result of the heat released by moisture formation. For the addition of heat to an ideal gas, it may be shown that

$$\frac{dP}{P} = \frac{\gamma M^2}{1-M^2} \left[\frac{dA}{A} - \frac{dQ}{C_p T}\right] \qquad 1)$$

For water vapor, it is easily estimated that at $M = 2$, a formation of 1% moisture at constant area is accompanied by about 7% variation in static pressure. As is later shown, it is possible to detect the onset of condensation at about .1% presence of moisture through simple static pressure measurements.

It may be seen from the above equations that pressure variation is increased by establishing conditions such that condensation occurs with Mach Number close to unity.

Willmarth and Nagamatsu,[64] and Arthur,[3] have shown that the ratio P/P_o' plotted against the streamwise variation of P_o'/P_o is an even more sensitive indicator of condensation, where P is the measured static pressure, P_o' is the measured total pressure behind a normal shock, and P_o is the original stagnation pressure.

An important consideration in any system designed to test homogeneous nucleation theory is the possible effects of contamination. As will be shown later, nozzle expansions from superheated to supersaturated state proceed in such an extremely short time that spontaneous nucleation will produce nuclei many orders of magnitude greater in number than those which could be present in the form of dust or other particles and the amount of moisture formed on such contaminants is entirely negligible. As will also be mentioned later, an exception to this is the case of a pre-condensing vapor.

The proceeding observations indicate that, with fairly simple instrumentation of a nozzle system, it is possible to obtain a complete history of a gas expansion and any condensation occurring within, with the reasonable assumption that no outside influences exist which would invalidate testing of homogeneous nucleation and drop growth theory in the same system.

C. Test Vapor Considerations

The selection of a vapor for testing is subject to the following

considerations. First, a large number of vapors are toxic, reactive to instrumentation materials, or do not exist as vapors at conditions most convenient for laboratory testing. Second, the state relations and other properties of many are so poorly defined, that application to any meaningful test of theory would be ill-founded. Neither of these considerations would be restrictive if the condensation data for a particular vapor were particularly needed, or if a test of theory were incidental to the experimental data. Third, two particular properties are desirable in a test vapor, both of which are more common to gases of low molecular weight. The first has been mentioned previously, and involves the shape of the coexistence line in relation to the isentrope. A preferred test gas has a coexistence line having rapid convergence with the isentrope. Also, the measure of heat release resulting from condensation compared with that needed to alter its vapor properties is important. This may be expressed through the parameter h_{fg}/C_p, for which typical values for various gases are presented in Table 1. Variations in the gas properties caused by condensation are increased with larger values of this parameter. A more applicable use of these values is, as seen from Equation 1, the form h_{fg}/C_pT at the test conditions of interest. For vapors such as alkali metals, higher values of h_{fg}/C_p are decreased in significance due to the high temperatures of the gas.

CO_2 was selected for this study because it satisfies all the foregoing criteria and in addition may be obtained in high purity at relative low cost, thus allowing its use in a system not necessitating recovery after expansion. Also, such physical properties as CO_2 vapor pressure, liquid surface tension, and solid and liquid density, necessary in the application of theory, are well established and readily available in numerous publications of physical property data.

Discussion of the application of these properties, and details of the theoretical mechanism and behavior of condensation are presented later.

The question could be raised concerning possible non-equilibrium of energy modes of CO_2 during such a rapid expansion. Kantrowitz[30] has shown that this would not be a problem with CO_2 in this case since 1)vibrational energy modes are not activated at the low temperatures of experimental test conditions and 2)the relaxation time constant of vibration is considerably less ($\approx 10^{-6}$ sec.) than that of the gas expansion. Camac[10] has recently formulated the pressure-temperature dependence of CO_2 vibrational relaxation time and his expression also yields times of the order 10^{-6} sec. in the region of experimental testing.

III. EXPERIMENTAL INVESTIGATIONS

A. Test Apparatus

Industrial Welding CO_2 having very high (moisture content less than .0045% by weight) purity was introduced via a manifold from a bank of nine 50 lb cylinders to a needle valve used for regulation of flow rate (See Figure 2). Thence the flow entered a stagnation tank and then the test nozzle. Exhaust was to atmosphere in earlier tests and later to a steam ejector system maintaining about 23" Hg. of vacuum. This modification facilitated lower minimum stagnation pressures without the interference of compression shock systems in the supersonic test section. Nine cylinders were employed in order to obtain a large mass flow source providing nearly constant conditions to the nozzles for extended periods of flow, despite the quasi-steady nature of the "blow-down" method.

The stagnation tank contained a calibrated pressure gauge and, extending into the flow just upstream of the nozzle entrance, a copper-constantan thermocouple using an ice reference. A 100 inch 25-tube mercury filled manometer board was used in connection with static wall taps to determine pressure readings along the nozzle. Pressure data was recorded by polaroid photograph of the manometer board. Test time durations were of the order of 1 minute.

The stagnation tank had a removable end plate and contained screens which allowed the packing of large amounts of steel wool inside a nylon filter bag upstream of the nozzle entrance. (Figure 5) When high stagnation temperatures were desired (i.e. non-condensing tests) an electric heating tape wrapped around the stagnation tank was energized and the steel wool used for heat storage and thermal inertia to decrease the rate of the temperature transient. When low temperatures were desired, the steel wool was removed and the heating tape not used.

B. Test Nozzles

Two test nozzles were employed for experimental measurements, henceforth referred to as Nozzle I and Nozzle II.

Nozzle I appears schematically in Figure 7 and in photos in Figures 6 and 9. It featured two removable parallel side walls which were plates of optical glass, used for interferometric measurements. By exchanging one of the plates for an identical metal one containing pressure taps, static pressure profiles could be obtained and the flow observed simultaneously through the remaining glass wall. Slotted "O-rings" provided sealing of the side walls. The nozzle was made wide in comparison to its height in order to minimize any contribution to error caused by boundary layer effects of the side walls on the interferometric measurements. This error was later estimated to be less than .2% of the measured densities.

The nozzle shape was also intended to provide nearly 2-dimensional flow, and in fact, interferometric photos to be discussed later show the flow to be effectively 1-dimensional between boundary layers. A region of isentropic flow was thus obtained between the boundary layers, which were of thickness $\approx$ .005" - .007" at the throat (Appendix E).

Pressure Taps in Nozzle I were spaced .2" apart, and later during the program, additional taps, resulting in .1" spacing, were added in the test section region.

Nozzle II is illustrated in Figures 8 and 10 and featured hinged upper and lower nozzle walls which could be placed at arbitrary angles between the fixed parallel side walls. This facilitated variable expansion rates in the test section, depending on the divergence angle of the test section, and it was hoped to thus establish a "best" angle of divergence to obtain the most informative pressure profiles. Since pressure variations due to heat addition approach maximum when Mach

Number approaches 1.00, it was expected that this result would be obtained for a very low angle of divergence.

Static pressure taps located in the side wall were located .25 inches apart for early runs, after which a new test plate with taps .1 inches apart in the test region was substituted.

C. Experimental Procedures

1. Pressure-Density Measurements

Tests were conducted using two persons and the following procedure.

1) The needle valve was opened until the approximate value of desired stagnation pressure was obtained.

2) One observer maintained a null-balance on the thermocouple-potentiometer circuit, while the other, manning a tripod-mounted polaroid camera, observed the manometer board.

3) When the manometer board reached a steady state, a polaroid photo was taken of the manometer board by the second observer while the first recorded the stagnation gauge pressure and terminated the null-balancing procedure on the thermocouple potentiometer.

4) The reading of the potentiometer at time of photograph was converted to a stagnation temperature reading, and the polaroid display of the pressure data developed, and all pertinent data involving the test run affixed to it (including local barometric pressure).

Interferometer runs were made in a similar manner, except for the use of 5" x 7" sheet film in the built-in camera of the interferometer, and requiring only the potentiometer null-balance prior to recording data.

Discussion of interferometry theory and the methods applied in this investigation plus related references are presented in Appendix G.

2. Stagnation Pressure Measurements

The stagnation pressure behind a normal shock was measured by means of a .030" O.D. pitot tube extending upstream from a micrometer mounted on the elbow downstream of the nozzle.(See Figure 6) All measurements were made on Nozzle I, by visually aligning (with the aid of lighting, and machinist's templates) the tip of the tube with the center of the corresponding wall tap with which static pressure was measured. Since the location of the shock was actually located a small distance upstream, a correction was made to the static pressure reading corresponding to this distance, (about .63 tube diameters at Mach 1.65 and about .30 tube diameters at Mach 2.45, decreasing further as Mach Number increases.)[55] Upstream stagnation pressures were measured with the calibrated gauge in the stagnation tank. As in the case of the static pressure profile measurements, photographs of the manometer board were taken simultaneously with stagnation temperature and pressure measurements, after steady pressure readings and a null potentiometer reading were obtained.

Total pressure measurements were made with all manometer tubes disconnected except the following 1)pitot tube 2)static wall tap at tip of pitot tube 3)throat static wall tap (recorded only for supplementary purposes).

Discussion and estimates of possible experimental error are contained in Appendix I.

D. Non-Condensing Measurements

1. Real Gas Behavior

It became necessary to consider the departure from perfect gas behavior of CO_2 near the very outset of this investigation, since one of the objects of experimental work was to compare the agreement of measured density profiles with measured pressure profiles. Failure to consider the proper

2. Stagnation Pressure Measurements

The stagnation pressure behind a normal shock was measured by means of a .030" O.D. pitot tube extending upstream from a micrometer mounted on the elbow downstream of the nozzle.(See Figure 6) All measurements were made on Nozzle I, by visually aligning (with the aid of lighting, and machinist's templates) the tip of the tube with the center of the corresponding wall tap with which static pressure was measured. Since the location of the shock was actually located a small distance upstream, a correction was made to the static pressure reading corresponding to this distance, (about .63 tube diameters at Mach 1.65 and about .30 tube diameters at Mach 2.45, decreasing further as Mach Number increases.)[55] Upstream stagnation pressures were measured with the calibrated gauge in the stagnation tank. As in the case of the static pressure profile measurements, photographs of the manometer board were taken simultaneously with stagnation temperature and pressure measurements, after steady pressure readings and a null potentiometer reading were obtained.

Total pressure measurements were made with all manometer tubes disconnected except the following 1)pitot tube 2)static wall tap at tip of pitot tube 3)throat static wall tap (recorded only for supplementary purposes).

Discussion and estimates of possible experimental error are contained in Appendix I.

D. Non-Condensing Measurements

1. Real Gas Behavior

It became necessary to consider the departure from perfect gas behavior of CO_2 near the very outset of this investigation, since one of the objects of experimental work was to compare the agreement of measured density profiles with measured pressure profiles. Failure to consider the proper

p-v-T relation for reduction of interferometric data resulted in considerable error in the density profile. It also introduced doubt as to how the proper density ratios should be converted to the corresponding isentropic pressure ratios for purposes of making comparison between measurements.

Existing tabulated properties of CO_2 also showed that the degree of departure from perfect gas behavior for CO_2 (as reflected by the compressibility factor, $z = \frac{Pv}{RT}$) increased markedly near the saturated region, and that the values of compressibility factor could easily be as low as .9 during an expansion. Also, existing tables did not extend to pressures and temperatures low enough to make adequate determination of what the real gas behavior of CO_2 is.

Since a meaningful test of the nucleation and drop growth predictions which were to follow must rest on the most precisely accurate information available regarding the gas dynamics, and since, as will be shown, the predictions are quite sensitive to errors in this respect, it was decided to establish the real gas behavior of CO_2 through use of an applicable equation of state.

Unfortunately, though the literature abounds with work, much of it recent, on high pressure and temperature properties of CO_2,[4,11,24,26,28, 33,51, & 59] it was possible to find only one equation of state that is applicable in the lower P-T range of these experiments, that being Plank's[47] (1929), which fits the data of Lowry and Erikson,[39] and Maass and Mennie[41] very well. Comparison of Plank's Equation of State and of their data is shown in Figure 14, showing maximum disagreement of about .1% of $\frac{Pv}{RT}$. For comparison, the equation of State of Martin & Hou, and Benedict, Webb, and Rubin, applied well outside their applicable region to the area of experimental interest, vary by as much as 10% from Plank's.

Plank's equation is stated and was applied as follows:

$$v = \frac{RT}{p} + \frac{(.0825 + .0012657p) \times 10^3}{(.01T)^3} \qquad (2)$$

Using the relations:

$$\frac{\partial h}{\partial p})_s = v = \frac{1}{\rho} \qquad (3)$$

$$dh = (\frac{\partial h}{\partial T})_p dT + (\frac{\partial h}{\partial p})_T dp \qquad (4)a$$

$$= C_p dT + (\frac{\partial(v\tau)}{\partial \tau})_p dp \qquad (4)b$$

where $\tau = \frac{1}{T}$, it is possible to use the zero pressure value[34] for C_p in the result

$$h = \int_o^T C_p dT + \int_o^p [\frac{\partial(v\tau)}{\partial \tau}]_p dp \qquad (4)c$$

The right hand term may be evaluated from the equation of state and hence it is possible to determine enthalpy at any desired pressure and temperature. To determine an isentrope, equation (3) is used and the change in h calculated for an arbitrary change in p. Thence, knowing new values of p and h, the corresponding value of T may be determined, either through the use of pre-calculated enthalpy tables, or by iterative integration of equation $(4)_c$. It is then a simple matter to calculate the new value of density from equation (2) and to thus determine a series of pressure, temperature, and density ratios along an isentrope for any given set of stagnation conditions.

Table 2 contains values of enthalpies calculated in this manner. Agreement within .1° to .3°K occurs at the juncture of those presented by Din.[15]

In addition to the comparison of pressure and density measurements, it was decided to apply an additional experimental test to the ability of the Plank Equation of State to predict the behavior of CO_2 gas dynamics in regions of low pressure and temperature yet below its known region of applicability, (0°C to -70°C). Measurement of the normal shock pressure

characteristics were made and compared with the predictions of "real" gas dynamics. For this purpose, it was necessary to include a computation scheme for solution of the continuity, momentum, energy, and state equations across a normal shock and to return along a new isentrope to the new stagnation conditions. A listing of this computation procedure is given in Appendix H.

2. Pressure-Density Measurements

Photographs of two interferometer fringe patterns for non-condensing flow are seen in Figures 11 and 12 and the resulting densities given in Table 3 and 4. The photographs are marked by an extended region of near verticle interference fringes between the upper and lower nozzle walls, indicating that this region is in 1-dimensional flow, and that the boundary layers are quite small (approximately .006" at the throat).

Results of the two sets of measured density and the corresponding pressure profiles of Nozzle I are shown in Figures 15a, 15b and 16a, 16b. Each comparison has been illustrated in two ways. Figures 15a and 16a show the density and pressure profiles in relation to nozzle position. Pressures have been directly measured and plotted at their tap locations. Measured density ratios have been converted to their corresponding pressure ratios through use of the real gas isentropic values based on the experimental stagnation conditions.

Figures 15b and 16b show the same data plotted in somewhat different form, illustrating the theoretical isentropic values of P/P_o vs. ρ/ρ_o and those values of P/P_o and ρ/ρ_o which were measured at identical points in the nozzle. On Figure 16b, the corresponding perfect gas conversion from density to pressure (based on zero pressure value of C_p/C_v) is also shown.

Figures 15 and 16 show very good agreement between measured pressures and densities, and those predicted from the Plank Equation of State. The fact that the conversion of density to pressure is not very significantly affected by the use of the equation of state rather than perfect gas relations, is indicated by the close proximity of the perfect gas line in Figure 16b, where the applied ratio of specific heats is the zero pressure value at stagnation temperature, $\gamma = 1.28$. However, it should be emphasized that even this use of the perfect gas approximations is preceeded by the use of real gas p-v-T relations in the reduction of interferometric fringe shift data to obtain values of density. The only noticeable departure from exact real gas agreement consistent to both tests occurs near the throat region where the measured pressures are slightly higher ($\approx$ 1.8" Hg) than those values based on measured density. This departure is concluded to be due to departure from 1-dimensional flow over the boundary layer of the lateral side walls in this region and an approximate numerical estimate of this effect in good agreement with the noted error is made in Appendix F.

Attempts to apply the interferometer to direct study of condensation were frustrated by increasing fluctuation and blurring of the interference fringes as stagnation pressure was increased. This effect was apparently due to thermal turbulence. Above pressures of 85 psia, complete blurring resulted upstream of the throat, although the interference bands again became visible downstream, where acceleration of the flow dampens the effects of turbulence. Consequently, no density profiles involving condensation were obtained although photographs of the condensation ice cloud showing the interference fringes within were obtained.

3. Normal Shock Total Pressure Measurements

A more sensitive test of the Plank Equation of State predictions versus those of perfect gas was made by applying each to the gas dynamics

of normal shock behavior and comparing experimental results with theoretical predictions based on the experimental stagnation conditions of each test.

Results of experimental normal shock measurements are shown in Figure 17, using the display of Willmarth and Nagamatsu, and Arthur, who made similar measurements for Nitrogen and Helium.[64,3] The predictions computed with Plank's Equation of State are shown in Figure 18. Test series No. 2 was taken with a great deal of regard for better accuracy in pitot tube positioning and establishment of steady state readings prior to taking data, with a resulting decrease in the amount of scatter. One-dimensional perfect gas predictions are shown for reference in the lines of constant γ, the appropriate zero pressure value for most of the test conditions being about $\gamma = 1.28$. It is seen that the real gas predictions are considerably more accurate than those of perfect gas in predicting the normal shock characteristics of CO_2, although there still exists some departure of the experimental results from those predicted with the Plank Equation of State. The experimental results indicate behavior very close to that of a perfect gas having a value of $\gamma = 1.40$. However, this is misleading, since treatment of CO_2 as a perfect gas, using this value of ratio of specific heats, does not successfully correlate the pressure-density measurements, or correctly predict local temperatures along an isentrope. In terms of the measured properties, the experiment indicated about 2% larger values of stagnation pressure behind the normal shock than those predicted.

Despite the above mentioned lack of complete agreement between Plank's Equation of State and measured normal shock pressure characteristics, it appears that such a "real gas" treatment of the gas dynamics is a considerably better description than perfect gas and so warranted application to the prediction of local conditions along the isentrope.

4. Influence of Equation of State Upon Isentropes

The influence of real gas treatment to the computation of CO_2 isentropes has quite a significant effect upon the values of local temperature calculated. Figures 19 and 20 compare two typical perfect gas isentropes with those predicted using Plank's Equation of State. These curves indicate that an error of 5°K could easily occur by attempting to describe the isentrope by a constant ratio of specific heats, and that a decrease in stagnation temperature could cause errors of possibly 10°K if one isentrope were applied to all experimental test conditions.

The resulting uncertainty in predicted nucleation rate, depending upon location within the supersaturated region, can be seen by referring to the classical nucleation rate profiles for CO_2 illustrated in Figure 21. Errors of 15 orders of magnitude could easily occur.

E. Condensation Measurements

1. Pressure Profiles and Local Conditions at Onset of Condensation

Results of experimental measurements involving condensation in Nozzle I, pressure tap plates 1 & 2 are shown in Figures 22 and 23. Results of Nozzle II, pressure tap plate 1 are shown in Figure 24, and of the same nozzle using pressure tap plate 2 in Figures 25 through 30. Figures 24, 25, 26, 27 and 28 are for Nozzle II at an included divergence angle of approximately 2.2° while Figures 29 & 30 are for Nozzle II at an angle of 0.80°. For convenience and due to manometer board limitations, pressure ratios are expressed in terms of the pressure at the tap nearest the throat, but may be easily converted to total pressure ratio. Data for each Figure is adjoined in Tables 5 through 13.

All experimental profiles showed a marked occurrence of pressure variation from non-condensing values at the point of occurrence of

condensation (verified visually in Nozzle I). By noting the pressure ratio at which condensation occurs, it is possible to determine the local conditions at occurrence using the isentropic relations for the equation of state previously discussed. Based on the range of applicability of Plank's Equation of State and comparison with the tables of Din,[15] it is estimated that temperatures in the vicinity of 190°K are accurate to within .3°K and temperatures in the region of 160°K accurate to perhaps 1° or 2°K. A plot of these points for all three nozzle geometries tested is shown in Figure 31.

Several characteristics of the condensation profiles and the local conditions at point of occurrence may be noted.

First, the shape of the profiles contain no sharp minimum at the point of occurrence of condensation such as those noted in the condensation of pure water vapor.[7,23] i.e. it is not appropriate to speak of condensation shock in this case, since the formation of moisture occurs along an extended region.

Second it appears that pressure level (or temperature level, or some dependent property) may influence the shape of the profile, i.e. the rate of formation of moisture, to some extent since the shapes of the condensation profiles appear to be more "spread out" for high stagnation pressures than for low stagnation pressures. See Figure 27. These effects are not explainable in terms of gas dynamics influences, and the cause is not apparent.

Third, a very definite influence of nozzle geometry upon the point of onset of condensation occurs, as seen in Figure 31. The rapid rate of nozzle divergence and expansion of Nozzle I results in higher supersaturation ratios and relatively greater delay of condensation. Progressively decreasing the rate of expansion through decrease of nozzle divergence

condensation (verified visually in Nozzle I). By noting the pressure ratio at which condensation occurs, it is possible to determine the local conditions at occurrence using the isentropic relations for the equation of state previously discussed. Based on the range of applicability of Plank's Equation of State and comparison with the tables of Din,[15] it is estimated that temperatures in the vicinity of 190°K are accurate to within .3°K and temperatures in the region of 160°K accurate to perhaps 1° or 2°K. A plot of these points for all three nozzle geometries tested is shown in Figure 31.

Several characteristics of the condensation profiles and the local conditions at point of occurrence may be noted.

First, the shape of the profiles contain no sharp minimum at the point of occurrence of condensation such as those noted in the condensation of pure water vapor.[7,23] i.e. it is not appropriate to speak of condensation shock in this case, since the formation of moisture occurs along an extended region.

Second it appears that pressure level (or temperature level, or some dependent property) may influence the shape of the profile, i.e. the rate of formation of moisture, to some extent since the shapes of the condensation profiles appear to be more "spread out" for high stagnation pressures than for low stagnation pressures. See Figure 27. These effects are not explainable in terms of gas dynamics influences, and the cause is not apparent.

Third, a very definite influence of nozzle geometry upon the point of onset of condensation occurs, as seen in Figure 31. The rapid rate of nozzle divergence and expansion of Nozzle I results in higher supersaturation ratios and relatively greater delay of condensation. Progressively decreasing the rate of expansion through decrease of nozzle divergence

condensation (verified visually in Nozzle I). By noting the pressure ratio at which condensation occurs, it is possible to determine the local conditions at occurrence using the isentropic relations for the equation of state previously discussed. Based on the range of applicability of Plank's Equation of State and comparison with the tables of Din,[15] it is estimated that temperatures in the vicinity of 190°K are accurate to within .3°K and temperatures in the region of 160°K accurate to perhaps 1° or 2°K. A plot of these points for all three nozzle geometries tested is shown in Figure 31.

Several characteristics of the condensation profiles and the local conditions at point of occurrence may be noted.

First, the shape of the profiles contain no sharp minimum at the point of occurrence of condensation such as those noted in the condensation of pure water vapor.[7,23] i.e. it is not appropriate to speak of condensation shock in this case, since the formation of moisture occurs along an extended region.

Second it appears that pressure level (or temperature level, or some dependent property) may influence the shape of the profile, i.e. the rate of formation of moisture, to some extent since the shapes of the condensation profiles appear to be more "spread out" for high stagnation pressures than for low stagnation pressures. See Figure 27. These effects are not explainable in terms of gas dynamics influences, and the cause is not apparent.

Third, a very definite influence of nozzle geometry upon the point of onset of condensation occurs, as seen in Figure 31. The rapid rate of nozzle divergence and expansion of Nozzle I results in higher supersaturation ratios and relatively greater delay of condensation. Progressively decreasing the rate of expansion through decrease of nozzle divergence

condensation (verified visually in Nozzle I). By noting the pressure ratio at which condensation occurs, it is possible to determine the local conditions at occurrence using the isentropic relations for the equation of state previously discussed. Based on the range of applicability of Plank's Equation of State and comparison with the tables of Din,[15] it is estimated that temperatures in the vicinity of 190°K are accurate to within .3°K and temperatures in the region of 160°K accurate to perhaps 1° or 2°K. A plot of these points for all three nozzle geometries tested is shown in Figure 31.

Several characteristics of the condensation profiles and the local conditions at point of occurrence may be noted.

First, the shape of the profiles contain no sharp minimum at the point of occurrence of condensation such as those noted in the condensation of pure water vapor.[7,23] i.e. it is not appropriate to speak of condensation shock in this case, since the formation of moisture occurs along an extended region.

Second it appears that pressure level (or temperature level, or some dependent property) may influence the shape of the profile, i.e. the rate of formation of moisture, to some extent since the shapes of the condensation profiles appear to be more "spread out" for high stagnation pressures than for low stagnation pressures. See Figure 27. These effects are not explainable in terms of gas dynamics influences, and the cause is not apparent.

Third, a very definite influence of nozzle geometry upon the point of onset of condensation occurs, as seen in Figure 31. The rapid rate of nozzle divergence and expansion of Nozzle I results in higher supersaturation ratios and relatively greater delay of condensation. Progressively decreasing the rate of expansion through decrease of nozzle divergence

results in earlier condensation. Comparative geometry and non-condensing pressure profiles of the three nozzles may be seen in Figure 32.

Fourth, the extremely low rate of divergence of Nozzle II in the 0.80° case (subsonic flow results at about 0.50° divergence) results in notable axial fluctuation of the pressure profile data (Figure 29) and some scatter of the point of onset of occurrence of condensation. (Figure 31) It should be remembered that differential changes in gas properties are proportional to $(1/1-M^2)$ and that at the pressure ratios present in these tests Mach Number remains very close to unity. ($M \approx 1.25$ at $P/P_o \approx .40$). Also, as heat of condensation is released, Mach Number is driven even closer to unity. This is coupled with the fact that at low angles of divergence, the value of the negative pressure gradient is greatly decreased, downstream of the throat, from those values which existed for the other two test nozzles. This would tend to create more rapid boundary layer growth and greater departure from 1-dimensional flow in the narrow angle case. It might be expected that larger departures from 1-dimensional flow, plus the magnifying effects of near unity Mach Numbers could contribute to larger pressure fluctuations.

2. Visual Observations

Experimental observations indicated that the pressure hump accompanying condensation occurred at a point coincident with the appearance of the ice cloud.

This at first seemed at variance with the expectation that pressure variation should occur prior to the appearance of visible condensate, due to the theoretically small sizes of forming nuclei. ($r \sim 10^{-7}$cm).

Yellot's[66,67] investigation of condensing steam was also accompanied by visual observation of the water cloud coincident with the location of onset of condensation as determined by pressure measurements. He

reported that this observation remained valid despite changes which resulted in the axial shift of condensation in the nozzle. The same was true in this investigation.

It is also mentioned that the data illustrated a very high degree of consistency and reproduceability, that illustrated in Figures 24 through 28 involving three separate sets of measurements over a period of six months, each set being separated by nozzle dismantlement, cleaning, and pressure tap plate alterations.

IV. INTERPRETATION OF EXPERIMENTAL RESULTS

As discussed in Sections I and II, there are reasons for supposing that the process of nozzle condensation is one involving homogeneous nucleation within the super-saturated vapor. The purpose of this section is to discuss homogeneous nucleation theory and the subsequent drop growth process and apply these processes to nozzle expansions for the purpose of testing the ability of existing theory to interpret the experimental results of CO_2 condensation. Attention is given to the physical properties upon which nucleation and drop growth theory depend, and to the uncertainties which exist in the applicable values of these properties as well as to the theory itself.

A. Nucleation Theory

A review of classical nucleation theory, following the development of Frenkel[19] is presented in Appendix B. For more comprehensive review of theory see Reference Numbers 5,6,12,18,38,56,58,65 and 68. The discussion of Yang,[65] accomplished while working under P.P. Wegener at Yale University, is particularly thorough.

1. General Form of Nucleation Rate Equation

The rate of production of nuclei in a supersaturated vapor has been shown by various authors to be of the form*

$$J = A \cdot \exp^{(-\Delta G^*/KT)} \tag{5}$$

where J = number of nuclei produced per unit time per unit volume,

ΔG^* = free energy of formation of a critical cluster (a cluster in unstable equilibrium with its supersaturated vapor)

And A is proportional to the incident flux of vapor molecules on a critical-sized cluster.

$$A = Cn \left[\frac{P}{\sqrt{2\pi mKT}}\right] 4\pi r^{*2} \tag{6}$$

---

* *See Appendix B for a review of nucleation theory development*

The value of C varies somewhat as derived in the classical treatments of Volmer,[58] Becker and Doring,[6] Frenkel,[19] Barnard,[5] Yang[65] and others. Though variations of one to two orders of magnitude occur over the range of values presented, the effect on nucleation rate is small, since for only a small additional expansion along a nozzle, the value of J can easily vary by 5 - 10 orders of magnitude. Since the change in local conditions is small for a variation in nucleation rate of this sort and, in fact, is scarcely noticeable for 1 to 2 order of magnitude variations in J, the differences in classical treatments of the theory are not significant.

In the classical treatments of the theory, the nucleus is considered as a stationery object, and the free energy of formation is merely:

$$\Delta G = 4\pi r^2\sigma - gKT \ln \frac{P}{P_\infty} \tag{7}$$

where the first term is the work of formation of surface area for a liquid having surface tension σ, and the second is the constant-temperature free energy change of g molecules which change state from vapor at P,T to saturated liquid at T. P_∞ is the flat film vapor pressure of the liquid at temperature T.

The critical cluster$^{(*)}$ is that for which the function ΔG is a maximum, and results in

$$\ln \frac{P}{P_\infty} = \frac{2m\sigma}{\rho_L KTr^*} \tag{8}$$

Using the procedure presented by Frenkel, for which the value of c becomes

$$C = \left[\frac{\ln P/P_\infty}{6\pi g^*}\right]^{1/2} \tag{9}$$

the expression for nucleation rate is

$$J = \left(\frac{P}{KT}\right)^2 \frac{m}{\rho_L} \left(\frac{2\sigma}{\pi m}\right)^{1/2} \exp\left[\frac{-4\pi\sigma r^{*2}}{3KT}\right] \tag{10}$$

As mentioned, Yang has shown that the results of the authors previously mentioned yield expressions for classical nucleation that are much alike (in some cases identical) and which yield quantitative predictions that are not significantly different.

More recent authors have pointed out the need for inclusion of additional terms to the free energy of formation of a critical cluster, which account for the fact that the cluster may have translational, rotational and vibrational energy modes. Kuhrt, Rodebush[53] Lothe and Pound,[38] and Courtney[12,13] have treated this problem but reach widely different conclusions as to the effect upon nucleation rate. The postulated correction factors for this "gassification" of the condensed clusters range from 10^4 to 10^{20}, depending on the treatment and molecular configuration chosen.

More recently, Feder, Russell, Lothe and Pound[18] have jointly made a very comprehensive review of this problem, and offered some new thoughts on the subject. For water vapor, they conclude that the effects of gassification are equivalent to a correction factor of about 10^{15}, but admit that this is not borne out by cloud chamber data. In general, such experimental data as does exist tends to more strongly verify classical theory[5,23] than the improved gassified theory, despite strong arguments for the greater theoretical validity of the latter.

2. Evaluation of Classical Nucleation Rate Equation

Essentially the same physical properties appear both in the exponential and pre-exponential terms of the nucleation rate equation. Of course, uncertainties in these properties will effect the calculated value of nucleation rate chiefly through the exponential. By substitution for the value of r* it is seen that the exponential is

$$\exp\left[\frac{-4\pi\sigma r^{*2}}{3KT}\right] = \exp\left[\frac{-4\pi}{3}\left(\frac{2m}{\rho_L \ln P/P_\infty}\right)^2\left(\frac{\sigma}{KT}\right)^3\right] \tag{11}$$

In evaluating this term correctly it is clear that four physical properties of the vapor must be known: 1)the liquid drop surface tension 2)local temperature 3)liquid drop density and 4)local supersaturation ratio.

Much attention has been given to the applicable values of surface energy for small droplets. However, here again there is little agreement as to what corrections should be made to flat film values to take account of the effect of droplet curvature, and the sign of the correction is itself a subject of controversy.

Effects of curvature are considered by some to cause a surface tension decreasing with drop radius such as in the Kirkwood-Buff Equation.

$$\sigma = \frac{\sigma_\infty}{(1 + 2\delta/r)} \tag{12}$$

where δ is a length, nearly constant, lying between .25 and 0.6 of the molecular radius.

In addition, Stever and Rathbun[56] have calculated a correction to take account of the radius dependency of surface tension which also results in a decrease for small radii. Compared with uncorrected surface tension these corrections lead to lower energies of formation of nuclei and hence higher nucleation rates for the same supersaturated conditions.

However, Oriani and Sundquist,[44] predict an increase in surface energy of about 25% in the case of water, using an analysis based on the breaking of intermolecular bonds. A bonding model used by Benson and Shuttleworth, however, predicts a 15% reduction in surface energy of correspondingly small water ice crystals. Bogdonoff and Lees,[8] also using considerations of binding energies of sodium and of nitrogen obtained a correction that results in larger critical clusters and also larger energies of formation, hence lower nucleation rates from the uncorrected case. For lack of a more

definite indication of the effects of small droplet sizes, most investigators use the flat film value of surface energy, and estimate the effects on the theoretical predictions of departure from it.

An additional uncertainty in surface energy occurs with CO_2 due to the fact that, at pressures below its ice point, 75.1 psia, it apparently condenses in the form of ice crystals rather than liquid droplets. Bondi[9] has shown that for metal crystals, which involve valence bonding, increases in surface energy from the liquid value are closely proportional to the heat of fusion and, depending also on the crystal planes involved, amount to increases of about 25% for those metals which he discusses. He further presumes that for molecular solids one might expect increases of from approximately 1/8 to 1/3 these amounts.

In the case of some gases there is doubt as to the proper value of droplet density to be applied. Though density does not vary too rapidly with temperature, there is doubt, in the case of CO_2, as to whether solid or liquid density should be used. Although the CO_2 may condense as ice particles, there is some argument for use of liquid density in order to be consistent with the spherical geometry and liquid surface energy applied to the liquid drop model, and in the absence of any knowledge of CO_2 crystal surface energies. Also, studies of Dorsch and Hacker[16] with very small water droplets indicated that the spontaneous freezing temperature decreases rapidly with decreasing droplet size. (Figure 33) This might tend to justify doubt on the reality of attempting to distinguish the difference between liquid and solid states at droplet sizes of critical clusters. [For CO_2, typical critical radii are of 7.5×10^{-8} cm to 10^{-7} cm (about 30 - 50 molecules) at supersaturation ratios of the order of 10, where noticeable quantities of moisture are condensed. Typical nucleation rates are 10^{17} to 10^{21} nuclei/cm^3 - sec.]

Figure 34 illustrates existing data on vapor pressures of CO_2 in the region of experimental condensation, and the computational approximations used in the condensation calculations. Accuracy of the vapor pressure data and the approximation below temperatures of about 180°K is uncertain, but is probably within 5% for higher temperatures. Supersaturation ratio may be determined within these limits of accuracy for a given local pressure if the temperature is also known.

Surface tension is considered to be described for flat film liquid by the function $\sigma_\infty = 5.00 - .193T(^\circ C)$ dynes./cm, based on data of References 21, 27, and 50, for which a linear dependence of σ_∞ on T down to 220°K is justified. An alternative function $\sigma = 75(1-\frac{T}{T_c})^{1.25}$(Reference 27) yields values of σ_∞ which vary by only 2% to 9%, in the 200°K to 160°K region of interest, from those of the linear function above.

Knowledge of local temperature, previously discussed, is important in evaluating the nucleation rate equation, not only because of its presence as a cubic in the exponent, but because the other variables are also dependent in value upon temperature. Effects of uncertainty in temperature do not cancel appreciably in their influence upon theoretical nucleation rate. At 200°K, a 1% error in temperature will result in about a 2% error of the opposite sign in surface tension and hence about a 3% error in the ratio σ/T for CO_2. These effects were illustrated in the earlier discussion of the potential uncertainty of local temperature unless an equation of state is used to determine the isentrope for CO_2. It is possible that some past applications of theory to experimental condensation data have erred through failure to consider these real gas effects.

Departures from perfect gas behavior affect the evaluation of the free energy required for the formation of a critical cluster, and also the drop growth relations dealt with in the following section, since both nucleation

and drop growth developments are based on perfect gas assumptions. This problem is dealt with in Section IVD, following the discussion of drop growth theory, and the application of nucleation and drop growth to condensation in nozzles.

B. Drop Growth Theory

Subsequent to the production of nuclei, additional formation of moisture will occur through the growth of the clusters due to vapor impingement. Nuclei may by this process grow to radii of up to about an order of magnitude greater than their original size, depending upon two important drop growth parameters introduced below. In the theoretical treatment, the distinction between nucleation and commencement of drop growth treatment is somewhat artificial, as it is necessary to establish some size of cluster at which the nucleated droplet exists and may commence growing. Becker and Doring have shown that at a cluster radius 1.3 times critical, the probability of clusters continuing to grow reaches better than 99%, and hence it is considered that this is a reasonable starting point for the application of drop growth equations. (Note: Computations showed that results were relatively insensitive to this starting radius.)

The growth of a droplet depends predominantly on two factors: 1)The rate of condensing mass flux 2)The rate of droplet energy transfer to the vapor environment.

It would appear that the first factor is itself a description of the drop growth process, but in actuality, it is greatly dependent upon not only local vapor conditions, but also the difference between droplet and vapor conditions. Both of these are strongly influenced by the second factor.

Two coefficients are defined to describe this behavior:

ξ = Condensation Coefficient. The fraction of impinging vapor molecules which are absorbed at the drop surface.

α = Thermal Accommodation Coefficient. The fractional temperature change which takes place in the reflected portion of incident molecules.

$$\alpha = \frac{T_R - T}{T_D - T} \tag{13}$$

Temperature variation across the droplet is assumed to be negligible, and the droplet is assumed to be spherical.

Based on mass and energy balance considerations presented and developed in Appendix C the following drop growth equations are obtained.

Conservation of Mass

$$\rho_L 4\pi r^2 \frac{dr}{dt} = 4\pi r^2 \left(\frac{\xi P}{(2\pi RT)^{1/2}} - \frac{\xi P_D}{(2\pi RT_D)^{1/2}}\right) \tag{14}$$

Conservation of Energy

$$4/3\pi r^3 \rho_L C \frac{dT_D}{dt} + 4\pi r^2 \frac{dr}{dt} \rho_L U_{fD} = \beta(2RT) - \xi\beta_D(2RT_D)$$

$$- (1 - \xi)\beta 2R[T + \alpha(T_D - T)] \tag{15}$$

These equations may be reduced, respectively, to

$$\frac{dr}{dt} = \frac{\xi}{\rho_L}(\beta - \beta_D) \tag{16}$$

$$0 = 2\xi\left(1 - \frac{\beta_D}{\beta}\frac{T_D}{T}\right) - 2(1 - \xi)\alpha\left(\frac{T_D}{T} - 1\right) - \xi\left(1 - \frac{\beta_D}{\beta}\right)\left(\frac{\gamma}{\gamma - 1}\right)(\lambda - 1) \tag{17}$$

where $\lambda = \frac{\gamma - 1}{\gamma} \frac{hfg}{RT}$

$$\beta = \frac{P}{(2\pi RT)^{1/2}} \qquad \beta_D = \frac{P_D}{(2\pi RT_D)^{1/2}}$$

And P_D is the equilibrium vapor pressure for a spherical liquid drop of temperature T_D in an environment of temperature T_D.

$$P_D = P_\infty(T_D) \exp\left(\frac{2\sigma}{\rho_L R T_D r}\right) \tag{18}$$

In the further application of these equations to streamwise growth of drops in a nozzle, additional assumptions are made. First, for an

acceptably simple computation scheme it is convenient to treat droplets of uniform size, where the radius is an average based either on surface area or volume. Ignoring the effects of coagulation, there is evidence that the actual distribution of drop sizes is narrow, and that the average droplet treatment does not introduce appreciable error.

One possible error that may occur as a result of the above assumption becomes likely when the supersaturation ratio P/P_∞, is reduced so rapidly as a result of condensation, that droplets, which have recently nucleated and begun to grow, will suddenly be of size less than the critical cluster size. In this case, considerable re-evaporation would occur among the smaller droplets of the actual size distribution, and the treatment of an "average" droplet does not account for this.

Relative motion between droplets and the gas stream is ignored, and though this is generally accepted, it may be possible that the same translational modes of energy required by recent authors in nucleation theory might also affect to some degree such things as incident mass and energy fluxes upon newly formed nuclei.

Values of α and ξ have been presented by numerous investigators for several vapors, excluding CO_2. Although earlier presented values of ξ were fairly low, there has been more recent substantiation of values close to 1.00 for most materials, including liquid metals, the previous errors having been caused by neglect of surface temperature depressions and the effects upon evaporation flux. However, there is also indication that molecules of higher dipole moment tend to have lower values of ξ, as with liquid water for which Alty and MacKay,[1,2] and Prueger[49] present values of less than $\xi = .04$. The influence of crystallization upon ξ may also be large, as Tschudin presents a value close to unity for water ice. Effects

of surface contamination and surface diffusion barriers (to recently evaporated particles due to insufficient vacuum and mean free path lengths,) are also thought to play a role in experimentation which tends to lower apparent values of ξ. No experimental values of ξ have been measured for CO_2, which has a dipole moment of about 1.5 compared with 80.0 for that of water.

The thermal accommodation coefficient for vapors and their liquids is generally accepted to be around unity. However, values may be much lower between vapors and solids, as Wachman[60] indicates for gases on clean metal surfaces. For CO_2, the value of α for the vapor and its solid crystal is unknown, and there is uncertainty as to which of the two situations above is the most applicable description.

Departures from perfect gas behavior also influence drop growth. Again, correct values of local temperature and supersaturation ratio will be influenced, and the perfect gas assumptions used in treating mass and energy balances leading to equations (16) and (17) may require modification.

In this study, considerable attention has been given to the behavior and influence of the above mentioned factors.

C. Application of Nucleation and Drop Growth Equations

The predicted effects of moisture formation during a nozzle expansion are determined by applying the time rate release of heat to the gas dynamics of the related expansion. By considering the process with respect to variable nozzle position, rather than time, a result is obtained which can be directly compared with experiment.

Interferometric measurements of density variations in the nozzle verified that the flow between boundary layers is in fact one-dimensional and allows the use of the one-dimensional gas dynamics relations;

Continuity

$$\mathring{m} = \frac{\rho A u}{1 - \mu} \tag{19}$$

Momentum

$$-A dp = \mathring{m} du \tag{20}$$

Energy

$$C_p dT + u du = h_{fg} d\mu \tag{21}$$

where $\mathring{m}$ is the mass rate of flow through the nozzle, μ the mass fraction of condensed moisture, u is the streamwise velocity of the vapor, and ρ, P, and T are the vapor density, pressure and temperature, respectively. A is the effective area of flow between boundary layer thickness, and is determined experimentally for non-condensing flow.

The rate of moisture formation is determined as follows and assumes the droplet velocities to be those of the vapor. A nucleus of radius r_o formed at some point x_o will grow to a larger size at some future time and distance x.

$$r = r_o + \int_{x_o}^{x} \frac{1}{u} \frac{dr}{dt} dx \tag{22}$$

and the surface area will be

$$a = 4\pi[r_o + \int_{x_o}^{x} \frac{1}{u} \frac{dr}{dt} dx]^2 \tag{23}$$

For a rate of growth $\frac{dr}{dt}$ predicted by drop growth, the increase in liquid mass per droplet will be

$$\rho_L a dr = \rho_L 4\pi[r_o + \int_{x_o}^{x} \frac{1}{u} \frac{dr}{dt} dx]^2 \frac{dr}{dt} \frac{1}{u} dx \tag{24}$$

And the fractional moisture change that occurs at x for the $dn_o = J(x_o)A(x_o)[\frac{dx_o}{u_o}]dx_o$ particles formed in the volume $A(x_o)dx_o$ is

$$d\mu_o = \frac{dn_o \rho_L a dr}{(\rho_o A_o dx_o)/(1-\mu_o)} = \frac{J(x_o)A(x_o) \frac{dx_o}{u_o} dx_o \rho_L 4\pi[r_o + \int_{x_o}^{x} \frac{1}{u} \frac{dr}{dt} dx]^2 \frac{dr}{dt} \frac{dx}{u}}{(\rho_o A_o dx_o)/(1 - \mu_o)} \tag{25}$$

Inclusion of the drop growth on all previously formed nuclei necessitates integrating the right hand term over all x_o. Noting that

$\dot{m} = \rho_o A_o u_o / 1 - \mu_o$ and considering also the moisture produced through additional nucleation at x, there results

$$\frac{d\mu}{dx} = \int_o^x J(x_o)\left(\frac{A(x_o)dx_o}{u}\right)\frac{\rho_L 4\pi}{\dot{m}} \left[r_o + \int_{x_o}^x \frac{1}{u}\frac{dr}{dt}dx\right]^2 \frac{dr}{dt} dx_o$$

$$+ \frac{4\pi r^{*3}}{3} \frac{\rho_L}{\dot{m}} J(x)A(x)$$

$$= \frac{4\pi\rho_L}{\dot{m}} \left[\int_o^x \left(r_o + \int_{x_o}^x \frac{1}{u}\frac{dr}{dt}dx\right)^2 J(x_o)A(x_o)\frac{1}{u}\frac{dr}{dt} 1x_o\right.$$

$$\left. + 1/3\ r^3 J(x)A(x)\right] \tag{26}$$

For nuclei generally only slightly larger than critical size, the theoretical drop growth rate is essentially independent of size.[23] Hence $\frac{dr}{dt}$ is assumed to have a value equal to that for large drops. Also, since it is practically impossible to keep account of the radii of each group of growing nuclei which formed at each section dx, it is assumed that the droplets can be represented by the "surface-area averaged" radius of droplets. As previously mentioned, volume averaging has little influence on the results. In addition, Lundgren has given experimental evidence that the actual size distribution of particles condensed in a nozzle expansion is quite narrow.

The foregoing equations are reduced to the following form for use with a Runge-Kutta-Merson integration procedure along the expansion path. (The detailed listing of computation procedure may be seen in Appendix H).

$$dY_1 = 8\pi JA$$

$$dY_2 = Y_1 \frac{dr}{dt} + r^* dY_1$$

$$dY_3 = Y_2 \frac{dr}{dt} + JA(4\pi r^{*2})$$

$$dY_4 = \frac{d\mu}{dx} = \frac{\rho_L}{\dot{m}}\left[Y_3 \frac{dr}{dt} + JA\left(\frac{4\pi r^{*3}}{3}\right)\right]$$

$$dY_5 = \frac{dP}{dx} = P\left[\left(\lambda - \frac{1}{1-\mu}\right)d\mu - \frac{1}{A}\frac{dA}{dx}\right] / \left[1 - (1-\mu)\left(\frac{\gamma - 1}{\gamma} + \frac{1}{\gamma M^2}\right)\right]$$

$$dY_6 = \frac{dT}{dx} = T\left[\lambda d\mu + \frac{\gamma - 1}{\gamma}(1-\mu)\frac{dP}{P}\right]$$

$$dY_7 = \frac{dM}{dx} = M\left[-\frac{(1-\mu)}{\gamma M^2}\frac{dP}{P} - \frac{dT}{2T}\right]$$

where

$$\lambda = h_{fg}/C_p T$$

$$\gamma = C_p/C_v$$

$$M = u/\sqrt{\gamma RT}$$

Initial values of the stagnation conditions, physical properties of the vapor and its liquid, values of α and ξ, and calculation starting point are given for each computation. Effects of contamination may also be considered by giving non-zero values to Y(1), Y(2) and Y(3), based on an initial concentration and size of contaminant. Effects of possible droplet energy modes upon free energy of cluster formation ("gassified" behavior of droplets - page 23) may be considered by multiplying nucleation rate by constant arbitrary factors, equivalent to the values proposed by various authors.

The various sub-routines of the listed computation scheme accomplish the determination of such things as the change in nozzle area, vapor and liquid properties, supersaturation ratios and solution to the drop growth equations when step-wise changes are made along the stream of the expansion. An error estimation is made for each computation and the size of the step, dx, is adjusted to reduce the error bounds to within the desired limits.

D. Real Gas Effects

The preceeding developments of nucleation and drop growth theory and application to nozzle condensation computations assume perfect gas behavior during the expansion. However, as earlier discussion illustrated, experimental measurements were being made for which values of $\frac{Pv}{RT}$ which were considerably less than unity. Consequently, the computational scheme was modified so that the effects of departure from perfect gas behavior could also be considered.

A feature of an isentropic expansion which facilitates fairly simple corrections to the gas dynamics, drop growth and nucleation equations is the

fact that for this particular thermodynamic process, the compressibility factor remains fairly constant, changes of less than 2% in the value of z generally occurring for expansion pressure ratios of 10 or more. This was found to be true for several other gases, including ammonia, and for CO_2 is valid throughout the superheated and supersaturated regions for which compressibility factors are in excess of about .88. Using this fact, it may be shown (Appendix D) that the following relations are approximately true for an isentropic expansion.

$$\frac{Pv}{RT} = z \simeq \text{constant} \tag{27}$$

$$\gamma' = \frac{\gamma}{1 + (\gamma-1)(1-z)} = \frac{dP}{d\rho}\left(\frac{\rho}{P}\right) \tag{28}$$

$$R' = \frac{\mathcal{R}z}{m} = zR \tag{29}$$

where γ' and R' are the effective ratio of specific heats and gas constant, respectively, that are applicable. It should be noted here, that the nucleation rate is effected in the following manner;

$$J \propto \exp\left(\frac{-4\pi\sigma r^{*2}}{3KT}\right); \qquad r^* = \frac{2m\sigma}{\rho_L zKT\ \ln P/P_\infty}$$

due to the change in free energy required to form a critical cluster.

To apply these effects to the perfect gas relations of the condensation computations, two additional steps were necessary. First, modifications which allowed for use of a variable ratio of specific heats ($\gamma = \gamma(T)$) were made. Second, each set of stagnation conditions which was to be placed in the condensation scheme first had its "real" isentrope, z, and effective isentropic exponent $\gamma'(T)$ determined, and from these the $\gamma(T)$ which corresponded to z and γ'. Computation input was $\gamma(T)$ and correction (compressibility factor) z. This resulted in an isentrope, providing the correct values of P vs. T being employed in each condensation calculation, plus the use of effective values of γ and R in the drop growth and nucleation calculations. Additional details of this procedure are presented in Appendix D.

E. Results of Application of Theory to Condensation of CO_2

1. Comparison of Theory and Experimental Data

Data shown in Table 14 and Fig. 31 illustrate the local conditions at the occurence of condensation for each of the experimental tests made. Local temperature was determined through computation of the isentrope for each test case, using the procedure discussed on page 13 based on Plank's Equation of State for CO_2. Reference to Figure 35 illustrates that .1% presence of moisture is a convenient and reasonable criteria for theoretical onset of condensation. Comparing the data and the predictions of theory involved two main comparisons; 1) The location of the onset of condensation, defined as the theoretical occurrence of .1% moisture, and 2) The shape of the pressure profiles. For lack of better knowledge, α, ξ and $\frac{\sigma}{\sigma_\infty}$ were originally assumed to be unity. Specific comparisons were made of the predictions of 1) Classical nucleation theory 2) Droplet "gassification" corrections to the theory 3) "Real" gas vs. perfect gas treatment of the classical theory (to determine whether or not a simplified approach, containing known errors, might yet yield a better prediction of observed behavior.) 4) Use of liquid vs. solid droplet density and 5) the predictions of the theory in nozzles of different geometry. Figures 36 through 39 illustrate these comparisons and support the following conclusions:

1) All predictions based on values of σ/σ_∞, α and ξ of unity predict condensation at considerably lower supersaturation ratios than those observed experimentally.

2) Real Gas treatment of the classical theory yields a closer prediction than perfect gas treatment, and the "gassification" corrections are in the wrong direction. (Fig. 36)

3) Use of liquid rather than solid droplet density yields a prediction nearer to experimental results, lacking any better knowledge of

what corrections might be applied to surface energies of small CO_2 crystals. (Fig. 37)

4) The unmodified theory does extremely poorly in predicting any effects of nozzle geometry. (Fig. 38)

5) The shape of condensation profiles predicted by values of α and ξ of unity are in extreme disagreement with those observed experimentally. (Figs. 45 and 46)

2. Influence of Nucleation and Drop Growth Theory on Theoretical Predictions.

It is concluded that homogeneous nucleation and drop growth theory fail in their ability to predict observed condensation behavior of CO_2, unless some modification in values of the nucleation and drop growth parameters σ, ρ_L, α, and ξ can be independently established. Toward better understanding of how these parameters influence predicted condensation phenomena, and with the idea in mind of finding corrections for the prediction of CO_2 condensation, a series of calculations based on arbitrary variations of σ, ρ_L, α and ξ were made.

Figures 39 and 40 show typical pressure profiles for condensation of CO_2, for various condensation and thermal accommodation coefficients. Shown in the lower portion of the figures is the nucleation rate, indicating how nucleation rate remains high for longer duration when drop growth is retarded. This results in condensation clouds of greater particle density and smaller particle size than in the case of ready drop growth. In addition, smaller total deflection in the static pressures (from non-condensing), indicating lesser amounts of moisture, exist for the downstream portions of profiles having lower drop growth parameters.

An important observation in these figures is that, beyond a certain reduction in the drop growth parameters, appreciable proportions of moisture

may be present primarily from nucleation. This is manifested in the form of a so-called "ramp" deflection in the pressure profile to which additional drop growth effects are super-imposed. Thus, for example in Figure 39, for an assumed α of .10, variations in ξ from 1.0 to .3 and then to .1 have progressively less effect on the point of departure of the condensation curve, and for lower values of ξ, the nucleation "ramp" becomes increasingly apparent. The same behavior occurs for decreasing values of α, (shown for an assumed value of $\xi = .04$) in Figure 40. It would be possible to obtain a deflection curve involving only nucleation, if drop growth were set at zero.

Figure 41 illustrates the influence of increasing or decreasing the nucleation rate by changing the free energy of formation of nuclei. Indicated are variations in the surface energy from flat film liquid value, though similar changes may be introduced by varying the droplet density ρ_L. The important parameter in the nucleation rate exponent is (ρ^3/ρ_L^2), since, with knowledge of temperature and supersaturation ratio, the uncertainties of surface energy corrections, small cluster densities, and non-spherical geometry may all be contained in this term.

Two interesting features may be noted in Figure 41. First is the effects of higher downstream velocities, which tend to "wash out" the curves further downstream, and second, the important observation that, for α and ξ of unity, condensation results in a return to near-equilibrium conditions, seen by the fact that condensation commencing at any point in the nozzle results in the same pressure deflection immediately further downstream.

a) Onset of Condensation

As the previous figures suggest, influence of the drop growth coefficients upon the point of onset of condensation is relatively small compared to that caused by changes in surface tension. However, uncertainties in α

and ξ still have appreciable effect upon values of surface energy necessary to bring the predictions of theory into agreement with experiment. Figures 42, 43, and 44 show the corrections to flat film surface tension necessary to provide agreement between theory and experiment (based on fitting the data of nozzle II(2.20°)). If the uncertainty in the values of α and ξ for CO_2 crystals, is given limits of from perhaps .01 to 1.0 for each, then the respective surface energy corrections necessary may range from about 20% to 38% increases in the flat film surface tension. For the absolute lower bound of uncertainty on α and ξ of zero, the necessary correction in surface energy is reduced to +17%.

It is noted in these figures that the theoretical effects of nozzle geometry are increased to some extent by use of small, but non-zero values of the drop growth parameters, but that the theory in all cases predicts less effect than that recorded experimentally.

b) Profile Shapes

Figure 45 illustrates the pressure profiles for a single expansion corresponding to the same values of α and ξ, and corresponding σ determined above, and indicates an additional distinct failing of the theory in its description of the early stages of condensation. It is apparently impossible to reconcile the experimental downstream pressure deflections, which indicate a considerable degree of supersaturation, or departure from equilibrium, with the apparent rates of formation of moisture immediately after onset. When drop growth parameters are adjusted to bring theoretical profiles into agreement regarding the amount of downstream pressure deflection, then the upstream theoretical rate of formation of moisture lags considerably behind the experimental results.

This problem may result from some of the approximations discussed in the numerical calculations, or may in fact indicate some physical "arrest"

of the condensation process, perhaps due to decreasing mass or thermal accommodation characteristics of crystals which grow rapidly colder during their passage downstream.

c) Downstream Moisture Formation

For purposes of calculating the amounts of carbon dioxide that will form, or the downstream pressure variations which will occur during a nozzle expansion of CO_2, the following parameters were determined, having arbitrarily set thermal accommodation coefficient, α, at unity. There results, as a best description of the three nozzles, the profiles shown in Figures 46, 47, 48 and 49 for $\alpha = 1.0$, $\xi = .00008$, $\rho_L = 1.18$ gm/cm^3, $\rho/\rho_\infty = 1.18$. These drop growth parameters have no physical significance, and are presented only as an aid in determining approximate amounts of CO_2 moisture formation subsequent to the occurrence of condensation in a nozzle expansion.

The best compromise to profile shape soon after onset has been a recipe which yields theoretical profiles lagging behind and below the experimental data early in the condensation, and which then pass slightly to the other side of the data by about the same amount for the remainder of the profile.

The condensation data of Nozzle II (0.80) indicates the presence of ~~so~~ some cyclic axial variation in the pressure ratios of all profiles. This suggests that at this narrow angle, some departure from 2-dimensional flow may be interfering with the condensation process. Friction, or compression shocks may be creating these fluctuations, and would also result in decreased supersaturation ratios in this region, offering a possible explanation as to why considerably less moisture is forming than the recipe predicts for that nozzle.

3. Influence of Contamination

Computations attempting to determine the influence of contamination of vapor in nozzles were carried out at intervals during this investigation. Original calculations were based on perfect gas assumptions and values of α, ξ, and $\frac{\sigma}{\sigma_\infty}$ of unity, in an attempt to establish whether or not condensation could possibly be due to reasonable amounts of contamination present in the test vapor. Such contaminants might be present in the form of dust, charged particles, or the result of an earlier condensation of some other vapor. Contamination of this sort would be expected to cause earlier condensation than would occur if the test vapor were perfectly homogeneous.

Junge[27] presents data for typical size density distributions of contamination in atmosphere. Upper limits of particle concentration in dirty atmosphere of a large city reach values of 5×10^5 cm^{-3} for particles of size less than 10^{-5} cm (.1 micron), about 10^3 cm^{-3} for sizes from .1 to 1.0 microns and 1.0 cm^{-3} for particles exceeding one micron in size.

Typical profiles of supersaturation obtained for increasing concentrations of contamination with microscopic particles are shown in Fig. 50. Beyond a limiting concentration of particles, (depending on size) the supersaturation ratio obtains lesser and lesser values, until the flow reaches a state where it is close to equilibrium throughout the expansion, due to the ready formation of moisture on contaminant particles.

Subsequent to the establishment of the "recipe" described in the previous section, additional computations for both microscopic and macroscopic contamination were made.

The results are shown graphically in Figures 51 and 52, and are briefly summarized:

1) Micron-sized particles in excess of $10^8/$ cm^3 are required to influence the theoretical condensation of CO_2. This is at least 5 orders of

magnitude larger than upper atmospheric concentrations of particles of this size.

2) Microscopic particles, such as might occur from the precondensation of another vapor, of size the order of 10^{-7} cm are required in excess of $10^{12}/cm^3$ to influence theoretical condensation of CO_2.

3) No appreciable difference between empirically fitted real and perfect gas theories results.

4) The difference between amounts of contamination necessary to influence condensation in the rapid expansion of Nozzle I and the slow expansion of Nozzle II (0.80°) is approximately one order of magnitude, independent of particle size.

5) The empirically fitted recipe predicts necessary concentrations of particles roughly two orders of magnitude larger than that predicted using values of α, ξ, and σ/σ_∞ of unity.

When the curves of Fig 52 are replotted in terms of $\left[\log_{10} \frac{V_{CNTAM}}{V_{TOTAL}}\right]$, the two curves tend to move together, since the first curve to drop downward represents larger volume contamination. This results in fairly localized values of supersaturation ratio at occurrence of condensation as a function of *volume* contamination, regardless of particle size.

Applying the volume amounts of contamination of CO_2 in nitrogen presented by Willmarth and Nagamatsu,[64] and Arthur,[3] a computation of the predicted effects of theoretical influence of contamination on nitrogen was made, using values of α, ξ, and α/α_∞ of unity and perfect gas assumptions for nitrogen. The results are shown in Figure 53, for various size particles typical of cluster sizes for CO_2, indicating reasonably good agreement with their data. This is taken to indicate some substantiation of the above calculations for contamination in CO_2, perhaps within one or two orders of magnitude of the calculated contamination levels needed to influence homogeneous condensation.

V. SUMMARY OF FINDINGS AND CONCLUSIONS

A. Experimental Findings

1. Consistent data regarding the supersaturation of CO_2 at onset of condensation plus the shape of pressure profiles has been obtained for three different nozzles.

2. Interferogram photographs and an approximate theoretical estimation show agreement that the boundary layer in the nozzle throat was of the order .006" and substantiates the treatment of flow in the mid-stream as 1-dimensional isentropic flow.

3. Departures from perfect gas behavior by CO_2 in the P-T range tested are significant, and must be accounted for in the calculation of local conditions along an isentropic expansion. Density and static pressure measurements plus total pressure measurements for non-condensing flow indicate that the Plank Equation of State gives a good description of low temperature CO_2 behavior.

4. Rates of CO_2 expansion, as determined by nozzle geometry have a large influence upon the degree of supersaturation obtained prior to occurrence of condensation.

B. Application of Nucleation and Condensation Theory

1. Classical nucleation and drop growth theory, as applied herein, will reasonably predict the conditions at which onset of CO_2 condensation occurs, if flat film liquid surface energies are corrected by amounts within suggested ranges of uncertainty for small droplets or crystals. In these calculations a droplet density equal to that of CO_2 liquid at the triple point, 1.18 gm/cm^3, has been assumed.

2. The appropriate correction to surface energy is dependent upon the values of mass and thermal accommodation coefficients, ξ and α, and has a correction uncertainty of about 21% of flat film values for maximum possible

uncertainty in ξ and α. ($\frac{\sigma}{\sigma_\infty}$ = 1.17 for $\xi = \alpha = 0.0$; $\frac{\sigma}{\sigma_\infty}$ = 1.38 for $\xi = \alpha = 1.0$.) Consequently, the applicable value of the parameter ($\sigma^3/\rho_L{}^2$) to be applied to the nucleation rate equation corresponds to values of $(\sigma^3/\rho_L^2)(\rho_{L_o}{}^2/\sigma_\infty^3)$ which lie between the limits $(1.17)^3$ and $(1.38)^3$ where ρ_{L_o} = 1.18 gm./cm^3 and σ_∞ is the linear temperature dependent function $\sigma_\infty = 5.00 - .193T(^\circ C)$ dyne/cm.

3. Pressure profiles obtained experimentally indicate that considerably less moisture is forming than that necessary to return the mixture of vapor and condensate to near equilibrium values, or zero supersaturation downstream of the onset of condensation. Values of ξ and α necessary to produce agreement between the theory and experiment in this respect require that one or both of these parameters be considerably less than what are thought to be minimal values (about .01, for each.)

4. Even at their best empirical fit, classical nucleation and drop growth theory as applied herein do not seem to provide any means of describing the exact shape of the pressure profiles obtained experimentally or the extent of effects of geometry noted experimentally, These failings, in addition to that of B3, above, are thought to indicate inadequate or incorrect assumptions in the treatment of the drop growth calculations.

5. Application of the so-called "gassification" corrections to classical nucleation theory results in corrections in the wrong direction, unless even larger corrections in the surface energy of formation of CO_2 ice crystals (than indicated above) can be established. Use of solid, rather than liquid, droplet density in the parameter (σ^3/ρ_L^2) further increases the necessary corrections to surface energies required to provide agreement with experiment.

6. The influence of dirt particles or other foreign particles on the

condensation of CO_2, and probably most other gases, may be completely disregarded in supersonic nozzles, unless the particles result from the precondensation of another gas in the stream. Amounts of micron-sized particles necessary to influence CO_2 condensation are about five orders of magnitude in excess of upper atmospheric limits of concentration, and particles of the order of 20 a° are necessary in excess of about 10^{12} particles/$cm.^3$ to influence homogeneous nucleation and condensation. Testing the condensation of nitrogen with pre-condensed particles of CO_2 in quantities mentioned by Willmarth and Nagamatsu, and Arthur, yields theoretical predictions which are in reasonable agreement with their experimental observations.

7. Additional knowledge of thermal and mass accommodation coefficients are necessary to allow better testing of homogeneous nucleation and condensation theory. In addition, comprehensive testing of the theory will await some better establishment of surface energy corrections for small particles. Until this information becomes available and an established treatment of nucleation and drop growth can be applied with confidence to many vapors, "recipe" fitting may provide the best means for predicting nozzle condensation behavior.

VI. SUGGESTIONS FOR FURTHER STUDY

One of the greatest difficulties in application of experimental results to a meaningful test of theoretical predictions results from the uncertainties in value of many of the important variables and parameters contained in nucleation and drop growth theory. Consequently, any methods or devices of experimentation which would decrease any of the uncertainties, or the effects of uncertainty, of such quantities as σ, ρ_L, α, ξ, local temperature and the gas dynamics in general would be of great assistance. One means of proceeding in this direction is to contain the test gas within large quantities of another gas which is non-condensing in the region of interest of the test gas, and whose gas properties are well-known, preferably being as near those of a perfect gas as possible. An immediate benefit of this is to provide a means of accurately determining local properties at all points of the isentrope with ease, since, the temperature of the test gas should be that of the ideal "carrier" gas, which dominates the gas dynamics. Second, the influence of thermal accommodation is greatly reduced due to the fact that the huge preponderance of incident molecules upon the surface of a formed droplet are those of "carrier" gas, and hence are reflected. The drop is consequently kept at or nearly at environmental temperature regardless of the value of α. Hence, there are advantages to be gained by testing gases for which these uncertainties exist (the huge preponderance of all gases) in a carrier stream of such gases as nitrogen, helium, or dry air. Several complications arise from this method, including the need for very precise measurement of mass fraction of test gas in the mixture, and more sensitive instrumentation to detect the lessened effects of condensation upon the gas properties.

Highly steady flow systems would aid in obtaining the accuracy necessary.

With regard to some of the uncertainties pertaining to CO_2, it would be of considerable interest to determine whether or not the experimental behavior of condensation is influenced by establishing liquid rather than ice formation of condensate particles. This could presumably be accomplished by raising pressure levels to a point where condensation occurs above the ice point, 75.1 psia. This would necessitate stagnation pressure in the range of 175 - 250 psia, mass rates of flow and a source of CO_2 which are proportionally larger, heavier construction of some important fixtures in the system, (such as the stagnation tank) and a means of pressure profile procurement other than manometer board.

It is felt that interferometric means of study offer enough advantages, particularly with more toxic or reactive gases, to warrant further application to study of condensation in nozzles. The inability to distinguish interference lines in the upstream region of the nozzle encountered at high pressure levels in this investigation could possibly be solved by facilitating higher camera shutter speeds (1/150 sec., the maximum possible, was used in these studies) or by establishing wall temperatures which are close to stream stagnation temperature. Two-dimensional nozzles, where interferometric study could be successfully employed, would decrease the problems of instrumentation and would be readily adaptable to studies of light scattering and polarization, yielding experimental information regarding droplet sizes. Interferometric photos involving condensation, although not applied in this report, were obtained, and showed interference bands very clearly within the region of condensation,

this region being marked plainly by the decreased light intensity resulting from the presence of the ice cloud.

Light scattering or other techniques which yield information regarding the average size of the ice particles at their initial appearance and after subsequent downstream growth would be very useful. Since, as previously mentioned, there is some indication that nucleation is the major contributor to moisture in its early stages of formation for CO_2, this information might be directly related to the critical cluster size of CO_2.

Additional investigation of crystal thermal and mass accommodation coefficients would be of help in further establishing the apparent indication from this investigation that either one or both have very low values for crystalline CO_2 at low temperatures. The carrier gas technique previously mentioned could isolate the influence of α and might facilitate a better means of studying ξ and its role in condensation.

BIBLIOGRAPHY

1. Alty, T. - "The Interaction of Vapor Molecules with a Crystal Surface" - Proc. Roy. Soc. (London) - Vol. 161A, pp. 68 - 79, (1937).

2. Alty, T. and MacKay, C. A. - "The Accommodation Coefficient and the Evaporation Coefficient of Water" - Proc. Roy. Soc. (London) - Vol. 149A, pp. 104 - 116, (1935)

3. Arthur, P. D. - "Effects of Impurities on the Supersaturation of Nitrogen in a Hypersonic Wind Tunnel" - Ph.D. Thesis - California Institute of Technology, (1952).

4. Bailey, Harry E. - "Equilibrium Thermodynamic Properties of Carbon Dioxide" - NASA, SP-3014, (1963).

5. Barnard, A. J. - Proc. Roy. Soc. (London) - A220, p. 132, (1953).

6. Becker, R. and Döring, W. - Ann. der Physics - Vol. 25, p. 719, (1935).

7. Binnie, A. M. and Green, T. R. - Proc. Roy. Soc. (London) - Vol. 181, p. 134, (1942).

8. Bogdonoff, S. M. and Lees, L. - "Study of the Condensation of the Components of Air in Supersonic Wind Tunnels" = Part I: "Absence of Condensation and Tentative Explanation" - Princeton Univ. Aeronaut. Eng. Lab. Rept. #146, (1949).

9. Bondi, A. - "The Spreading of Liquid Metals on Solid Surfaces" - Chem. Rev., Vol. 52, No. 2, pp. 417 - 458, April 1953.

10. Camac, M. - "CO_2 Relaxation Processes in Shock Waves" - AVCO RR 194, (BSD-TDR-64-96), October 1964.

11. Chen, L. H. - "Thermodynamic Properties of CO_2, Papers, Lafayette, Indiana - pp. 358 - 369, (1959) or (Electric Boat, Groton, Conn. - GA 1038, p. 157, (1959)).

12. Courtney, W. G. - Jour. Chemistry and Physics - Vol. 34, p. 2018, (1962).

13. Courtney, W. G. - "Re-Examination of Nucleation and Condensation of Water" (not yet published).

14. Dean, R. C. Jr., - *Aerodynamic Measurements*, M. I. T. Gas Turbine Laboratory - Chapter IX: DeFrate, Barry and Bailey - "Optical Techniques", pp. 167 - 208, (1952).

15. Din, F. - *Thermodynamic Functions of Gases* - Vol. 1 - British Oxygen Co., Ltd., (1956).

16. Dorsch, R. G. and Hacker, P. T. - "Photomicrographic Investigation of Spontaneous Freezing Temperatures of Supercooled Water Droplets" - NACA TN-2142, July 1950.

17. Faro, I., Small, T. R. and Hill, F. K. - Jour. Applied Physics - Vol. 34, p. 40, (1952).

18. Feder, J.*, Russell, K. C. **, Lothe, J., Pound, G. M. - "Homogeneous Nucleation and Growth of Droplets in Vapors"; toward partial fulfillment of degrees - (*) Cand. Real., Fysik Institute, Univ. of Oslo; (**) Ph.D., Fac. of Eng. & Sci., Carnegie Institute of Technology, (1964).

19. Frenkel, J. - *Kinetic Theory of Liquids* - Oxford Univ. Press, (1946).

20. General Dynamics Corp., Liquid Carbonics Div. - "Physical Properties of Carbon Dioxide and Temperature-Entropy Chart" - Tech. Bulletin #48.

21. *Handbook of Chemistry and Physics*, 45th. Ed., Chemical Rubber Co., (1964).

22. Hill, P. G., Witting, H. and Demetri, E. P. - ASME Trans., Jour. of Heat Transfer - p. 303, November 1963.

23. Hill, P. G. - "Homogeneous Nucleation of Supersaturated Water Vapor in Nozzles" - M. I. T. Gas Turbine Laboratory Report #78, January 1965.

24. Hilsenrath, J.; Becket, C. W.; Benedict, W. S.; Fana, L.; Hoge, H. J.; Masi, J. F.; Nuttal, R. L.; Touloukian, Y. S. and Wooley, H. W. - "Tables of Thermal Properties of Gases" - NBS Cir. 564, U. S. Dept. of Commerce, (1955).

25. Hirth, J. P. - Ann. N. Y. Academy of Science - Vol. 101, p. 805, (1963).

26. Holley, Worlton and Zeigler - Compressibility Factors - from the Beattie-Bridgman Equation for H_2, N_2, O_2, CO_2, NH_3, and other gases - U. S. Atomic Energy Commission, Los Alamos, La-2271, 51 pp., (1959).

27. *International Critical Tables* - McGraw-Hill Book Co., New York -(1926-30).

28. Jorgensen, L. H. and Redmond, R. J. - Charts for Equilibrium Flow Properties of CO in Hypervelocity Nozzles - NASA SP-3015, (1965).

29. Junge, C. E. - *Air Chemistry & Radioactivity* - Academic Press (1963).

30. Kantrowitz, A. R., - "Effects of Heat Capacity Lag in Gas Dynamics" - NACA Wartime Report L-457, January 1944.

31 Kantrowitz, A. R. and Huber, P. W. - "Heat Capacity Lag in Turbine Working Fluids" - NACA Wartime Report L-21, May 1944.

32. Kantrowitz, A. R., - Physics Review - Vol. 77, p. 572, (1950).

33. Katkhe, O. I. - "Equation of State of CO_2" - (Eng. Inst. Merchant Marine, Odessa) - Inshener, Fiz. Zhur., Akad. Nauk Belorus,U.S. S. R. - Vol. 1, No. 5, pp. 95 - 98, (1958).

34. Keenan, J. H. and Kaye, J. - *Gas Tables* - Wiley & Sons, Inc. - New York - (1948).

35. Kennedy, G. C. - American Journal of Science - 252, 225, (1954).

36. Ladenburg, R., Van Voorhis, C. C. and Winckler, J. - "Interferometric Study of Supersonic Phenomena" - NavOrd Report 69-46, (1946).

37. Liley, P. E. - Jour. Chem. and Eng. Data - Vol. 4, No. 3, p. 238, July 1959.

38. Lothe, J and Pound, G. M. - Jour. Chemistry & Physics - Vol. 36, p. 2080, (1962).

39. Lowry and Erikson - Jour. Am. Chem. Soc. - Vol. 49, p. 2729, (1927).

40. Maass, O. and Barnes - Proc. Roy. Soc. (London) - Ser. A., Vol. 111, p. 224, (1926).

41. Maass, O. and Mennie, J. H. - Proc. Roy. Soc. (London) - Ser. A., Vol. 110, p. 198, (1926).

42. Matheson Company Inc. - *Matheson Gas Data Book* - James Grey, Inc. (1961).

43. Nichols, L. R., Nozek, S. M, Winzig, C. H. and Goldman, L. J. - "Experimental Determination of Sodium Vapor Expansion Characteristics with Inert Gas Injection Pressure Measuring Technique" - NASA TN D-2276, April 1964.

44. Oriani, R. A. and Sundquist, B. E. - Jour. Chemistry & Physics - Vol. 38, p. 2082, (1963).

45. Oswatitsch, K. - Z. Angew. Math. und Mech. - Vol. 22, p. 1, (1942).

46. Paul, B. - ARS Journal - Vol. 32, No. 9, p. 1321, (1962).

47. Plank, R. and Kuprianoff, J. - Z. Ges. Kalteind. Beih. - Vol. 1, No. 1, (1929).

48. Probstein, R. F. - "Time Lag in the Self-Nucleation of a Supersaturated Vapor" - Jour. Chem. Physics - Vol. 19, No. 5, p. 619, May 1951.

49. Prueger, W. - "Die Verdampfungsgeschwindigkeit der Fluessigkeiten" - Z. Physik - Vol. 115, pp. 202 - 244, (1940).

50. Quinn, E. L. and Jones, C. L. - *Carbon Dioxide* - Reinhold Publishing Co. - New York, (1936).

51. Raymond, J. L. - "Thermodynamic Properties of Carbon Dioxide to 24,000°K with Possible Application to the Atmosphere of Venus" - RM-2292, The Rand Corporation, November 1958.

52. Reisse, R. - Jour. Chemistry & Physics - Vol. 20, p. 1216, (1952).

53. Rodebush, W. H. - Ind. and Eng. Chem. - Vol. 44, No. 6, p. 1289, June 1952.

54. Rossbach, R. J. - "Critical Flow of Potassium Vapor Through Instrumented Converging-Diverging Nozzle" - ASME Rep. 65-GTP-22, January 1965.

55. Shapiro, A. H. - *Dynamics and Thermodynamics of Compressible Fluid Flow* - Ronald Press - New York - Vol. II, p. 887, (1953).

56. Stever, H. G. and Rathbun, K. C. - "Theoretical and Experimental Investigation of Condensation of Air in Hypersonic Wind Tunnels" - NACA Tech. Note 2559, (1951).

57. Stodola, A. - *Steam and Gas Turbines* - McGraw-Hill Pub. Co. - pp. 117 - 128, 1034 - 1073, (1927).

58. Volmer, M. and Flood, H. - Z. Phys. Chem. - Vol. A170, p. 273, (1934).

59. Vukalovich, M. P. and Altunin, V. V. - "Experimental Research on PVT Relation of CO_2" - Teploenergetika, Vol. 6, No. 11, pp. 58 - 65, (1959).

60. Wachman, H. Y. - "The Thermal Accommodation Coefficient: A Critical Survey" - ARS Journal, Vol. 32, pp. 2 - 12, (1962).

61. Wakeshima, H. - Phys. Soc. of Japan - Vol. 10, No. 2, p. 141, (1955).

62. Wegener, P. P. - "Condensation Phenomena in Nozzles" - AIAA Preprint No. 63, p. 509, (1963).

63. Wegener, P. P. and Pouring, A. A. - Physics of Fluids - Vol. 7, p. 352, (1964).

64. Willmarth, W. W. and Nagamatsu, H. T., - Jour. Applied Physics - Vol. 23, p. 1089, (1952).

65. Yang, W. T. - "A Study of Homogeneous Nucleation from Vapor to Droplets" Doctoral Dissertation - Yale University, (1963).

66. Yellott, J. I. - Trans. ASME, Vol. 56, p. 411, (1934).

67. Yellott, J. I. and Holland C. K. - Trans. ASME, Vol. 59, p. 171, (1937).

68. Zeldovich, J. J. - Exp. Theor. Phys. (USSR), Vol. 12, p. 525, (1942).

APPENDIX A.

LIST OF FIGURES AND TABLES

Figure 1	Typical Co-Existence Lines Versus Isentropic Expansion Paths	A1
Table 1	Typical Values of h_{fg}/C_p for Various Gases	A2
Figure 2	Schematic Arrangement of Test Apparatus	A3
Figure 3	General View of Test Apparatus	A4
Figure 4	Stagnation Tank, Pressure Gauge and Thermocouple Location	A5
Figure 5	Stagnation Tank with End Plate Removed, Showing Screen and Filter Bag Containing Steel Wool	A6
Figure 6	Nozzle I Showing Total Pressure Tube in Test Position	A7
Figure 7	Assembly View and Geometry of Nozzle I	A8
Figure 8	Detail of Nozzle II	A9
Figure 9	Nozzle I; Disassembled, Showing Optical Glass and Metal Pressure Tap Plate Side Walls, and Metal Clamp Bars	A10
Figure 10	Nozzle II; Disassembled, Showing Hinged Upper and Lower Walls, and Pressure Tap Plates 1 and 2	A11
Figure 11	Interferometric Photographs for Test 1 of Density Profiles	A12
Figure 12	Interferometric Photographs for Test 2 of Density Profiles	A13
Figure 13	Graphical Representation of Determination of Fringe Shifts - Test No. 1	A14
Figure 14	Comparison of the Plank Equation of State and Data Upon Which It Was Formulated	A15
Table 2	Carbon Dioxide Enthalpy Tables	A16
Table 3	Interferometric Measurement and Calculation of Density (Test No. 1)	A19
Table 4	Interferometric Measurement and Calculation of Density (Test No. 2)	A20
Figure 15a	Nozzle I Profiles of Measured Pressure Ratio and Isentropically Converted Measured Density Ratio, Test No. 1	A21
Figure 15b	Measured Versus Theoretical Pressure and Density Ratios, Test No. 1	A22
Figure 16a	Nozzle I Profiles of Measured Pressure Ratio and Isentropically Converted Measured Density Ratio, Test No. 2	A23
Figure 16b	Measured Versus Theoretical Pressure and Density Ratios, Test No. 2	A24

Figure 17 Experimental Normal Shock Characteristics of CO_2 A25

Figure 18 Predicted Normal Shock Characteristics of CO_2-- Plank Equation of State A26

Figure 19 Comparison of Predicted CO_2 Isentropes A27

Figure 20 Comparison of Predicted CO_2 Isentropes A28

Figure 21 Constant Nucleation Rate Profiles of Classical Nucleation Theory for CO_2, $\frac{\sigma}{\sigma_\infty} = 1.00$ A29

Figure 22 Experimental Pressure Ratio Profiles. Nozzle I, Pressure Plates 1 & 2 A30

Table 5 Pressure Data for Figure No. 22 A31

Figure 23 Experimental Pressure Ratio Profiles. Nozzle I, Pressure Plates 1 & 2 A32

Table 6 Pressure Data for Figure No. 23 A33

Figure 24 Experimental Pressure Ratio Profiles. Nozzle II, Pressure Plate 1, Angle of Divergence = 2.18° A34

Table 7 Pressure Data for Figure No. 24 A35

Figure 25 Experimental Pressure Ratio Profiles. Nozzle II, Pressure Plate 2, Angle of Divergence = 2.18° A36

Table 8 Pressure Data for Figure No. 25 A37

Figure 26 Experimental Pressure Ratio Profiles. Nozzle II, Pressure Plate 2, Angle of Divergence = 2.22° A38

Table 9 Pressure Data for Figure No. 26 A39

Figure 27 Experimental Pressure Ratio Profiles. Nozzle II, Pressure Plate 2, Angle of Divergence = 2.22° A40

Table 10 Pressure Data for Figure No. 27 A41

Figure 28 Experimental Pressure Ratio Profiles. Nozzle II, Pressure Plate 2, Angle of Divergence = 2.22° A42

Table 11 Pressure Data for Figure No. 28 A43

Figure 29 Experimental Pressure Ratio Profiles. Nozzle II, Pressure Plate 2, Angle of Divergence = 0.80° A44

Table 12 Pressure Data for Figure No. 29 A45

Figure 30 Experimental Pressure Ratio Profiles. Nozzle II, Pressure Plate 2, Angle of Divergence = 0.80° A46

Table 13 Pressure Data for Figure No. 30 A47

Figure 31 Condensation Data. Local Conditions at Onset of Condensation A48

Table 14 Experimental Data. Local Conditions at Onset of Condensation A49

Figure 32 Comparison of Nozzle Geometries and Non-Condensing Pressure Profiles A50

Figure 33 Spontaneous Freezing Temperature of Supercooled Water Droplets on Platimun and Copper Surfaces A51

Figure 34 Low Temperature Vapor Pressure Values A52

Figure 35 Presence of Moisture in a Typical Condensation Profile A53

Figure 36 Onset of Condensation, Nozzle II, Comparison of Theory and Experiment A54

Figure 37 Influence Upon Theory of Use of Liquid Versus Solid Droplet Density. Nozzle II(2.20°) A55

Figure 38 Predicted Influence of Nozzle Geometry on Occurrence of Condensation. Using $\xi, \alpha, \sigma/\sigma_\infty$ of Unity. $\rho_L = 1.18$ gm/cm^3 A56

Figure 39 Influence of Mass Accommodation Coefficient on Condensation of CO_2, (Theoretical) A57

Figure 40 Influence of Thermal Accommodation on Theoretical Condensation of CO_2 A58

Figure 41 Theoretical Influence of Surface Tension on Condensation of CO_2 A59

Figure 42 Theoretical Occurrence of .1% Moisture for $\alpha = \xi = 1.00$, Corrected Surface Tension $\sigma/\sigma_\infty=1.38$ A60

Figure 43 Theoretical Occurrence of .1% Moisture for $\alpha = \xi = .01$, Corrected Surface Tension $\sigma/\sigma_\infty=1.20$ A61

Figure 44 Theoretical Occurrence of .1% Moisture for $\alpha = \xi = 0.0$, Corrected Surface Tension $\sigma/\sigma_\infty=1.17$ A62

Figure 45 Comparison of Experimental and Theoretical Pressure Profiles for Various ξ and α A63

Figure 46 Comparison of Empirically Fitted Theoretical Condensation and Experimental Data - Nozzle I. $\alpha = 1.0$, $\xi = .00008$, $\sigma/\sigma_\infty = 1.18$ A64

Figure 47 Comparison of Empirically Fitted Theoretical Condensation and Experimental Data, Nozzle II (2.20°) Pressure Tap Plate No. 1. $\alpha = 1.00$, $\sigma/\sigma_\infty = 1.18$, $\xi = .00008$ A65

Figure 48 Comparison of Empirically Fitted Theoretical Condensation and Experimental Data - Nozzle II (2.20°) $\alpha = 1.0$, $\xi = .00008$, $\sigma/\sigma_\infty = 1.18$ A66

Figure 49 Comparison of Empirically Fitted Theoretical Condensation and Experimental Data - Nozzle II (0.80°) $\alpha = 1.0$ $\xi = .00008$, $\sigma/\sigma_\infty = 1.18$ A67

Figure 50 Theoretical Influence of Contamination on Condensation of CO_2 A68

Figure 51 Theoretical Influence of Macroscopie Contamination on Condensation of CO_2, Using Theory Empirically Fitted to Homogeneous Condensation Data A69

Figure 52 Theoretical Influence of Microscopic Contamination on Condensation of CO_2, Using Theory Empirically Fitted to Homogeneous Condensation Data. $\xi = .00008$, $\sigma/\sigma_\infty =1.18$, $\rho_L = 1.18$ GM./CM A70

Figure 53 Theoretical Effect of CO_2 Contamination on Nitrogen Condensation. Supersaturation at .1% Moisture A71

Table 15 Values of γ_a, γ_b and z Used to Match Real Gas Isentropes A72

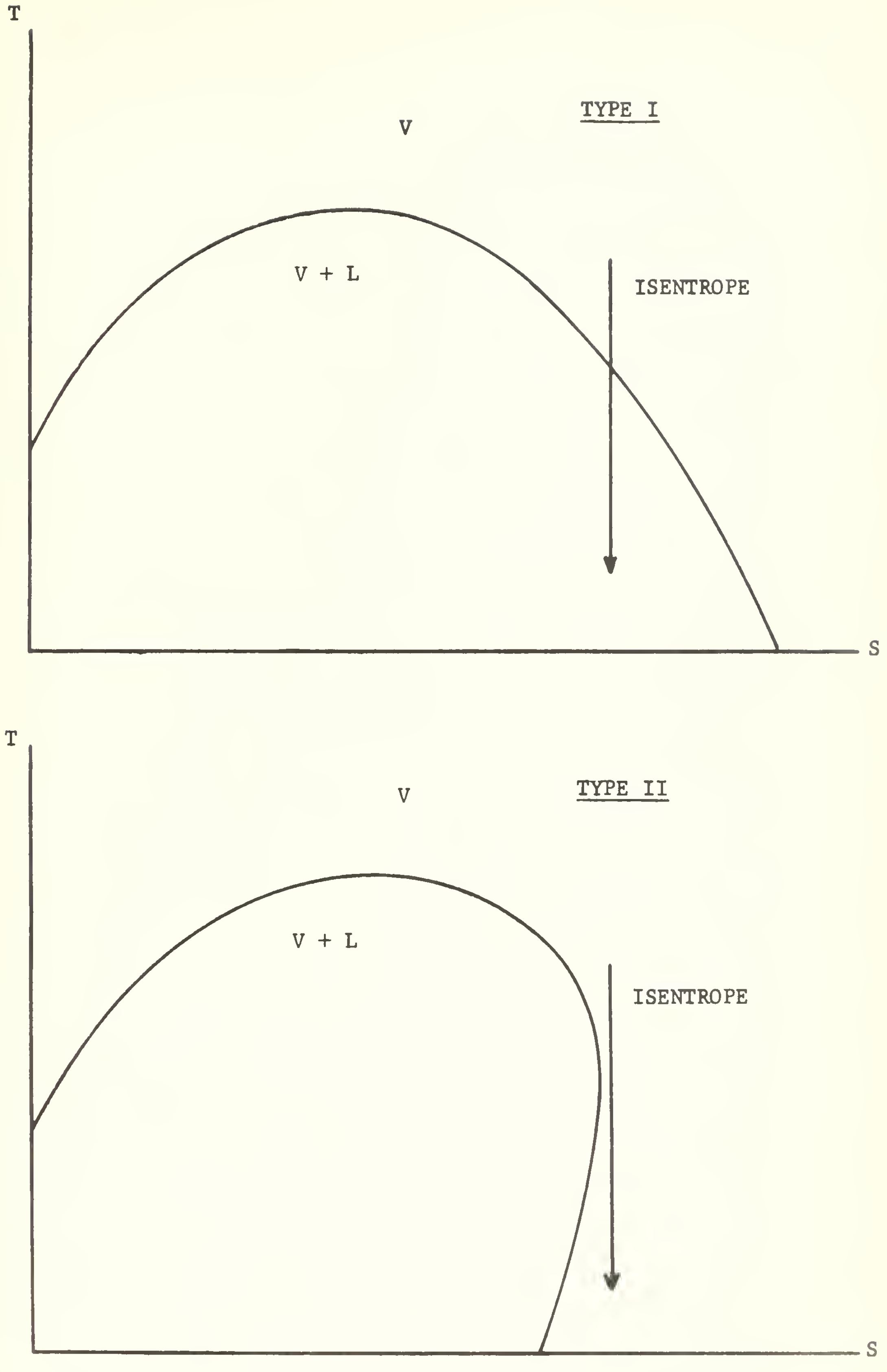

FIGURE 1, TYPICAL CO-EXISTENCE LINES VERSUS ISENTROPIC EXPANSION PATHS.

TABLE 1

TYPICAL VALUES OF h_{fg}/C_p FOR VARIOUS GASES

FLUID	(h_{fg}) Lat. Heat of Vap. BTU/lbm	C_p Specific Heat BTU/lbm-°F	h_{fg}/C_p	T_s @ 1 atm
C_2H_6O (Ethyl Al.)	406	.342 ~~°F~~	1.19×10^3	173 °F
CH_4O (Methyl Al.)	482	.295 ~~°F~~	1.63×10^3	152 °F
H_2O	840	.445 ~~°F~~	1.89×10^3	212 °F
C_6H_6 (Benzene	172	.280 ~~°F~~	6.15×10^2	175.3 °F
$CHCl_2F$ (Genetran 21)	140.15	.140 ~~°F~~	1.01×10^3	48 °F
NH_3 (Ammonia)	589.4	.523 ~~°F~~	1.12×10^3	- 28 °F
BCl_3 (Boron Chloride)	68.8	.127 ~~°F~~	5.4×10^2	54.5 °F
Butene-1	168	.382 ~~°F~~	4.4×10^2	20.7 °F
Butene-2	179	.375 ~~°F~~	4.78×10^2	38.7 °F
CO_2	247	.198 ~~°F~~	1.24×10^3	-109.3 °F
Freon-22	100	.152 ~~°F~~	6.6×10^2	- 41 °F
Difluoroethylene	276	.224 ~~°F~~	1.23×10^3	-117 °F
Dimethylamine	252	.374 ~~°F~~	6.74×10^2	44.4 °F
Ethyl Chloride	164	.244 ~~°F~~	6.74×10^2	54.3 °F
Ethylene Oxide	250	.268 ~~°F~~	9.31×10^2	51.3 °F
Isobutane	158	.355 ~~°F~~	4.46×10^2	10.9 °F
Methyl Acetylene	234	.357 ~~°F~~	6.55×10^2	- 9.6 °F
Monethylamine	260	.330 ~~°F~~	7.87×10^2	61.8 °F
Monmethylamine	358	.320 ~~°F~~	1.12×10^3	20.6 °F
SO_2	171	.117 ~~°F~~	1.45×10^3	14 °F
Freon-11	78.3	.135 ~~°F~~	5.8×10^2	74.8 °F

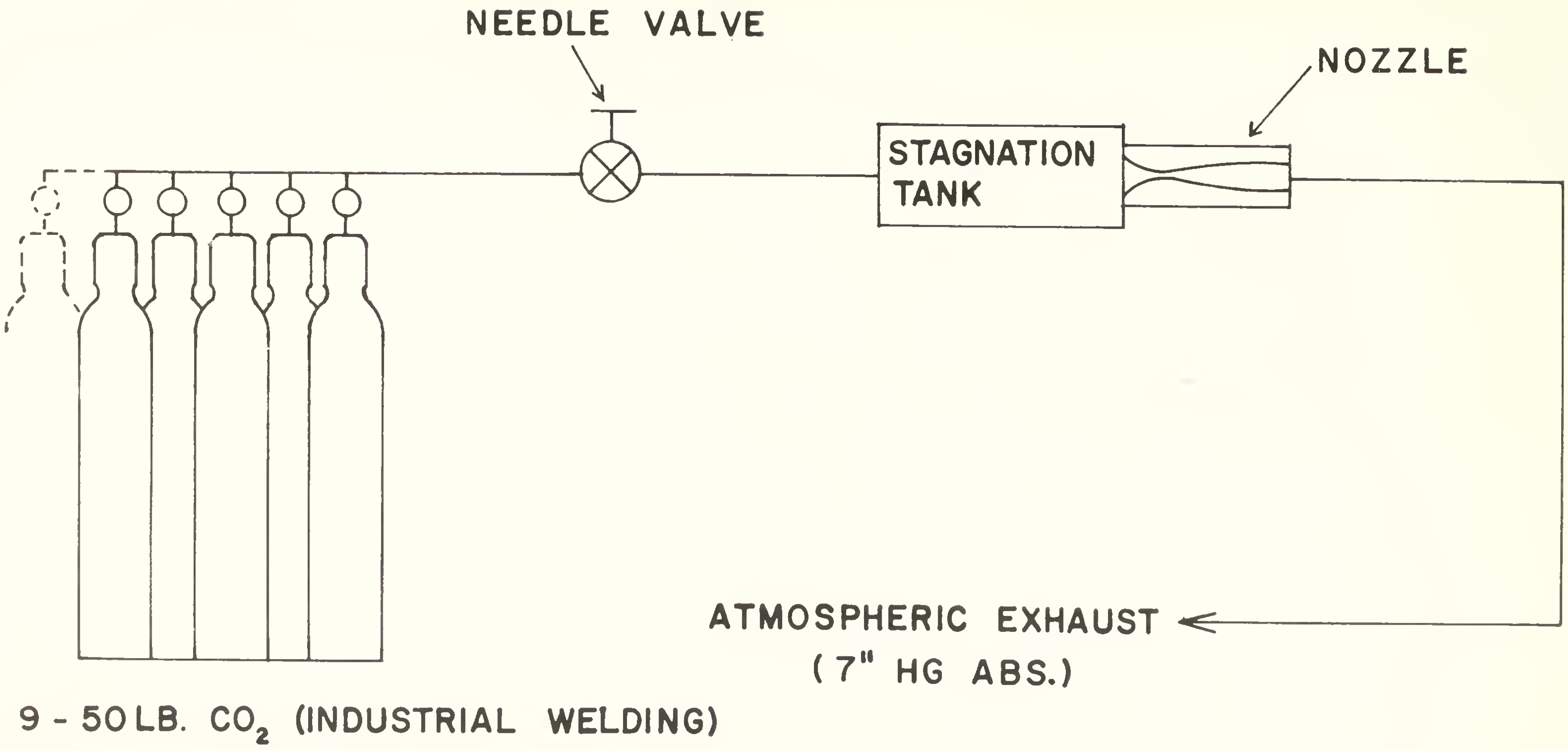

FIG 2 SCHEMATIC ARRANGEMENT OF TEST APPARATUS

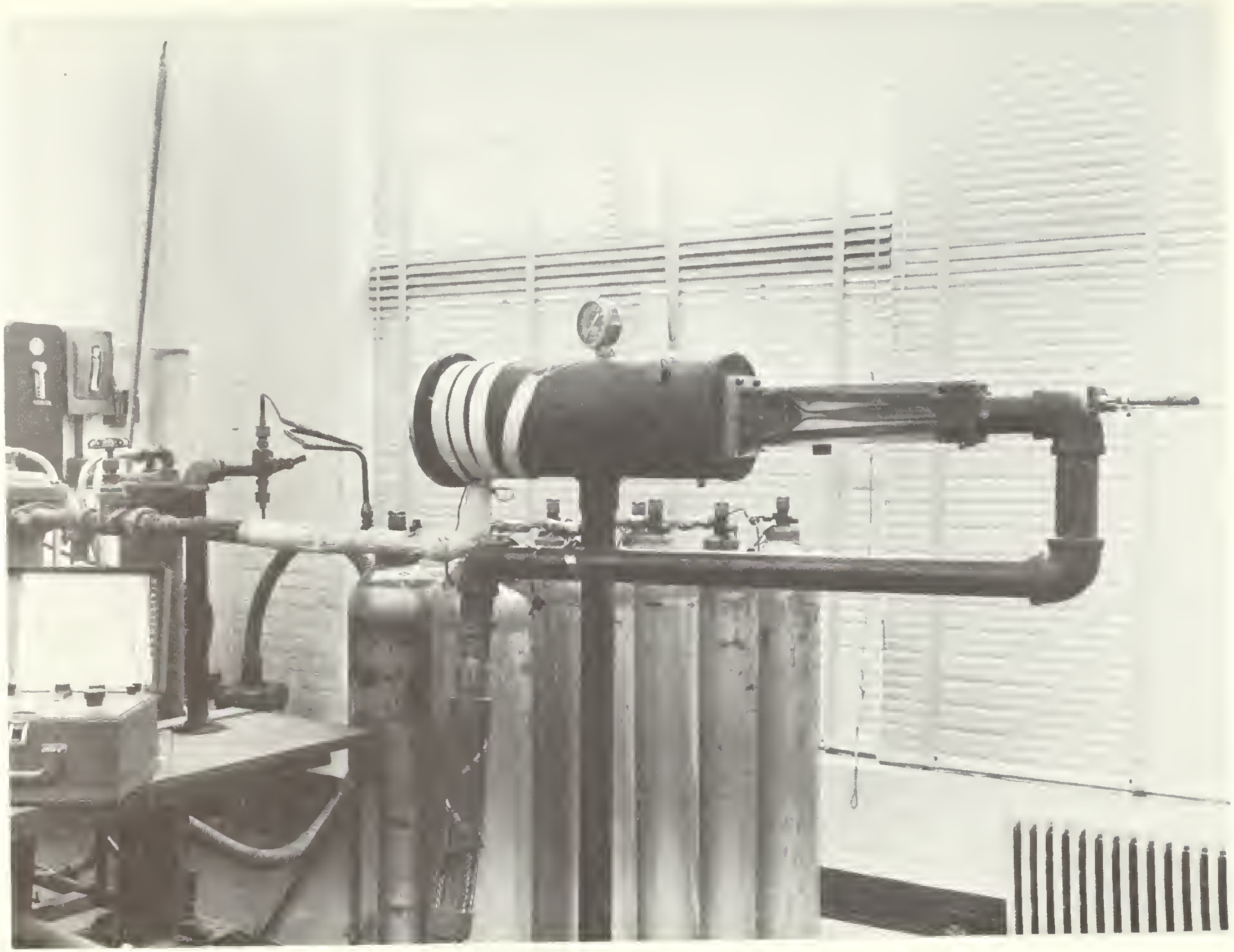

FIGURE 3, GENERAL VIEW OF TEST APPARATUS

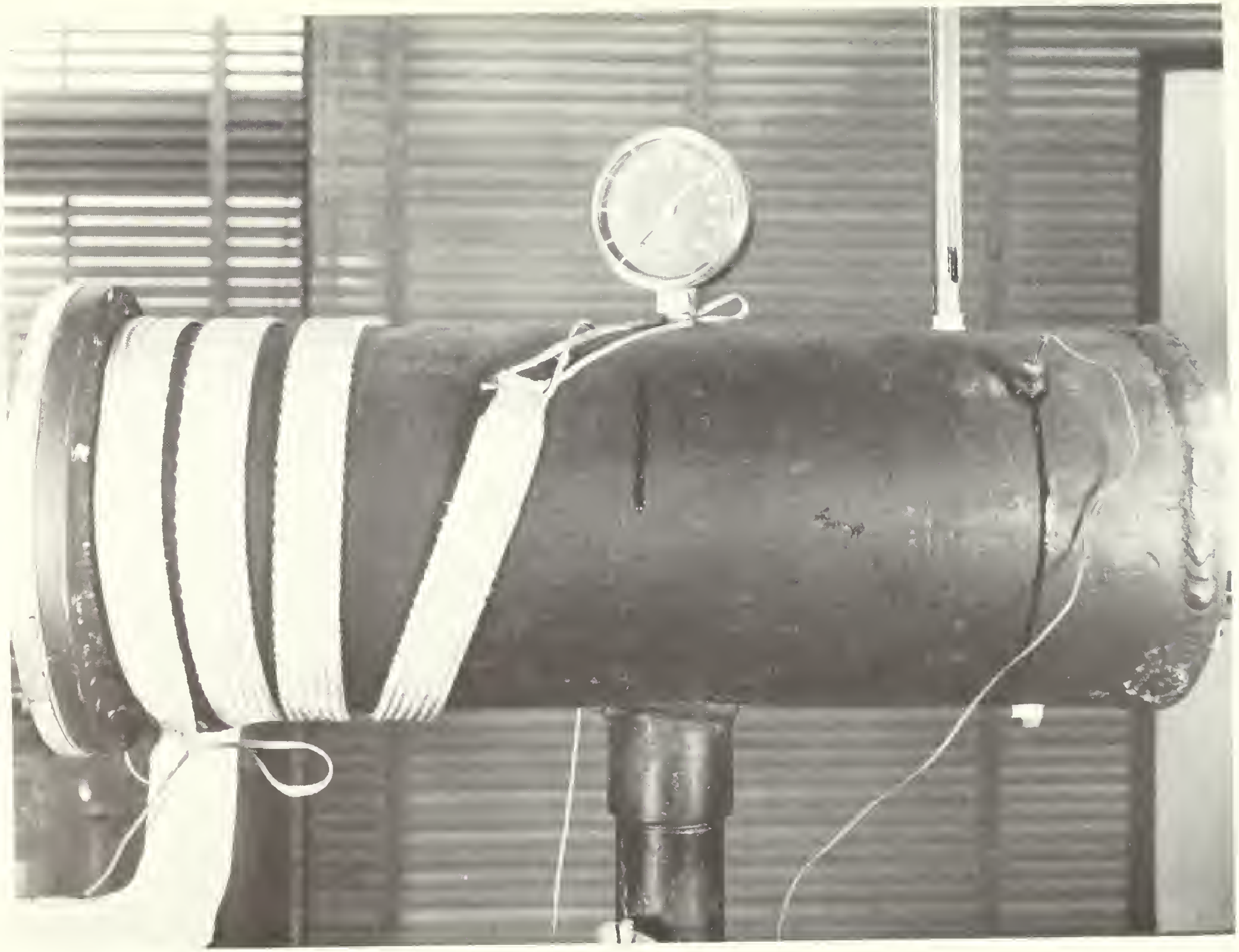

FIGURE 4, STAGNATION TANK, PRESSURE GAUGE AND THERMOCOUPLE LOCATION.

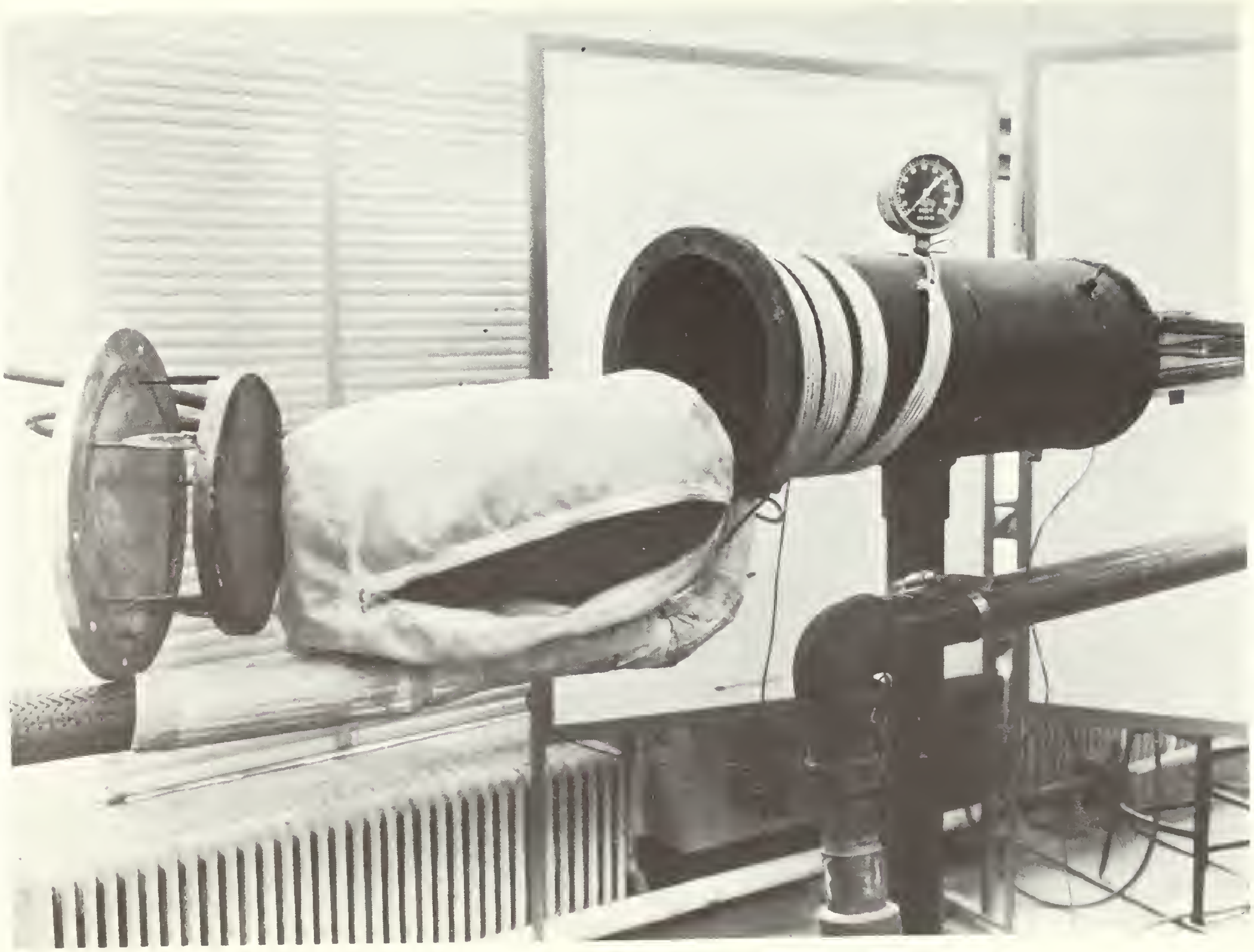

FIGURE 5, STAGNATION TANK WITH END PLATE REMOVED, SHOWING SCREEN AND FILTER BAG CONTAINING STEEL WOOL.

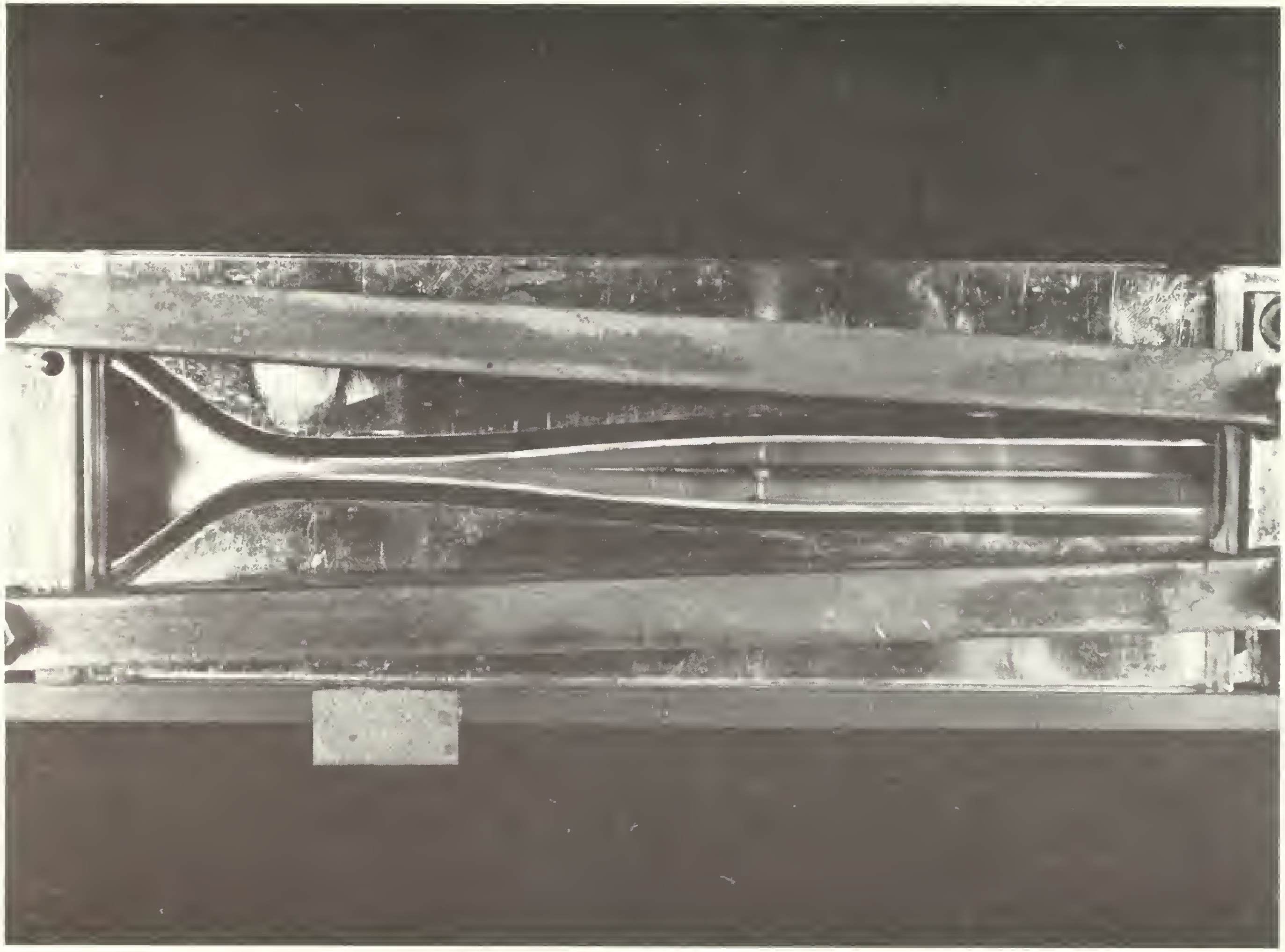

FIGURE 6, NOZZLE I SHOWING TOTAL PRESSURE TUBE IN TEST POSITION.

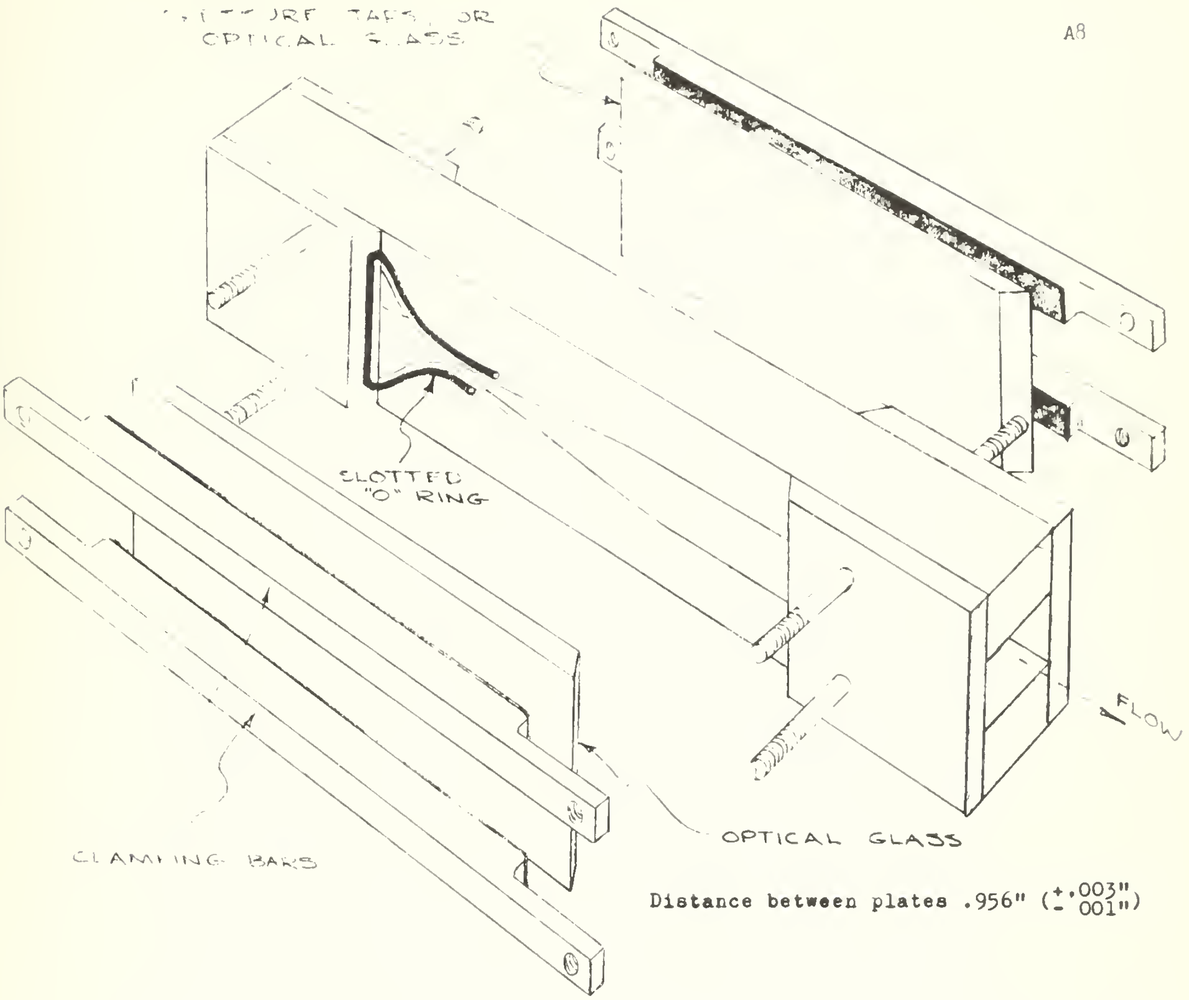

Distance between plates .956" ($^{+.003"}_{-.001"}$)

x(±.005)	b	x	b	x	b	x	b	x	b
0	1.0	1.11	.101	1.325	.055	2.07	.074	3.11	.225
.63	.550	1.15	.090	1.350	.054	2.15	.078	3.23	.250
.84	.300	1.165	.086	1.400±.015	.0531±.0001	2.21	.086	3.51	.300
.89	.250	1.190	.078	1.500	.054	2.27	.090	3.86	.358
.92	.225	1.200	.074	1.570	.055	2.38	.101	4.27	.404
.95	.200	1.220	.069	1.620	.056	2.46	.110	4.67	.428
.97	.175	1.235	.066	1.670	.057	2.52	.120	5.20	.432
1.01	.150	1.250	.063	1.735	.060	2.63	.135	on	"
1.04	.135	1.270	.060	1.820	.063	2.71	.150		
1.07	.120	1.290	.057	1.920	.066	2.84	.175		
1.09	.110	1.305	.056	1.990	.069	2.98	.200		

FIGURE 7, ASSEMBLY VIEW AND GEOMETRY OF NOZZLE I.

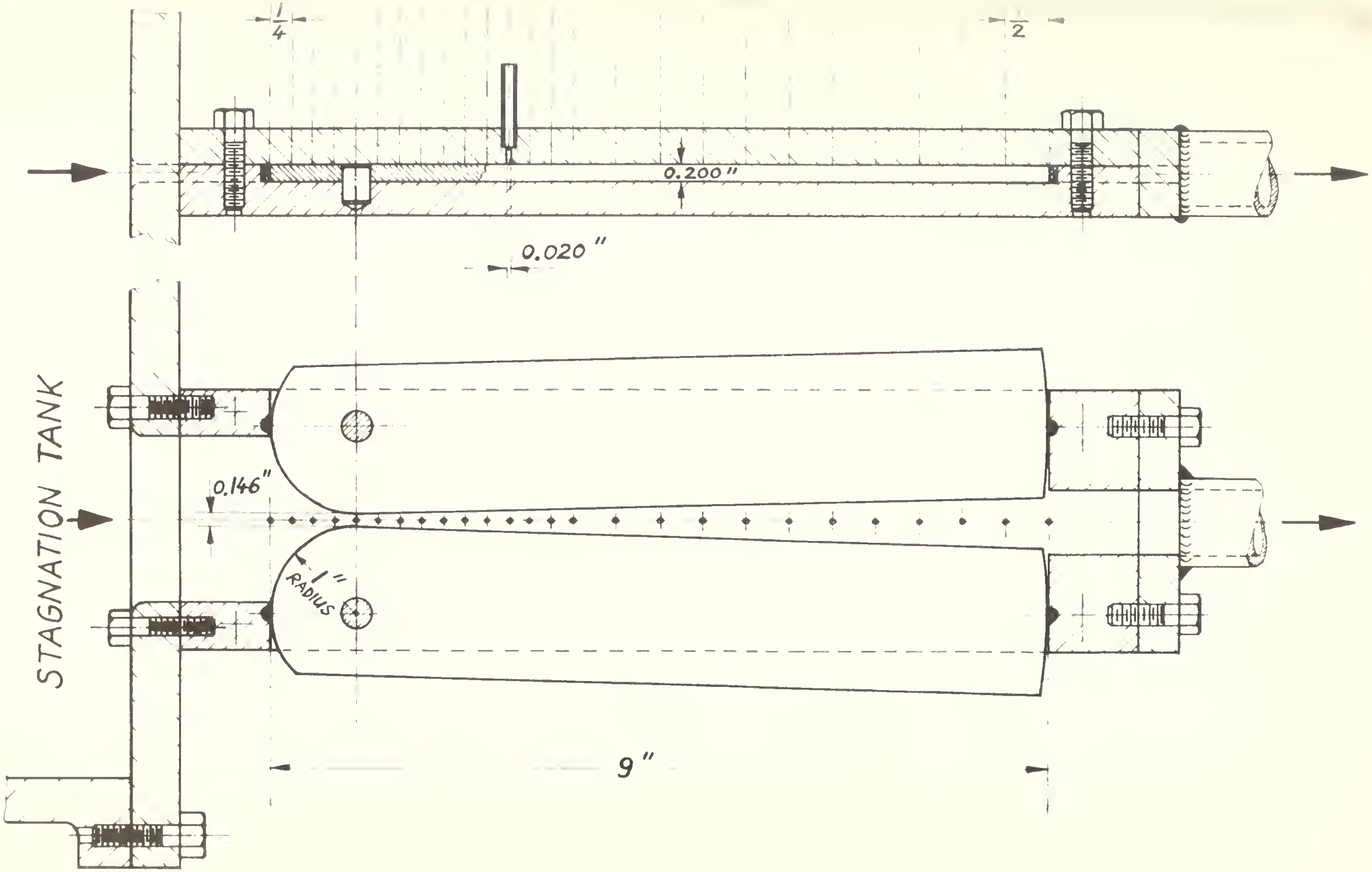

FIGURE 8, DETAIL OF NOZZLE II

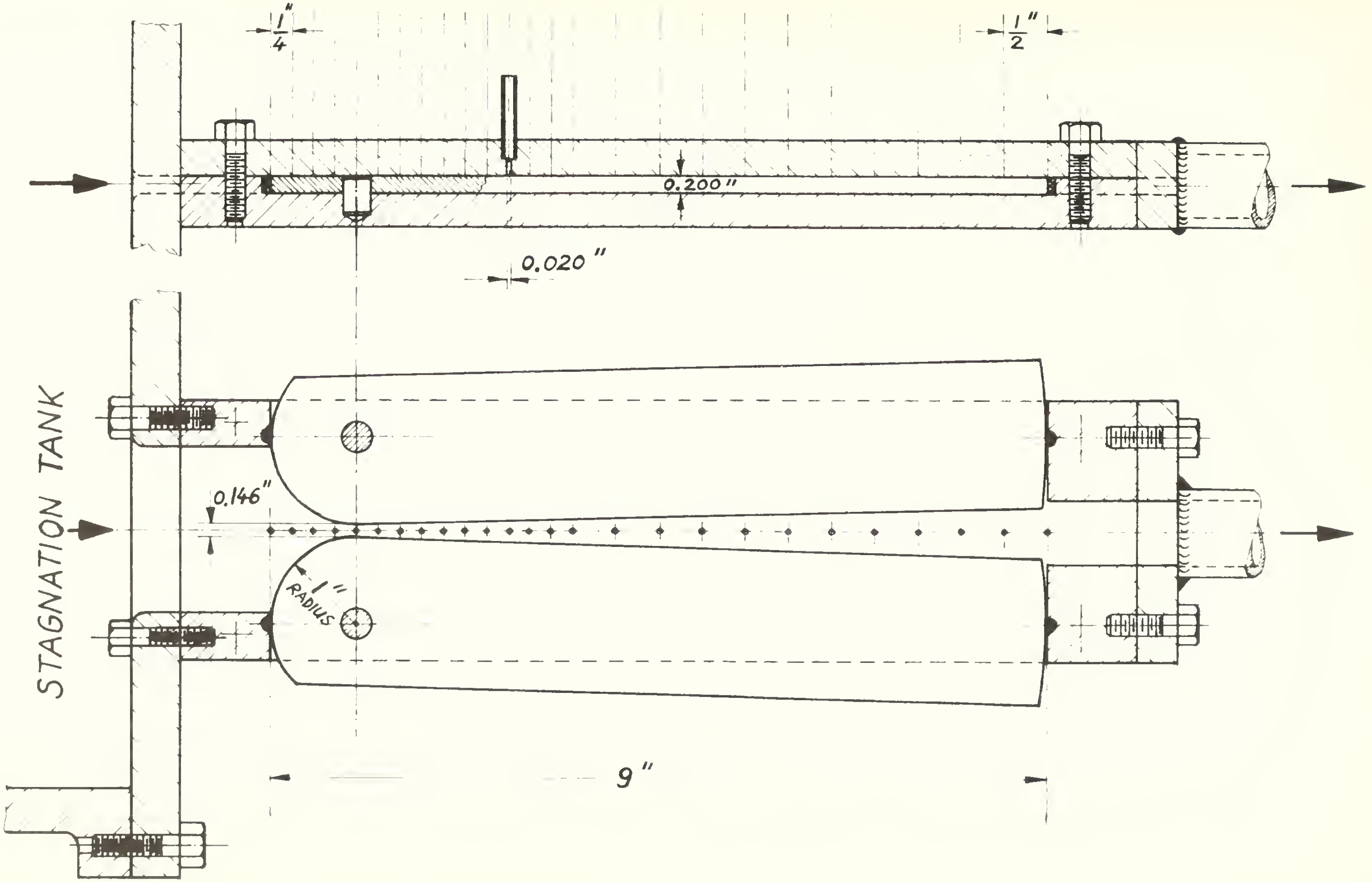

FIGURE 8, DETAIL OF NOZZLE II

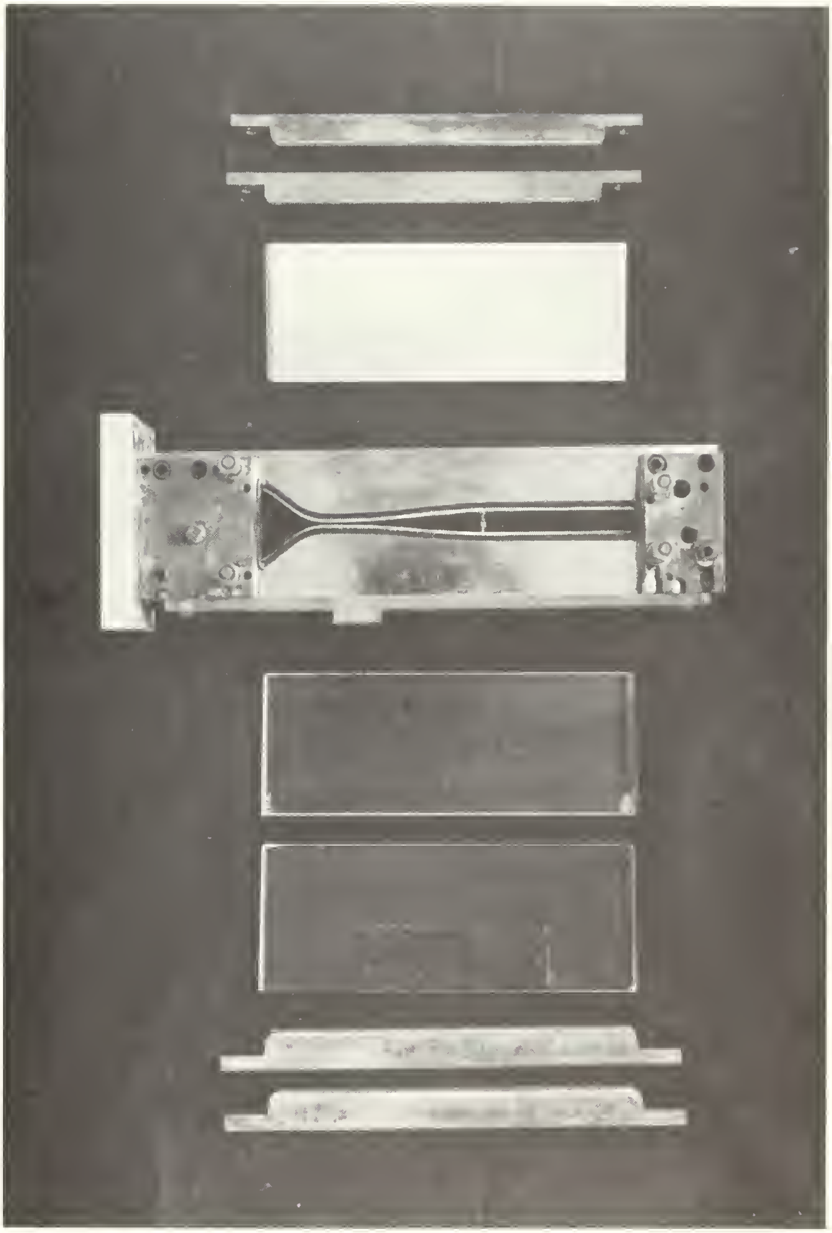

FIGURE 9, NOZZLE I; DISASSEMBLED, SHOWING OPTICAL GLASS AND METAL PRESSURE TAP PLATE SIDE WALLS, AND METAL CLAMP BARS.

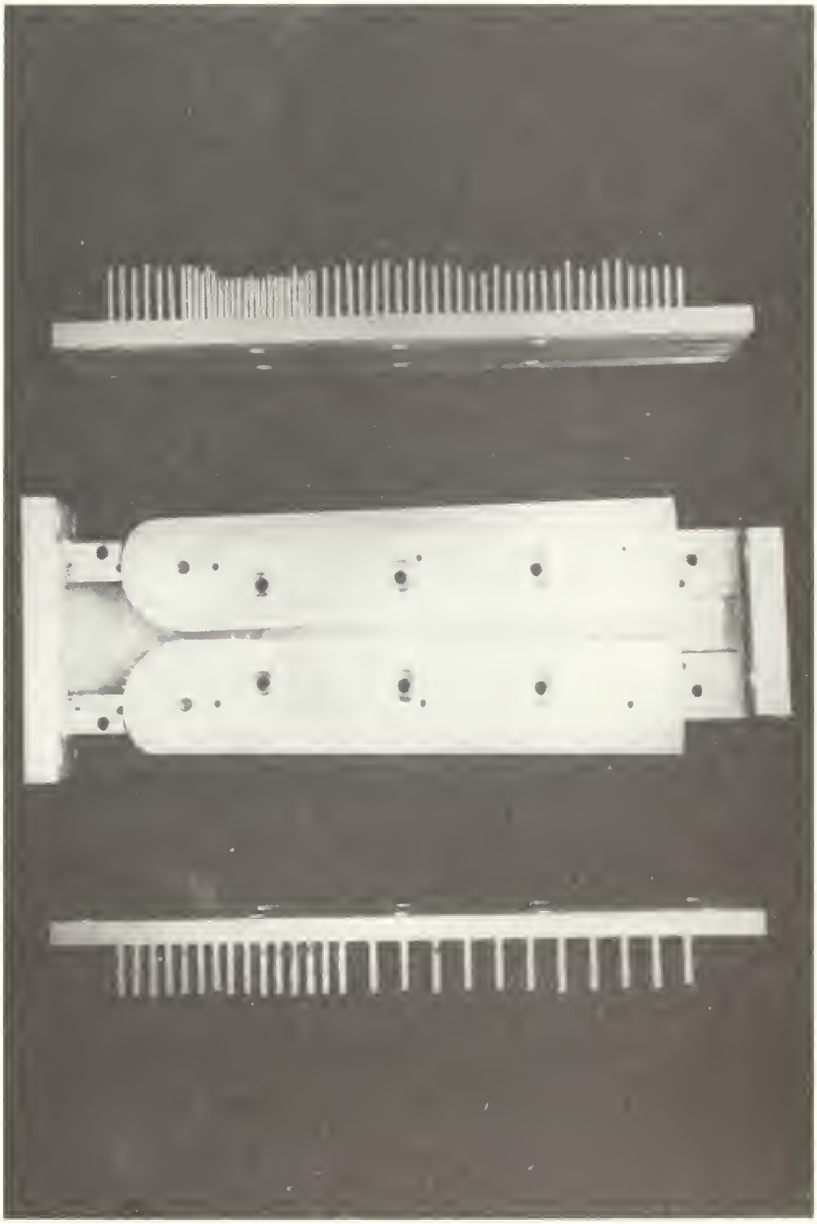

FIGURE 10, NOZZLE II; DISASSEMBLED, SHOWING HINGED UPPER AND LOWER WALLS, AND PRESSURE TAP PLATES 1 AND 2

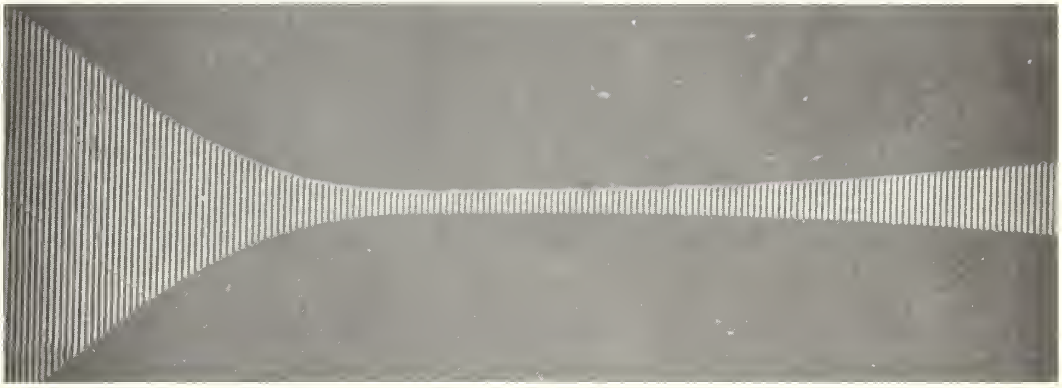

(A) NO FLOW

(B) SCALING PLATE (1.00")

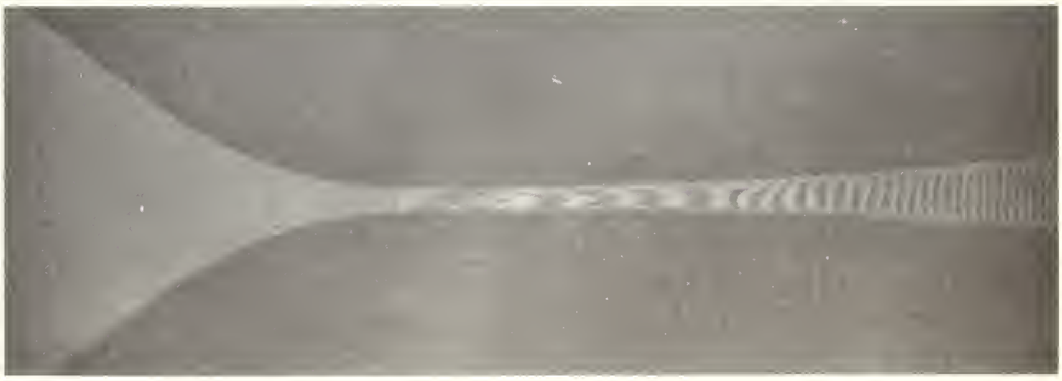

(C) FLOW, SHOWING SHIFT IN INTERFERENCE BANDS

FIGURE 11, INTERFEROMETRIC PHOTOGRAPHS FOR TEST 1 OF DENSITY PROFILES.

(A) NO FLOW

(B) SCALING PLATE (1.00")

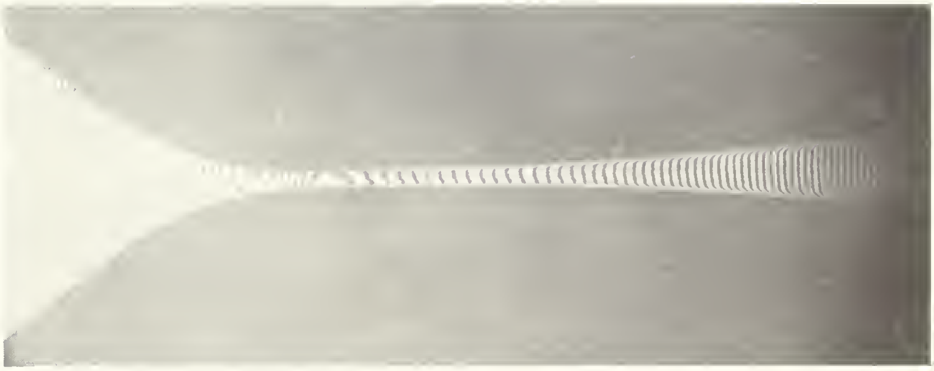

(C) FLOW, SHOWING SHIFT IN INTERFERENCE BANDS

FIGURE 12, INTERFEROMETRIC PHOTOGRAPHS FOR TEST 2 OF DENSITY PROFILES.

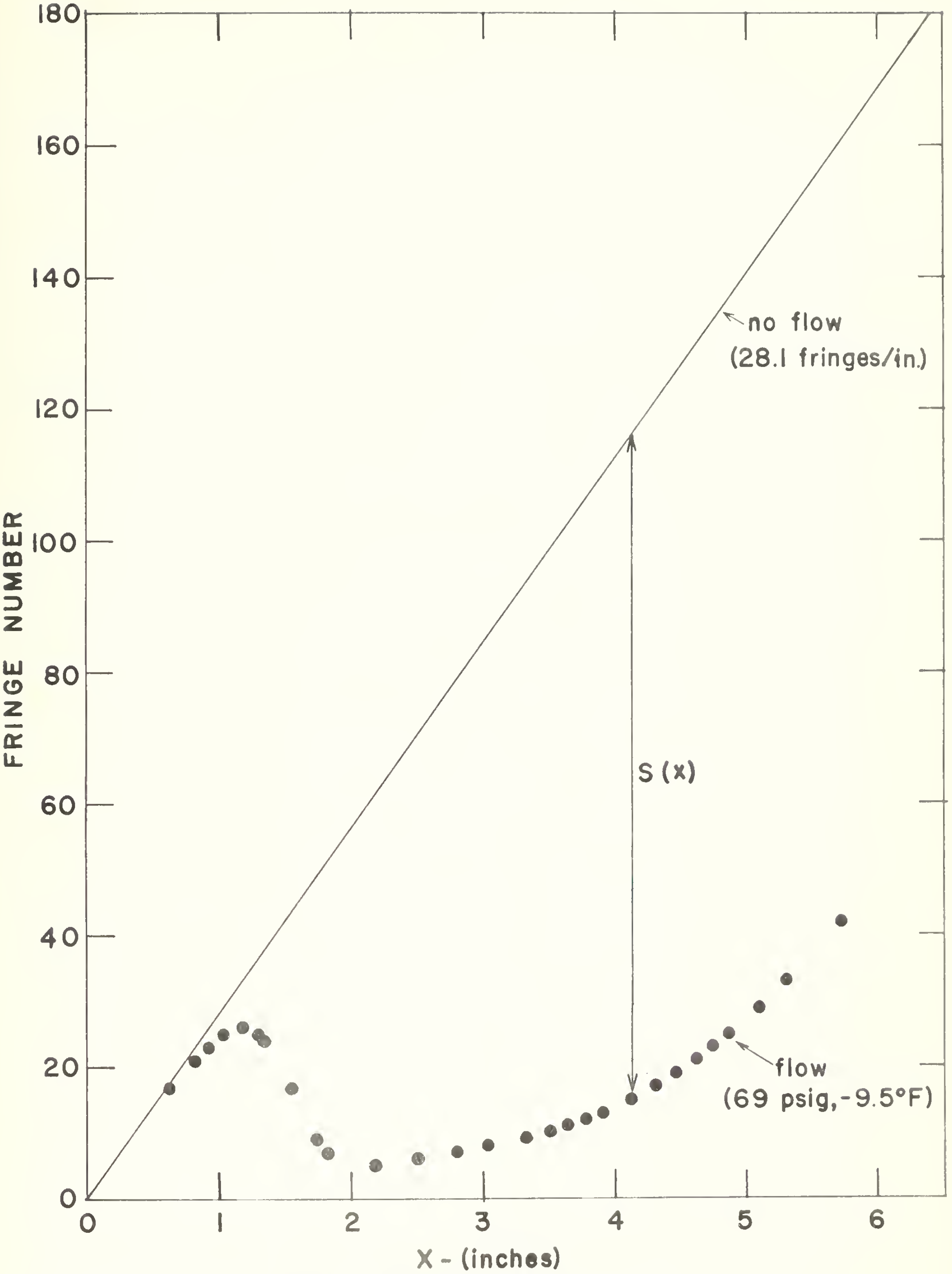

FIG 13 GRAPHICAL REPRESENTATION OF DETERMINATION OF FRINGE SHIFTS - TEST NO 1

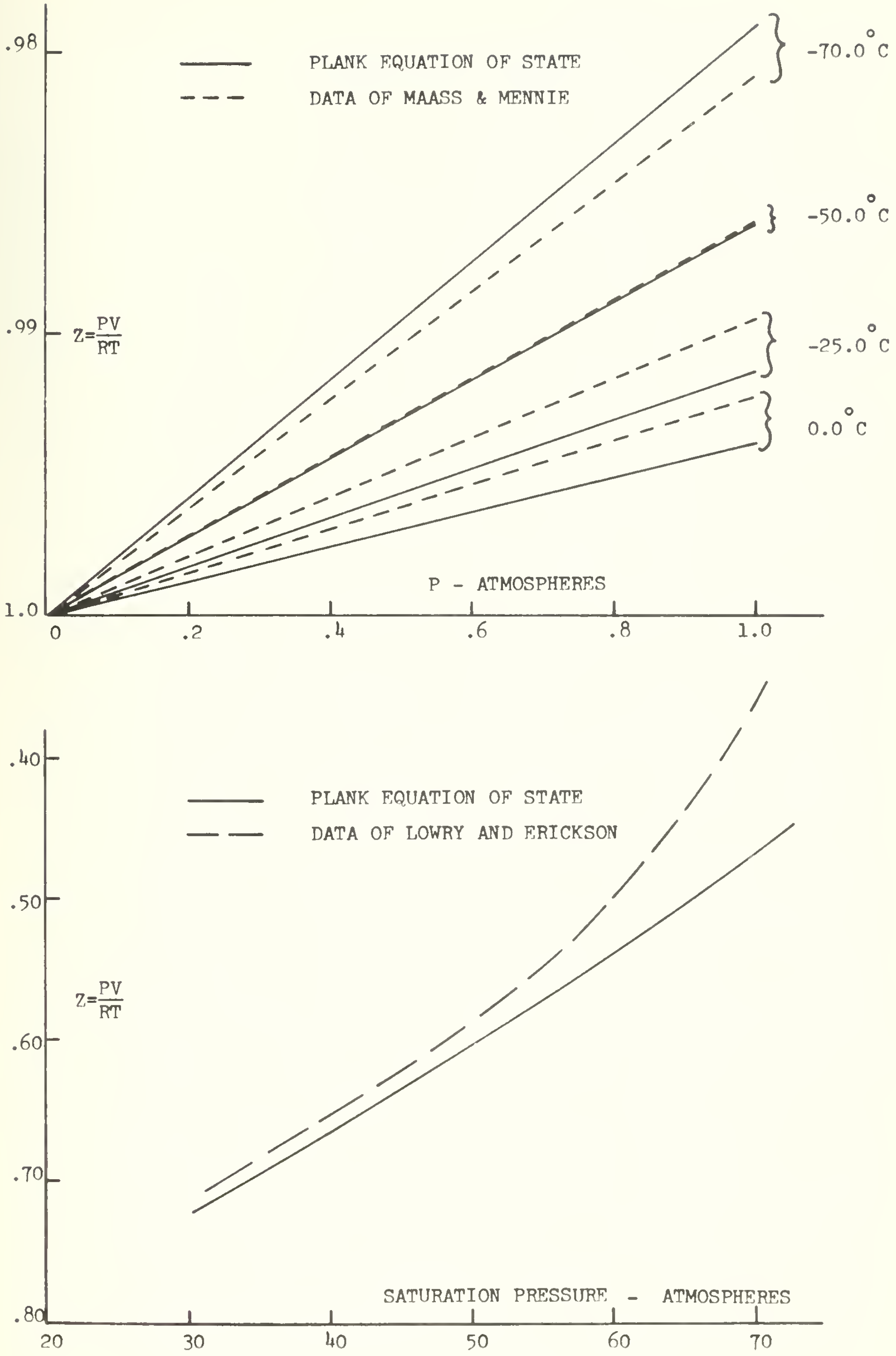

FIGURE 14, COMPARISON OF THE PLANK EQUATION OF STATE AND DATA UPON WHICH IT WAS FORMULATED

TABLE 2

CARBON DIOXIDE ENTHALPY TABLES

Enthalpy in cal/gm, p in atm, T in deg K

p	T = 100.0	110	120	130	140	150
.5	154.03	156.83	159.19	161.35	163.36	165.29
1.0	149.60	153.61	156.78	159.50	161.92	164.14
1.5	145.10	150.33	154.33	157.63	160.45	162.98
2.0	140.54	147.01	151.84	155.72	158.97	161.79
2.5	135.91	143.64	149.64	153.79	157.46	160.60
3.0	131.21	140.22	146.77	151.83	155.93	159.38
3.5	126.45	136.76	144.17	149.85	154.38	158.15
4.0	121.62	133.24	141.54	147.83	152.80	156.90
4.5	116.73	129.68	138.88	145.79	151.21	155.63
5.0	111.77	126.07	136.17	143.72	149.59	154.34
5.5	106.74	122.41	133.43	141.63	147.95	153.04
6.0	101.64	118.70	130.66	139.50	146.29	151.72
6.5	96.48	114.94	127.85	137.35	144.61	150.39
7.0	91.26	111.14	125.00	135.17	142.91	149.04
7.5	85.96	107.29	122.12	132.96	141.19	147.67
8.0	80.60	103.39	119.20	130.73	139.44	146.28
8.5	75.18	99.44	116.25	128.46	137.67	144.87
9.0	69.68	95.44	113.25	126.17	135.88	143.45
9.5	64.13	91.39	110.23	123.85	134.07	142.01
10.0	58.50	87.30	107.16	121.51	132.24	140.56
10.5	52.81	83.16	104.06	119.13	130.38	139.08
11.0	47.05	78.97	100.93	116.73	128.51	137.59
11.5	41.23	74.73	97.76	114.30	126.61	136.08
12.0	35.34	70.44	94.55	111.85	124.69	134.56
12.5	29.38	66.10	91.30	109.36	122.75	133.02

p	T = 160	170	180	190	200	210
.5	167.16	168.99	170.81	172.63	174.44	176.28
1.0	166.23	168.23	170.19	172.10	174.01	175.90
1.5	165.29	167.47	169.55	171.57	173.56	175.52
2.0	164.34	166.69	168.91	171.04	173.11	175.14
2.5	163.37	165.90	168.26	170.49	172.65	174.75
3.0	162.39	165.10	167.59	169.94	172.18	174.35
3.5	161.40	164.29	166.92	169.38	171.71	173.95
4.0	160.39	163.46	166.24	168.81	171.23	173.54
4.5	159.37	162.63	165.55	168.23	170.74	173.13
5.0	158.33	161.78	164.85	167.65	170.25	172.71
5.5	157.28	160.92	164.14	167.06	169.75	172.29
6.0	156.22	160.05	163.42	166.46	169.25	171.86
6.5	155.14	159.17	162.70	165.85	168.73	171.42
7.0	154.05	158.28	161.96	165.23	168.22	170.98
7.5	152.94	157.38	161.21	164.61	167.69	170.54
8.0	151.83	156.47	160.46	163.98	167.16	170.08
8.5	150.69	155.54	159.69	163.34	166.62	169.63
9.0	149.55	154.60	158.92	162.69	166.07	169.16
9.5	148.39	152.65	158.13	162.04	165.52	168.69
10.0	147.21	152.70	157.34	161.38	164.96	168.22

p	160	170	180	190	200	210
10.5	146.02	151.72	156.54	160.71	164.40	167.74
11.0	144.82	150.74	155.73	160.03	163.83	167.25
11.5	143.61	149.75	154.91	159.34	163.25	166.76
12.0	142.38	148.74	154.08	158.65	162.67	166.27
12.5	141.13	147.73	153.24	157.95	162.07	165.76

p	T = 220	230	240	250	260	270
.5	178.12	179.99	181.87	183.77	185.70	187.65
1.0	177.80	179.71	181.63	183.56	185.51	187.48
1.5	177.48	179.43	181.38	183.35	185.33	187.32
2.0	177.15	179.15	181.14	183.13	185.14	187.15
2.5	176.81	178.86	180.89	182.92	184.95	186.98
3.0	176.48	178.56	180.63	182.69	184.75	186.81
3.5	176.13	178.27	180.38	182.47	184.56	186.64
4.0	175.78	177.97	180.12	182.24	184.36	186.46
4.5	175.43	177.66	179.85	182.01	184.15	186.28
5.0	175.07	177.35	179.58	181.78	183.95	186.10
5.5	174.71	177.04	179.31	181.54	183.74	185.92
6.0	174.34	176.72	179.04	181.30	183.53	185.73
6.5	173.97	176.40	178.76	181.06	183.31	185.55
7.0	173.59	176.08	178.47	180.81	183.10	185.35
7.5	173.21	175.75	178.19	180.56	182.88	185.16
8.0	172.82	175.41	177.90	180.31	182.66	184.97
8.5	172.43	175.07	177.61	180.05	182.43	184.77
9.0	172.03	174.73	177.31	179.79	182.21	184.57
9.5	171.63	174.39	177.01	179.53	181.98	184.36
10.0	171.22	174.04	176.70	179.26	181.74	184.16
10.5	170.81	173.68	176.40	179.00	181.51	183.95
11.0	170.40	173.32	176.09	178.72	181.27	193.74
11.5	169.98	172.96	175.77	178.45	181.03	183.53
12.0	169.55	172.59	175.45	178.17	180.78	183.31
12.5	169.12	172.22	175.13	177.89	180.54	183.10

p	T = 280	290	300	310	320	330
.5	189.62	191.60	193.63	195.67	197.70	199.82
1.0	189.47	191.47	193.51	195.57	197.61	199.74
1.5	189.33	191.34	193.40	195.46	197.52	199.65
2.0	189.18	191.21	193.28	195.36	197.42	199.57
2.5	189.03	191.08	193.16	195.25	197.33	199.48
3.0	188.88	190.94	193.04	195.14	197.23	199.39
3.5	188.73	190.81	192.92	195.03	197.13	199.30
4.0	188.57	190.67	192.80	194.92	197.03	199.21
4.5	188.41	190.53	192.67	194.81	196.93	199.12
5.0	188.25	190.38	192.54	194.70	196.83	199.03
5.5	188.09	190.24	192.41	194.58	196.72	198.94
6.0	187.92	190.09	192.28	194.46	196.62	198.84
6.5	187.76	189.94	192.15	194.34	196.51	198.74
7.0	187.59	189.79	192.02	194.22	196.40	198.65
7.5	187.42	189.64	191.88	194.10	196.29	198.55
8.0	187.24	189.49	191.74	193.98	196.18	198.45
8.5	187.07	189.33	191.60	193.85	196.07	198.35
9.0	186.89	189.17	191.46	193.73	195.96	198.24
9.5	186.71	189.01	191.32	193.60	195.84	198.14

p	280	290	300	310	320	330
10.0	186.53	188.85	191.17	193.47	195.72	198.03
10.5	186.34	188.69	191.03	193.34	195.61	197.93
11.0	186.16	188.52	190.88	193.21	195.49	197.82
11.5	185.97	188.35	190.73	193.07	195.37	197.71
12.0	185.78	188.19	190.58	192.94	195.25	197.60
12.5	185.59	188.01	190.43	192.80	195.12	197.49

TABLE 3

INTERFEROMETRIC MEASUREMENT AND CALCULATION OF DENSITY

Test No. 1

$T_o = -9.5^oF$

$P_o = 83.7$ psia

No Flow: Average 28.1 fringes/inch

$$\frac{\lambda}{\ell} = \frac{5461 \times 10^{-8}}{(.956)(2.54)} = 2248 \times 10^{-8}$$

Photograph Scale: 2.39 in./in.

$$\rho_o = \frac{P}{zRT} = .806 \text{ lbm/ft}^3$$

$$G\rho_o = N_o - 1 = (.3673 \times 10^{-2})(.806) = 296.0 \times 10^{-5}$$

Fringe Number	x_{photo}	$S(x)$	$\frac{S\lambda}{\ell} \times 10^5$	$(n_o-1)-S\lambda/\ell$	ρ/ρ_o	x_{nozzle}
0	0	0	0			
1	.035					
9	.335	0	0			
17	.630	.46	1.035	294.96	.997	.268
21	.810	1.45	3.26	292.74	.990	.345
23	.920	2.50	5.62	290.38	.982	.392
25	1.040	3.82	8.59	287.41	.971	.442
26	1.180	6.8	15.3	280.7	.949	.502
25	1.300	11.1	25.0	271.0	.916	.552
24	1.350	13.5	30.4	265.6	.897	.574
17	1.550	26.2	58.9	237.1	.801	.659
9	1.730	39.2	88.2	207.8	.702	.735
7	1.820	43.8	98.6	197.5	.668	.774
5	2.180	56.0	126.0	170.0	.575	.918
6	2.510	64.4	145.0	151.0	.510	1.067
7	2.805	71.8	161.8	134.2	.454	1.192
8	3.030	77.1	173.6	122.4	.414	1.289
9	3.315	84.1	189.3	106.7	.360	1.410
10	3.510	88.6	199.5	96.5	.326	1.492
11	3.630	91.0	204.8	91.2	.308	1.545
12	3.765	94.0	211.5	84.5	.2855	1.602
13	3.900	96.7	217.7	78.3	.2645	1.660
15	4.120	101.0	226.3	69.7	.2355	1.753
17	4.310	104.2	234.6	61.4	.2072	1.833
19	4.460	106.5	239.8	57.2	.1933	1.899
21	4.610	108.7	244.5	51.5	.1740	1.960
23	4.740	110.4	248.6	47.4	.1601	2.018
25	4.860	111.7	251.3	44.7	.1510	2.067
29	5.09	114.2	257.2	38.8	.1311	2.165
33	5.30	116.1	261.5	34.5	.1165	2.253
42	5.72	119.0	267.8	28.2	.0953	2.453

TABLE 4
INTERFEROMETRIC MEASUREMENT AND CALCULATION OF DENSITY

Test No. 2

$T_o = 117.0^\circ F$ $\qquad$ $P_o = 58.7$ psia

$\rho_o = \frac{P}{zRT} = .4235\ lbm/ft^3$ $\qquad$ $\frac{\lambda}{\ell} = \frac{5461 \times 10^{-8}}{2.54(.970)} = 2.215 \times 10^{-5}$

$G\rho_o = N_o - 1 = (.3673 \times 10^{-2})(.4235) = 155.6 \times 10^{-5}$

f (flow)	x_{photo}	f (no flow)	S	$\frac{S\lambda}{\ell} \times 10^5$	$G\rho o - S\lambda/\ell$	ρ/ρ_o	x_{nozzle}
0	0	0	0	0	155.6	1.000	0
8	.295	8.5	.5	1.10	154.5	.994	.160
12	.455	13.1	1.1	2.4	153.2	.986	.248
14	.545	15.7	1.7	3.8	151.8	.975	.297
16	.650	18.7	2.7	6.0	149.6	.961	.354
17	.715	20.6	3.6	8.0	147.6	.949	.389
18	.850	24.4	6.4	14.2	141.4	.910	.462
17	.945	27.2	10.2	22.6	133.0	.855	.514
16	1.000	28.8	12.8	28.4	127.2	.819	.545
14	1.085	31.3	17.3	38.4	117.2	.754	.590
13	1.135	32.8	19.8	43.9	111.7	.718	.617
12	1.195	34.7	22.7	50.3	105.3	.677	.650
12	1.380	39.8	27.8	61.6	94.0	.604	.751
13	1.520	44.3	31.3	69.4	86.2	.555	.827
14	1.625	47.5	33.5	74.3	81.3	.523	.883
16	1.795	52.6	36.6	81.1	74.5	.479	.975
18	1.945	57.0	39.0	86.4	69.2	.445	1.057
20	2.110	61.9	41.9	92.9	62.7	.403	1.147
22	2.260	66.4	44.4	98.5	57.1	.367	1.228
24	2.420	71.1	47.1	104.5	51.1	.329	1.315
26	2.580	75.9	49.9	110.7	44.9	.289	1.402
28	2.725	80.1	52.1	115.5	40.1	.258	1.482
30	2.860	84.1	54.1	120.0	35.6	.229	1.555
32	2.980	87.8	55.8	123.6	32.0	.206	1.620
34	3.100	91.1	57.1	126.6	29.0	.186	1.685
36	3.210	94.4	58.4	129.3	26.3	.169	1.745
40	3.415	100.4	60.4	133.8	21.8	.141	1.857
44	3.600	105.8	61.8	137.0	18.6	.120	1.958
48	3.785	111.3	63.3	140.3	15.3	.099	2.060
52	3.950	116.0	64.0	141.8	13.8	.089	2.148
60	4.245	124.6	64.6	143.2	12.4	.080	2.308

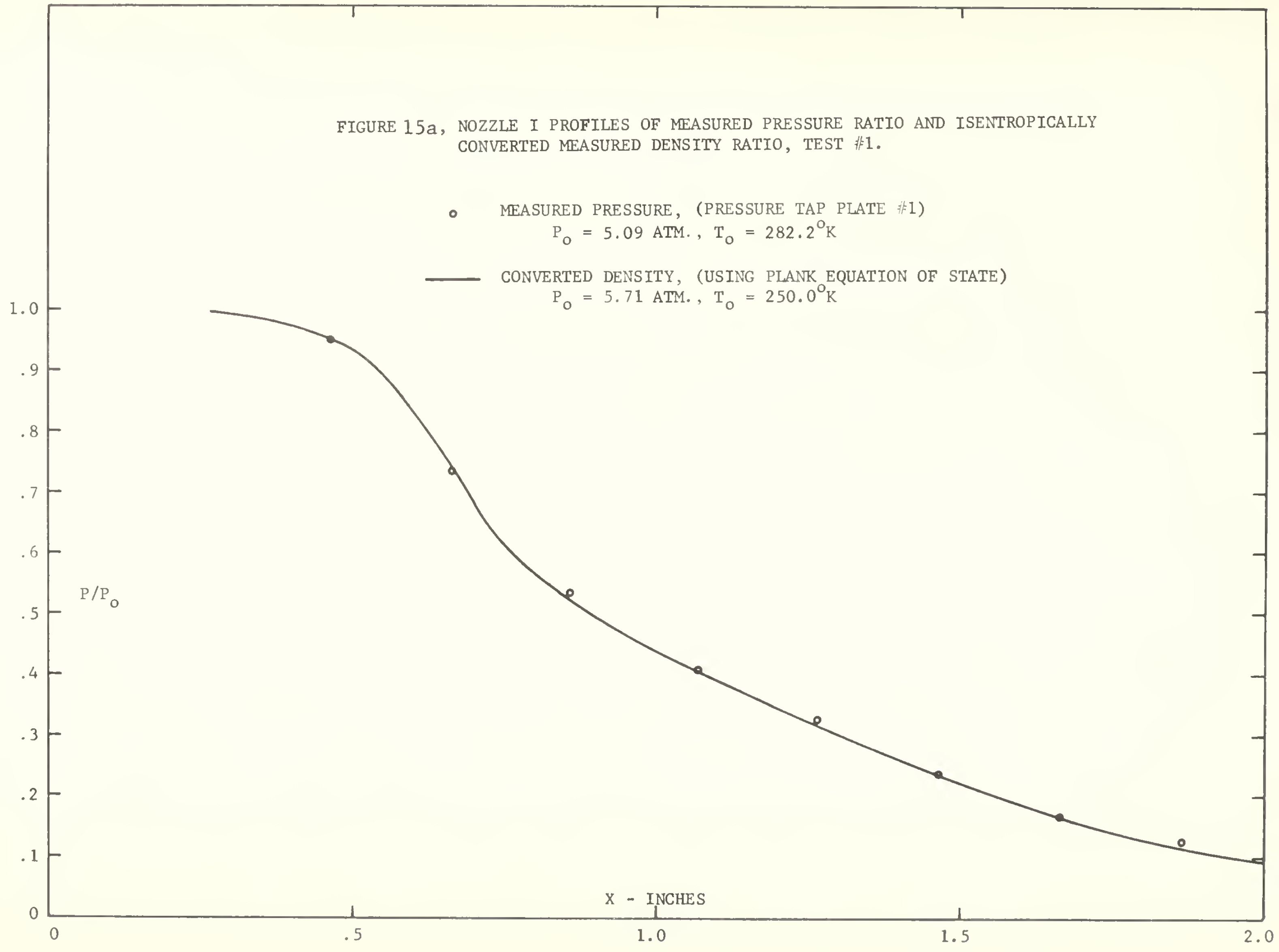

FIGURE 15a, NOZZLE I PROFILES OF MEASURED PRESSURE RATIO AND ISENTROPICALLY CONVERTED MEASURED DENSITY RATIO, TEST #1.

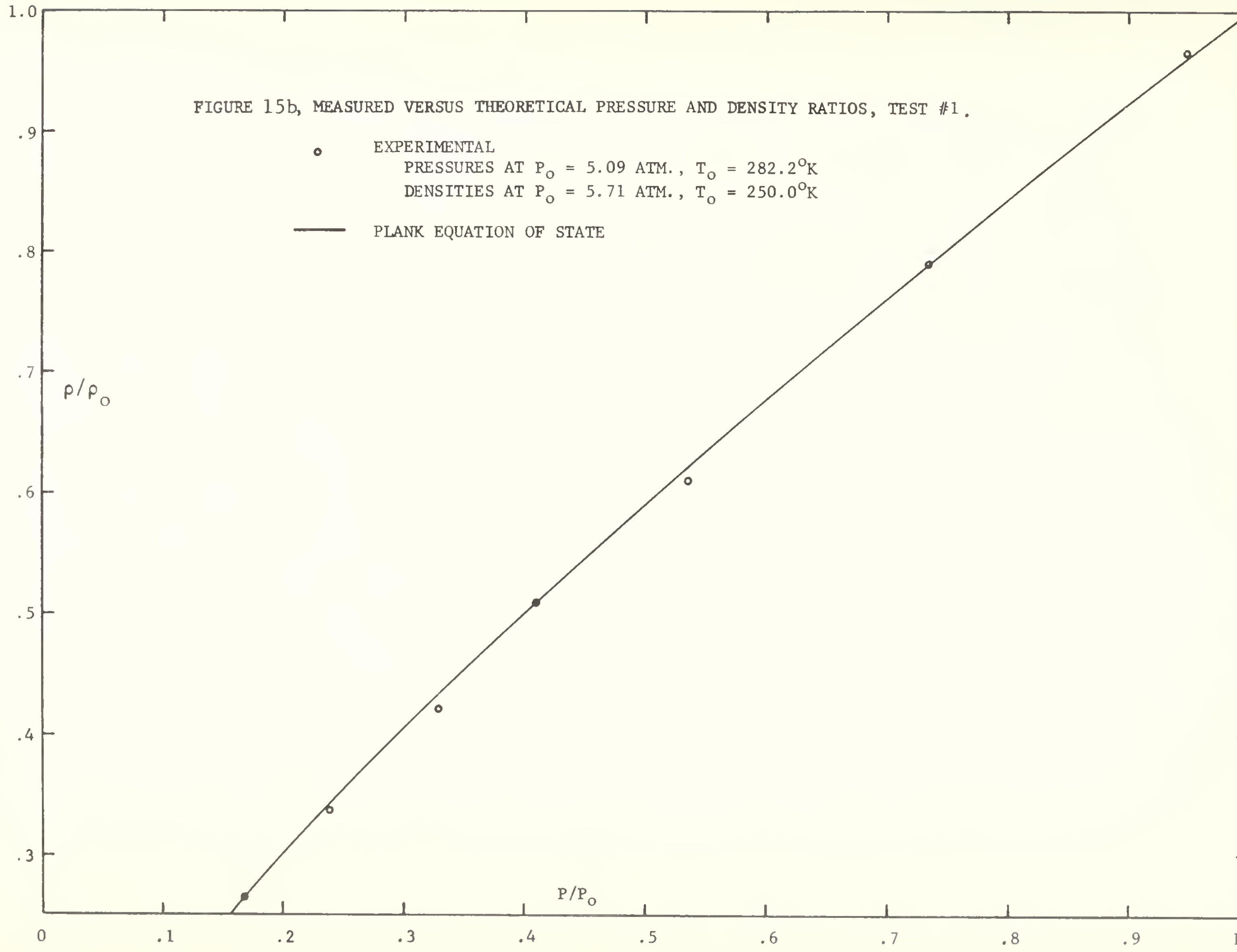

FIGURE 15b, MEASURED VERSUS THEORETICAL PRESSURE AND DENSITY RATIOS, TEST #1.

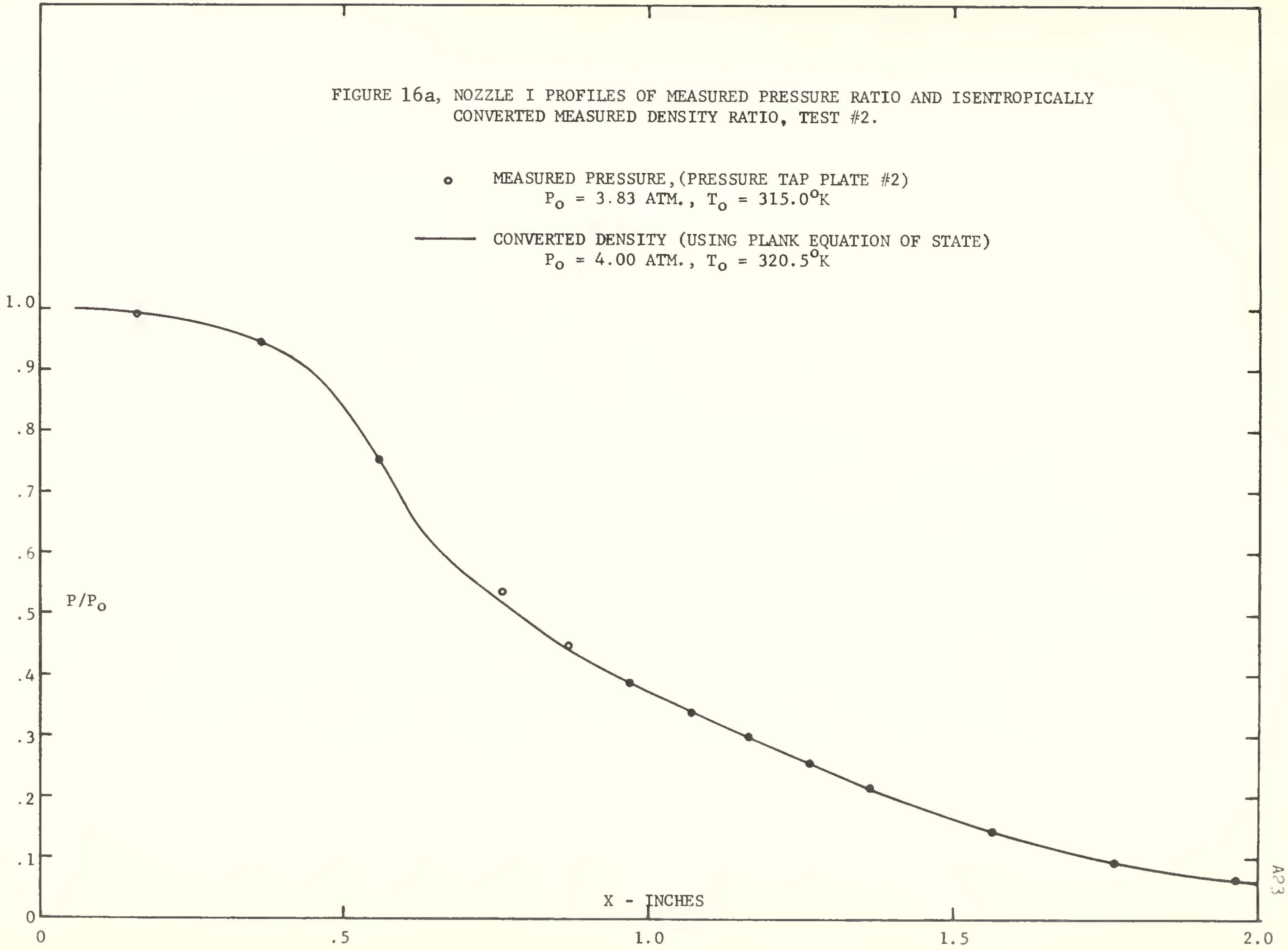
FIGURE 16a, NOZZLE I PROFILES OF MEASURED PRESSURE RATIO AND ISENTROPICALLY CONVERTED MEASURED DENSITY RATIO, TEST #2.

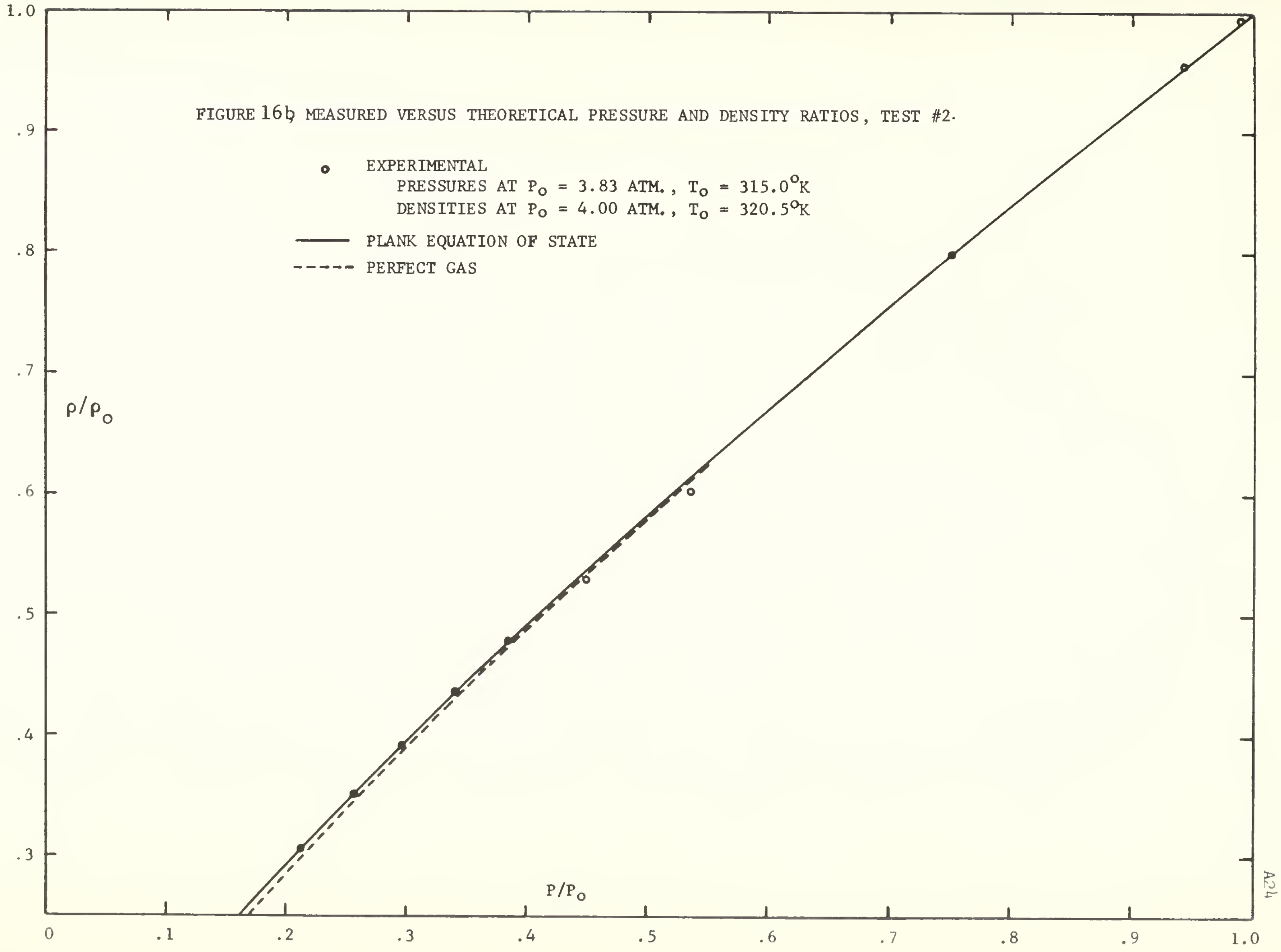

FIGURE 16b MEASURED VERSUS THEORETICAL PRESSURE AND DENSITY RATIOS, TEST #2.

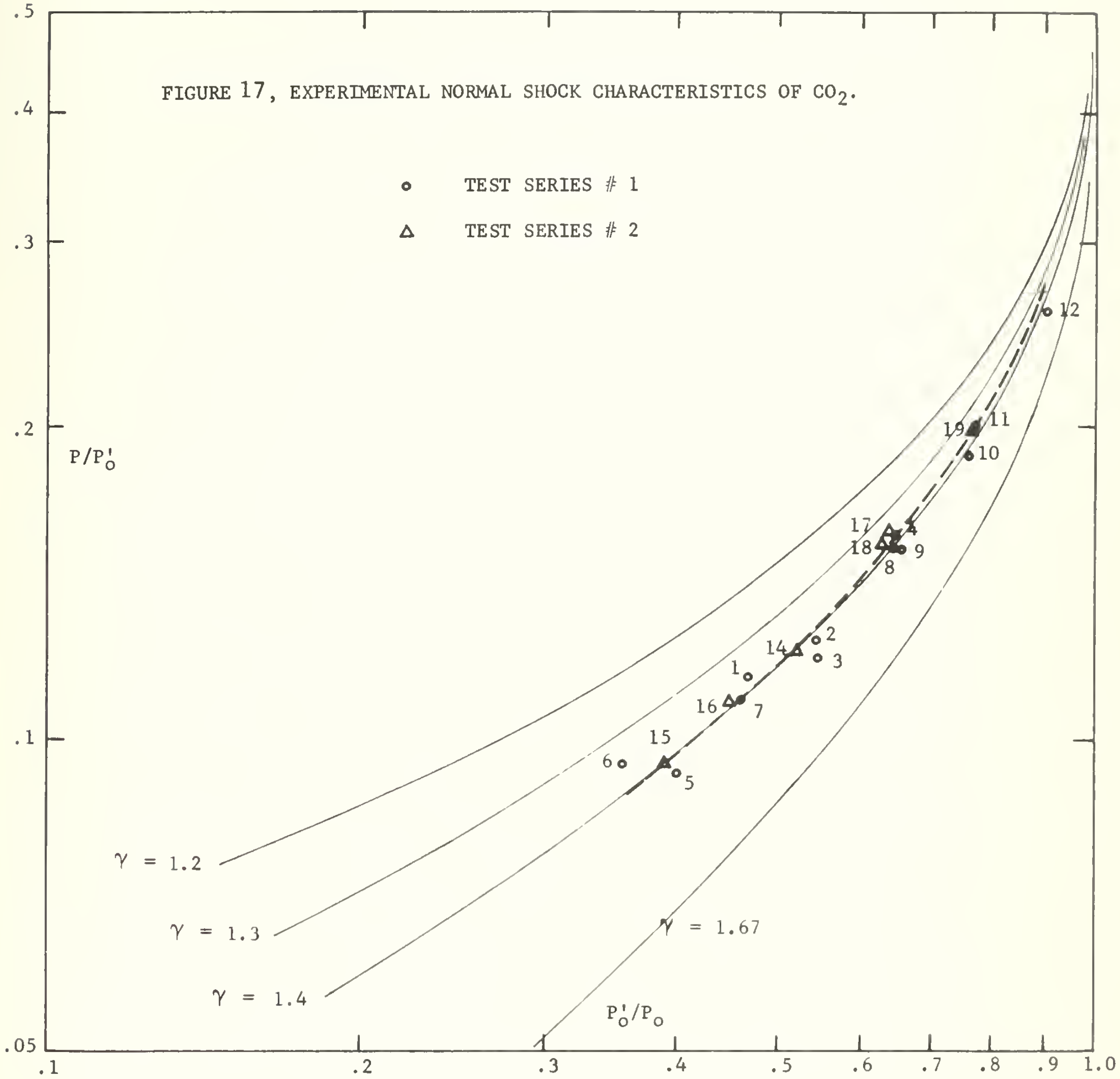

FIGURE 17, EXPERIMENTAL NORMAL SHOCK CHARACTERISTICS OF CO_2.

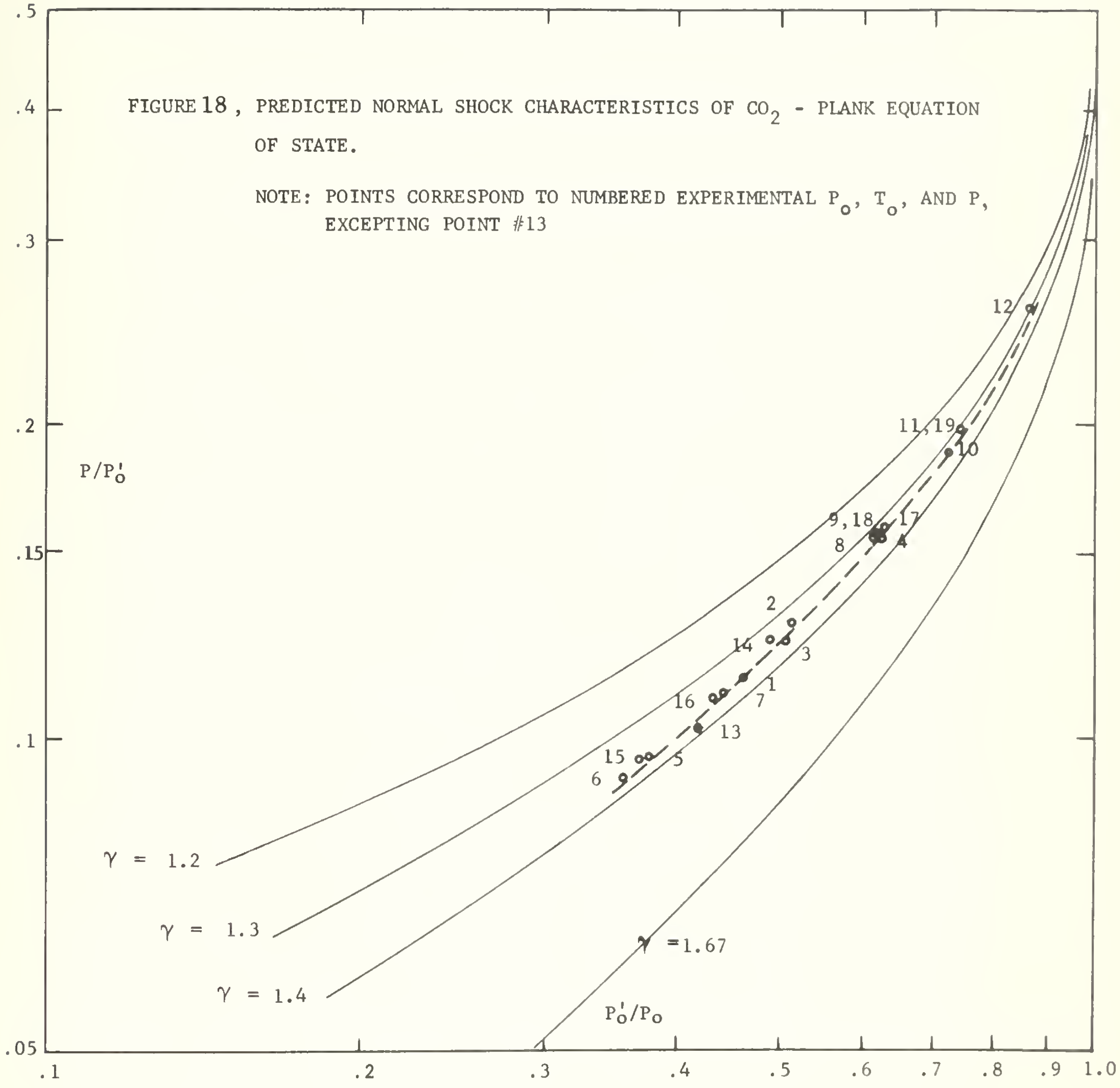

FIGURE 18, PREDICTED NORMAL SHOCK CHARACTERISTICS OF CO_2 - PLANK EQUATION OF STATE.

NOTE: POINTS CORRESPOND TO NUMBERED EXPERIMENTAL P_o, T_o, AND P, EXCEPTING POINT #13

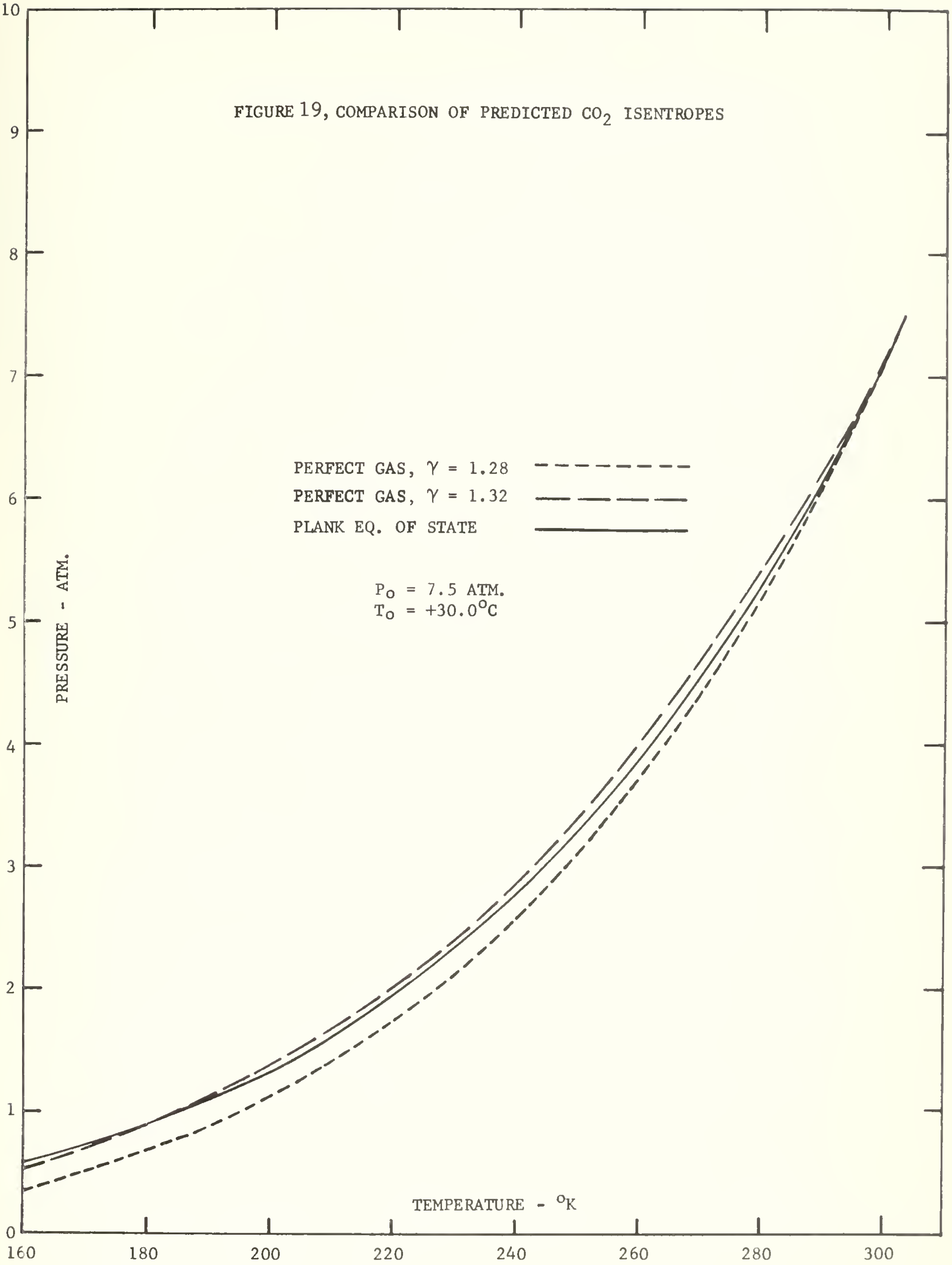

FIGURE 19, COMPARISON OF PREDICTED CO_2 ISENTROPES

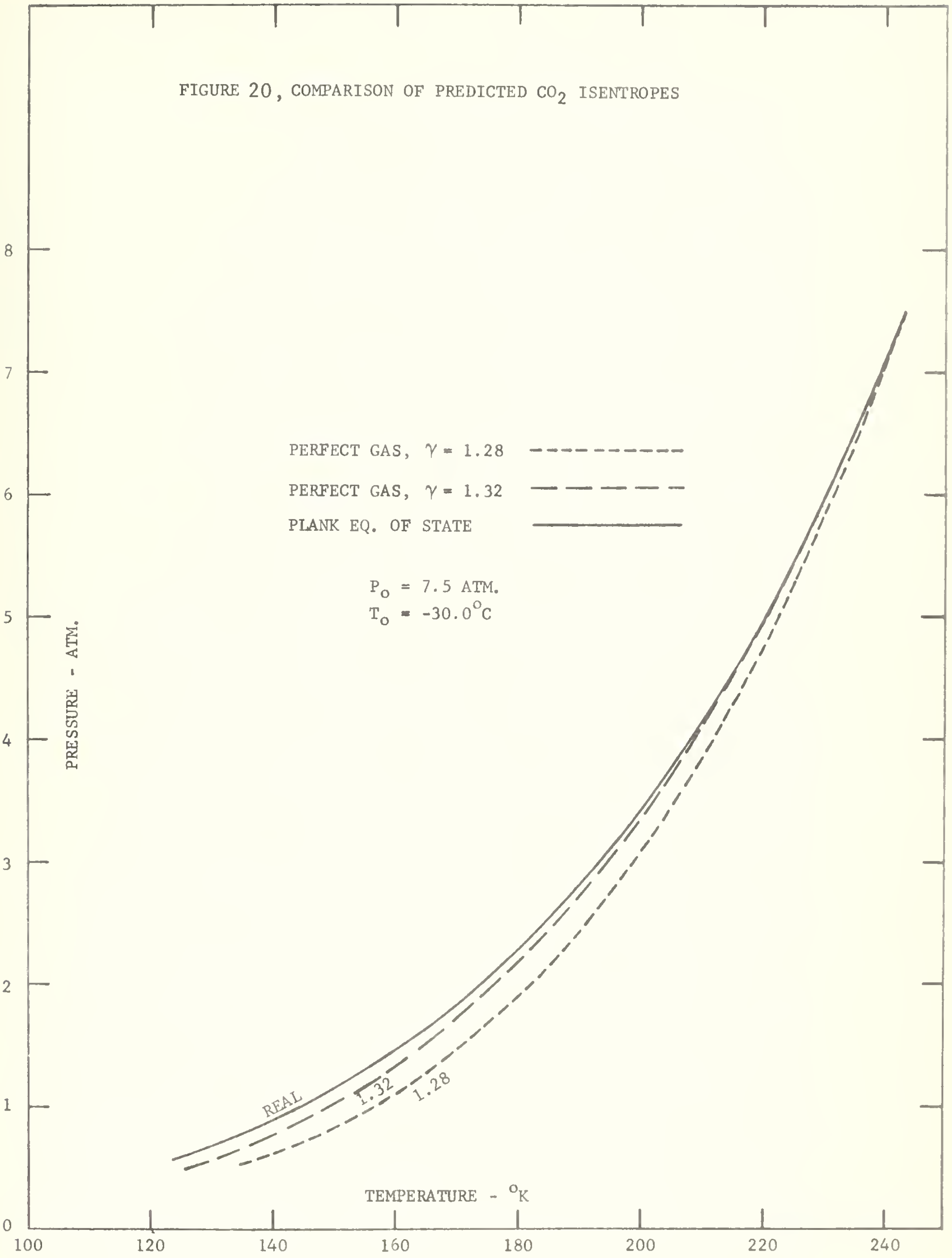

FIGURE 20, COMPARISON OF PREDICTED CO_2 ISENTROPES

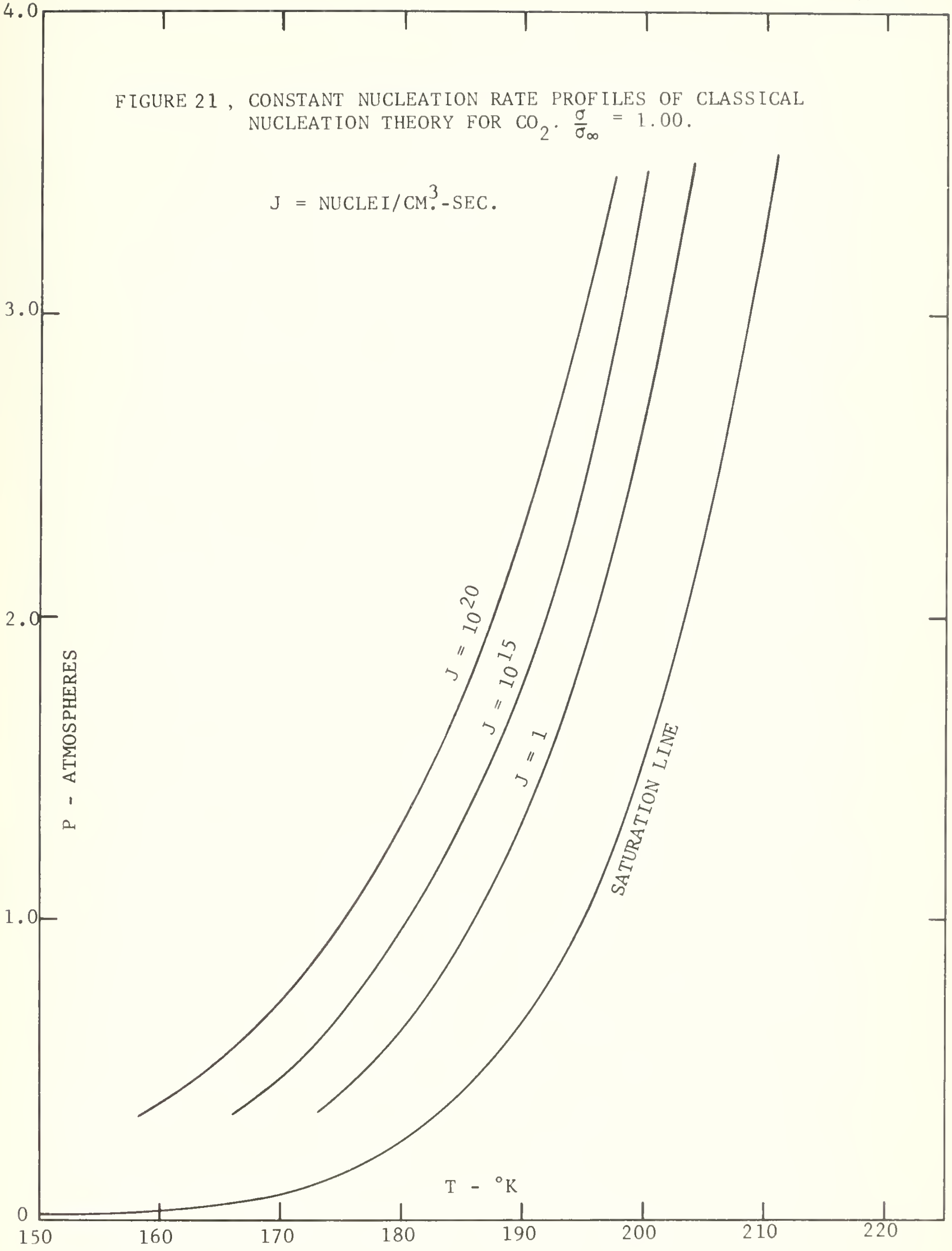

FIGURE 21 , CONSTANT NUCLEATION RATE PROFILES OF CLASSICAL NUCLEATION THEORY FOR CO_2. $\frac{\sigma}{\sigma_\infty} = 1.00$.

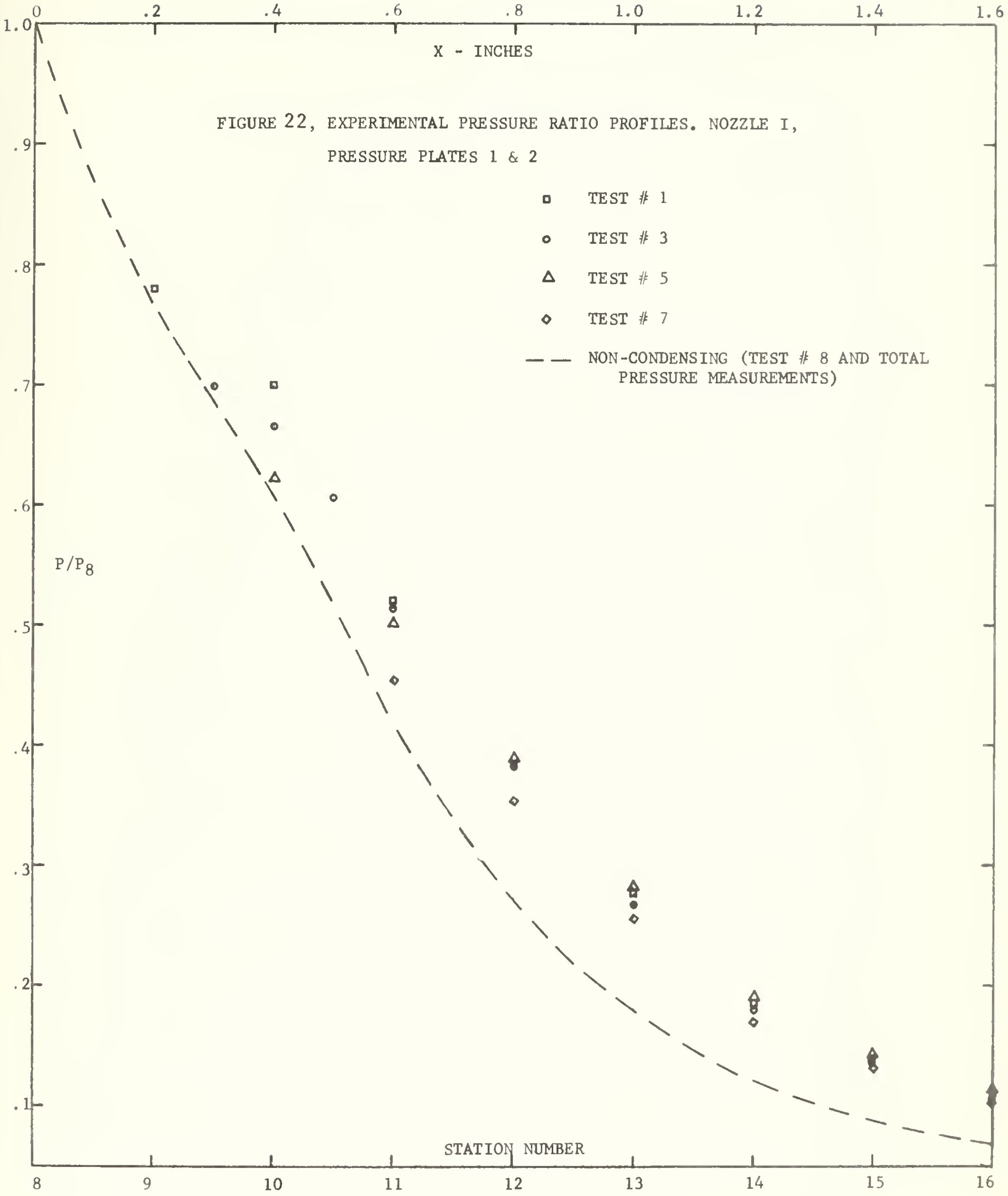

FIGURE 22, EXPERIMENTAL PRESSURE RATIO PROFILES. NOZZLE I, PRESSURE PLATES 1 & 2

TABLE 5

Pressure Data for Figure No. 22

	Run No. 1_I		Run No. 3_I		Run No. 5_I		Run No. 7_I		Run No. 8_I
	P_o = 112.2 psia		P_o = 228.5"Hg (calculated)		P_o = 104.7 psia		P_o = 152.7"Hg (calculated)		
	T_o = 50.6°F		T_o = -47.2°F		T_o = -45°F ±2		T_o = -35°F ±5°F		
Station No.	P("Hg)	P/P_8	P("Hg)	P/P_8	P("Hg)	P/P_8	P("Hg)	P/P_8	
8	122.2	1.000	122.3	1.000	112.4	1.000	81.6	1.000	
8½			107.0	.874					
9	95.4	.780	93.5	.764	86.0	.765	62.6	.767	
9½			85.6	.699					
10	85.4	.699	81.5	.665	70.0	.622	50.7	.621	
10½			74.1	.605					
11	63.5	.519	63.1	.515	56.3	.501	37.0	.453	
12	47.3	.388	47.0	.384	43.9	.390	28.8	.353	
13	33.8	.276	33.0	.269	31.8	.282	21.0	.257	
14	22.6	.185	22.1	.180	21.5	.191	13.8	.169	
15	17.0	.139	16.7	.1364	16.6	.1453	10.7	.131	
16	13.0	.106	12.8	.1045	12.6	.1120	8.4	.103	See Table 6
17	10.8	.0884	10.8	.0880	10.4	.0925	10.8	.132	
18	10.0	.0818	10.0	.0815	9.5	.0844	12.2	.149	
19	9.3	.0761			8.9	.0793			
20	8.9	.0728			8.6	.0765			
21	8.3	.0678			8.4	.0748			
22	7.9	.0646			8.6	.0765			
23	7.6	.0621							
24	6.8	.0556							

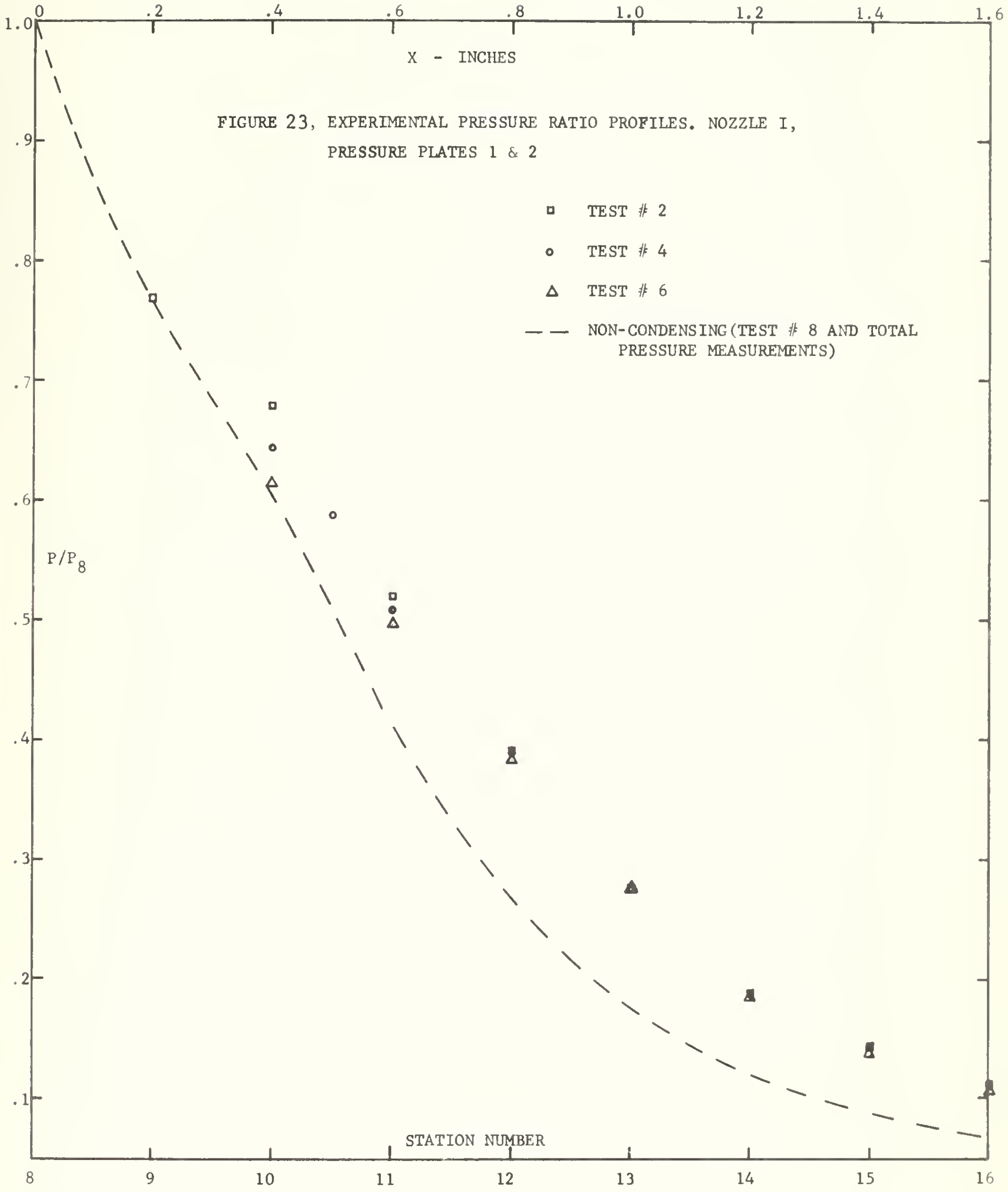

FIGURE 23, EXPERIMENTAL PRESSURE RATIO PROFILES. NOZZLE I, PRESSURE PLATES 1 & 2

TABLE 6

Pressure Data for Figure No. 23

Station No.	Run No. 2_I P_o = 112.7 psia T_o = -48.2°F P("Hg)	 P/P_8	Run No. 4_I P_o = 221.5"Hg (calculated) T_o = -45°F P("Hg)	 P/P_8	Run No. 6_I P_o = 97.7 psia T_o = -45°F ±2°F P("Hg)	 P/P_8	Run No. 8_I P_o =75.7 psia T_o = +48.4°F P("Hg)	 P/P_8
7½			129.0					
8	122.7	1.000	118.4	1.000	105.8	1.000	81.6	1.000
8½			104.7	.884				
9	94.5	.770	90.8	.766	80.8	.764	62.4	.765
9½			81.2	.685				
10	83.1	.677	76.4	.644	65.1	.615	50.0	.611
10½			68.8	.588				
11	63.8	.520	60.6	.511	52.5	.497	--	.417*
12	48.0	.391	46.3	.390	40.6	.384	--	.273*
13	34.0	.277	32.9	.278	29.4	.279	--	.181*
14	22.8	.186	22.1	.186	19.9	.189	--	.121*
15	17.0	.1385	16.8	.142	15.4	.1453	--	.090*
16	13.0	.106	12.7	.107	11.9	.1125	--	.067*
17	10.8	.088	10.5	.0885	9.9	.0936	--	.060*
18	9.9	.0806	9.4	.0793	9.3	.0878	--	
19	9.4	.0765	9.3		8.9		--	
20	9.1	.0740	8.8		8.8		--	
21	8.7	.0708	8.3		9.3		--	
22	8.3	.0675	7.8		9.8			
23	7.8	.0635	7.8					
24	7.0	.0570	9.2					
25	7.3							

*Indicates improved values determined from subsequent total pressure tests.

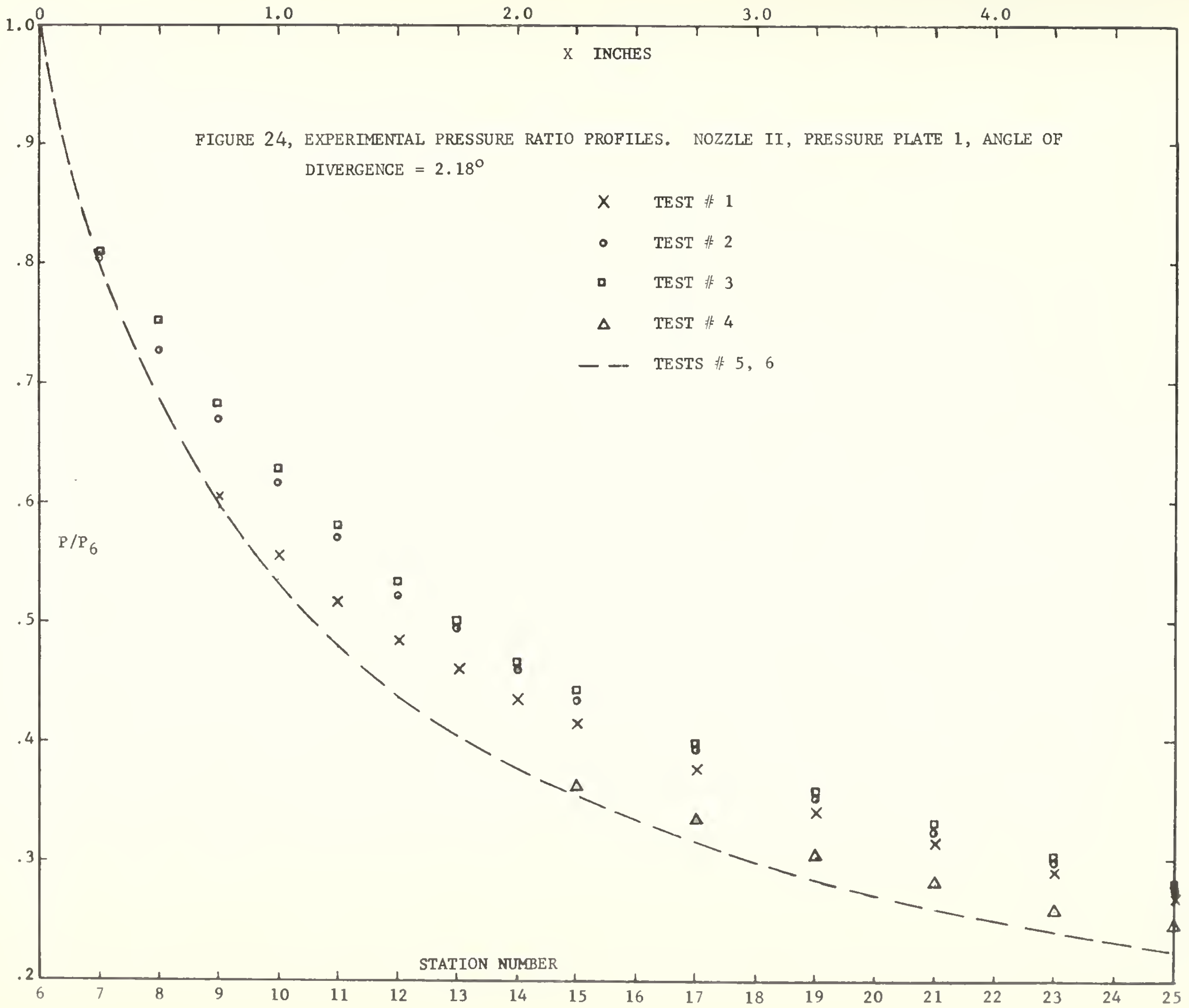

FIGURE 24, EXPERIMENTAL PRESSURE RATIO PROFILES. NOZZLE II, PRESSURE PLATE 1, ANGLE OF DIVERGENCE = 2.18°

TABLE 7

Pressure Data for Figure No. 24

		Test No. 1_{II}		Test No. 2_{II}		Test No. 3_{II}		Test No. 4_{II}		Test No. 5_{II}		Test No. 6_{II}	
		P_o=114.7 psia		P_o=117.7 psia		P_o=117.7 psia		P_o=108.2 psia		P_o=113.7 psia		P_o=96.7 psia	
		T_o=-27.7°F		T_o=-41.1°F		T_o=-45.0°F		T_o=+9.0°F		T_o=72.0°F		T_o=100.4°F	
Tube No.	Station	P	P/P_6	P	P/P_6	P	P/P_6	P	P/P_6	P	P/P_6	P	P/P_6
6	6	127.0	1.000	130.4	1.000	130.4	1.000	118.1	1.000	124.9	1.000	105.6	1.000
7	7	101.9	.801	104.9	.804	105.4	.809	94.5	.801	100.0	.801	84.3	.799
8	8	87.8	.691	94.9	.727	98.0	.752	81.2	.689	85.8	.687	72.5	.687
9	9	76.8	.605	87.1	.669	89.1	.684	70.7	.599	74.5	.596	62.9	.595
10	10	70.6	.556	80.3	.616	81.9	.628	63.8	.540	66.9	.535	56.5	.535
11	11	65.6	.517	74.2	.570	75.7	.580	56.7	.480	59.8	.478	50.6	.479
12	12	61.6	.485	68.0	.521	69.5	.533	51.6	.437	54.2	.434	46.1	.436
13	13	58.5	.461	64.4	.494	65.4	.501	48.2	.409	50.5	.404	42.8	.405
14	14	55.2	.435	59.9	.459	60.8	.466	44.2	.374	46.6	.373	39.7	.376
15	15	52.7	.415	56.6	.434	57.6	.442	42.7	.362	44.5	.356	37.7	.357
16	17	47.7	.376	51.1	.392	51.9	.398	39.3	.333	39.7	.318	33.6	.318
17	19	43.1	.340	45.7	.351	46.5	.358	35.7	.302	35.0	.280	29.7	.281
18	21	39.9	.314	42.3	.324	43.1	.331	33.0	.280	32.2	.258	27.3	.258
19	23	36.8	.290	39.0	.299	39.5	.303	30.3	.257	29.7	.238	25.3	.239
20	25	34.0	.268	35.9	.275	36.5	.280	28.8	.244	27.8	.2225	23.6	.223
21	27	32.3	.254	34.0	.261	34.4	.264			26.1	.209	22.2	.210
22	29	30.3	.239	32.2	.248					24.5	.196	20.8	.197

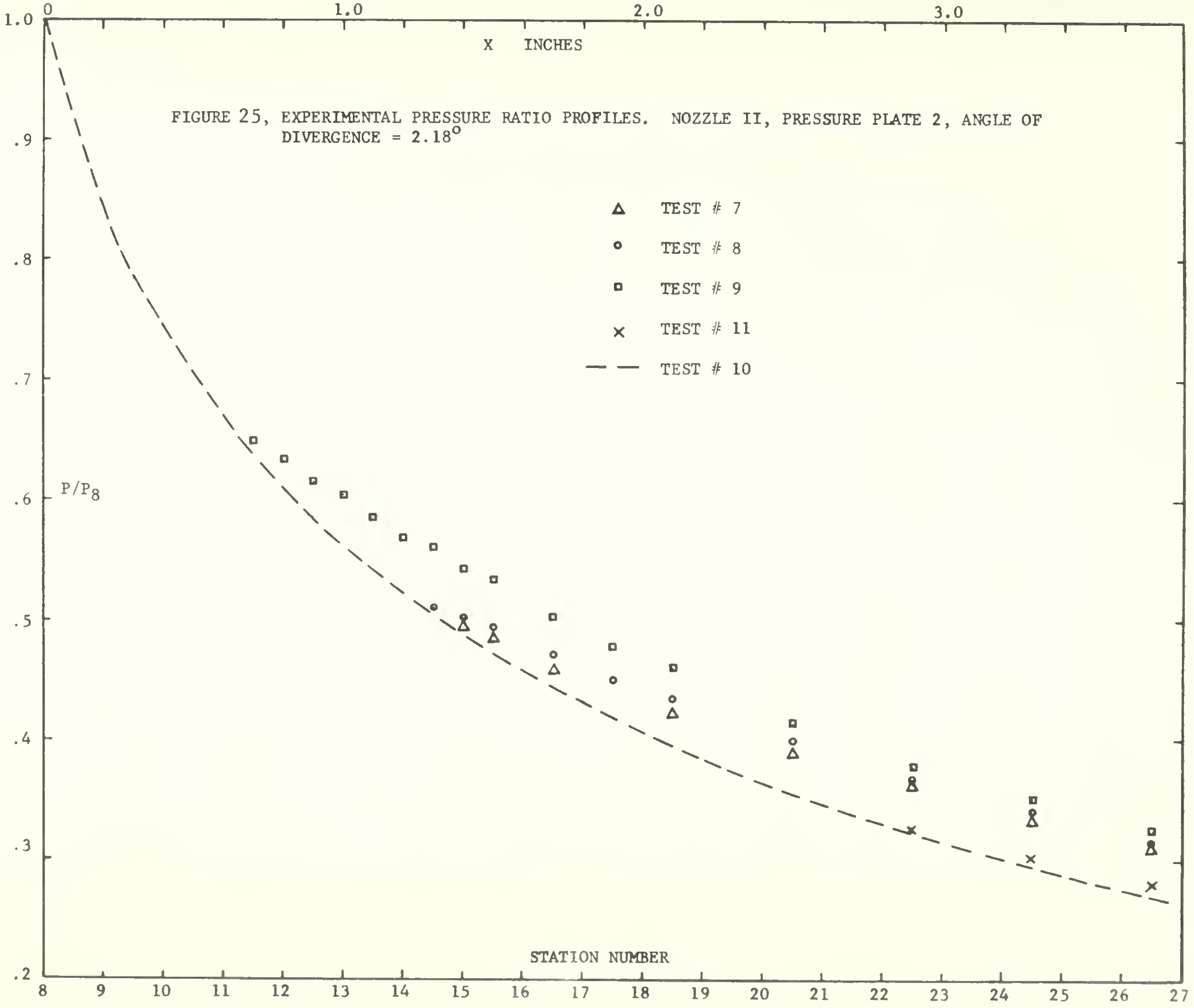

FIGURE 25, EXPERIMENTAL PRESSURE RATIO PROFILES. NOZZLE II, PRESSURE PLATE 2, ANGLE OF DIVERGENCE = 2.18°

TABLE 8

Pressure Data for Figure No. 25

		Run No. 7_{II}		Run No. 8_{II}		Run No. 9_{II}		Run No. 10_{II}		Run No. 11_{II}	
		P_o = 80.7 psia T_o = -30.6°F		P_o = 86.2 psia T_o = -37.8°F		P_o = 114.7 psia T_o = -33.6°F		P_o = 84.7 psia T_o = 79.3°F		P_o = 112.7 psia T_o = -1.5°F	
Tube No.	Sta. No.	P("Hg)	P/P_8	P("Hg)	P/P_8	P("Hg)	P/P_8	P("Hg)	P/P_8	P("Hg)	P/P_8
3	8	92.6	1.000	98.8	1.000	130.1	1.000	97.3	1.000	129.4	1.000
4	8½	85.3	.921	90.8	.919	119.9	.919	89.3	.918	119.0	.919
5	9	78.4	.846	83.1	.841	110.2	.845	81.9	.841	109.2	.844
6	9½	72.8	.787	77.2	.782	103.1	.790	76.2	.783	102.2	.789
7	10	69.0	.745	73.3	.741	96.4	.740	72.6	.746	96.4	.745
8	10½	65.1	.703	68.9	.696	91.9	.706	68.6	.705	90.9	.702
9	11	61.3	.662	65.1	.659	86.7	.667	65.2	.670	86.2	.666
10	11½	58.5	.632	62.2	.630	84.2	.649	61.9	.635	82.2	.635
11	12	56.4	.609	59.6	.603	82.1	.632	59.6	.613	78.5	.606
12	12½	54.0	.583	57.1	.578	79.8	.615	57.1	.586	75.6	.584
13	13	52.1	.562	55.2	.559	78.4	.604	55.0	.565	72.6	.561
14	13½	50.4	.544	53.5	.541	76.0	.585	53.0	.545	70.2	.542
15	14	47.9	.518	51.0	.516	73.8	.567	50.8	.522	67.1	.519
16	14½	46.6	.503	50.4	.510	72.8	.560	48.8	.501	64.9	.501
17	15	45.7	.493	49.5	.501	70.6	.542	47.8	.491	63.1	.488
18	15½	44.7	.483	48.8	.494	69.5	.533	46.7	.480	61.7	.476
19	16½	42.2	.456	46.5	.471	65.5	.502	43.3	.445	57.2	.442
20	17½	40.3	.435	44.4	.449	62.2	.477	40.8	.419	54.4	.420
21	18½	39.0	.421	42.9	.434	59.8	.460	38.5	.396	51.0	.394
22	20½	36.0	.389	39.3	.398	54.0	.414	34.6	.355	46.0	.355
23	22½	33.6	.363	36.3	.367	49.3	.378	31.4	.322	42.2	.326
24	24½	30.7	.332	33.7	.341	45.8	.352	28.9	.297	39.1	.302
25	26½	28.5	.308	31.1	.315	42.4	.326	26.5	.272	36.3	.281

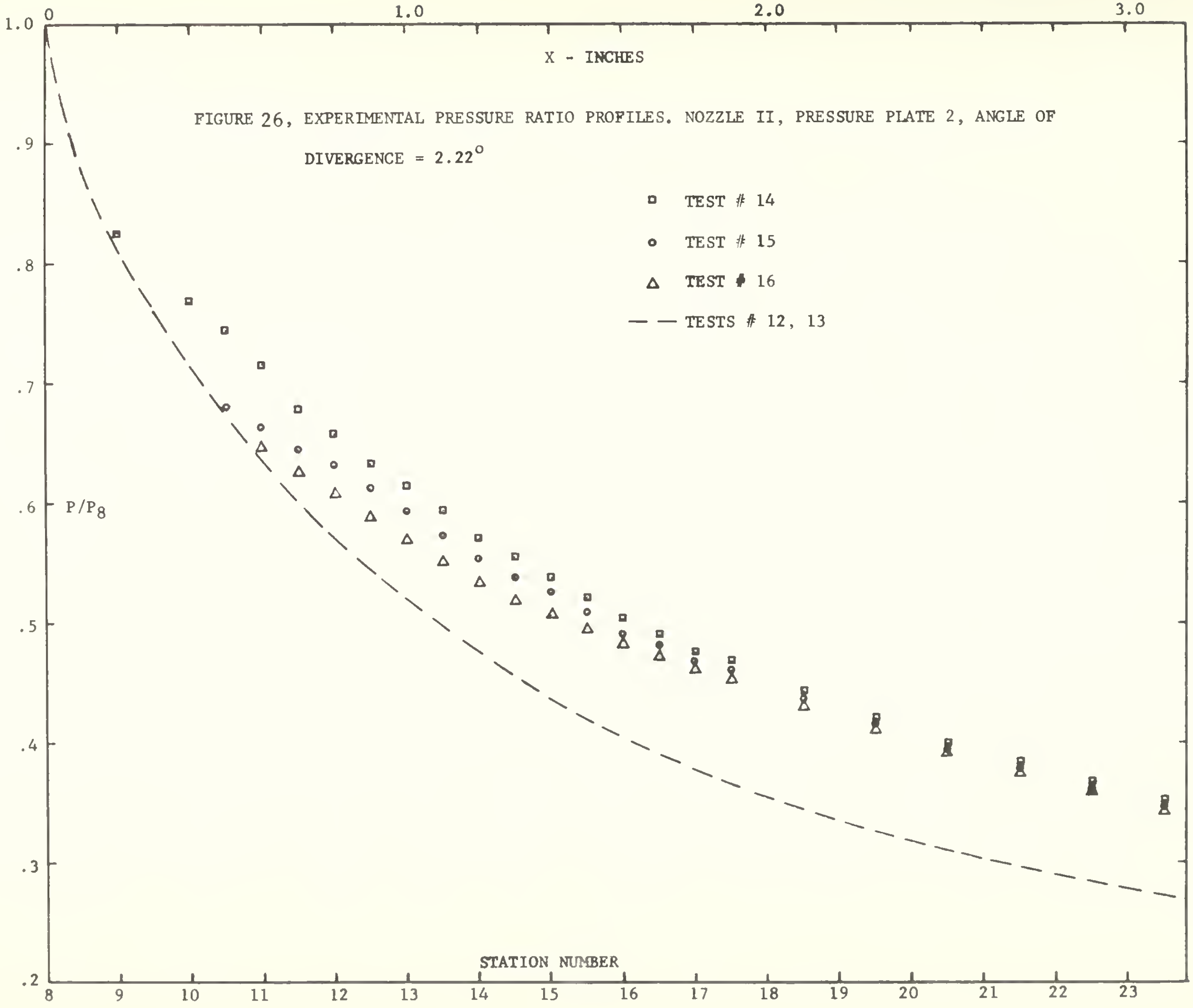
FIGURE 26, EXPERIMENTAL PRESSURE RATIO PROFILES. NOZZLE II, PRESSURE PLATE 2, ANGLE OF DIVERGENCE = 2.22°

TABLE 9

Pressure Data for Figure No. 26

Tube No.	Station	Test No. 12_{II} P_o=106.2 psia T_o=146.7°F P("Hg)	 P/P_8	Test No. 13_{II} P_o=96.2 psia T_o=126°F P("Hg)	 P/P_8	Test No 14_{II} P_o=135.2 psia T_o=-37.0°F P("Hg)	 P/P_8	Test No. 15_{II} P_o=103.2 psia T_o=-43.2°F P("Hg)	 P/P_8	Test No. 16_{II} P_o=112.2 psia T_o=-39.0°F P("Hg)	 P/P_8
1	8	119.3	1.000	108.5	1.000		*	116.9	1.000	127.3	1.000
2	9	96.9	.811	88.1	.812	127.4	.827	96.4	.825	105.3	.826
3	10	85.1	.713	77.1	.711	118.6	.769	8 .6	.716	91.3	.712
4	10½	80.2	.672	72.6	.670	114.6	.744	79.5	.680	86.3	.673
5	11	75.6	.634	68.5	.631	110.1	.715	77.5	.663	83.0	.647
6	11½	71.4	.598	64.7	.596	104.5	.678	75.2	.644	80.1	.625
7	12	68.3	.572	61.8	.569	101.4	.658	73.7	.631	77.9	.607
8	12½	65.0	.545	58.8	.542	97.5	.632	71.5	.612	75.5	.589
9	13	62.4	.523	56.3	.519	94.7	.614	69.2	.593	73.0	.569
10	13½	60.6	.508	54.7	.505	91.6	.594	66.9	.572	70.5	.550
11	14	54.7	.459	49.4	.455	87.9	.570	64.6	.553	68.4	.533
12	14½	53.8	.451	48.6	.448	85.6	.555	62.9	.538	66.4	.517
13	15	52.0	.436	46.9	.432	83.1	.538	61.3	.525	64.9	.506
14	15½	50.4	.422	45.7	.421	80.4	.521	59.4	.508	62.9	.494
15	16	48.7	.408	43.4	.400	77.6	.503	57.3	.490	61.2	.481
16	16½	47.0	.394	42.3	.390	75.6	.490	56.2	.481	60.0	.471
17	17	44.7	.375	40.3	.372	73.5	.476	54.7	.468	58.5	.460
18	17½	43.6	.366	39.5	.364	72.2	.468	53.7	.460	57.5	.452
19	18½	40.9	.343	36.7	.338	68.2	.442	50.9	.436	54.6	.429
20	19½	39.2	.328	35.5	.327	64.9	.420	48.4	.414	52.2	.410
21	20½	38.1	.319	34.5	.318	61.6	.399	46.1	.394	49.6	.390
22	21½	35.1	.294	32.0	.295	59.1	.383	44.2	.378	47.8	.375
23	22½	34.3	.287	31.1	.286	56.6	.367	42.2	.361	45.6	.358
24	23½	3[illegible].5	.272	29.5	.272	54.2	.352	40.5	.347	43.6	.342
25	24½	32.8	.275	29.6	.273	52.0	.337	39.0	.334	42.0	.330

* Assumed Station 8 Total Pressure Ratio P_8/P_o = .560

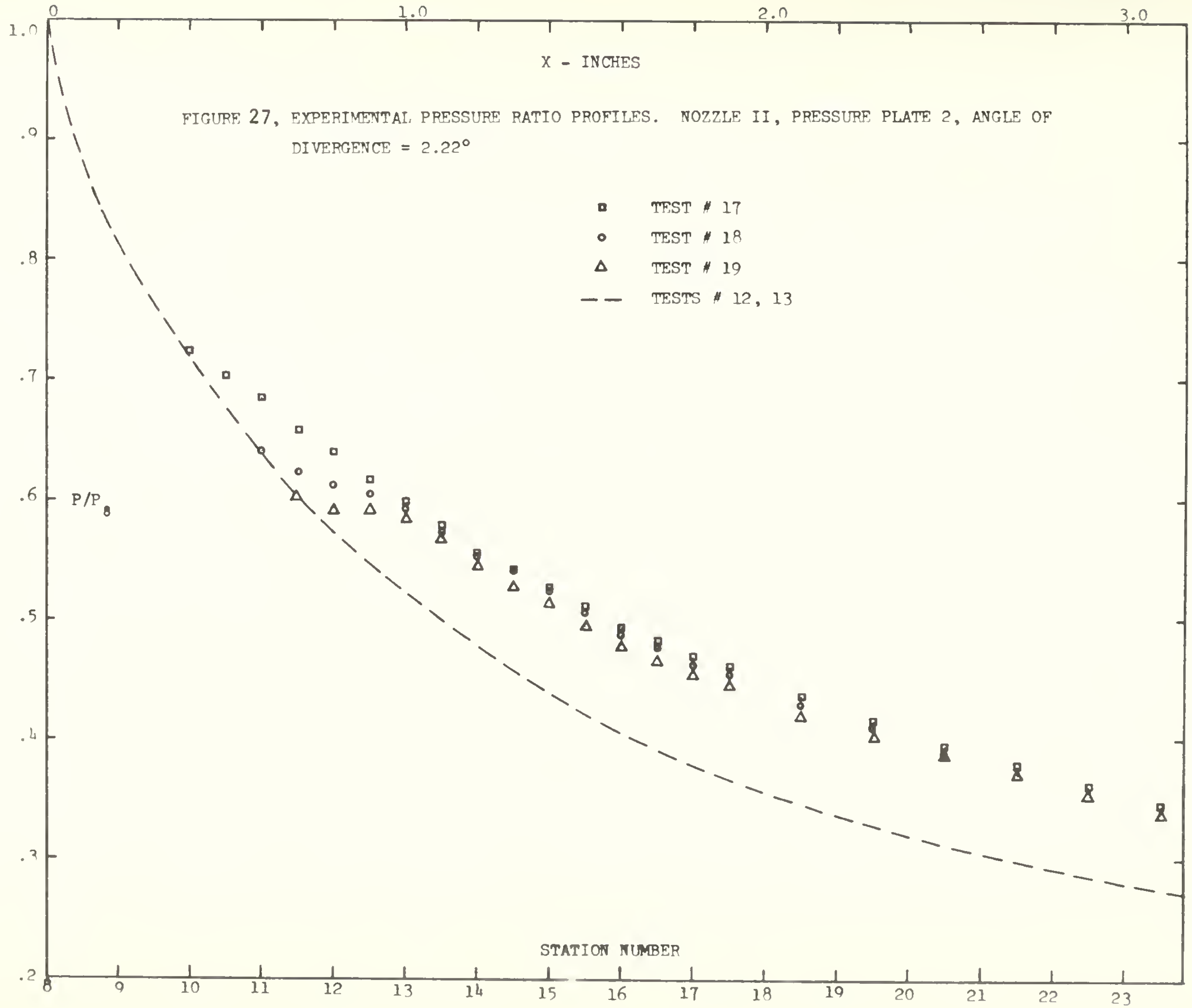

FIGURE 27, EXPERIMENTAL PRESSURE RATIO PROFILES. NOZZLE II, PRESSURE PLATE 2, ANGLE OF DIVERGENCE = 2.22°

TABLE 10

Pressure Data for Figure No. 27

		Test No. 17_{II}		Test No. 18_{II}		Test No. 19_{II}		Test No. 12_{II}	Test No. 13_{II}
		P_o=112.7 psia		P_o=84.7 psia		P_o=64.2 psia			
		T_o=-42.0°F		T_o=-47.2°F		T_o=-43.0°F			
Tube No.	Station	P("Hg)	P/P_8	P("Hg)	P/P_8	P("Hg)	P/P_8		
1	8	127.9	1.000	95.4	1.000	72.1	1.000		
2	9	105.6	.826	78.7	.825	59.4	.825		
3	10	92.4	.723	68.3	.716	51.9	.719		
4	10½	89.6	.701	64.2	.673	48.5	.673		
5	11	87.4	.684	61.1	.640	46.0	.638		
6	11½	84.0	.657	59.3	.622	43.5	.603		
7	12	81.7	.640	58.3	.611	42.5	.590		
8	12½	78.7	.616	57.6	.604	42.5	.590		
9	13	76.4	.598	56.4	.591	42.1	.584		
10	13½	73.9	.578	54.6	.572	40.9	.567	(See Table 9)	
11	14	71.0	.555	52.8	.553	39.2	.544		
12	14½	69.1	.541	51.6	.541	38.0	.527		
13	15	67.2	.526	50.0	.524	36.9	.512		
14	15½	65.1	.510	48.2	.505	35.6	.494		
15	16	62.9	.492	46.4	.486	34.3	.476		
16	16½	61.6	.482	45.5	.476	33.5	.465		
17	17	59.9	.469	44.1	.462	32.6	.452		
18	17½	58.8	.460	43.2	.453	32.0	.444		
19	18½	55.6	.435	40.9	.429	30.2	.419		
20	19½	53.0	.415	39.1	.410	28.9	.401		
21	20½	50.4	.394	37.0	.388	26.7	.370		
22	21½	48.3	.378	35.3	.370	23.8	.330		
23	22½	46.1	.361	33.7	.353	23.0	.319		
24	23½	44.1	.345	32.3	.338	21.1	.293		
25	24½			31.2	.327	20.7	.287		

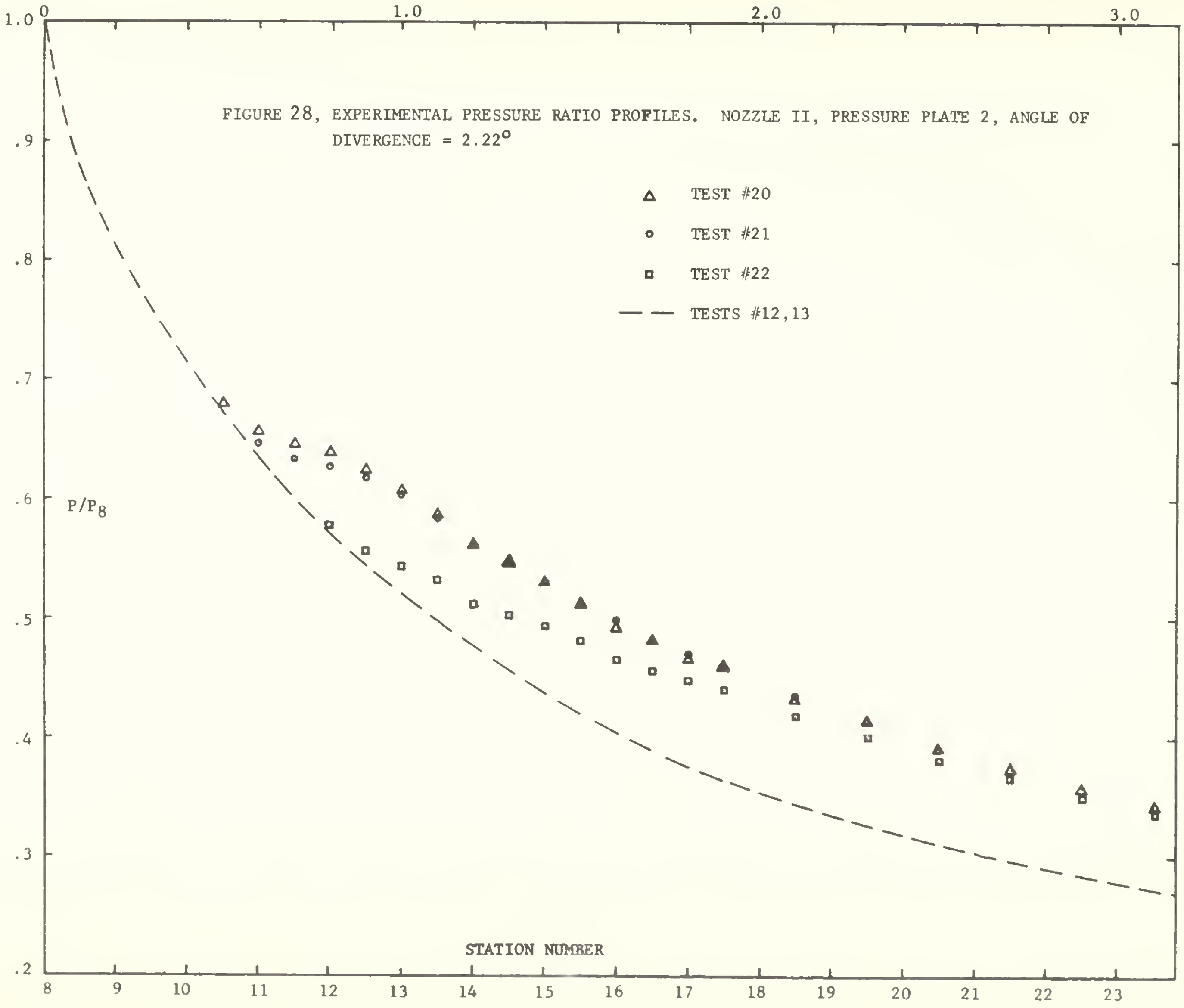

FIGURE 28, EXPERIMENTAL PRESSURE RATIO PROFILES. NOZZLE II, PRESSURE PLATE 2, ANGLE OF DIVERGENCE = 2.22°

TABLE 11

Pressure Data for Figure No. 28

		Test No. 20_{II}		Test No. 21		Test No. 22_{II}		Test No. 12_{II}	Test No. 13_{II}
		P_o=95.2 psia		P_o=90.2 psia		P_o=108.7 psia			
		T_o=-44.0°F		T_o=-44.5°F		T_o=-27.5°F			
Tube No.	Station	P("Hg)	P/P_8	P("Hg)	P/P_8	P("Hg)	P/P_8		
1	8	107.2	1.000	101.6	1.000	123.3	1.000		
2	9	88.6	.826	83.8	.825	102.0	.826		
3	10	76.8	.716	72.8	.716	88.4	.716		
4	10½	72.7	.679	68.4	.673	83.2	.675		
5	11	70.3	.656	65.7	.647	78.8	.639		
6	11½	69.1	.645	64.3	.633	74.2	.601		
7	12	68.4	.638	63.7	.627	71.2	.577		
8	12½	66.8	.623	62.8	.618	68.6	.556		
9	13	65.0	.606	61.3	.604	67.0	.543		
10	13½	62.8	.586	59.2	.583	65.5	.531		
11	14	60.2	.561	57.0	.561	63.1	.511	(See Table 9)	
12	14½	58.7	.548	55.5	.546	61.9	.502		
13	15	56.7	.529	53.9	.530	60.7	.492		
14	15½	54.8	.511	52.0	.512	59.1	.480		
15	16	52.7	.492	50.6	.498	57.4	.465		
16	16½	51.6	.481	48.9	.481	56.3	.456		
17	17	50.0	.466	47.8	.470	55.2	.447		
18	17½	49.1	.458	46.8	.460	54.2	.440		
19	18½	46.2	.431	44.3	.436	51.4	.417		
20	19½	44.1	.411	42.0	.413	49.3	.400		
21	20½	42.0	.392	39.5	.389	46.8	.380		
22	21½	40.1	.374	36.8	.362	45.0	.365		
23	22½	38.4	.358	35.3	.347	43.0	.349		
24	23½	36.8	.343	33.0	.325	41.1	.333		
25	24½	35.4	.330	32.0	.315	39.7	.324		

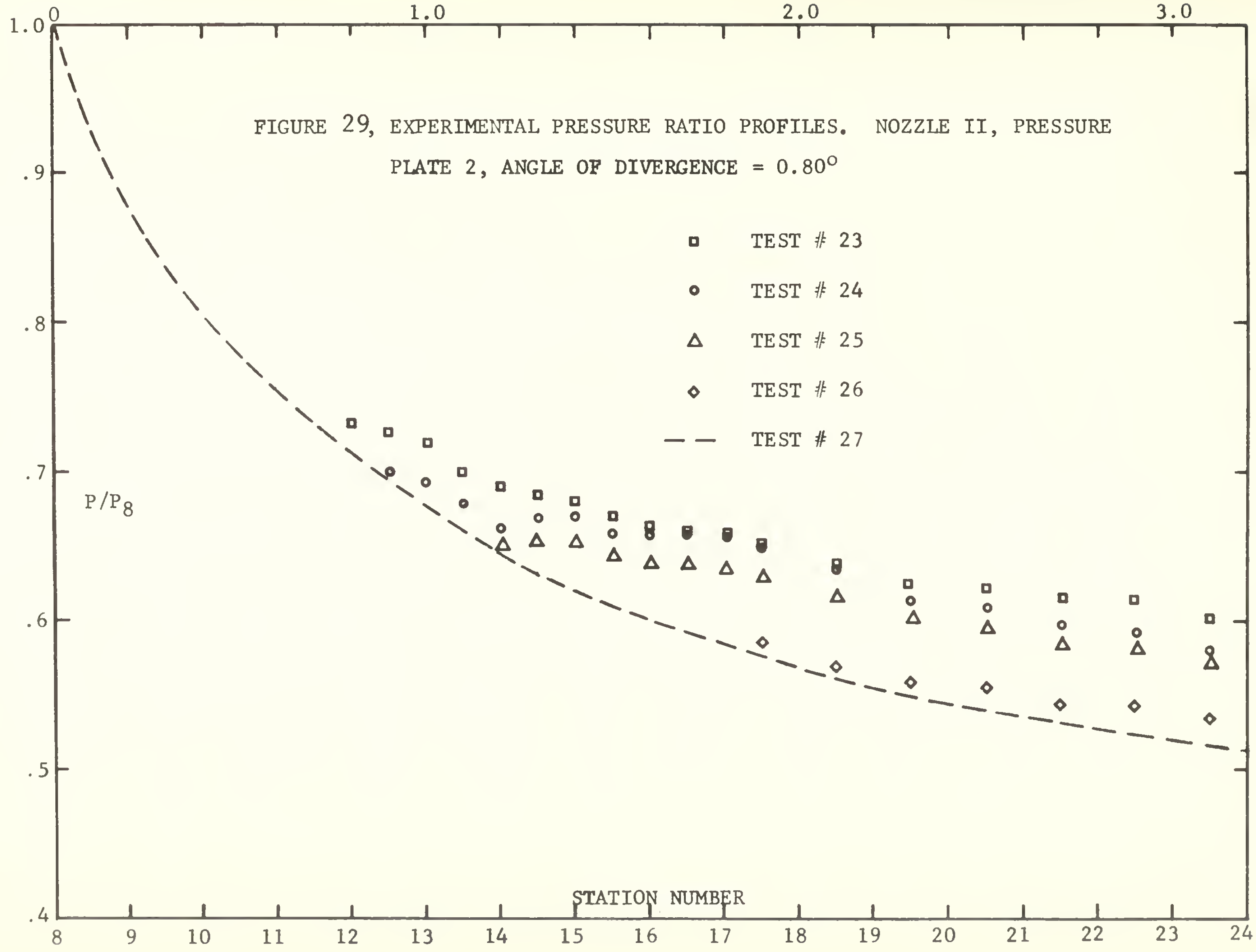

FIGURE 29, EXPERIMENTAL PRESSURE RATIO PROFILES. NOZZLE II, PRESSURE PLATE 2, ANGLE OF DIVERGENCE = 0.80°

TABLE 12

Pressure Data for Figure No. 29

Tube No.	Station	Test No. 23_{II} P_o=128.2 psia T_o=-40.6°F P("Hg)	 P/P_8	Test No. 24_{II} P_o=121.7 psia T_o=-39.9°F P("Hg)	 P/P_8	Test No. 25_{II} P_o=131.7 psia T_o=-32.9°F P("Hg)	 P/P_8	Test No. 26_{II} P_o=101.7 psia T_o=-26.5°F P("Hg)	 P/P_8	Test No. 27_{II} P_o=93.7 psia T_o=1.0°F P("Hg)	 P/P_8
1	8		*		*		*	129.8	1.000	119.7	1.000
2	9							114.0	.879	105.2	.879
3	10	131.1	.803	124.7	.803	134.7	.802	104.3	.805	96.4	.805
4	10½	127.9	.781	121.0	.779	131.3	.782	101.4	.781	93.5	.781
5	11	124.4	.760	117.3	.756	127.1	.756	98.0	.755	90.6	.757
6	11½	119.9	.733	113.1	.729	122.2	.728	94.4	.727	87.5	.731
7	12	120.0	.734	110.7	.713	119.8	.714	92.3	.712	85.5	.715
8	12½	119.0	.727	108.8	.700	116.8	.695	90.0	.694	83.3	.696
9	13	117.5	.719	107.6	.693	114.8	.684	87.8	.677	81.1	.678
10	13½	114.1	.698	105.2	.678	111.9	.665	85.3	.658	79.1	.661
11	14	111.5	.681	102.8	.661	109.1	.650	82.4	.635	76.0	.635
12	14½	112.2	.686	103.9	.669	109.7	.653	82.1	.633	75.7	.633
13	15	111.5	.681	103.9	.669	109.5	.652	81.1	.625	74.7	.625
14	15½	109.4	.669	102.4	.659	108.0	.643	79.2	.611	72.9	.609
15	16	108.6	.664	102.0	.657	107.2	.639	77.9	.600	71.6	.598
16	16½	108.2	.661	102.0	.657	107.3	.639	77.2	.595	71.0	.593
17	17	107.9	.659	101.8	.655	106.8	.635	76.1	.587	69.8	.583
18	17½	106.7	.652	100.7	.648	105.9	.630	75.7	.584	68.9	.576
19	18½	104.5	.639	98.3	.634	103.6	.616	73.8	.569	67.1	.561
20	19½	102.3	.625	95.8	.613	101.1	.602	72.5	.559	65.6	.549
21	20½	102.0	.623	94.5	.609	99.7	.594	71.4	.550	64.6	.540
22	21½	100.4	.614	92.6	.596	98.0	.583	70.5	.544	63.6	.532
23	22½	100.4	.614	91.9	.592	97.7	.581	70.4	.543	63.2	.528
24	23½	98.4	.601	89.9	.579	95.7	.570	69.1	.533	61.6	.515
25	24½	96.4	.589	87.6	.575	93.6	.557	68.1	.525	60.7	.507

* Assumed Station 8 Total Pressure Ratio P_8/P_o = .627

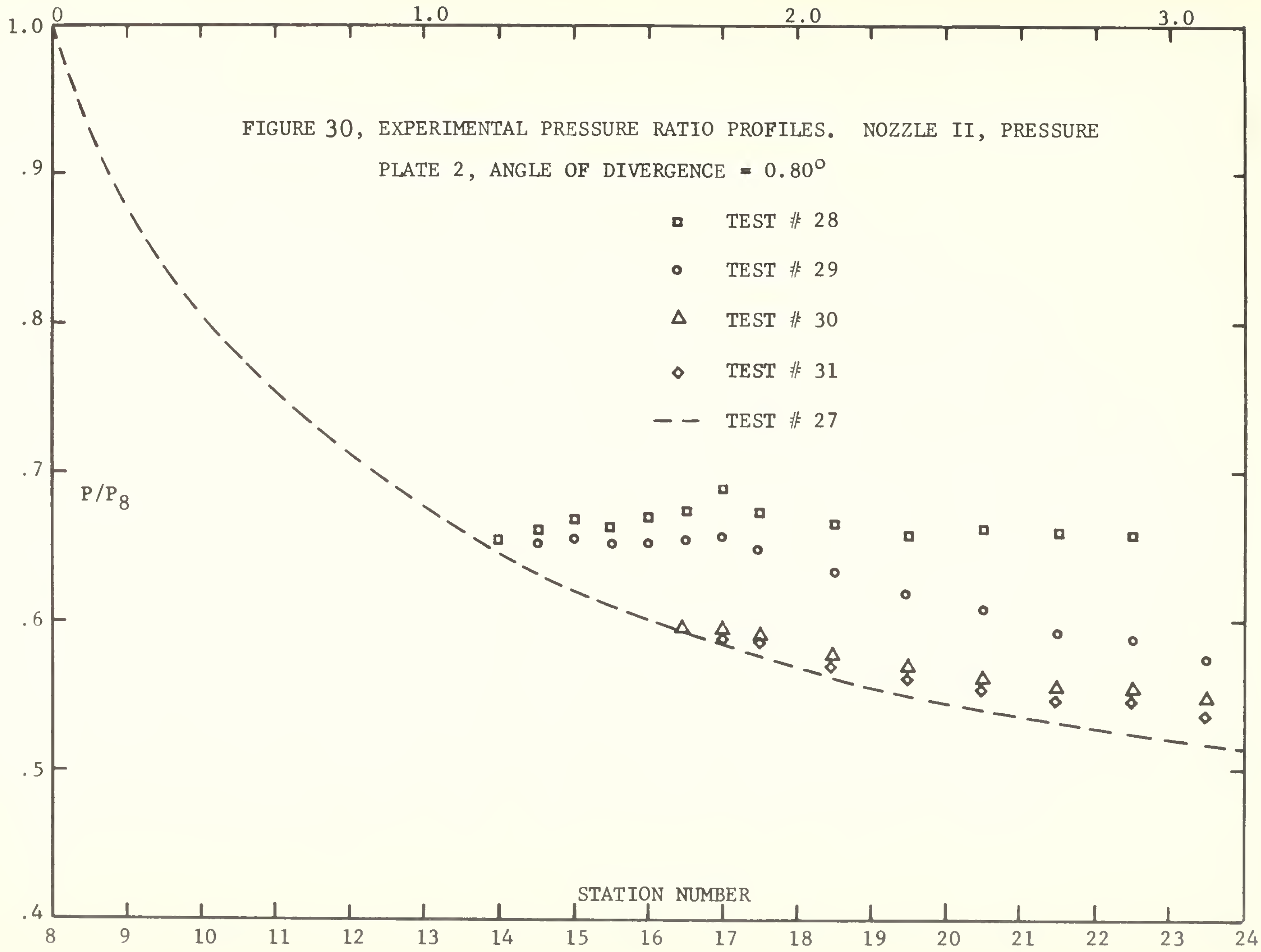

FIGURE 30, EXPERIMENTAL PRESSURE RATIO PROFILES. NOZZLE II, PRESSURE PLATE 2, ANGLE OF DIVERGENCE = 0.80°

TABLE 13

Pressure Data for Figure No. 30

Tube No.	Station	Test No. 28_{II} P_o=91.7 psia T_o=-53.2°F P("Hg)	 P/P_8	Test No. 29_{II} P_o=101.2 psia T_o=-40.1°F P("Hg)	 P/P_8	Test No. 30_{II} P_o=115.7 psia T_o=-29.0°F P("Hg)	 P/P_8	Test No. 31_{II} P_o=96.2 psia T_o=-31.6°F P("Hg)	 P/P_8	Test No. 27_{II}
1	8		*		*		*	123.1	1.000	
2	9					129.0	.875	108.2	.878	
3	10	93.6	.805	103.7	.804	118.0	.800	99.1	.805	
4	10½	90.6	.779	100.7	.780	114.9	.779	96.3	.493	
5	11	88.1	.757	97.7	.758	112.3	.761	93.1	.756	
6	11½	84.9	.729	94.4	.732	107.2	.728	89.7	.729	
7	12	83.3	.715	92.2	.715	105.0	.712	87.7	.713	
8	12½	81.0	.695	90.0	.698	102.2	.694	85.4	.693	
9	13	79.7	.685	88.2	.684	99.9	.678	83.2	.676	
10	13½	77.5	.665	85.6	.664	97.0	.659	81.1	.659	(See Table 12)
11	14	76.0	.653	83.1	.644	94.0	.638	78.5	.638	
12	14½	76.9	.660	83.9	.651	93.5	.635	78.1	.635	
13	15	77.6	.666	84.3	.654	92.2	.626	77.3	.628	
14	15½	77.1	.662	83.7	.649	90.1	.611	75.2	.611	
15	16	77.8	.668	83.8	.650	88.7	.602	74.2	.603	
16	16½	78.3	.672	84.1	.653	87.9	.596	73.3	.595	
17	17	80.2	.689	84.0	.652	87.1	.591	72.3	.587	
18	17½	78.3	.672	83.2	.646	86.6	.588	71.8	.583	
19	18½	77.3	.664	81.1	.630	84.8	.575	69.9	.568	
20	19½	76.4	.656	79.0	.613	83.2	.565	68.5	.556	
21	20½	76.8	.659	77.8	.604	82.5	.560	67.5	.548	
22	21½	76.7	.658	75.9	.589	81.4	.552	66.4	.539	
23	22½	76.5	.656	75.1	.583	81.4	.552	66.5	.540	
24	23½	74.1	.636	73.5	.570	80.1	.544	65.3	.531	
25	24½	71.8	.616	71.7	.556	78.9	.536	64.4	.524	

* Assumed Station 8 Total Pressure Ratio P_8/P_o = .627

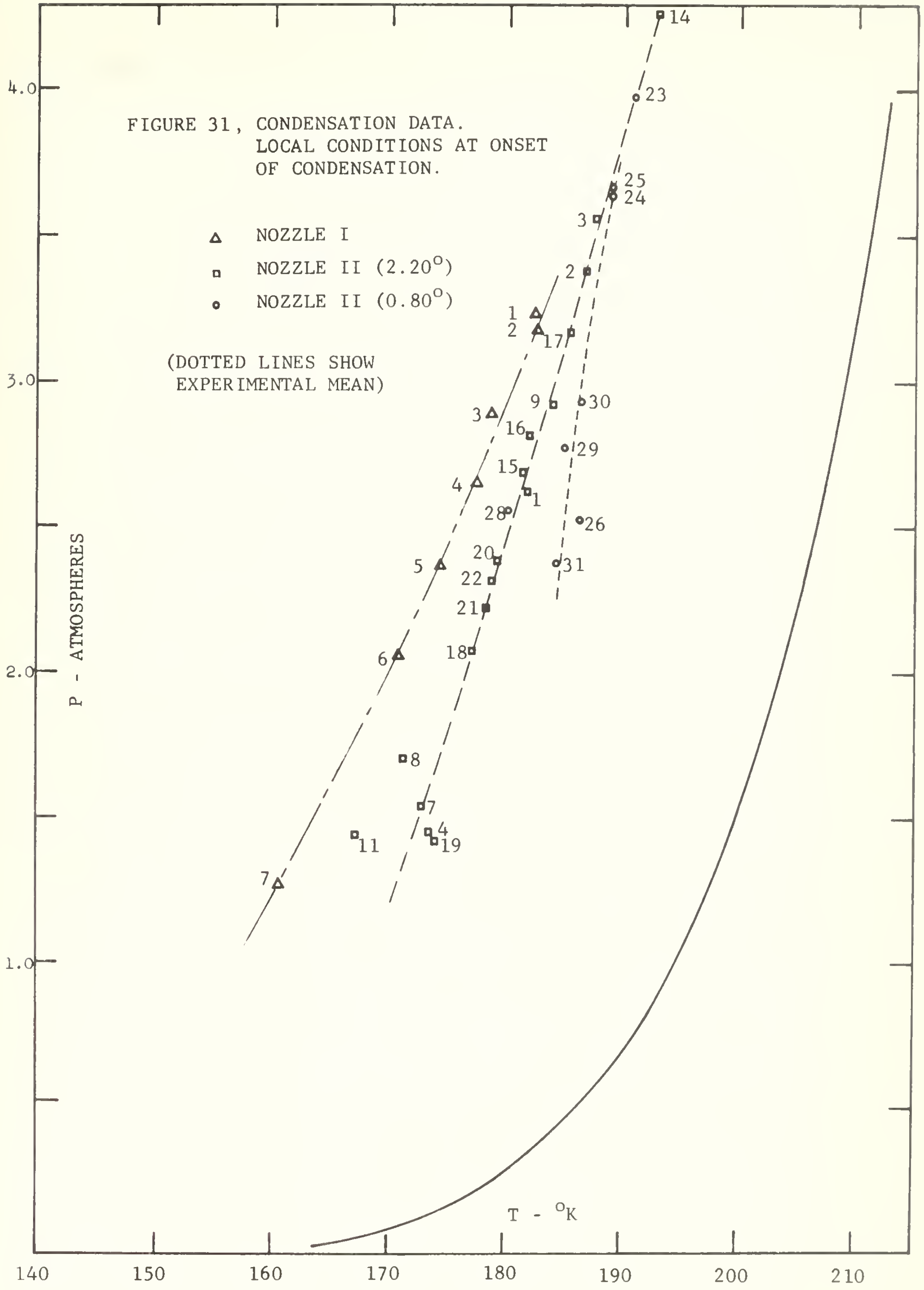

FIGURE 31, CONDENSATION DATA. LOCAL CONDITIONS AT ONSET OF CONDENSATION.

TABLE 14

EXPERIMENTAL DATA

LOCAL CONDITIONS AT ONSET OF CONDENSATION

Run	P_o (atm)	T_o °K	z_o	P (atm)	T °K	z
1_{I}	7.64	227.2	.892	3.23	182.5	.889
2_{I}	7.67	228.6	.895	3.18	182.6	.892
3_{I}	7.66	229.1	.896	2.89	178.7	.892
4_{I}	7.42	230.[illegible]	.902	2.66	177.3	.898
5_{I}	7.04	230.3	.907	2.37	174.5	.903
6_{I}	6.65	230.3	.913	2.06	170.8	.908
7_{I}	5.14	230.3	.934	1.26	160.8	.927
1_{II}	7.81	239.9	.913	2.62	181.9	.910
2_{II}	8.01	232.4	.897	3.38	186.9	.895
3_{II}	8.01	230.3	.893	3.56	187.6	.891
4_{II}	7.36	260.0	.942	1.46	173.5	.938
5_{II}			Non-Condensing			
6_{II}			Non-Condensing			
7_{II}	5.47	238.3	.939	1.54	172.9	.935
8_{II}	5.37	234.4	.929	1.71	171.3	.925
9_{II}	7.81	236.6	.907	2.92	184.1	.905
10_{II}			Non-Condensing			
11_{II}	7.66	254.6	.934	1.45	167.2	.929
12_{II}			Non-Condensing			
13_{II}			Non-Condensing			
14_{II}	9.19	234.8	.886	4.25	193.1	.884
15_{II}	7.02	231.3	.909	2.69	181.3	.906
16_{II}	7.63	233.6	.905	2.84	181.8	.902
17_{II}	7.66	232.0	.901	3.17	185.5	.899
18_{II}	5.76	231.1	.926	2.07	178.2	.923
19_{II}	4.37	231.4	.946	1.43	174.1	.942
20_{II}	6.48	230.9	.916	2.39	179.2	.912
21_{II}	6.14	230.5	.920	2.23	178.3	.915
22_{II}	7.40	240.0	.918	2.31	178.7	.914
23_{II}	9.72	232.8	.888	4.00	191.0	.886
24_{II}	8.28	233.1	.895	3.64	189.2	.893
25_{II}	8.95	237.0	.893	3.68	189.2	.891
26_{II}	6.92	240.6	.925	2.52	185.5	.922
27_{II}			Non Condensing			
28_{II}	6.24	225.7	.911	2.57	185.1	.907
29_{II}	6.88	233.0	.914	2.77	185.1	.911
30_{II}	7.86	239.2	.911	2.97	186.4	.909
31_{II}	6.54	237.8	.925	2.[illegible]8	184.2	.923

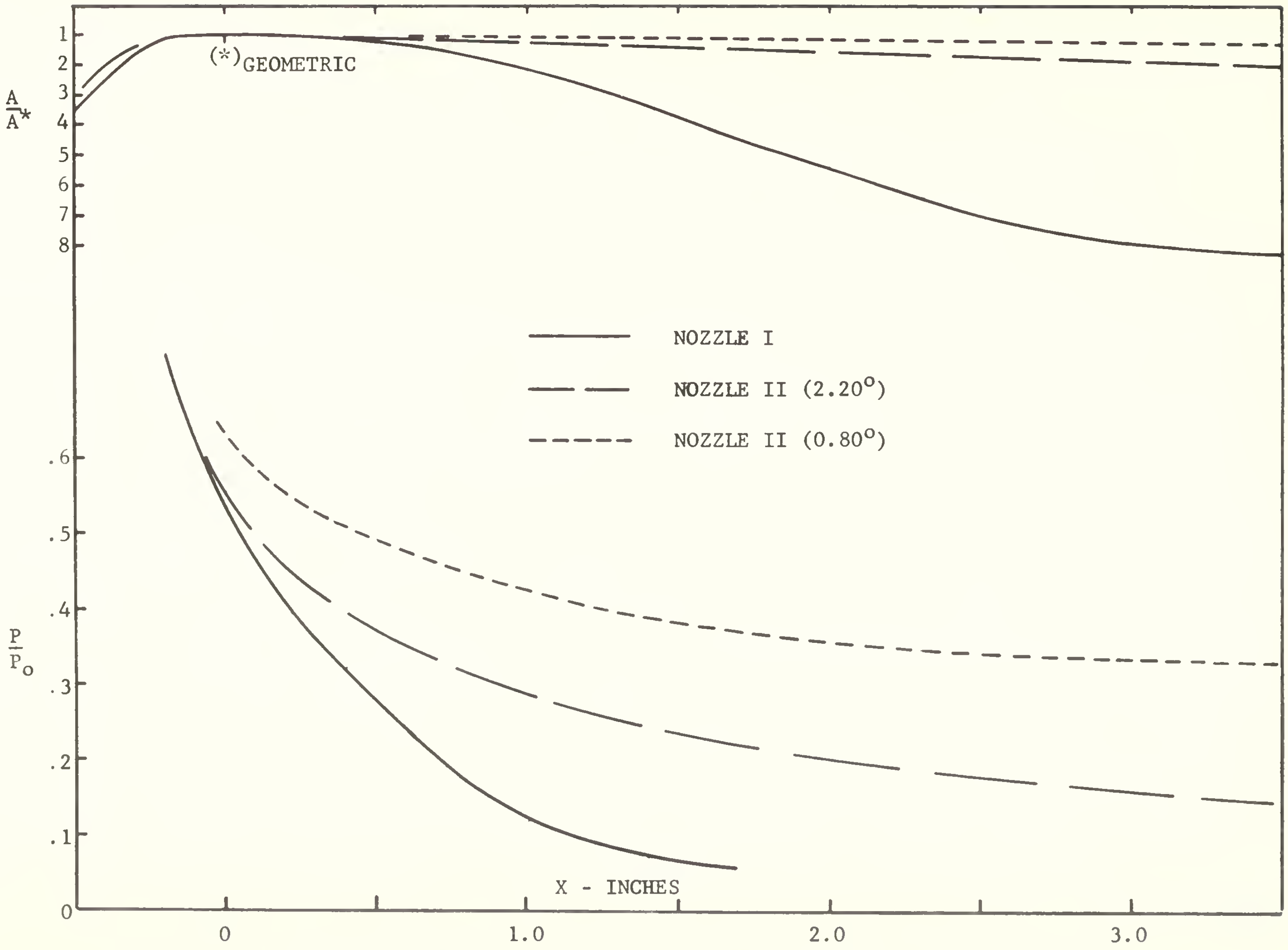

FIGURE 32, COMPARISON OF NOZZLE GEOMETRIES AND NON-CONDENSING PRESSURE PROFILES.

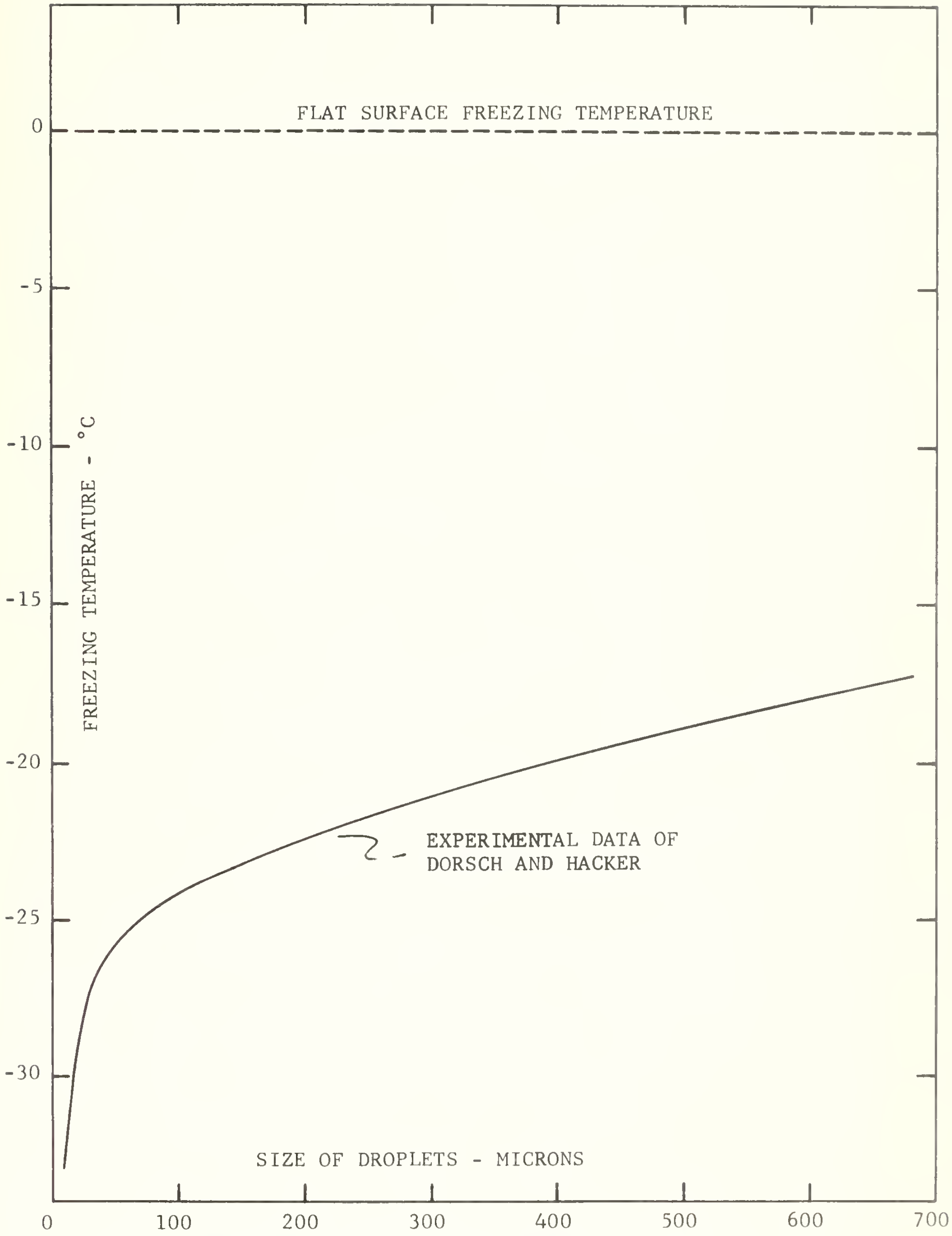

FIGURE 33, SPONTANEOUS FREEZING TEMPERATURE OF SUPERCOOLED WATER DROPLETS ON PLATIMUN AND COPPER SURFACES.

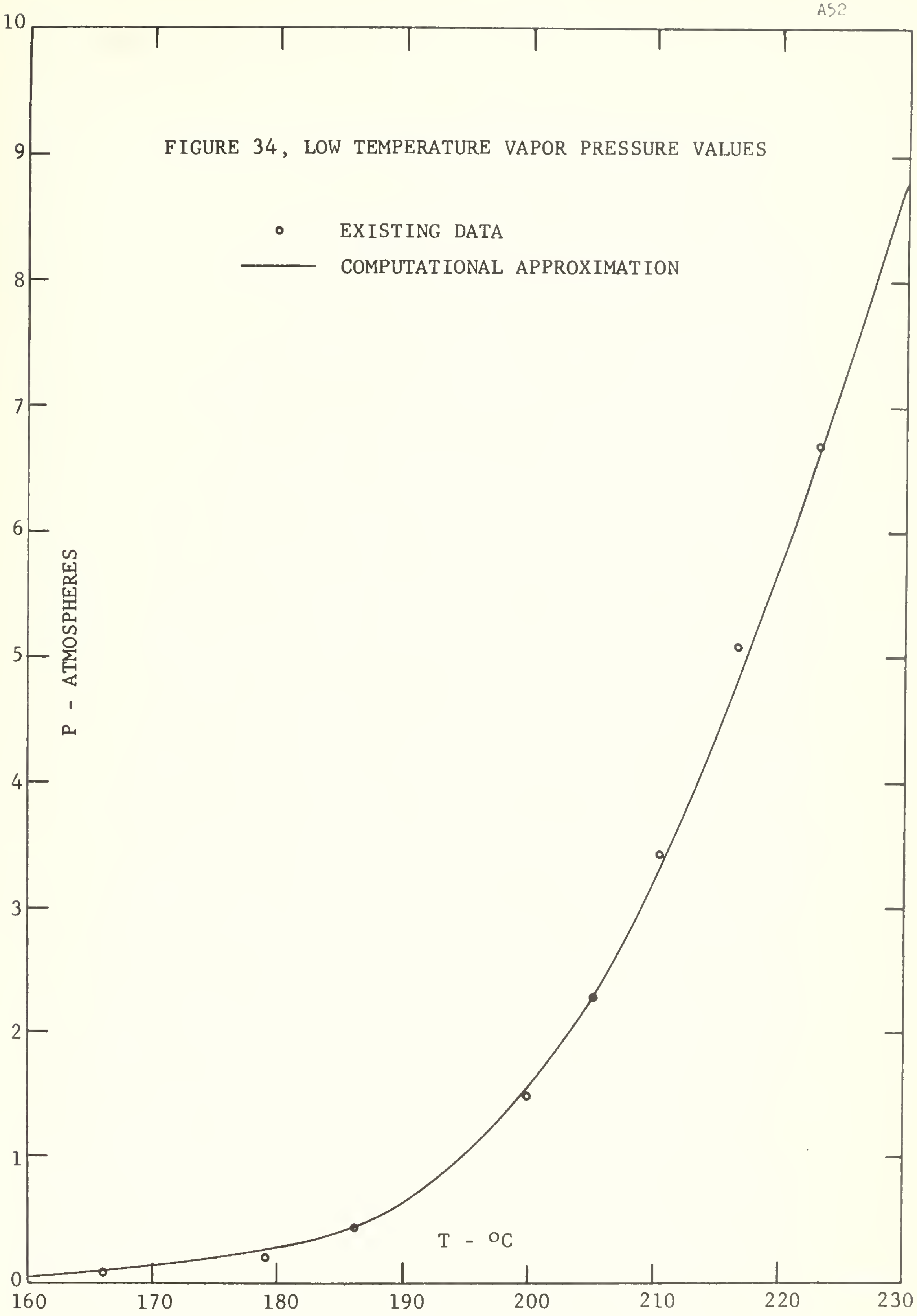

FIGURE 34, LOW TEMPERATURE VAPOR PRESSURE VALUES

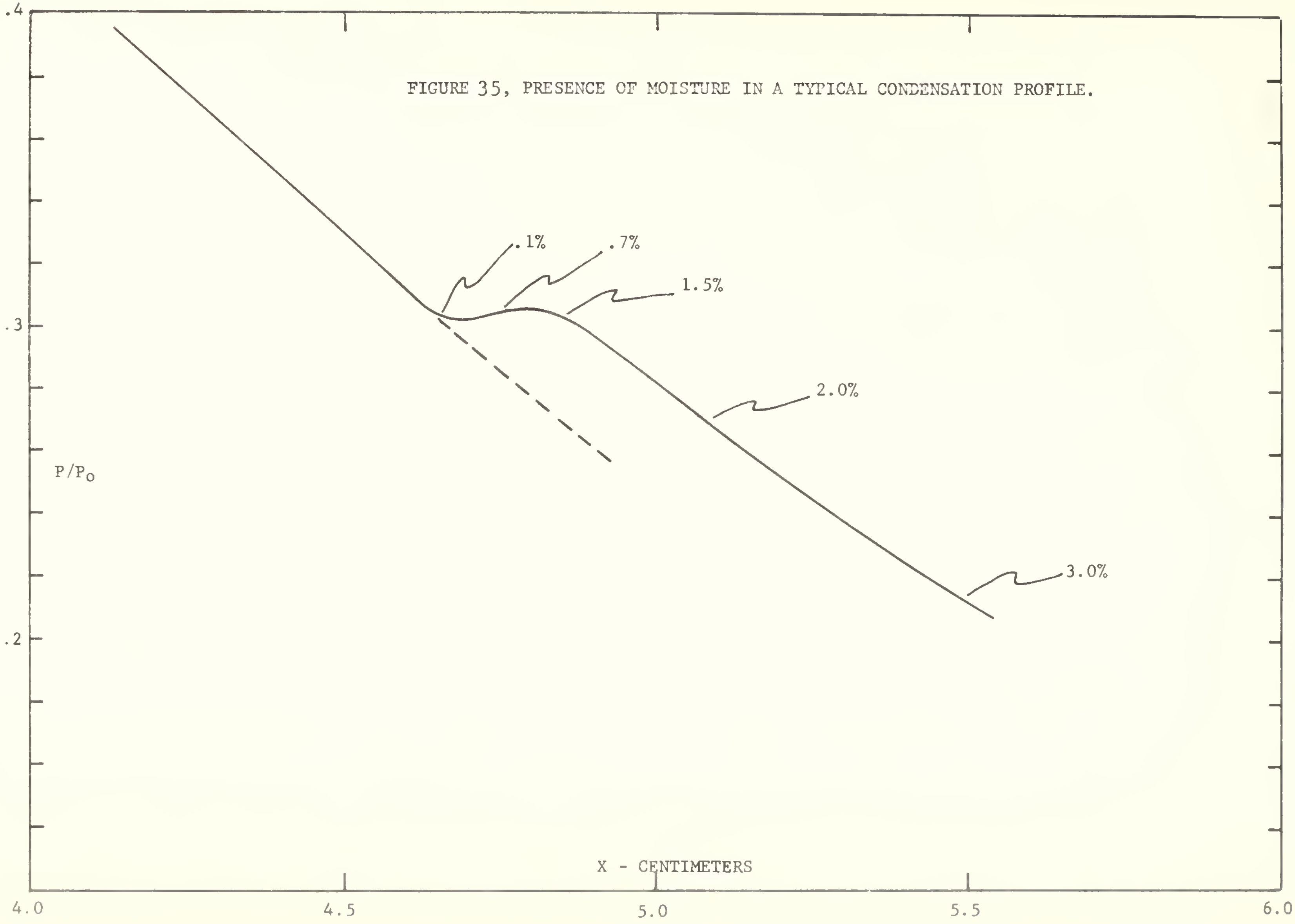

FIGURE 35, PRESENCE OF MOISTURE IN A TYPICAL CONDENSATION PROFILE.

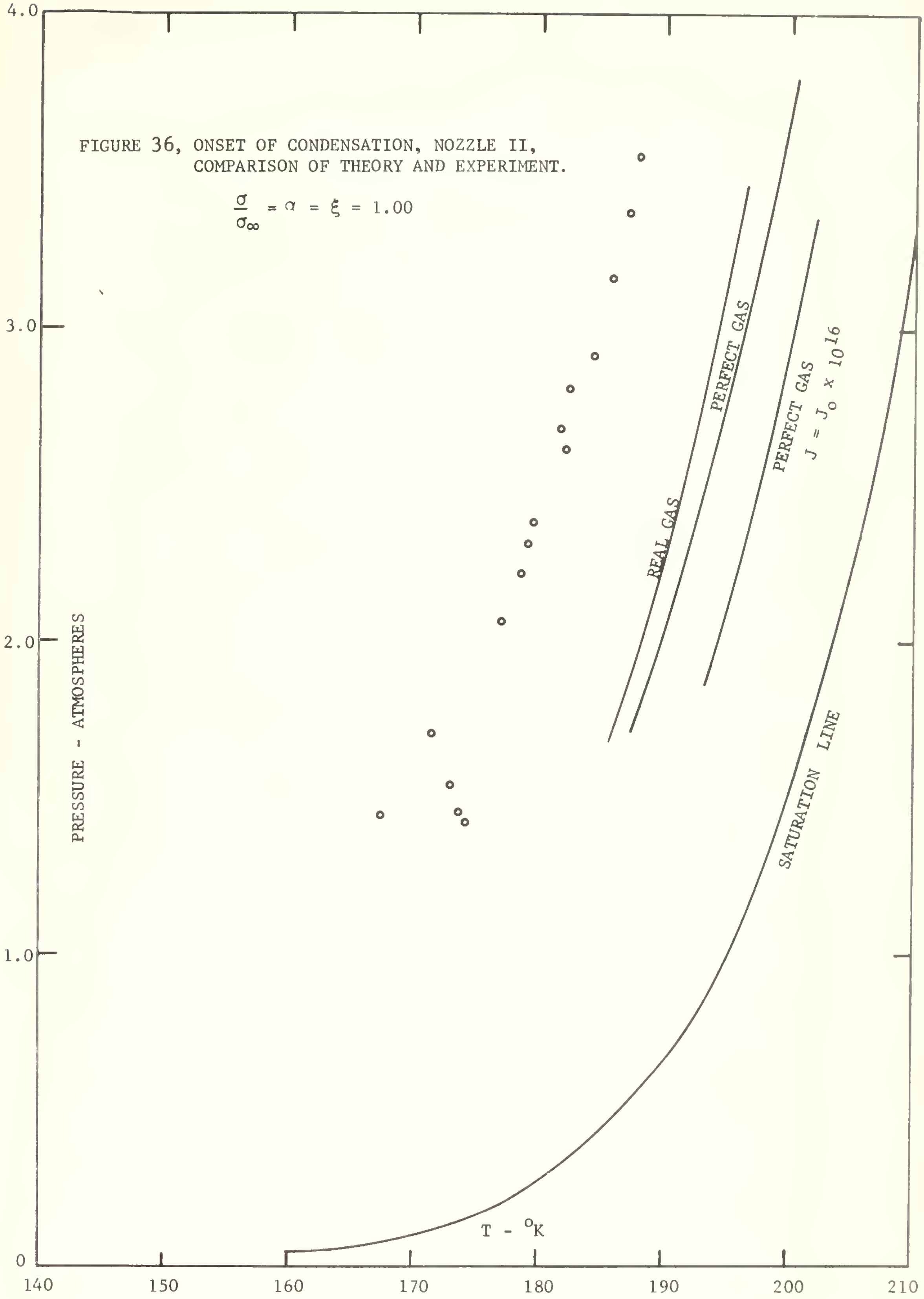

FIGURE 36, ONSET OF CONDENSATION, NOZZLE II, COMPARISON OF THEORY AND EXPERIMENT.

$\frac{\sigma}{\sigma_\infty} = \alpha = \xi = 1.00$

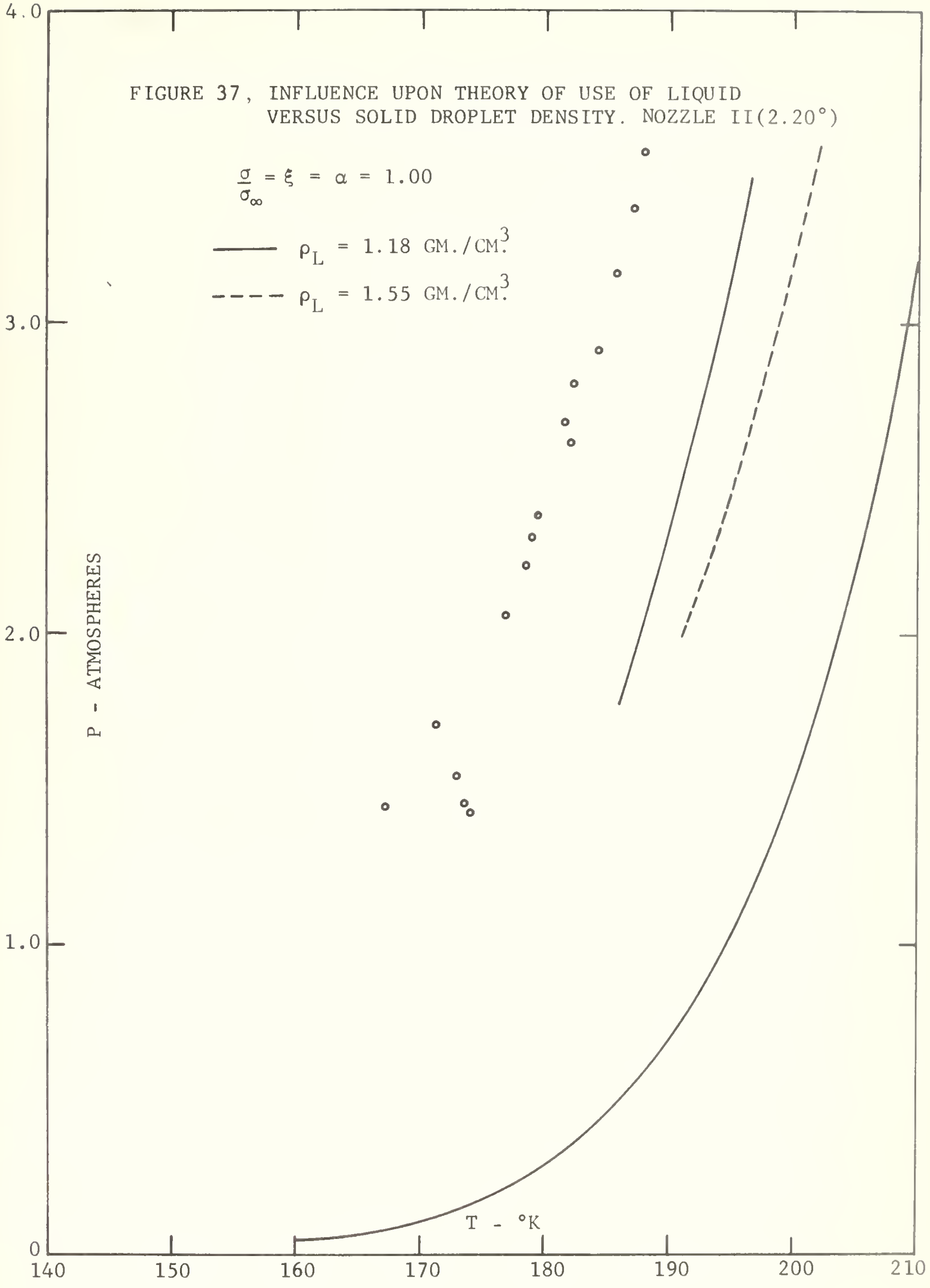

FIGURE 37, INFLUENCE UPON THEORY OF USE OF LIQUID VERSUS SOLID DROPLET DENSITY. NOZZLE II(2.20°)

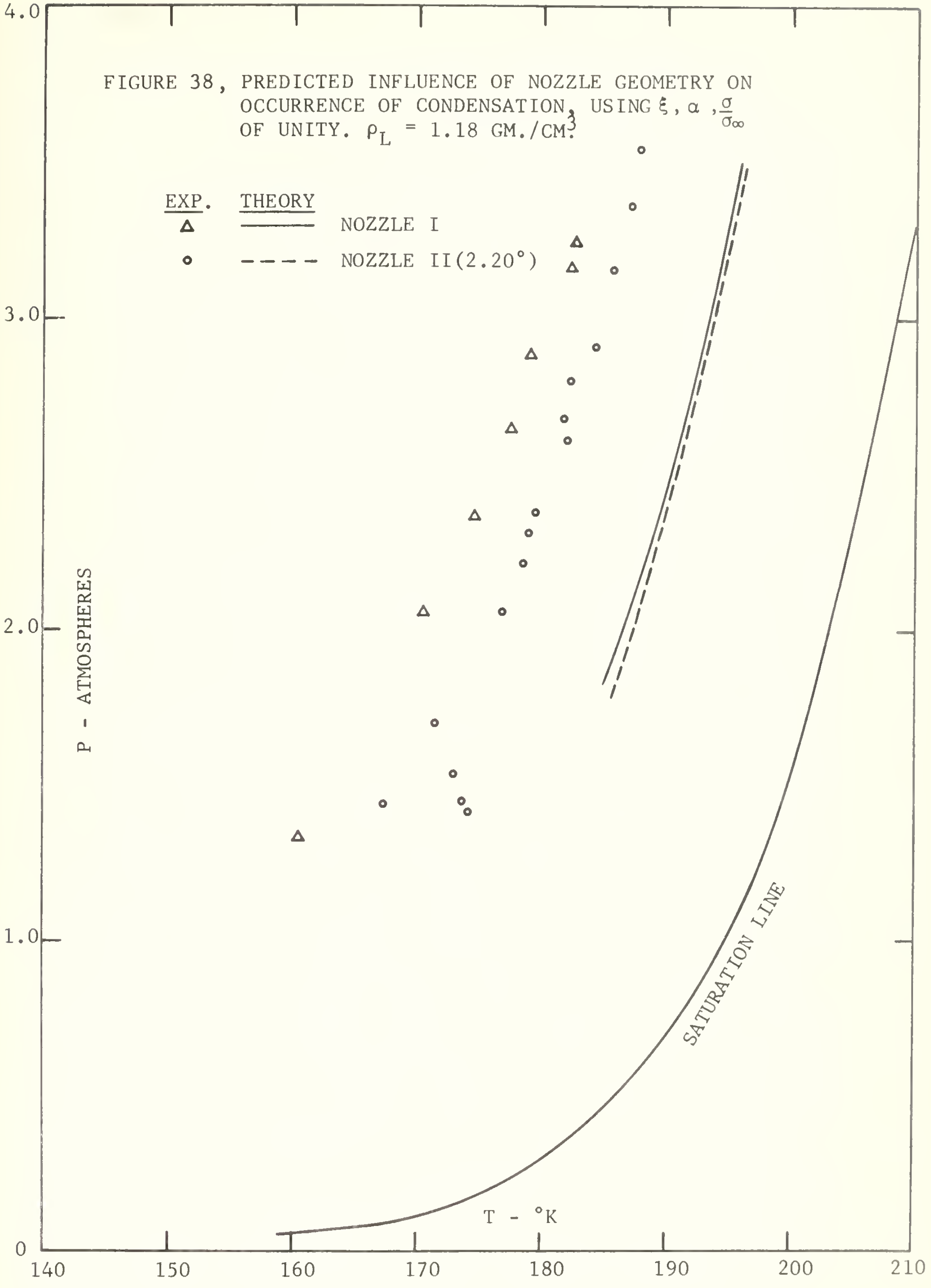

FIGURE 38, PREDICTED INFLUENCE OF NOZZLE GEOMETRY ON OCCURRENCE OF CONDENSATION, USING ξ, α, $\frac{\sigma}{\sigma_\infty}$ OF UNITY. $\rho_L = 1.18$ GM./CM.^{3}

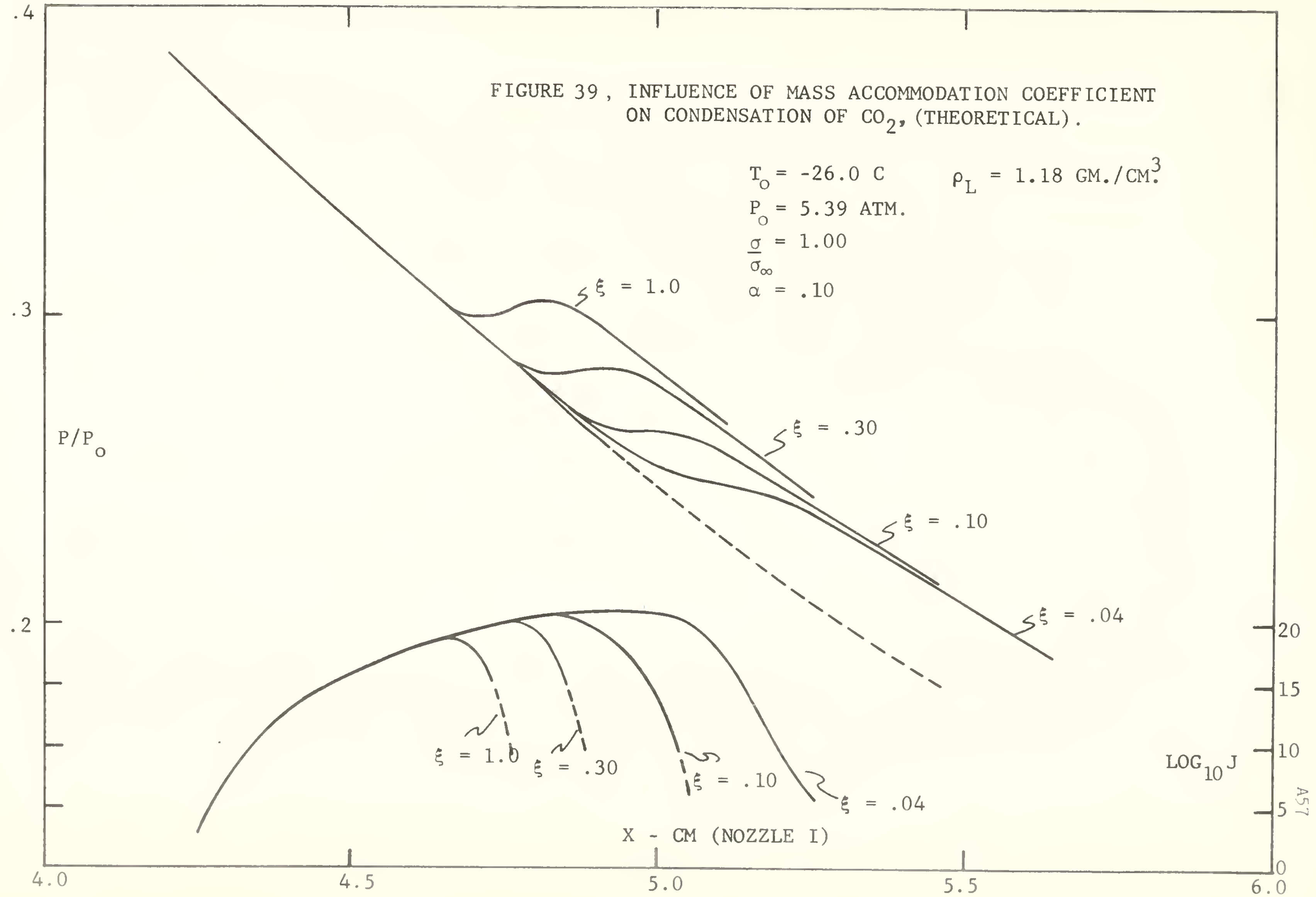

FIGURE 39, INFLUENCE OF MASS ACCOMMODATION COEFFICIENT ON CONDENSATION OF CO_2, (THEORETICAL).

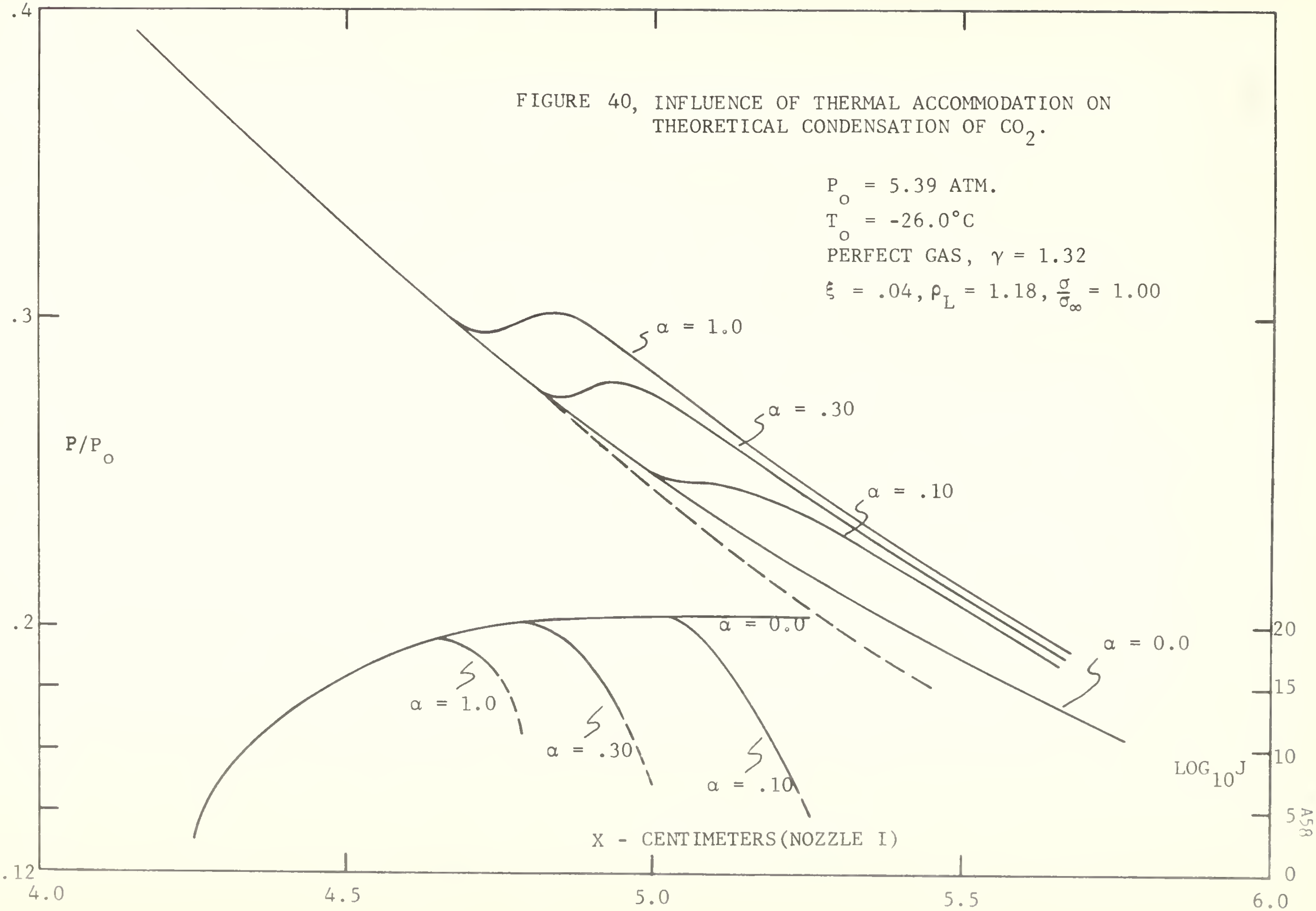

FIGURE 40, INFLUENCE OF THERMAL ACCOMMODATION ON THEORETICAL CONDENSATION OF CO_2.

$P_o = 5.39$ ATM.
$T_o = -26.0°C$
PERFECT GAS, $\gamma = 1.32$
$\xi = .04, \rho_L = 1.18, \frac{\sigma}{\sigma_\infty} = 1.00$

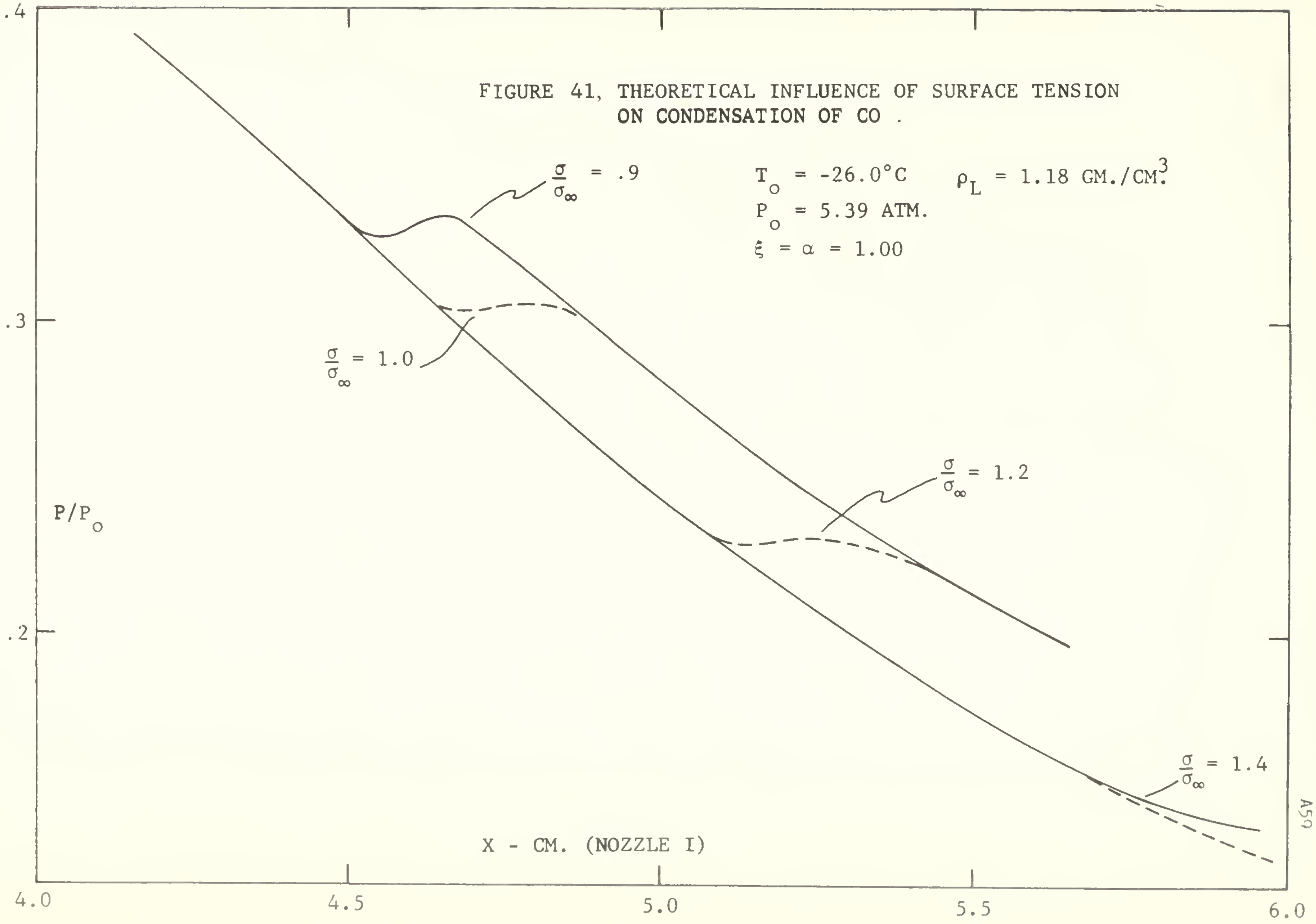

FIGURE 41, THEORETICAL INFLUENCE OF SURFACE TENSION ON CONDENSATION OF CO .

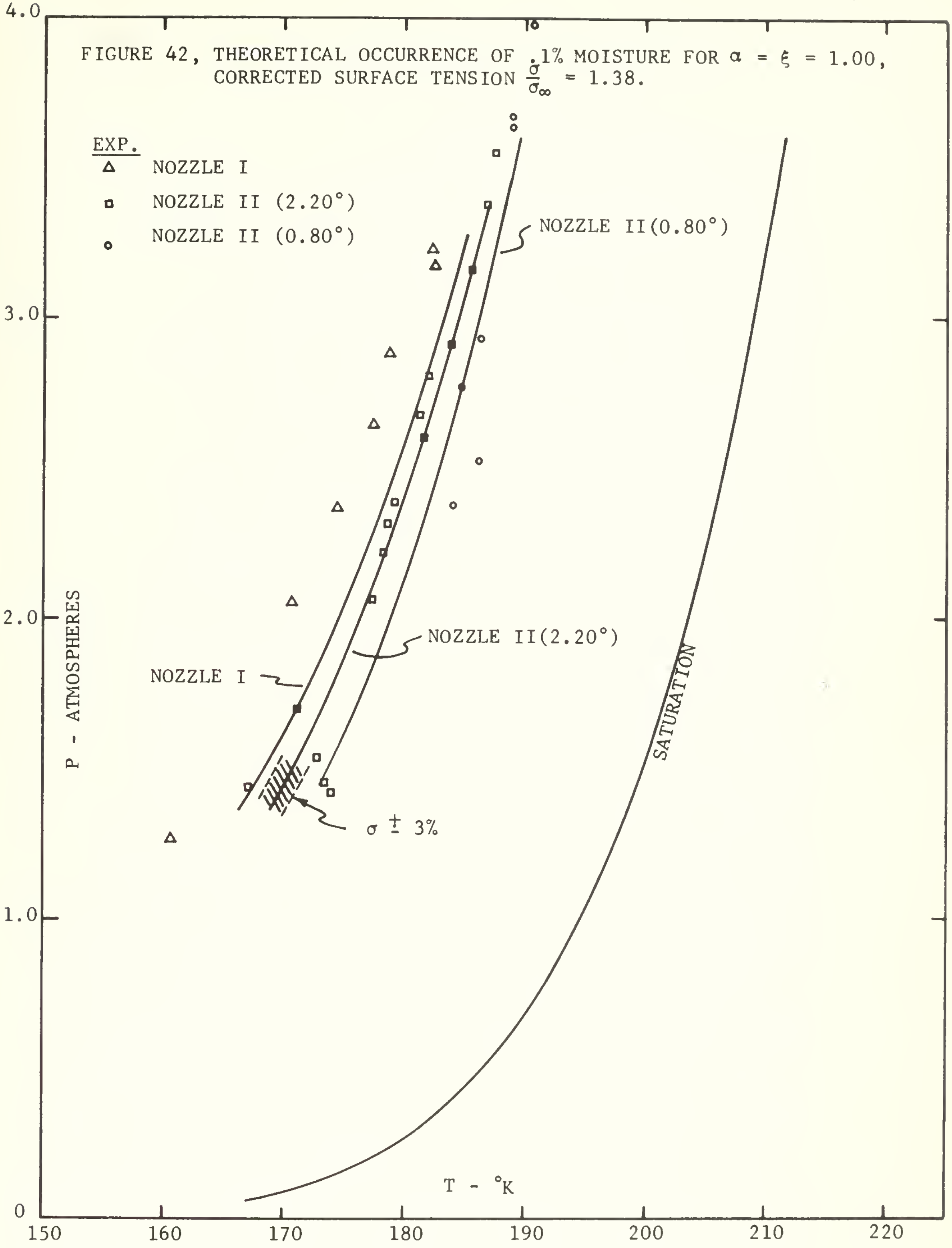

FIGURE 42, THEORETICAL OCCURRENCE OF .1% MOISTURE FOR α = ξ = 1.00, CORRECTED SURFACE TENSION $\frac{\sigma}{\sigma_\infty}$ = 1.38.

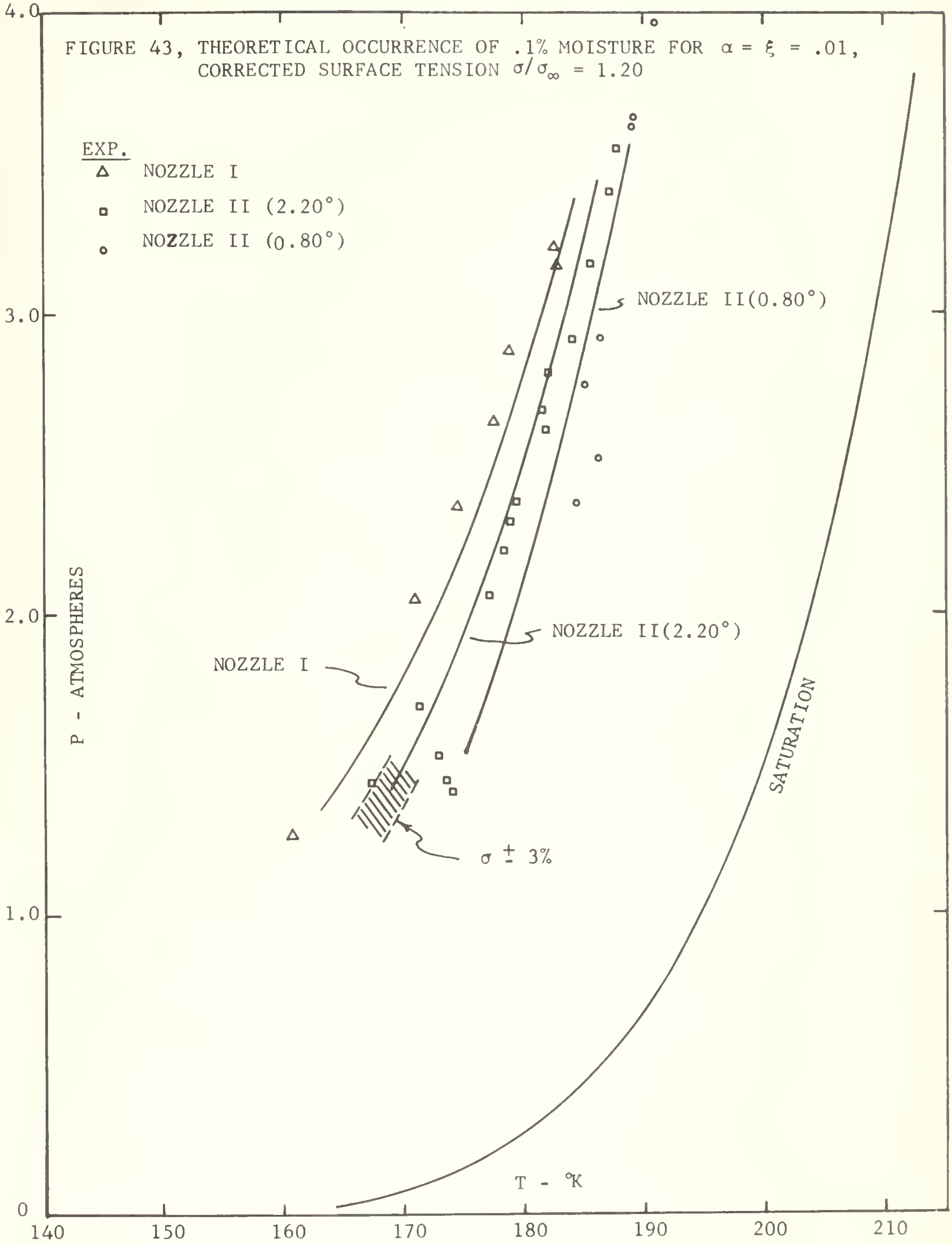

FIGURE 43, THEORETICAL OCCURRENCE OF .1% MOISTURE FOR $\alpha = \xi = .01$, CORRECTED SURFACE TENSION $\sigma/\sigma_\infty = 1.20$

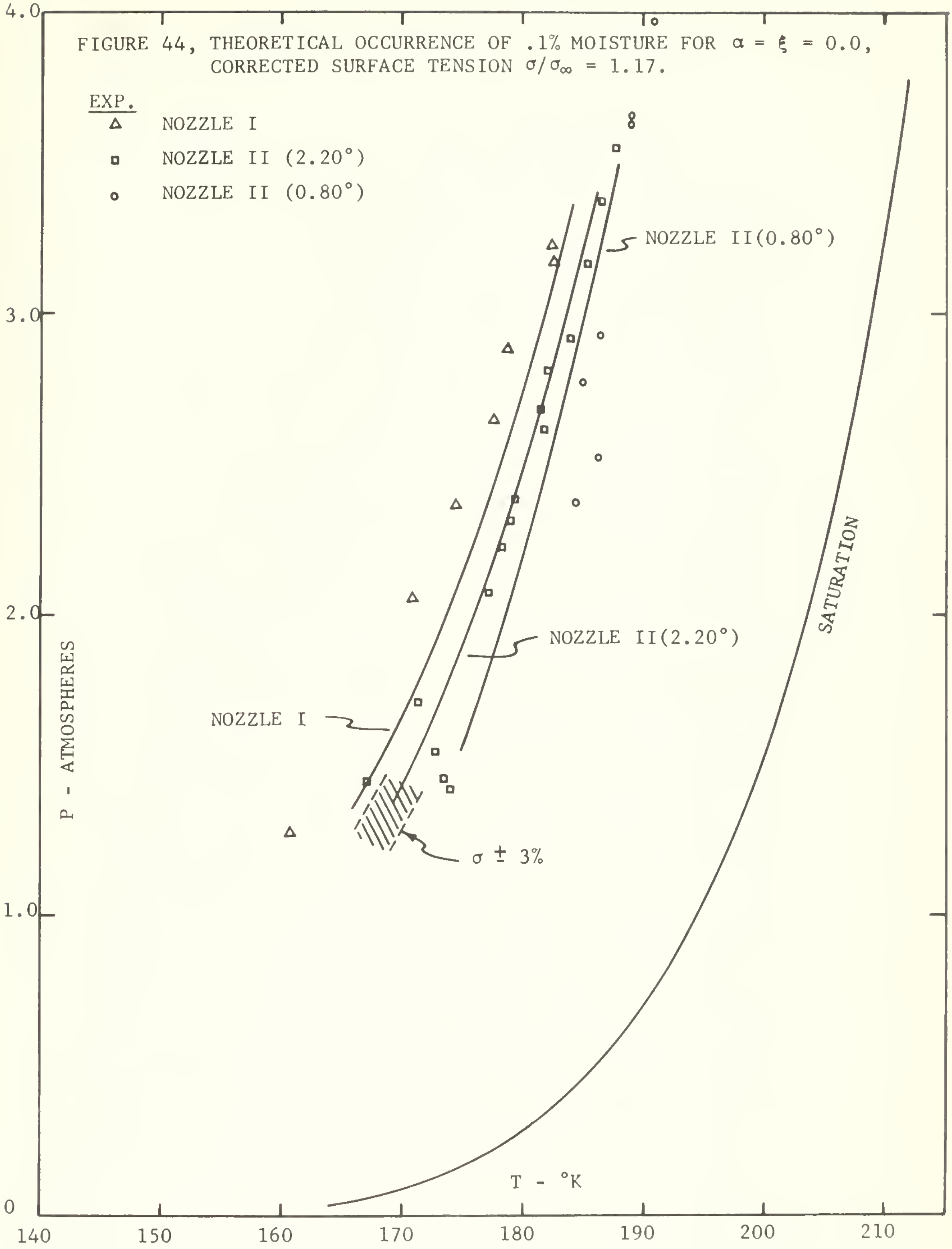

FIGURE 44, THEORETICAL OCCURRENCE OF .1% MOISTURE FOR $\alpha = \xi = 0.0$, CORRECTED SURFACE TENSION $\sigma/\sigma_\infty = 1.17$.

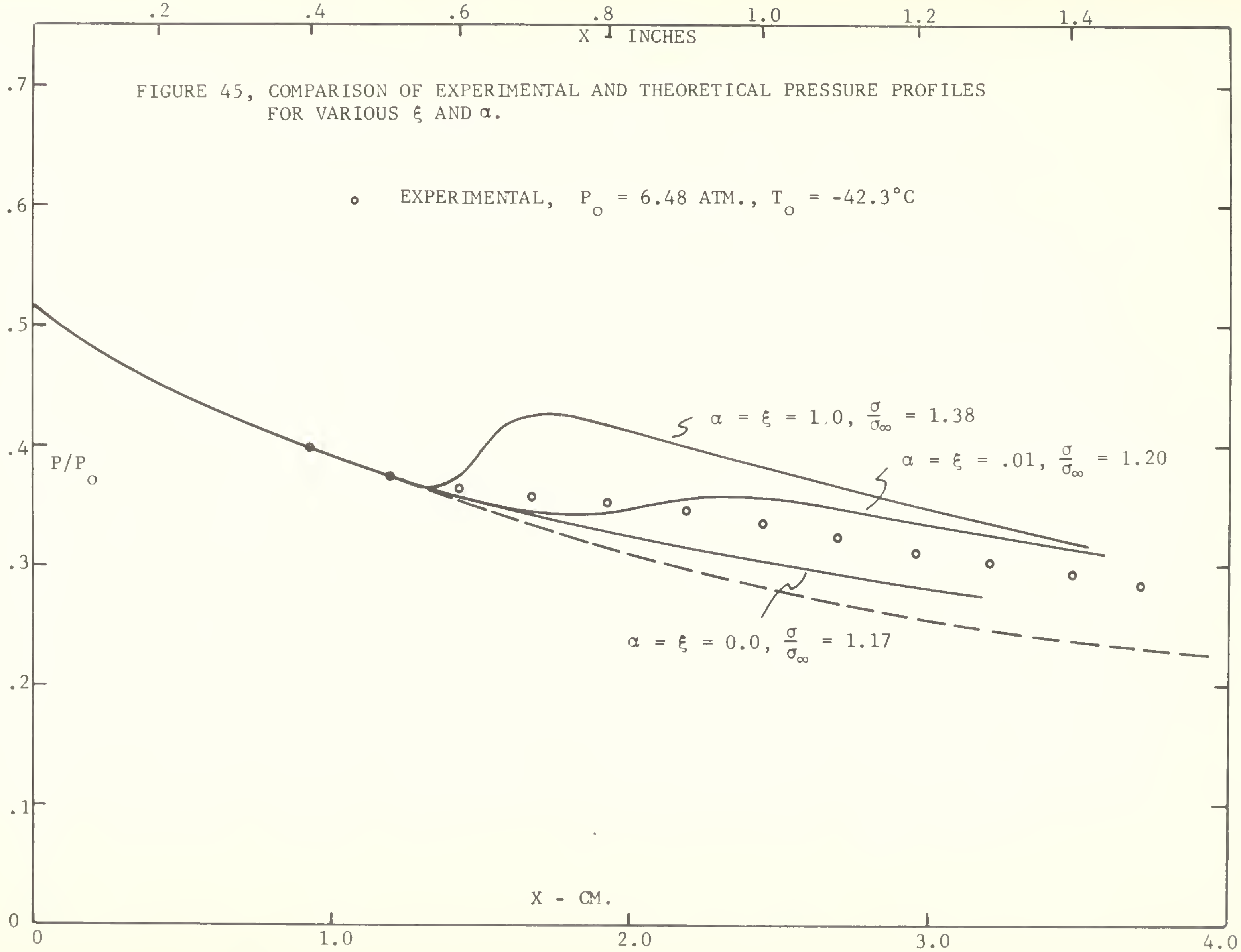

FIGURE 45, COMPARISON OF EXPERIMENTAL AND THEORETICAL PRESSURE PROFILES FOR VARIOUS ξ AND α.

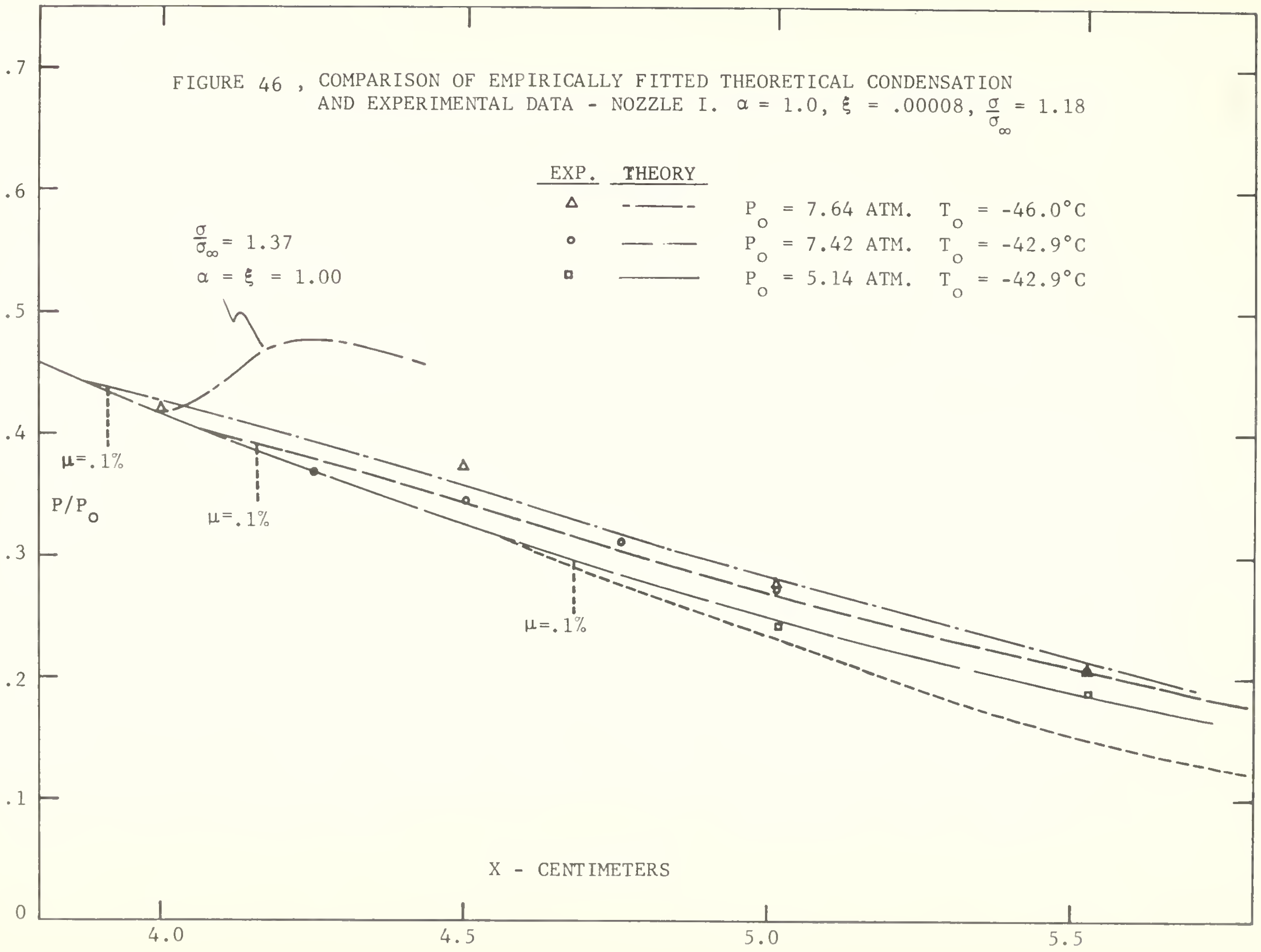
FIGURE 46 , COMPARISON OF EMPIRICALLY FITTED THEORETICAL CONDENSATION AND EXPERIMENTAL DATA - NOZZLE I. $\alpha = 1.0$, $\xi = .00008$, $\frac{\sigma}{\sigma_\infty} = 1.18$

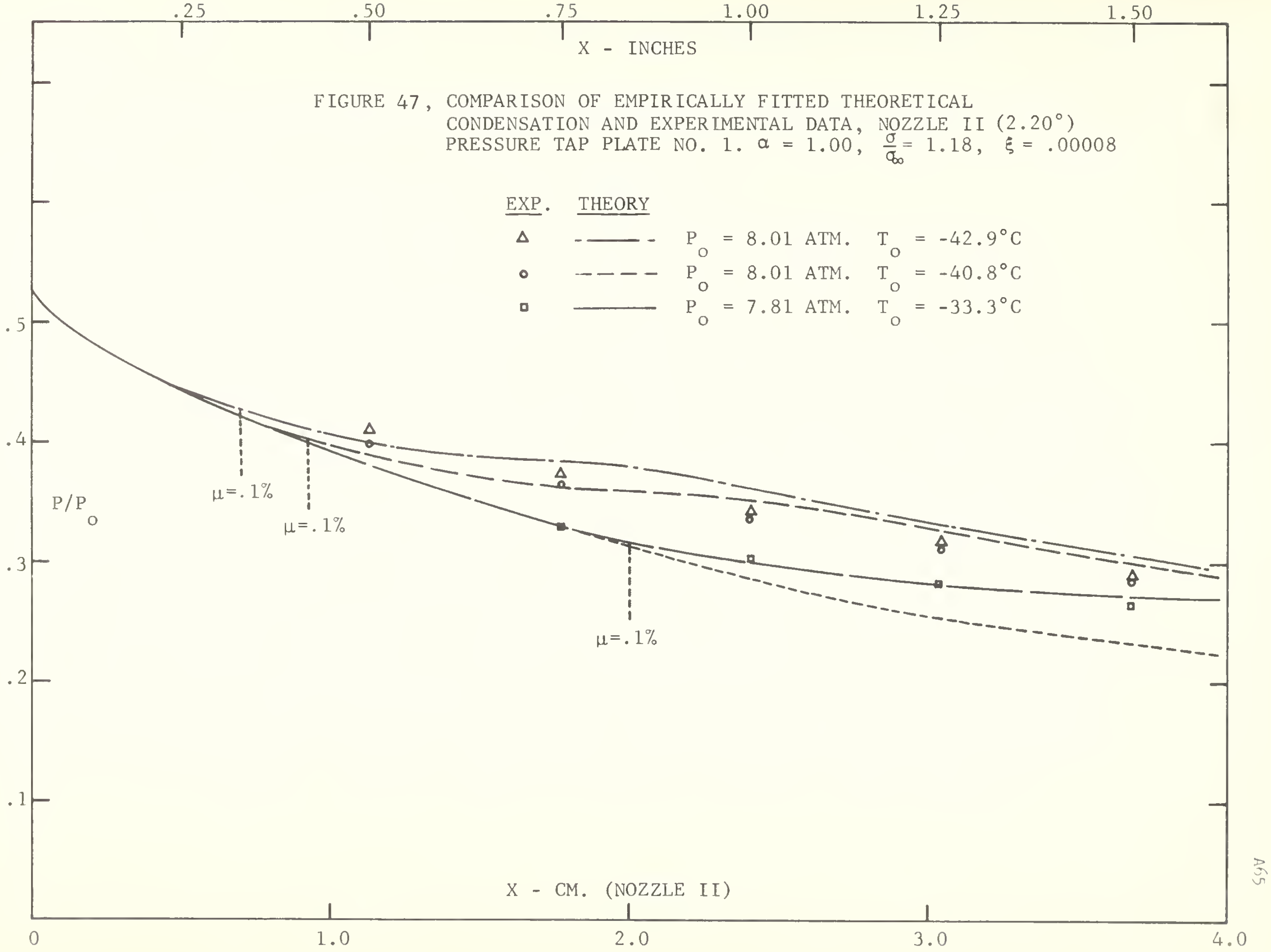

FIGURE 47, COMPARISON OF EMPIRICALLY FITTED THEORETICAL CONDENSATION AND EXPERIMENTAL DATA, NOZZLE II (2.20°) PRESSURE TAP PLATE NO. 1. $\alpha = 1.00$, $\frac{\sigma}{\sigma_\infty} = 1.18$, $\xi = .00008$

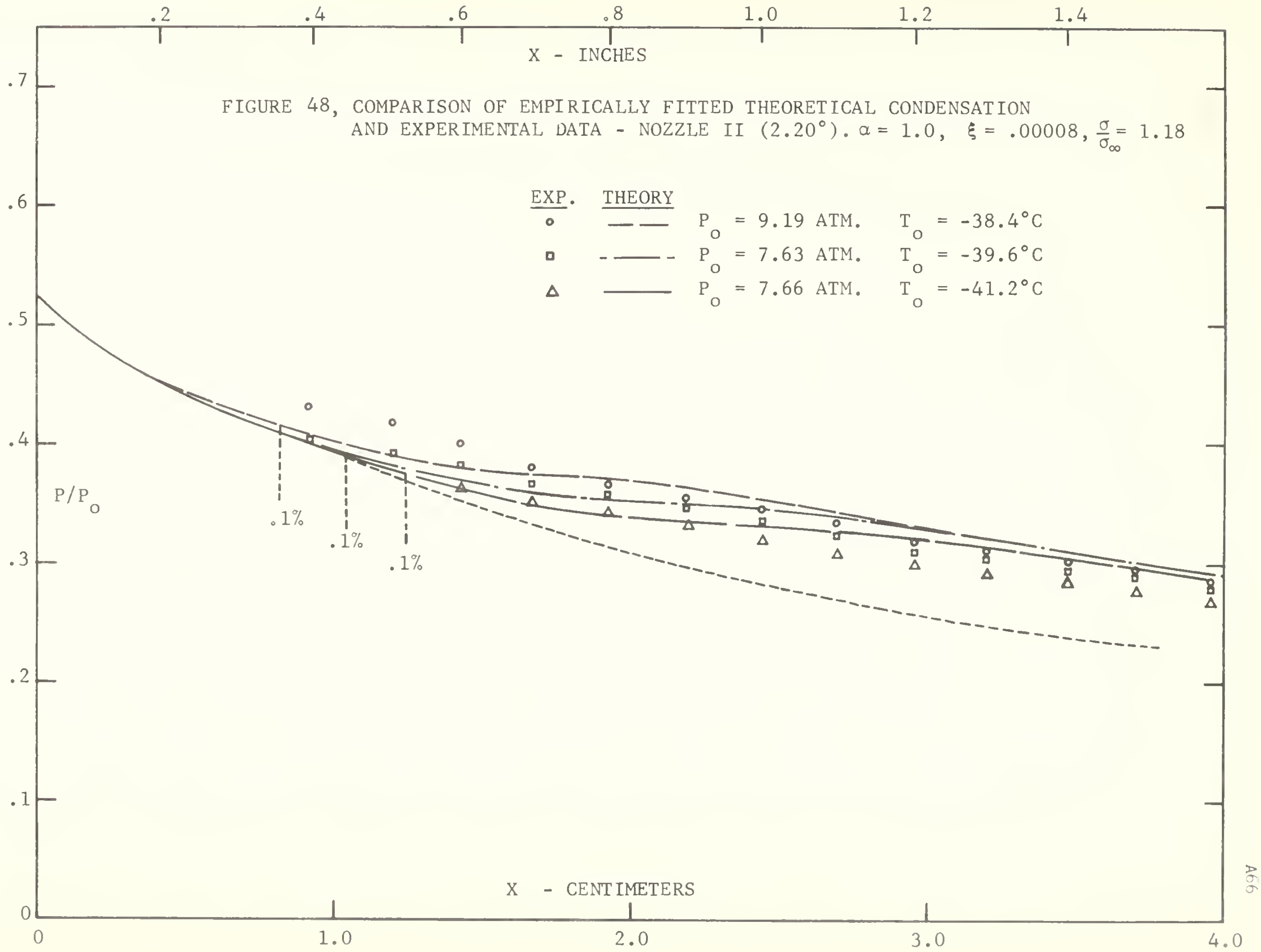

FIGURE 48, COMPARISON OF EMPIRICALLY FITTED THEORETICAL CONDENSATION AND EXPERIMENTAL DATA - NOZZLE II (2.20°). $\alpha = 1.0$, $\xi = .00008$, $\frac{\sigma}{\sigma_\infty} = 1.18$

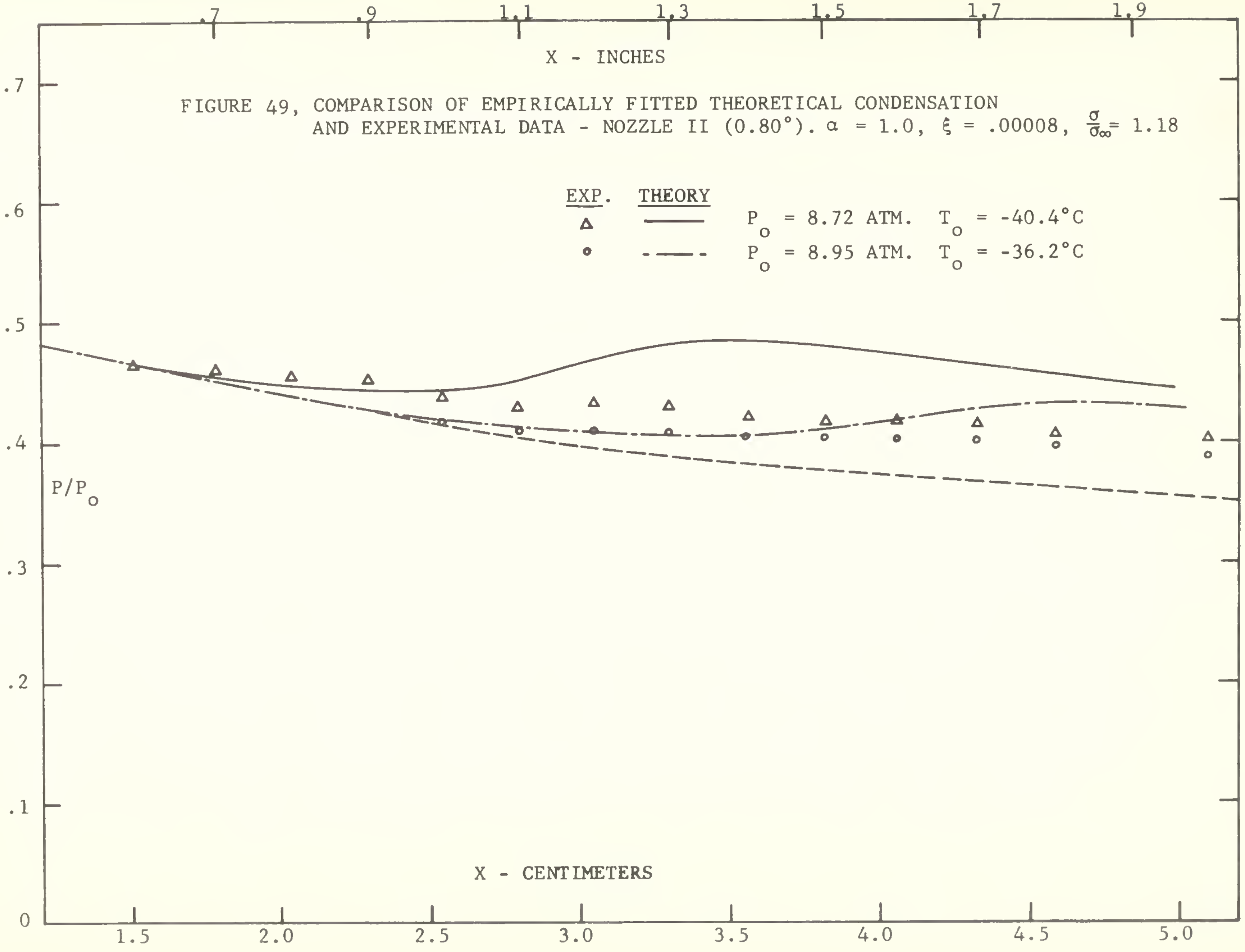

FIGURE 49, COMPARISON OF EMPIRICALLY FITTED THEORETICAL CONDENSATION AND EXPERIMENTAL DATA - NOZZLE II (0.80°). $\alpha = 1.0$, $\xi = .00008$, $\frac{\sigma}{\sigma_\infty} = 1.18$

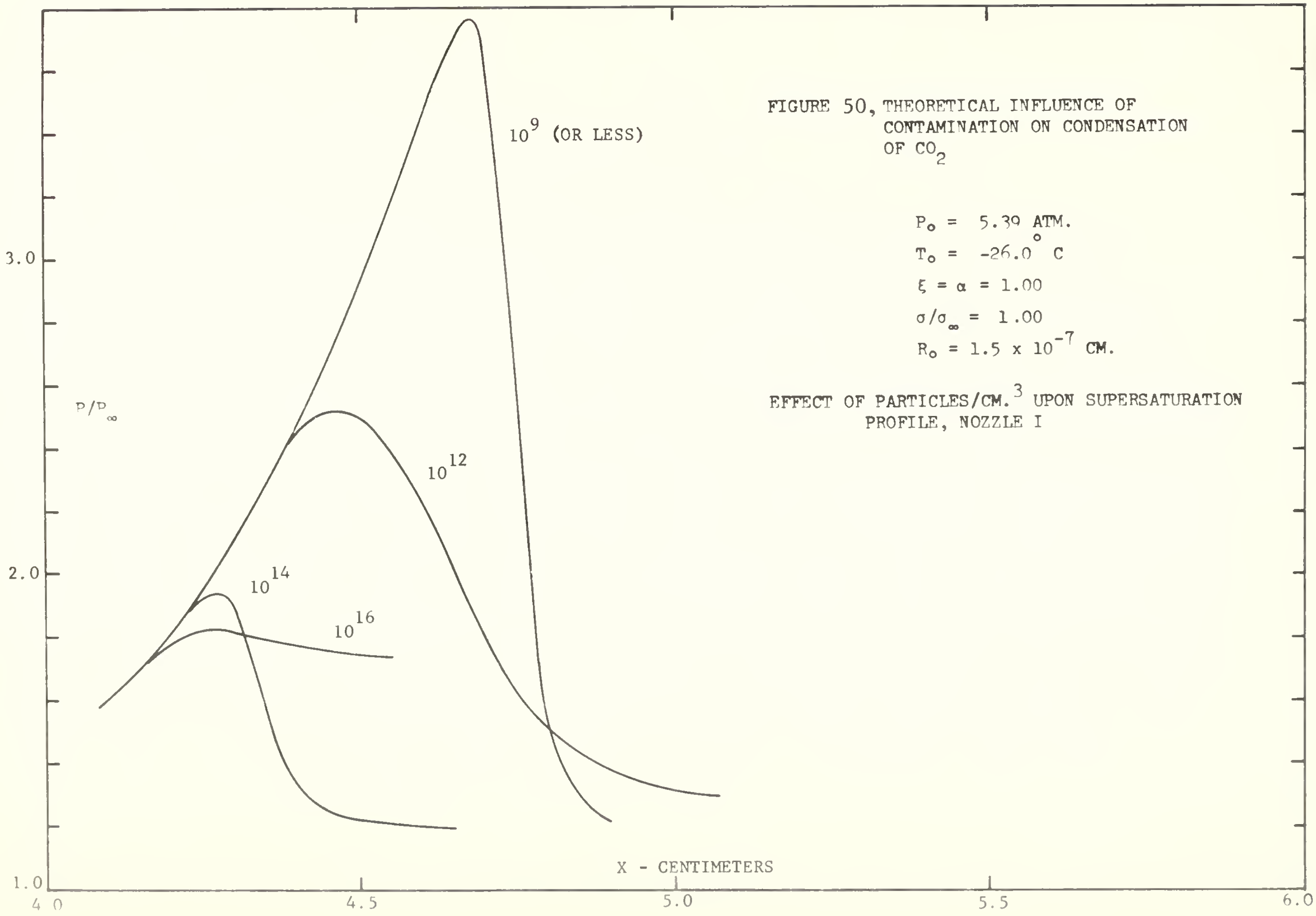

FIGURE 50, THEORETICAL INFLUENCE OF CONTAMINATION ON CONDENSATION OF CO_2

$P_o = 5.39$ ATM.
$T_o = -26.0^\circ$ C
$\xi = \alpha = 1.00$
$\sigma/\sigma_\infty = 1.00$
$R_o = 1.5 \times 10^{-7}$ CM.

EFFECT OF PARTICLES/CM.^{3} UPON SUPERSATURATION PROFILE, NOZZLE I

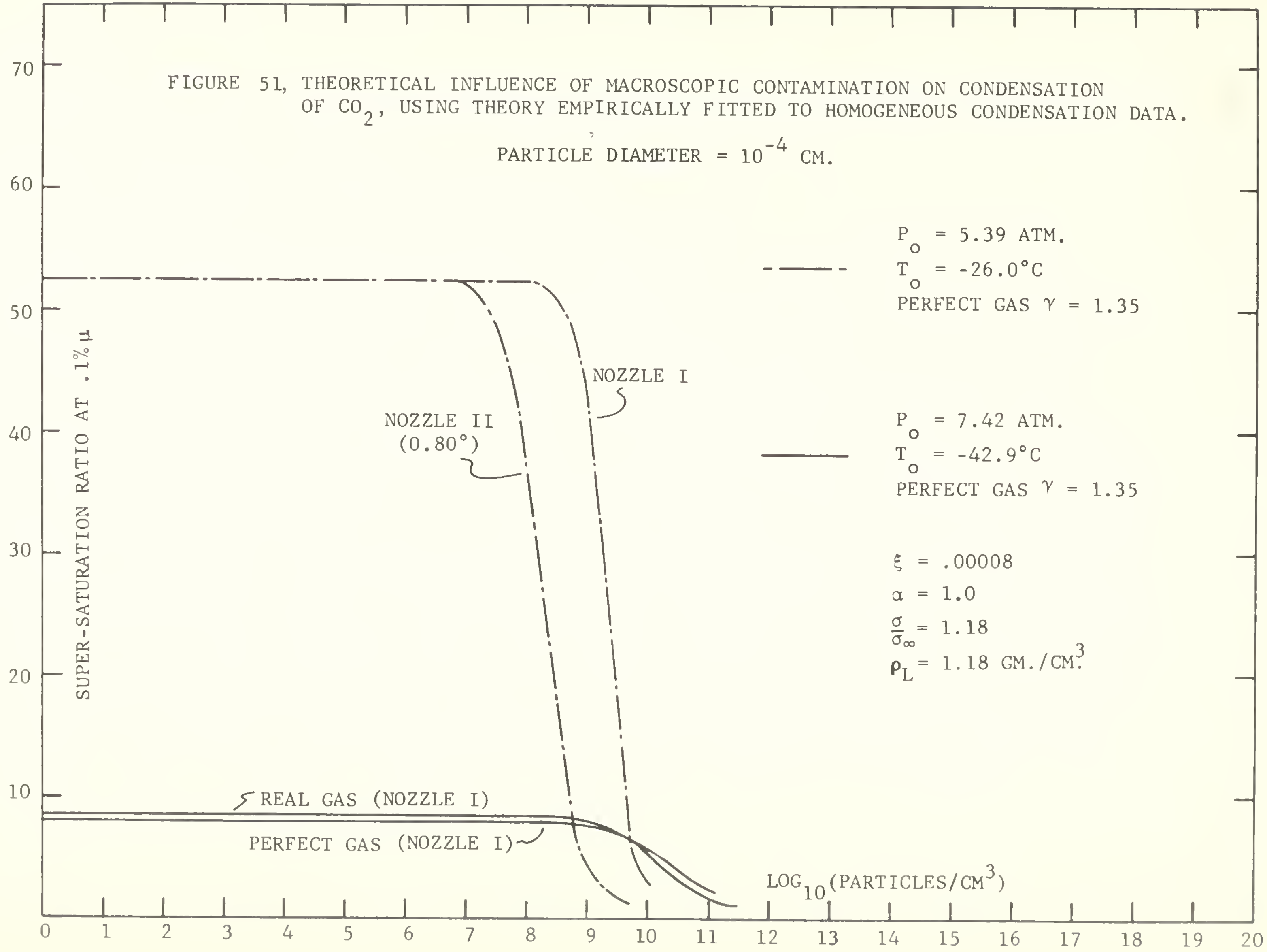

FIGURE 51, THEORETICAL INFLUENCE OF MACROSCOPIC CONTAMINATION ON CONDENSATION OF CO_2, USING THEORY EMPIRICALLY FITTED TO HOMOGENEOUS CONDENSATION DATA.

PARTICLE DIAMETER = 10^{-4} CM.

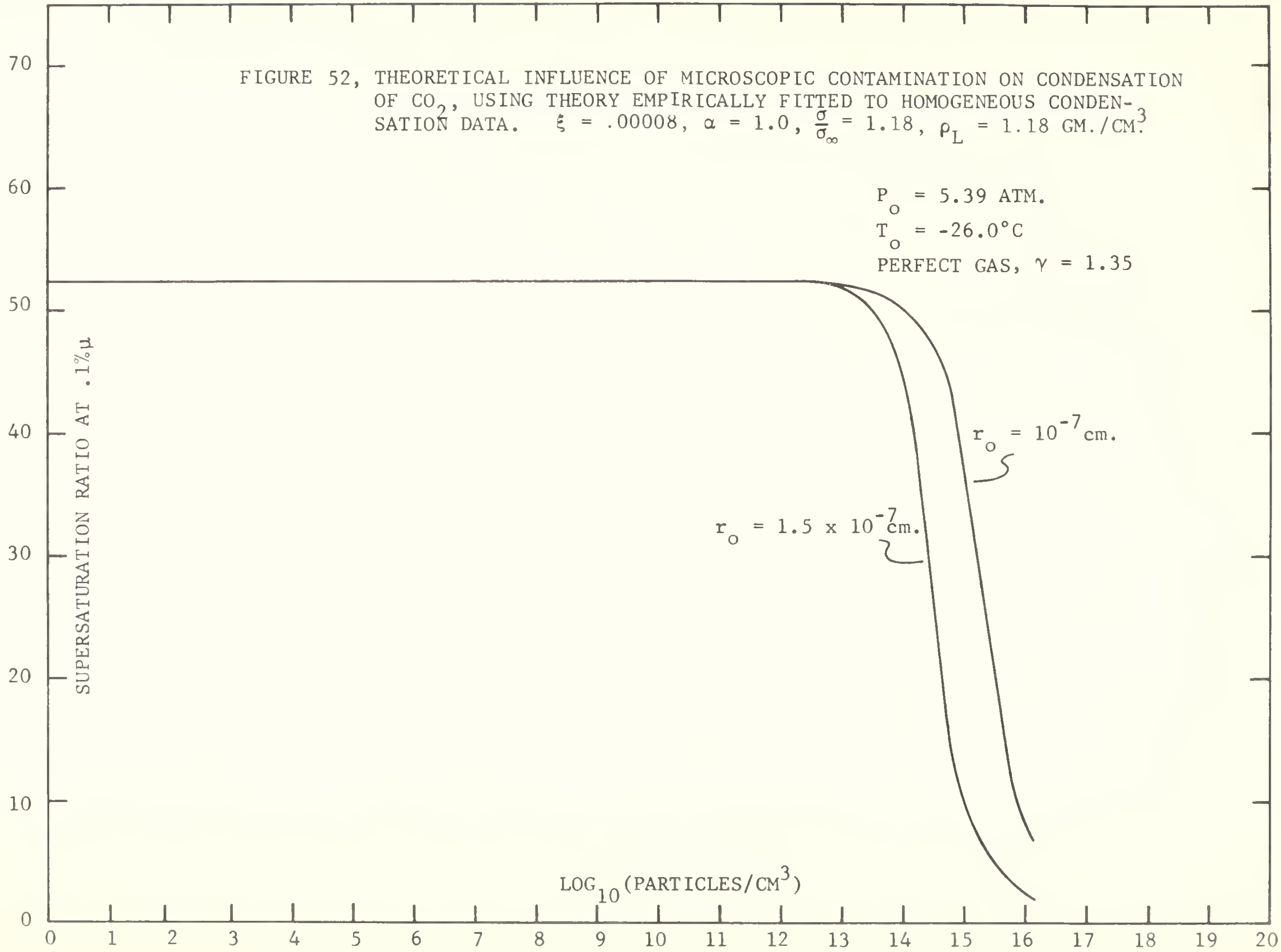

FIGURE 52, THEORETICAL INFLUENCE OF MICROSCOPIC CONTAMINATION ON CONDENSATION OF CO_2, USING THEORY EMPIRICALLY FITTED TO HOMOGENEOUS CONDENSATION DATA. $\xi = .00008$, $\alpha = 1.0$, $\frac{\sigma}{\sigma_\infty} = 1.18$, $\rho_L = 1.18$ GM./CM.^{3}

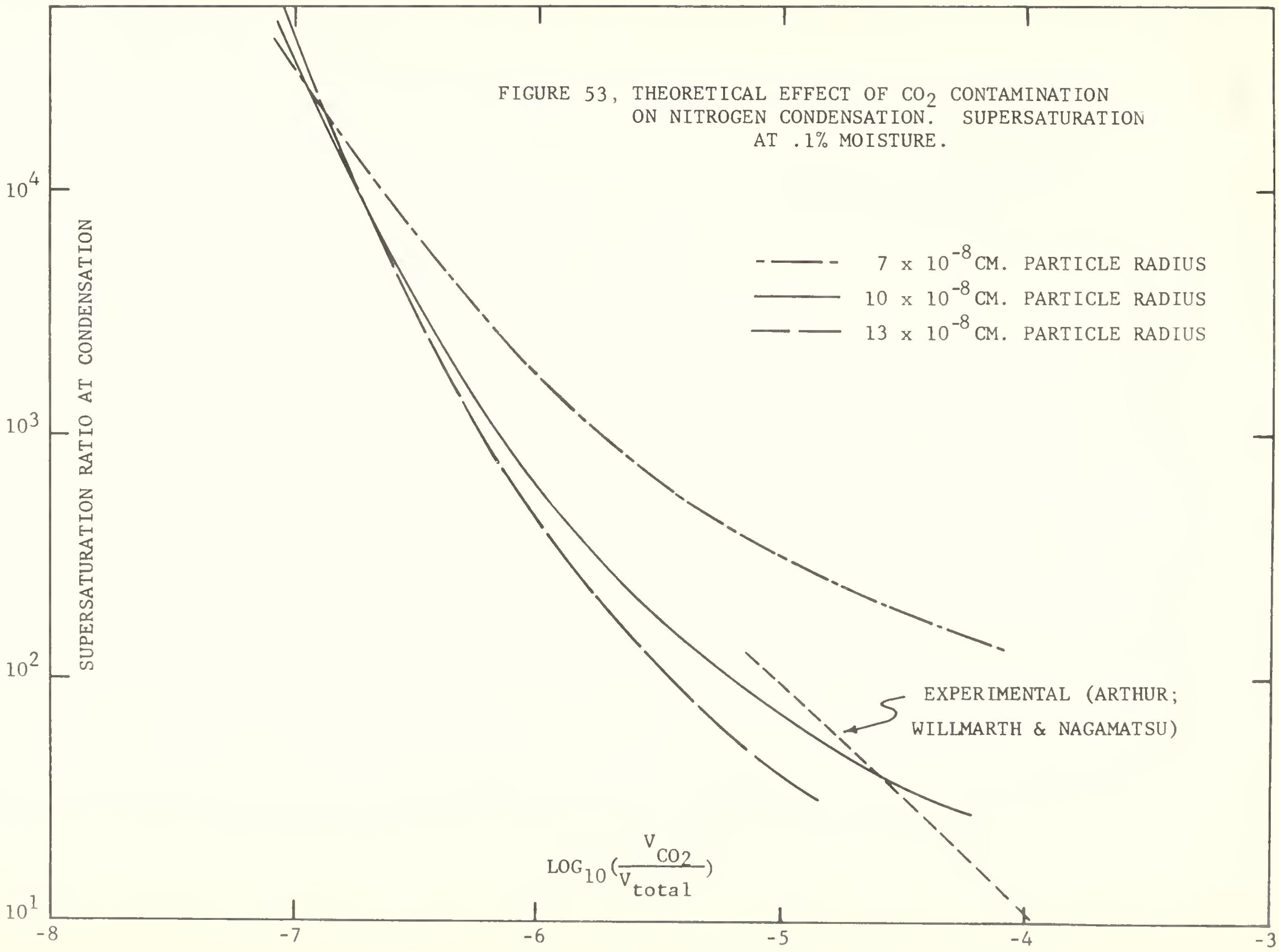

FIGURE 53, THEORETICAL EFFECT OF CO_2 CONTAMINATION ON NITROGEN CONDENSATION. SUPERSATURATION AT .1% MOISTURE.

TABLE 15

VALUES OF γ_a, γ_b and z USED TO MATCH REAL GAS ISENTROPES

Run	p_o (atm)	T_o °K	γ_a	γ_b	z
1_I	7.64	227.2	1.3736	.000400	.8902
2_I	7.67	228.6	1.3717	.000407	.8949
3_I	7.66	229.1	1.3685	.000431	.8932
4_I	7.42	230.3	1.3643	.000442	.8988
5_I	7.04	230.3	1.3597	.000449	.9045
6_I	6.65	230.3	1.3539	.000481	.9101
7_I	5.14	230.3	1.3403	.000560	.9314
1_{II}	7.81	239.9	1.3557	.000453	.9114
2_{II}	8.01	232.4	1.3711	.000401	.8949
3_{II}	8.01	230.3	1.3735	.000398	.8906
4_{II}	7.36	260.0	1.3342	.000505	.9416
7_{II}	5.47	238.3	1.3335	.000536	.9367
8_{II}	5.87	234.4	1.3419	.000500	.9277
9_{II}	7.81	236.6	1.3606	.000445	.9057
11_{II}	7.66	254.6	1.3415	.000455	.9335
14_{II}	9.19	234.8	1.3795	.000376	.8841
15_{II}	7.02	231.3	1.3566	.000469	.9067
16_{II}	7.63	233.6	1.3614	.000450	.9031
17_{II}	7.66	232.0	1.3675	.000397	.8990
18_{II}	5.76	231.1	1.3435	.000500	.9247
19_{II}	4.37	231.4	1.3278	.000570	.9438
20_{II}	6.48	230.9	1.3515	.000483	.9141
21_{II}	6.14	230.5	1.3477	.000500	.9183
22_{II}	7.40	240.0	1.3513	.000465	.9167
23_{II}	8.72	232.8	1.3782	.000387	.8857
24_{II}	8.28	233.1	1.3718	.000394	.8937
25_{II}	8.95	237.0	1.3768	.000358	.8917
26_{II}	6.92	240.6	1.3457	.000390	.9232
28_{II}	6.24	225.7	1.3544	.000488	.9083
29_{II}	6.88	233.0	1.3551	.000455	.9118
30_{II}	7.86	239.2	1.3566	.000456	.9098
31_{II}	6.54	237.8	1.3440	.000493	.9237

APPENDIX B

REVIEW OF NUCLEATION RATE EQUATION DEVELOPMENT

The following is a review of the classical nucleation rate equation as developed by J. Frenkel(19). Although Frenkel was not the first to investigate nucleation theory, his result is not greatly different from earlier authors mentioned in the text, and his method provides relatively straightforward consideration of the important aspects and assumptions in classical nucleation theory

Frenkel's droplet model was based on Volmer's(58) earlier model of droplets as generalized molecules, neglecting intermolecular forces, and his method of development was based on that of Zeldovich(68). He showed that the distribution of clusters of vapor molecules, resulting from the kinetic interaction of the molecules could be described by a Boltzmann distribution. That is, that (in equilibrium)

$$N(g) = N_o \exp^{(-\Delta\Phi/KT)} \tag{B-1}$$

where N_o = total number of molecules

$\Phi = H - TS$

$\Delta\Phi = \Phi_L - \Phi_V$ = change in free energy of a group of (g) free molecules when forming a liquid embryo.

Several simplifying assumptions of debatable validity are made at this point. First, the droplet model is taken to be a liquid sphere, having surface energy described by the flat-film liquid surface tension (or some corrected function thereof). Second, the total change in free energy is assumed to be the work of formation of the surface of the droplet, plus the change in free energy resulting from the change in state of g molecules condensing from vapor to liquid, with the spherical droplet assumed to be stationary in the vapor system, and having no rotational or vibrational energy. This is the important distinction between classical and more recent "gassified"

droplet models of nucleation theory. Third, the droplet is assumed to form at environmental temperature, an assumption which may also be invalid(32).

Using these assumptions, and defining ϕ as the free energy per molecule, $\Delta\Phi$ can then be writeen:

$$\Delta\Phi = g(\phi_L - \phi_V) + 4\pi r^2\sigma \tag{B-2}$$

$$= - T(\Delta S) + 4\pi r^2\sigma$$

$$= - gKT \ \ell n \frac{p}{p_\infty} + 4\pi r^2\sigma \tag{B-3}$$

where p_∞ equals the flat surface equilibrium pressure of a formed embryo of (g) molecules and p is the existing local pressure.

Hence,

$$N(g) = N_o \exp(g \ \ell n \frac{p}{p_\infty} - \frac{4\pi r^2\sigma}{KT}) \tag{B-4}$$

Saying that:

$$gm = \frac{4}{3}\pi r^3\rho_L \tag{B-5}$$

yields

$$N(g) = N_o \exp \{ g \ \ell n \frac{p}{p_\infty} - \frac{4\pi\sigma}{KT} (\frac{3gm}{4\pi\rho})^{2/3}\} \tag{B-6}$$

$$= N_o \exp \{ g \ \ell n \frac{p}{p_\infty} - (\frac{\varepsilon}{KT}) g^{2/3}\}$$

where $\varepsilon = 4\pi\sigma(\frac{3m}{4\pi\rho})^{2/3}$

Inspection of Eq. (B-6) shows that a reasonable equilibrium distribution results when p is less than p_∞, that is, in a superheated vapor. However, in a supersaturated vapor, an unreasonable and, in fact, impossible equilibrium distribution is predicted as seen in Fig. (B-1), since it predicts $N(g) \to \infty$ as $g \to \infty$. Acknowledging that an equilibrium distribution of drop sizes is unreasonable under supersaturated conditions, early authors treated the system as one in a state of quasi-equilibrium, where droplets are imagined to be removed after reaching some size larger than the critical radius, r*, which occurs at the maximum of the supersaturated free energy change. This maximum in $\Delta\Phi$ (minimum in N(g)) occurs when;

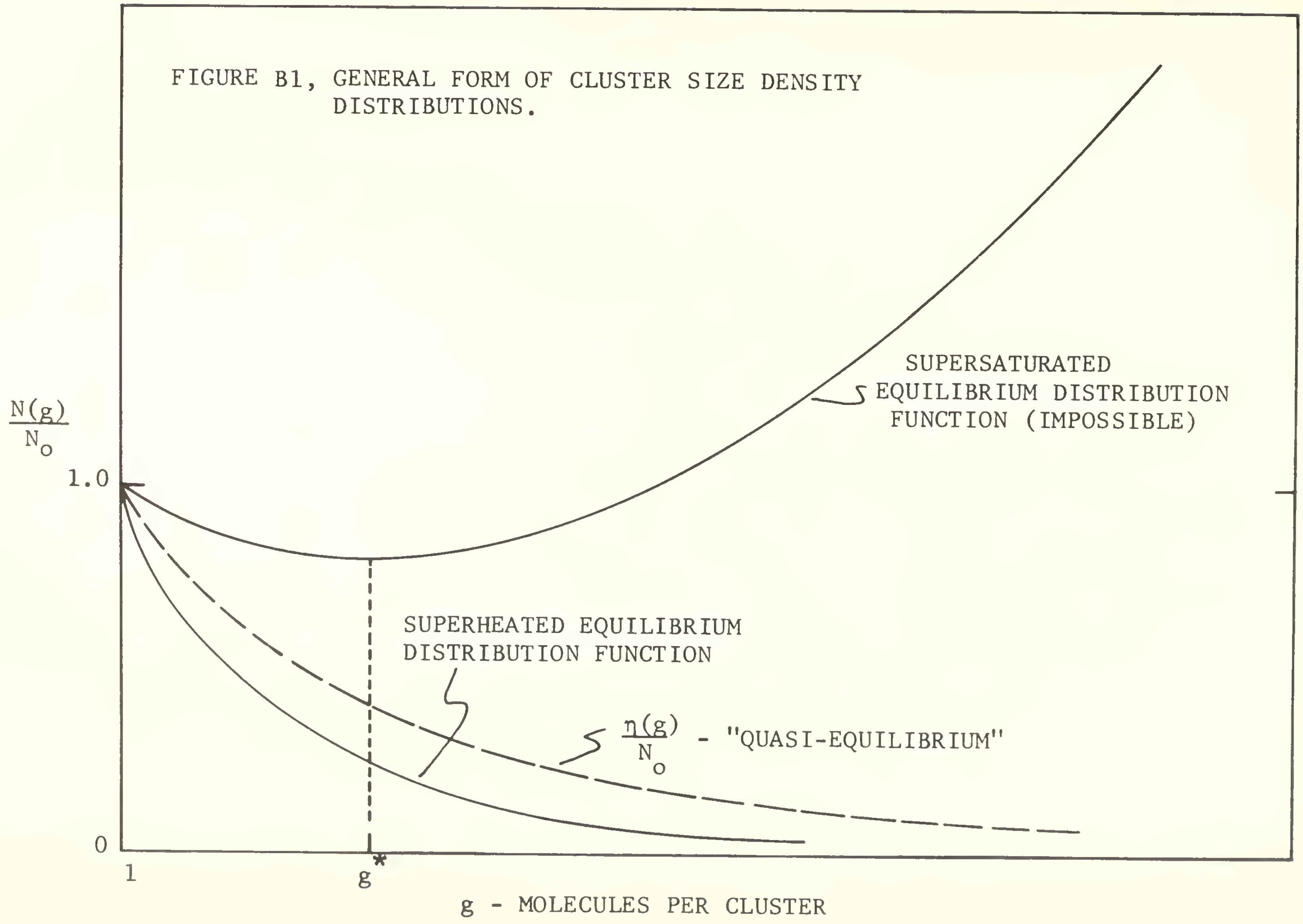
FIGURE B1, GENERAL FORM OF CLUSTER SIZE DENSITY DISTRIBUTIONS.

$$\frac{d}{dg}(\Delta\Phi) = 0 = -KT\ \ell n\ \frac{p}{p_\infty} + \frac{2}{3}\ \varepsilon g^{-1/3}$$

$$KT\ \ell n\ \frac{p}{p_\infty} = \frac{2}{3}\ \varepsilon g^{-1/3}$$

$$\Delta\Phi_{max} = \frac{1}{3}\ \varepsilon g^{2/3} = \frac{4}{3}\ \pi r^2 \sigma .$$

Then

$$\Delta\Phi_{max} = -\ gKT\ \ell n\ \frac{p}{p_\infty} + 4\pi r^2\sigma = \frac{4}{3}\ \pi r^2\sigma \qquad \text{(B-7)}$$

Hence

$$KT\left(\frac{4}{3}\ \pi r^3\ \frac{\rho_L}{m}\right)\ \ell n\ \frac{p}{p_\infty} = \frac{8}{3}\ \pi r^2\sigma$$

$$\ell n\ \frac{p}{p_\infty} = \frac{2m\sigma}{\rho_L KTr^*} \qquad \text{(B-8)}$$

Equation (B-8) is the Kelvin-Helmholtz expression describing the conditions under which a liquid drop may remain in equilibrium with its vapor phase. The radius (r*) and the number (g*) of atoms of a critical embryo are thus determined. A variation of r (or g) in either direction results in a decrease of free energy from the maximum, and consequently the drop is in unstable equilibrium at this point.

In considering the quasi-equilibrium state, and ignoring interaction between nuclei, it is said that nucleation rate is the net rate at which particles of a given size (g) are formed. To maintain quasi-equilibrium, it is further assumed the net rate at which (g+1)-sized droplets are formed from (g)-sized droplets is equal to the rate at which (g)-sized droplets are formed from (g-1)-sized droplets, and so on. That is, nucleation rate is independent of g, in order that the number of droplets of any size remains constant and the rate at which droplets of larger size are imagined to be removed is also equal to the nucleation rate. Correspondingly, it is imagined that single molecules are added to the system at a rate equal to the depletion due to nucleation.

Using this model then, and assuming that growth of nuclei is due only to interaction with free molecules, the nucleation rate is

$$J(g + 1, t) = \beta\ s(g) \times \eta(g, t) - \gamma(g + 1)\ s(g + 1)\ \eta(g + 1, t) \qquad \text{(B-9)}$$

where β = rate at which molecules strike unit surface area.

$\gamma(g)$ = rate at which molecules leave the surface per unit area

$\eta(g,t)$ = distribution of non-equilibrium drops

$s(g)$ = surface area of a g-sized drop.

Assuming that no effects of droplet curvature exist, and neglecting the cluster motion,

$$\beta = \frac{p}{(2\pi mKT)^{1/2}}$$

Also, it is said that if nucleation rate were zero, then the non-equilibrium (or quasi-equilibrium) distribution would in that case have to be equal to the equilibrium distribution N(g). This is easy enough to see in the superheated case, but perhaps a bit difficult to accept when N(g) is the fictitious mathematical result corresponding to supersaturation.

Applying this, when $J(g, t) = 0$

$$\gamma(g + 1)\ s(g + 1)\ \eta(g + 1) = \beta\ s(g)\ \eta(g)$$

when $\eta(g) = N(g)$

Hence,

$$\gamma(g + 1)\ s(g + 1)\ N(g + 1) = \beta\ s(g)\ N(g)$$

and Equation (B-9) becomes

$$J(g, t) = \beta\ s(g)\ N(g) \left(\frac{\eta(g, t)}{N(g)} - \frac{\eta(g + 1, t)}{N(g + 1)} \right) \qquad \text{(B-10)}$$

Here some rather notable simplifications and manipulations facilitate a solution to (B-10). For large values of (g) where these functions may be treated as continuous, this is approximately:

$$J(g, t) = \beta\ s(g)\ N(g) \frac{d}{dg} \left(\frac{\eta}{N}\right)$$

Hence, since it is assumed that $J(g, t) = J(t)$

$$\int d\left(\frac{\eta}{N}\right) = -\frac{J}{\beta} \int \frac{dg}{s(g)\ N(g)} \qquad \text{(B-11)}$$

Using the boundary conditions

(a) $\frac{n}{N} = 1.0$ at $g = 1$ (b) $\lim\limits_{g \to \infty} \frac{n}{N} = 0$

One obtains

$$J = \frac{\beta}{\int_1^\infty \frac{dg}{sN}} \tag{B-12}$$

Since $\frac{1}{N} = \frac{1}{N_o} \exp\left[\frac{\Delta\Phi}{KT}\right]$ has a sharp maximum in the vicinity of $g = g^*$, it is possible to approximate (B-12) as:

$$J = \frac{\beta\ s(g^*)\ N_o}{\int_1^\infty \exp\ (\Delta\Phi/KT)\ dg} \tag{B-13}$$

Using Equations (B-5), (B-6) and (B-8), the exponent may be written:

$$\frac{\Delta\Phi}{KT} = -\ g\ \ell n\ \frac{p}{p_\infty} + \frac{\varepsilon}{KT}\ g^{2/3}$$

$$= -\ g\left[\frac{2m\sigma}{\rho_L KTr^*}\right] + \frac{4\pi\sigma}{KT}\left[\frac{3m}{4\pi\rho_L}\right]^{2/3} g^{2/3}$$

$$= A\ \left[\ 3(g/g^*)^{2/3} - 2(g/g^*)\ \right]$$

where

$$A = \frac{\sigma m}{\rho_L KT}\left(\frac{4\pi\rho_L}{3m}\right)^{1/3} g^{*2/3} = \frac{4\pi\sigma r^{*2}}{3KT}$$

$$J = \frac{\beta\ s(g^*)\ N_o}{\int_1^\infty \exp\ \left\{ A \left[\ 3(g/g^*)^{2/3} - 2(g/g^*)\right] \right\}\ dg} \tag{B-14}$$

This integral occurs in the Becker and Doring, and Frenkel derivations, and can be solved approximately with the introduction of

$$\Omega = (g/g^*)^{1/3} - 1 \tag{B-15}$$

Since the integrand of (B-14) has a very sharp maximum e^A at $g = g^*$, the important values of Ω are small, and the limits of the integral may be taken at $+\infty$ and $-\infty$.

Also, since $(g/g^*)^{2/3} = \Omega^2 + 2\Omega + 1$

$$dg = 3(1 + \Omega)^2\ g^* d\Omega$$

And $3(g/g^*)^{2/3} - 2(g/g^*) = -\ 3\Omega^2 - 2\Omega + 1$

The integral may be written approximately

$$3g^*e^A \int_{-\infty}^{\infty} (1 + \Omega)^2 \exp\ (-\ 3A\Omega^2 - 2A\Omega^3)\ d\Omega$$

$$\simeq 3g^*e^A \int_{-\infty}^{\infty} \exp\ (-\ 3A\Omega^2)\ d\Omega$$

$$= 3g^{*}e^{A}(\pi/3A)^{1/2} \qquad \text{(B-16)}$$

Hence, the nucleation rate finally becomes

$$J = \frac{\beta s(g^{*})N_{o}}{g^{*}}\left[\frac{A}{3\pi}\right]^{1/2}\exp(-A) \qquad \text{(B-17)}$$

with

$$N_{o} = p/KT$$

$$\beta = p/(2\pi mKT)^{1/2}$$

$$s(g^{*}) = \frac{\varepsilon(g^{*})^{2/3}}{\sigma}$$

and with the definitions of ε and A, (B17) can be shown equivalent to

$$J = \left(\frac{p}{KT}\right)^{2}\frac{m}{\rho}\left(\frac{2\sigma}{\pi m}\right)^{1/2}\exp\left(\frac{-4\pi\sigma r^{*2}}{3KT}\right) \qquad \text{(B-18)}$$

This is an expression of the number of nuclei formed per unit volume per unit time, due to the existence of a non-equilibrium distribution $\eta(g)$. By assuming (J) was independent of (g) as Becker and Doring did, it was evaluated using only the boundary conditions of $\eta(g)$ and the properties of $\Delta\Phi(g)$.

Discussion and criticism of Eq. (B-17), and of the importance of its various constituent values is contained in the text.

APPENDIX C

REVIEW OF DEVELOPMENT OF DROP GROWTH EQUATIONS

The following development follows the method of Oswatitch(45) in considering the necessary conservation of mass and energy of growing droplets. Included are a correction of average incident energy to be 2RT rather than 3/2RT, and with generalized non-unity values of both mass and thermal accommodation. An important assumption is that molecular velocity distribution are Maxwellian before *and* after collision and accommodation with the droplet surface.

Consider a drop of temperature T_D in an atmosphere p and T. It has an incident mass flux equal to

$$\frac{p}{(2\pi RT)^{1/2}}$$

with a proportion ξ (condensation coefficient) condensing and the rest being reflected. Since the drop is very small, its temperature is assumed to be constant throughout. The mass transfer from the drop is equal to that which would be incident in an environment T_D and p_D, the equilibrium values of temperature and pressure, where

$$\ell n \;\frac{p_D}{p_{sat}(T_D)} = \frac{2m\sigma}{\rho_L KTr}$$

Hence, the mass flux per unit area passing out through the surface is

$$\frac{\xi p_D}{(2\pi RT_D)^{1/2}}$$

Thus, the conservation of mass may be written

$$\rho_L 4\pi r^2 \left(\frac{dr}{dt}\right) = 4\pi r^2 \left[\frac{\xi p}{(2\pi RT)^{1/2}} - \frac{\xi p_D}{(2\pi RT_D)^{1/2}}\right]$$

or

$$\frac{dr}{dt} = \frac{\xi}{(2\pi R)^{1/2}}\left(\frac{p}{T^{1/2}} - \frac{p_D}{T_D{}^{1/2}}\right) \qquad \text{(C-1)}$$

assuming that ξ is constant, or at most, a function of the drop temperature only.

Considerations of energy conservation are made after first defining the

the thermal accommodation coefficient, involving the change in temperature of reflected incident molecules.

$$\alpha = \frac{T_{refl.} - T}{T_D - T} \qquad \text{(Thermal Accommodation Coefficient)} \qquad \text{(C-2)}$$

The energy flux to the drop is, per unit area

$$\frac{p}{(2\pi RT)^{1/2}} \left[2RT \right]$$

and the energy leaving, upon reflection

$$\frac{(1 - \xi)p}{(2\pi RT)^{1/2}} \left\{ 2R \left[T + \alpha(T_D - T) \right] \right\}$$

In addition, the evaporating mass flux carries energy

$$\frac{\xi p_D}{(2\pi RT_D)^{1/2}} \left[2RT_D \right]$$

assuming the evaporating mass flux also to be Maxwellian.

The rate of change of droplet internal energy is

$$\frac{4}{3} \pi r^3 \rho_L c \frac{dT_D}{dt} + 4\pi r^2 \frac{dr}{dt} \rho_L U_{fD}$$

$$U_{fD} \approx h_{fD} = \frac{\gamma}{\gamma - 1} RT - h_{fg}$$

Hence, conservation of energy requires,

$$\frac{4}{3} \pi r^3 \rho_L c \frac{dT_D}{dt} + 4\pi r^2 \frac{dr}{dt} \rho_L \left(\frac{\gamma}{\gamma - 1} RT - h_{fg}\right) =$$

$$\beta(2RT) - \xi\beta_D(2RT_D) - (1 - \xi)\,\beta 2R \left[T + \alpha(T_D - T) \right]$$

or

$$\frac{r\rho_L c}{3RT} \cdot \frac{dT_D}{dt} = 2\beta\xi \left[1 - \frac{\beta_D}{\beta} \frac{T_D}{T} \right] - (1 - \xi)\beta \left[2\alpha\left(\frac{T_D}{T} - 1\right) \right]$$

$$- \frac{\rho_L}{RT} \frac{dr}{dt} \left[\frac{\gamma}{\gamma - 1} RT - h_{fg} \right]$$

where $\beta = \frac{p}{(2\pi RT)^{1/2}}$ $\qquad \beta_D = \frac{p_D}{(2\pi RT_D)^{1/2}}$

An order of magnitude analysis shows that the left hand term is small compared to the last term on the right hand side. Taking typical values;

$r \sim 10^{-7}$ cm

$h_{fg}/C_p T \sim 3$

$c \sim .3$ cal/gm °K

$R \sim .045$ cal/gm °K

$T \sim 250$°K

$\gamma/(\gamma - 1) \sim 4$

$dT_D/dr \sim 7 \times 10^7$ °K/cm

$$\frac{rc\,\frac{dT_D}{dr}}{(3RT)\left(\frac{\gamma}{\gamma - 1}\right)\left(\frac{h_{fg}}{C_pT} - 1\right)} = .008 \sim 10^{-2}$$

This signifies that the energy required to change the droplet temperature during the expansion is much less than the latent heat imparted from condensing incident molecules. Neglecting this term, the energy equation becomes:

$$0 = 2\xi\left(1 - \frac{\beta_D}{\beta}\frac{T_D}{T}\right) - 2(1 - \xi)\,\alpha\left(\frac{T_D}{T} - 1\right) + \frac{\rho_L}{\beta}\frac{dr}{dt}\left(\frac{\gamma}{\gamma - 1}\right)(\lambda - 1)$$

where $\lambda = \frac{h_{fg}}{C_pT}$

Since

$$\frac{dr}{dt} = \frac{\xi}{\rho_L}(\beta - \beta_D) \qquad \text{(C-1)}$$

The energy equation can be further reduced to

$$0 = \left(1 - \frac{\beta_D}{\beta}\frac{T_D}{T}\right) - \alpha\left(\frac{1}{\ } - 1\right)\left(\frac{T_D}{T} - 1\right) + \frac{1}{2}\left(1 - \frac{\beta_D}{\beta}\right)\left(\frac{\gamma}{\gamma - 1}\right)(\lambda - 1) \qquad \text{(C-3)}$$

Solution to the drop growth equations involves an iterative determination of drop temperature, T_D, from Eq. (C-3) and the resulting value of growth rate from Eq. (C-1).

An interesting indication of the importance of considering both mass and energy balance may be seen by closer inspection of Eqs. (C-1) and (C-3). It is seen that the requirement for a drop to grow is that

$$\frac{dr}{dt} = \frac{\xi\beta}{\rho_L}\left(1 - \frac{\beta_D}{\beta}\right) > 1 \qquad \therefore \frac{\beta_D}{\beta} < 1 \qquad \text{(C-4)}$$

Re-arranging Eq. (C-3) into the form:

$$\frac{\beta_D}{\beta}\left[\frac{T_D}{T} + \frac{1}{2}\left(\frac{\gamma}{\gamma - 1}\right)(\lambda - 1)\right] = 1 - \alpha\left(\frac{1}{\xi} - 1\right)\left(\frac{T_D}{T} - 1\right) + \frac{1}{2}\left(\frac{\gamma}{\gamma - 1}\right)(\lambda - 1)$$

we obtain

$$\frac{\beta_D}{\beta} = \frac{\left[1 + \frac{1}{2}\left(\frac{\gamma}{\gamma - 1}\right)(\lambda - 1)\right] - \alpha\left(\frac{1}{\xi} - 1\right)\left(\frac{T_D}{T} - 1\right)}{\frac{T_D}{T} + \frac{1}{2}\left(\frac{\gamma}{\gamma - 1}\right)(\lambda - 1)} \qquad \text{(C-5)}$$

It is clear that whenever $T_D > T$ the denominator of Eq. (C-5) is always greater than the numerator. Hence from Eq. (C-4) the droplet will grow. Even in the most unfavorable case, that of $\alpha = 0$, where the drop temperature becomes much hotter than the surrounding environment, the value of β_D/β will remain less than unity and the drop will grow. This is really a proof of the intuitive fact that a droplet of size greater than critical radius must continue to grow in a supersaturated environment. Conversely when $T_D < T$, β_D/β is greater than unity and the drop evaporates, supporting our knowledge that evaporating liquids are cooler than their superheated environments.

APPENDIX D.

MODIFICATION OF FOREGOING GAS DYNAMICS, NUCLEATION AND DROP GROWTH EQUATIONS FOR DEPARTURE FROM PERFECT GAS DURING AN ISENTROPIC EXPANSION.

The following corrections introduced into the perfect gas relations to account for departure from perfect gas behavior are based on the empirical observation that compressibility factor $z = Pv/RT$ is almost constant during an isentropic expansion. This is illustrated by Table 15 which lists the values of P, T and z for all of the condensation tests of this investigation. Changes in z generally encountered were less than .5% from stagnation pressure to maximum supersaturation prior to condensation. This in effect allows introduction of "effective" perfect gas relations,

$$Pv = R'\,T \quad \text{where } R' = zR \tag{D-1}$$

and the gas dynamics are affected accordingly:

$$\begin{aligned} Tds &= 0 = C_p dT - vdp \\ &= C_p \frac{pdv}{Rz} + \frac{vdp}{Rz} - vdp \\ &= \frac{\gamma}{\gamma-1}\left[-\frac{d\rho}{\rho} + \frac{dp}{p}\right] - \frac{\gamma-1}{\gamma}\frac{dp}{p} \end{aligned}$$

Hence
$$\frac{d\rho}{\rho} = \frac{dp}{p}\left[1 - z\left(\frac{\gamma-1}{\gamma}\right)\right] = \frac{dp}{p}\left(\frac{1}{\gamma'}\right) \tag{D-2}$$

Hence, the isentropic relations of a perfect gas may be modified by replacing γ with γ' as defined in equation (D-2).

Similarly, the free energy of formation of a nucleus is modified as follows. The free energy change from vapor to liquid of (g) molecules (added to the free energy of surface formation in the classical droplet model) is

$$d\phi = dH - d(TS)$$

If it is assumed that the nucleus forms at environmental temperature.

$$dH = SdT = 0$$

$$d\phi = -TdS = vdp = zRT \cdot \frac{dp}{p}$$

$$\phi_2 - \phi_1 = zgkT \ \ell n \frac{p_2}{p_1} = - zgkT \ \ell n \frac{p}{p_\infty}$$

or, the total change in free energy of formation of a classical model droplet becomes

$$\Phi_2 - \Phi_1 = -zgkT \ \ell n \frac{p}{p_\infty} + 4\pi r^2 \sigma$$

By proceeding as in Appendix B, it can be further shown that

$$\Delta\Phi_{max} = \frac{4}{3} \pi r^2 \sigma \quad \text{at} \quad r = r^*$$

and

$$\ell n \frac{p}{p_\infty} = \frac{2m\sigma}{\rho_L \ zKTr^*}$$

These, plus the corrections to the drop growth equations, may be introduced to the perfect gas equations by the simple substitutions

$$m' = \frac{m}{z} \tag{D-3}$$

$$\gamma' = \frac{\gamma}{1 + (\gamma - 1)(1 - z)} \tag{D-4}$$

In a computation involving condensation of a "real" gas, it is necessary to first determine the real isentrope, determined through use of the equation of state as mentioned in the text.

From this, by use of the equation of state and Equation D2, respectively, z and γ' are established at all points of the expansion and it is then a simple matter to determine the value of γ to be entered into the computation. The value of z is taken as the mean of stagnation and condensation values (indicated in Table 14) and a linear, temperature dependent approximation to γ between the same two points is made,

$$\gamma = \gamma_a - \gamma_b \ T(^\circ C)$$

where values of γ_a and γ_b are given in Table 15.

Consequently, the computation scheme treats a value of γ which will yield the real isentropic exponent γ' when treated with the corrections (D-3) and (D-4). This matches the isentrope prior to condensation with the best

estimate of local conditions and calculates corrected nucleation and drop growth rates within the theoretical framework of perfect gas.

Perfect gas calculations may be made by simply setting $z = 1.00$, and entering the desired value of $\gamma = \gamma_a$, $\gamma_b = 0$.

It might be pointed out that the compressibility factor begins to vary more rapidly after condensation commences, and that the computation scheme ignores this. Some error in profile shapes may result, but probably are no more in doubt than those resulting from perfect gas treatment. The value of this treatment lies in its attempt at establishment of the best estimate of conditions and behavior at the point of *onset* of condensation.

Another possibility for the consideration of real gas behavior in condensation would be to completely rewrite the entire processes of nucleation, drop growth and gas dynamics in terms of an equation of state, as was done for the non-condensing isentropes and total pressure computations. This could only be done by greatly increasing the complexity of an already complex computation and at the cost of excluding the many perfect gas relationships which so greatly simplify the mathematical treatment of condensation in gas flow processes.

APPENDIX E. A CLOSED FORM SOLUTION TO THE MOMENTUM INTEGRAL BOUNDARY LAYER EQUATION INCLUDING APPROXIMATE EFFECTS OF STREAMWISE DENSITY VARIATION

In most cases involving the study of boundary layers, effects of changing density are negligible. However, in such cases as nozzle flow, where sonic velocities are approached or exceeded, acceleration forces due to the presence of the density gradient become appreciable, and near the throat of a supersonic nozzle are of the same order as those due to area change in their influence on main stream velocity and hence boundary layer growth. A study of the momentum integral equation has revealed that a closed form solution is possible for both laminar and turbulent flow. In the laminar case, an extremely simple form of solution is possible, enabling one to determine estimates of boundary layer growth and depression in supersonic nozzles, using only slide-rule calculations.

If it is assumed that density and pressure vary in the direction of flow, but not across the boundary layer, the momentum integral equation may be written as follows:

$$\frac{d}{dx} \rho \int_o^\delta (U - u)u\,dy + \rho \frac{dU}{dx} \int_o^\delta (U - u)\,dy = \tau_{y=o} \tag{E-1}$$

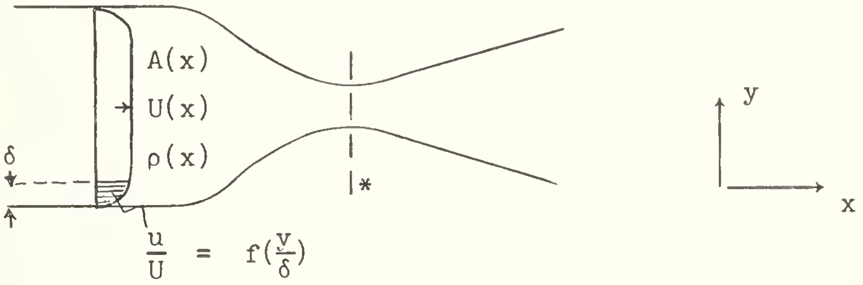

For the general case, it is assumed that

$$u/U = f(y/\delta) \tag{E-2a}$$

$$\tau_o/\rho U^2 = a_1 \left(\frac{\nu}{U\delta}\right)^{1/n} \tag{E-2b}$$

Then, Equation (1) may be reduced to:

$$b_1 \frac{d}{dx}(\rho\delta U^2) + b_2\, \rho\delta U \frac{dU}{dx} = a_1 \left(\frac{\nu}{U\delta}\right)^{1/n} \rho U^2 \qquad \text{(E-3)}$$

where b_1, b_2 and a_1 are dependent upon the assumed profile.

Equation (E-3) may be manipulated to appear in the form:

$$\frac{b_1}{2}\frac{d(\delta^2)}{dx} + \delta^2 \left[\frac{2b_1 + b_2}{U}\frac{dU}{dx} + \frac{b_1}{\rho}\frac{d\rho}{dx}\right] = a_1 \left(\frac{\nu}{U\delta}\right)^{1/n} \delta$$

or

$$\frac{d(\delta^2)}{dx} + \delta^2 \left[\frac{C_1}{U}\frac{dU}{dx} + \frac{2}{\rho}\frac{d\rho}{dx}\right] = C_2 \left(\frac{\nu}{U\delta}\right)^{1/n} \delta \qquad \text{(E-4)}$$

where $C_1 = \dfrac{2(2b_1 + b_2)}{b_1}$ $\qquad C_2 = \dfrac{2a_1}{b_1}$

Equation (E-4) may be put into integrable form by using the integration factor:

$$m = C^{\int P dx}; \quad Pdx = C_1 \frac{dU}{U} + 2\frac{d\rho}{\rho}$$

Hence, m takes the convenient form:

$$m = U^{C_1} \rho^2 \qquad \text{(E-5)}$$

or, more conveniently $\quad m = \left(\dfrac{U}{U_o}\right)^{C_1} \left(\dfrac{\rho}{\rho_o}\right)^2$

and the new form of the differential equation is:

$$\frac{d}{dx}(m\delta^2) = mQ \qquad \text{(E-6)}$$

where $\quad Q = C_2 \left(\dfrac{\nu}{U\delta}\right)^{1/n} \delta$

Hence

$$\frac{d}{dx}(m\delta^2) = C_2\, m\left(\frac{\nu}{U}\right)^{1/n} \cdot \delta^{1-1/n}$$

$$= C_2\, m^{\left(1 - \frac{n-1}{2n}\right)} \left(\frac{\nu}{U}\right)^{1/n} (m\delta^2)^{\frac{n-1}{2n}}$$

and: $\quad (m\delta^2)^{-\left(\frac{n-1}{2n}\right)} \dfrac{d}{dx}(m\delta^2) = C_2 m^{\frac{n+1}{2n}} \cdot \left(\dfrac{\nu}{U}\right)^{1/n}$

Integrating, one finally obtains:

$$\left[(m\delta^2)^{\frac{n+1}{2n}}\right]_{x_o}^{x} = \frac{C_2(n+1)}{2n} \int_{x_o}^{x} m^{\frac{n+1}{2n}} \left(\frac{\nu}{U}\right)^{1/n} dx \qquad \text{(E-7)}$$

Equation (E-7) is the most general form of solution to the momentum integral equation, approximately valid for a compressible gas in either a laminar or turbulent boundary layer.

It should be noted that the integrating factor m can often be more conveniently expressed as follows:

$$pdx = \left[C_1 \left(- \frac{dA}{A} - \frac{d\rho}{\rho}\right) + 2 \frac{d\rho}{\rho}\right]$$

$$m = e^{\int pdx} = A^{-C_1} \rho^{2-C_1}$$

or, more conveniently:

$$m = \left(\frac{A}{A^*}\right)^{-C_1} \left(\frac{\rho}{\rho_o}\right)^{2-C_1} \qquad \text{(E-8)}$$

Laminar Boundary Layer

Considering Equation (E-7) for the case of a laminar boundary layer, where *n = 1*, we immediately have:

$$\left[m\delta^2\right]_{x_o}^{x} = C_2 \int_{x_o}^{x} m\left(\frac{\nu}{U}\right) dx \qquad \text{(E-7a)}$$

Assuming that viscosity μ is nearly constant and substituting for m with Equation (8) yields:

$$\delta^2 = \frac{C_2\mu}{m} \int_{x_o}^{x} m\left(\frac{1}{\rho U}\right) dx + \frac{m_o}{m} \delta_o^2$$

$$= C_2\mu \left(\frac{A}{A^*}\right)^{C_1} \left(\frac{\rho}{\rho_o}\right)^{C_1-2} \int_{x_o}^{x} \left(\frac{A}{A^*}\right)^{-C_1} \left(\frac{\rho}{\rho_o}\right)^{2-C} \left(\frac{1}{\rho U}\right) dx + \frac{m_o}{m} \delta_o^2$$

Further, for a nozzle: mass flow rate = constant = $\rho UA = \rho^* U^* A^*$

Hence:

$$\delta^2 = \left\{ \frac{C_2\mu}{\rho^* U^*} \left(\frac{A}{A^*}\right)^{C_1} \left(\frac{\rho}{\rho_o}\right)^{C_1 -2} \int_{x_o}^{x} \left(\frac{A}{A^*}\right)^{1-C_1} \left(\frac{\rho}{\rho_o}\right)^{2-C_1} dx \right\} + \frac{m_o \delta_o^2}{m} \qquad \text{(E-9)}$$

Equation (E-9) is the specialized form of Equation (E-7) for a laminar boundary layer. Reviewing Equations (E-3) and (E-4), it is seen that the constants C_1 and C_2 will depend on the polynomial used to approximate the shape of the boundary layer velocity profile.

For flow in a nozzle, (A/A^*) is known and (ρ/ρ_o) can be easily determined. Hence, the function:

$$F = m\left(\frac{A}{A^*}\right) = \left(\frac{A}{A^*}\right)^{1-C_1} \left(\frac{\rho}{\rho_o}\right)^{2-C_1} \qquad \text{(E-10)}$$

may be also easily determined and plotted. The integral may be determined by the area under the curve F, and at any point, x:

$$\delta^2 = K_1 m^{-1} \int_{x_o}^{x} F\,dx + \frac{m_o}{m}\delta_o^2$$

For $\delta_o = 0$ at $x = 0$:

$$\delta^2 = K_1 m^{-1} \int_{x_o}^{x} F\,dx \qquad \text{(E-9a)}$$

where $K_1 = \dfrac{C_2 \mu}{\rho^* U^*}$

Equation (E-6) was applied to a nozzle of known geometry, using the assumption:

$$\frac{u}{U} = \frac{2y}{\delta} - \left(\frac{y}{\delta}\right)^2$$

for which $C_1 = 9 \quad C_2 = 30$

At first glance, the assumption of a laminar boundary layer may seem unjustified. However, Launder(R1) has shown that turbulent boundary layers under sufficiently negative pressure gradients will revert to a definite laminar form. Also, for the conditions of this calculation the observed boundary layer at the nozzle throat was such that the boundary layer Reynolds Number was about 2000 at the throat. This is less than the transition value and would indicate that a reversion to a laminar form could have taken place(R1). Hence, the laminar assumption is not unreasonable.

Calculations were made according to Table I for CO_2 at stagnation conditions of 84 psia and -10^oF, according to the corresponding values.

$$F = (A/A^*)^{-8} (\rho/\rho_o)^{-7} \qquad p_o = 84 \text{ psia}$$

$$K_1 = \frac{30\mu}{\rho^* U^*} \qquad \text{for } CO_2 \text{ at } T_o = -10^oF$$

Results of calculations are shown in Figure E1.

At the conditions noted above and for the nozzle in question, limited interferometer data provided visual means of measuring the boundary layer thickness, and four values are shown in Figure E1. These observations are estimated to be accurate ± 15%.

Also shown in Figure 1, to assist in estimating the relative size of the boundary layer, are those values of uniform flow flat plate laminar boundary layers calculated for the densities and velocities at the entrance and throat of the nozzle, respectively.

It is seen that the limited experimental data seems to agree well with the approximate calculation of boundary layer thickness. More experimental data is necessary for a more thorough evaluation.

The extremely small boundary layers resulting in the pressure gradients which occur when compressibility becomes important make it appear that further interferometer observations would be an advisable method of gaining such data if it is not readily available in the literature.

The fact that the past "history" of the boundary layer has a greatly decreased effect on the value of boundary layer thickness in the region of rapid acceleration is quite apparent both from the curve in Figure 1 and from inspection of the equations. Equation (E-9) shows that the value of δ_o^2, which exists at the beginning of integration must be multiplied by the ratio m_{xo}/m_x. Hence, if the value of m increases appreciably, as it does when flow area A and density ρ decrease, then the term $(m_{xo}/m_x)\delta_o^2$ contributes

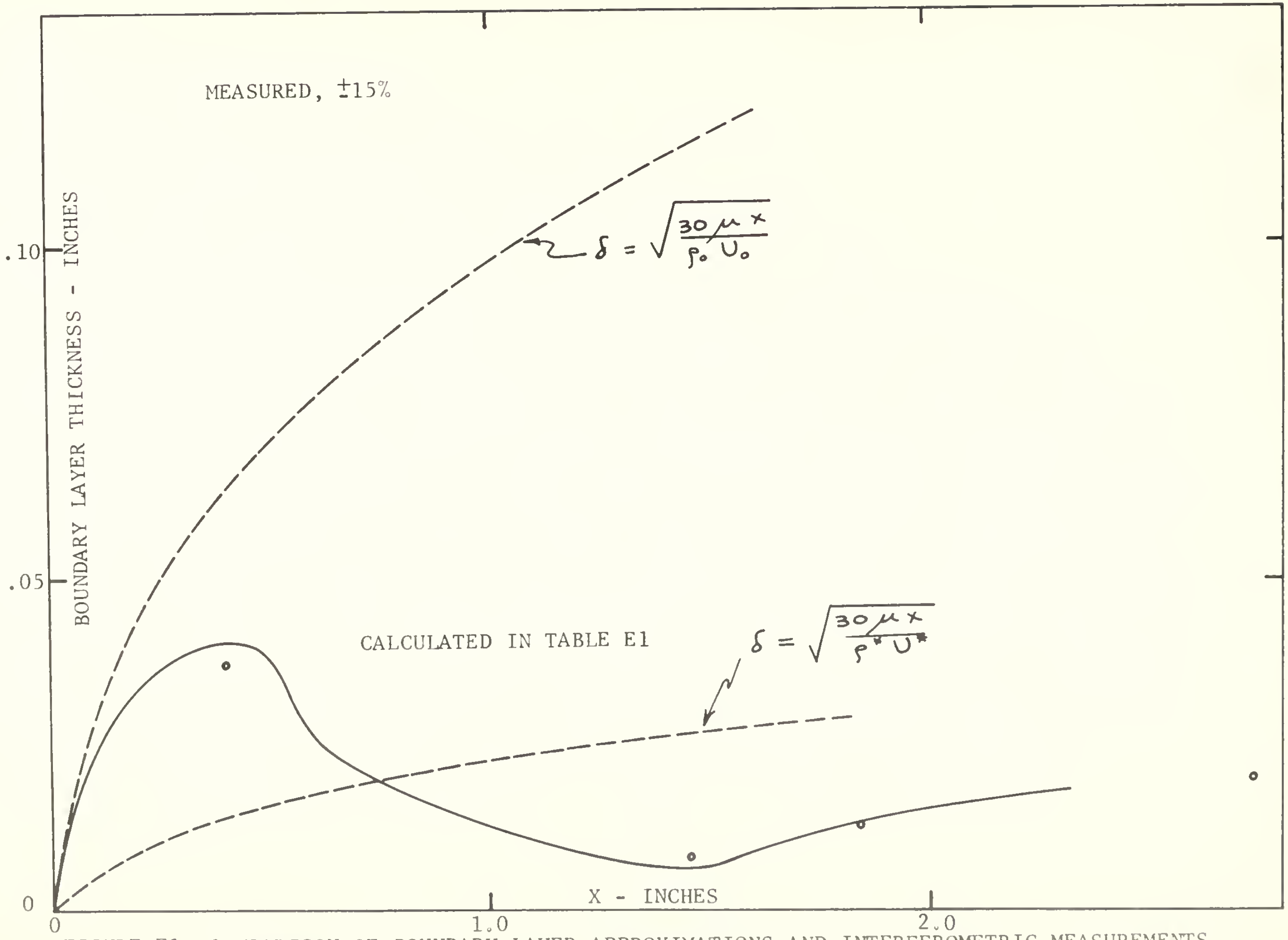

FIGURE E1, COMPARISON OF BOUNDARY LAYER APPROXIMATIONS AND INTERFEROMETRIC MEASUREMENTS IN A TWO-DIMENSIONAL SUPERSONIC NOZZLE.

little when added to the integral term.

The fact that one is limited to an assumed boundary layer velocity profile during an integration does not restrict the possibility of breaking the flow into regions, and applying Equation (E-9) to different velocity profiles (i.e. different constants C_1 and C_2) over the various intervals of x, with relative ease.

Turbulent Boundary Layer

It is apparent that Equation (E-7) is readily applicable to turbulent boundary layers in its present form, merely by selecting the expressions desired for Equations (E-2a) and (E-2b), that is, the velocity profile and wall shear dependence.

However, since most persons are accustomed to referring to turbulent boundary layer behavior in terms of momentum thickness θ, and shape factor $H = \delta^*/\theta$, it is worthwhile to re-derive Equation (E-7) in terms of θ and H.

$$\frac{d}{dx} \rho \int_o^\delta (U - u)u\,dy + \rho \frac{dU}{dx} \int_o^\delta (U - u)\,dy = \tau_o$$

$$\frac{d}{dx}(\rho U^2\theta) + \rho\delta^* U \frac{dU}{dx} = \tau_0 = a_1 \left(\frac{\nu}{U}\right)^{1/n} \rho U^2$$

This can be written as:

$$\rho U^2 \frac{d\theta}{dx} + \theta \frac{d}{dx}(\rho U^2) + \rho H\theta U \frac{dU}{dx} = \alpha_1 \left(\frac{\nu}{U\theta}\right)^{1/n} \rho U^2$$

$$\frac{d\theta}{dx} + \theta \left[\frac{1}{\rho U^2} \frac{d(\rho U^2)}{dx} + H \frac{1}{U} \frac{dU}{dx}\right] = \alpha_1 \left(\frac{\nu}{U\theta}\right)^{1/n}$$

Again:

$$\frac{d}{dx}(m\theta) = mQ$$

where $Q = \alpha_1 \left(\frac{\nu}{U\theta}\right)^{1/n}$

and $m = e^{\int p\,dx}$

$$p\,dx = \left[\frac{d(\rho U^2)}{\rho U^2} + H \frac{dU}{U}\right]$$

$$m = \left(\frac{\rho U^2}{\rho_o U_o^2}\right)\left(\frac{U}{U_o}\right)^H \qquad \text{or} \qquad \rho U^{H+2}$$

Hence, it is seen that:

$$(m\theta)^{1/n} \frac{d}{dx} (m\theta) = m^{\frac{n+1}{n}} \quad \alpha\left(\frac{\nu}{U}\right)^{1/n}$$

Integrating yields:

$$\left[(m\theta)^{\frac{n+1}{n}}\right]_{x_o}^{x} = \frac{\alpha(n + 1)}{n} \int_{x_o}^{x} m^{\frac{n+1}{n}} \left(\frac{\nu}{U}\right)^{1/n} dx \qquad \text{(E-7b)}$$

Inspection will also show that Equation (7b) could have been obtained directly from Equation (7), using the relationship between the two integrating factors, and between δ and θ. Note that $C_1 = 2(H + 2)$.

Substituting for m in Equation (7b) yields:

$$(\rho U^{H+2}\theta)^{\frac{n+1}{n}} = \frac{n + 1}{n} \alpha\nu^{1/n} \int_{x_o}^{x} \left(\frac{\rho U^{H+2}}{U^{1/n}}\right)^{\frac{n+1}{n}} dx + (\rho_o U_o^{H+2}\theta_o)^{\frac{n+1}{n}}$$

This can be further simplified to either of two forms:

$$\theta^{\frac{n+1}{n}} = (\rho U^{H+2})^{-\frac{n+1}{n}} \left[\frac{n + 1}{n} \alpha\nu^{1/n} \int_{x_o}^{x} \rho^{\frac{n+1}{n}} U^{\eta} dx + C_o\right] \qquad \text{(E-11)}$$

or

$$\theta\left(\frac{U\theta}{\nu}\right)^{1/n} = \rho^{-\frac{n+1}{n}} U^{-\eta} \left[\frac{n + 1}{n} \alpha\int_{x_o}^{x} \rho^{\frac{n+1}{n}} U^{\eta} dx + C_o'\right] \qquad \text{(E-12)}$$

where $\eta = (H + 2)\frac{(n + 1)}{n} - \frac{1}{n}$

$C_o = (\rho U^{H+2}\theta)^{\frac{n+1}{n}}_{@x = x_o}$

$C_o' = C_o/\nu^{1/2}$

For the case of negligible density gradient Equation (E12) reduces to Equation (22.8) in Schlichting[(R2)].

References

R1) Launder, B.E. - "Laminarization of the Turbulent Boundary Layer by Acceleration" - Gas Turbine Laboratory Report #77 - M.I.T. November 1964.

R2) Schlichting, H. - *Boundary Layer Theory* - McGraw-Hill

TABLE E1

					(F)			(1/m)	K_o	δ†
1	2	3	4	5	6	7	8	9	10	11
x	A/A*	ρ/ρ_o	$(A/A^*)^{-8}$	$(\rho/\rho_o)^{-7}$	(4)x(5)	$\int_x^{x+\delta x} F dx$	$\int_o^x F dx$	(2)/(6)	(8)x(9)	$.0219(10)^{1/}$
0	20	1	$1/256 \times 10^{-8}$	1	3.92×10^{-11}	1.58×10^{-11}				
.2	17.4	1	$1/84 \times 10^{-8}$	1	1.19×10^{-10}	3.52×10^{-11}	1.58×10^{-11}	14.6×10^{10}	2.31	.0333
.4	16.0	1	$1/42.9 \times 10^{-8}$	1	2.33×10^{-10}	3.97×10^{-10}	5.10×10^{-11}	6.86×10^{10}	3.50	.0410
.6	11.35	1	$1/2.68 \times 10^{-8}$	1	3.74×10^{-9}	2.82×10^{-8}	4.48×10^{-10}	3.04×10^{9}	1.36	.0256
.8	6.6	1	$1/3.6 \times 10^{-6}$	1	2.78×10^{-7}	1.70×10^{-5}	2.86×10^{-8}	2.38×10^{7}	.680	.0180
1.0	3.02	.978	$1/68.9 \times 10^{-2}$	1/.855	1.70×10^{-4}	1.62×10^{-2}	1.70×10^{-5}	1.78×10^{4}	.303	.0120
1.2	1.415	.875	1/16	1/.387	.162	1.64	1.62×10^{-2}	8.73	.142	.00825
1.4	1.020	.655	1/1.173	1/.0518	16.4	1.46	1.66	.0621	.103	.0070
1.46	1.000	.609	1	1/.0311	32.2	6.18	3.10	.0311	.097	.0068
1.6	1.04	.538	1/1.36	1/.0131	56.1	13.59	9.28	.0185	.172	.0091
1.8	1.170	.447	1/3.5	1/.00358	79.8	21.70	22.87	.0147	.336	.0127
2.0	1.321	.360	1/9.29	$1/7.84 \times 10^{4}$	137.2	32.62	44.57	.00963	.429	.0143
2.2	1.565	.2835	1/36	6800	189.0		77.19	.00827	.638	.0175

† $\delta^2 = \frac{30\mu}{p^* U^*} K_o = 4.8 \times 10^{-4} K_o \text{ in}^2$

$\delta = .0219 \sqrt{K_o} \text{ in}$

for which

$$V \approx 820 \text{ ft/sec.}$$

$$\rho \approx .25 \text{ lbm/ft}^3$$

$$R \approx .67 \text{ ft}$$

Hence, the estimated pressure gradient over the top of the boundary layer at the throat is

$$\frac{dp}{dn} = \rho\frac{V^2}{R} \approx 7500 \frac{\text{lbf}}{\text{ft}^3} = 4.33 \frac{\text{psi}}{\text{in}}$$

The side walls are approximately 1" apart. At a point midway between them, the pressure gradient is zero. Assuming the pressure gradient is linear,

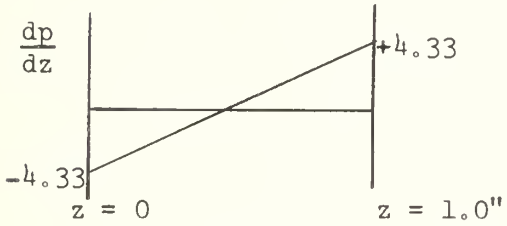

$$\frac{dp}{dz} = -4.33 + 8.66z$$

And:

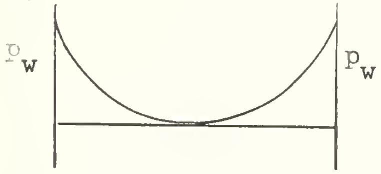

$$p = p_w - 4.33z + 4.33z^2$$

$$\therefore \bar{p} = \left[p_w z - \frac{4.33z^2}{2} + \frac{4.33z^3}{3}\right]_0^1$$

$$= p_w - .71$$

Hence: $p_w - \bar{p} \approx .71$ psi

This is of sufficient magnitude to offer a possible explanation of the less than 1 psi difference between average mainstream and measured wall pressure at the throat.

It is noted that greater rates of curvature of the boundary layer occur upstream of the throat at relatively negligible velocities. Downstream, where velocities continue to increase the boundary layer has very little curvature.

APPENDIX G

DISCUSSION OF INTERFEROMETRY APPLICATION TO TWO-DIMENSIONAL NOZZLE FLOW

Extensive discussions of the theory behind interferometry techniques are numerous. References (14) and (36) are included for the reader who may desire additional detail.

Basically, an interferometer consists of a monochromatic source of light which is focused into a beam of nearly parallel rays. The beam is then split into two beams traveling separate paths of identical distance after which the beams are rejoined and focused on a viewing, or photographic, plate. An interference pattern of parallel light and dark bands, as seen in Fig. 12 is formed when the two beams are rejoined due to the fact that the various rays of each beam travel slightly different distances depending on the geometry of the mirror arrangement.

One beam is passed perpendicularly through the test section. To compensate for the change in optical path length caused by the glass side walls, "compensating" glasses of exactly the same thickness, must be placed in the path of the other beam. During testing, the only change which occurs is the density of the vapor in the test section which influences the velocity of light passing through it according to the relation, for two-dimensional flow:

$$\frac{S\lambda_o}{l} = n_1 - n_2$$

where n is the index of refraction of the gas in the test section, l is the width of test section through which light passes, λ_o is the wave length of light being used, and S is the number of fringe shifts which occur at the point in question due to a change in the index from n_1 to n_2.

The index of refraction is related to the density by the relationship

$$G\rho = n - 1$$

where G is the Gladstone-Dale constant, fixed for any gas.

The technique used in this investigation was to first photograph the interference fringe pattern for no flow and then take another photograph under test conditions. The fringes of each were then numbered from a common point which effectively represented stagnation conditions. For each distance x it was then a simple, though time consuming, matter to determine the fringe shift S and thence to calculate the density ratio. Photos used in calculating the density curves in Fig. 15(a), (b) and Fig. 16(a), (b) are shown in Figs. 11 and 12, respectively. A graphical illustration of the determination of S for test 1 (Fig. 15) is given in Fig. 13. Test 2 was done more precisely by measuring the distances to each fringe in the no-flow picture as measurements in the flow picture proceeded, since it was detected that slight departure from perfectly even spacing of the no-flow fringes occurs, probably due to minute differences in thickness of the optical glasses. (Note differences in Tables 3 and 4.)

Although interferometric methods did not succeed in producing measured effects of condensation, as mentioned in the text, the results obtained for non-condensing flow does offer a recommendation for possible further application in this direction. One important unfavorable aspect of it, however, is the extreme amount of time and effort required to reduce the photographs to meaningful data. Each of the two tests presented here require alignment of the interferometer with the nozzle (a process which may take as long as two days, after which, however, it is permanent), photography, development of negatives and prints (another day), measurements from prints, and calculations based on the measurements. If pressure measurements are taken, coordinating the location of pressure and density measurements also requires painstaking accuracy.

Such a laborious process in reducing the data is still predicated upon a two-dimensional nozzle and becomes prohibitively difficult for three-

dimensional flow. Reference 36 involves the analysis of *one* three-dimensional nozzle photograph.

APPENDIX H

COMPUTATIONAL PROGRAM

Part 1:	Comparison of Equations of State
Part 2:	Isentrope and Enthalpy Calculations
Part 3:	Normal Shock Calculations
Part 4:	Nucleation Contours Calculations
Part 5:	Condensation Calculations

PART 1

```
*M3851-3374,FMS,DEBUG, 1,1,10,1              KARL M DUFF
*      XEQ
C      COMPARISON OF EQUATIONS OF STATE
       READ 4, TO,VO
C      CALCULATION USING BENEDICT WEBB RUBIN EQUATION OF STATE
       R= .08207
       V= VO*44./16.08
       T=TO/1.8
       AO=2.62392
       BO=0.052074
       CO=0.133670
       A=0.133333
       B=0.00396667
       C=14814.8
       ALPHA=0.0000890
       GAMMA =0.00557
       PBWR = R*T/V + (BO*R*T-AO-CO/(T*T))/(V*V) + (B*R*T-A)/(V**3) + A*A
      1LPHA/(V**6) + (C*(1. +GAMMA*(V*V))/(T*T*V**3))*EXPF(-GAMMA/(V*V))
       PBWR = PBWR*14.696
       PRINT 1, PBWR
C      CALCULATION USING MARTIN AND HOU EQUATION OF STATE
       V = VO
       T = TO
       BV=.007495
       ATWO=-8.9273631
       BTWO=.005262476
       CTWO=-150.97587
       ATHRE=.18907819
       BTHRE=-.0000704617
       CTHRE=.0831424
       AFOUR=-.0002112459
       BFIVE=1.9565593*10.**(-8)
       TC=547.5
       R= .24381
       PMH = R*T/(V-BV) + (ATWO+BTWO*T+CTWO*EXPF(-5.475*T/TC))/((V-BV)**2
      1) + (ATHRE + BTHRE*T + CTHRE*EXPF(5.475*T/TC))/((V-BV)**3) + AFOUR
      2/((V-BV)**4) + BFIVE*T/((V-BV)**5)
       PRINT 2, PMH
C      CALCULATION USING PLANK EQUATION OF STATE
C      FIND LOCATION OF ZERO REMAINDER
       R= 1.8644
       T=TO/1.8
       J=1
       K=1
       PP=PBWR/14.696
       DELP=.1*PP
11     VP=R*T/PP+(.0825+.0012657*PP)*1000./((.01*T)**3)
       VP= VP/62.43
       IF (VP-V) 5,15,25
5      IF (1.0001*VP-V) 6,6,15
6      IF (J-2) 7,8,8
7      J=2
8      IF (K-2) 10,9,9
9      DELP= .5*DELP
10     PP= PP-DELP
```

```
      GO TO 11
25    IF (.9999*VP-V) 15,26,26
26    IF (K-2) 27,28,28
27    K=2
28    IF (J-2) 30,29,29
29    DELP=.5*DELP
30    PP= PP+DELP
      GO TO 11
15    PP= 14.696*PP
      PRINT 3, PP
1     FORMAT (15H PRESSURE(BWR)=, F12.7)
2     FORMAT (15H PRESSURE(MH) =, F12.7)
3     FORMAT (15H PRESSURE(P)  =, F12.7)
4     FORMAT (F5.1, F5.3)
      END
```

PART 2

```
C      MAIN FOR ISENTROPE DECREASING P
       DIMENSION MARK(4),XOUT(200), Y(1), TOL(1), YMIN(1)
      1   ,DY(1)
       COMMON PZERO ,HZERO  ,TZERO
       CALL ENT (P,T,H,4)
  100  READ4,PZERO,TZERO,DELTAP,MP
  4    FORMAT (3F12.0,I4)
       X=0.
       CALL ENT (PZERO,TZERO,Y(1),3)
       HZERO=Y(1)
       TOL(1)=.0001
       YMIN(1)=10.
       H=DELTAP/3.
       XOUT(1)=X
       DO 2 I=2,MP
  2    XOUT(I)=XOUT(I-1)+DELTAP
       MARK(1)=1
       MARK(2)=MP
       MARK(4)=0
       CALL RUNGE (1,X,Y,TOL,YMIN,H,XOUT,MARK)
       GO TO 100
       END
                                                                    0022

                                                            TOTAL   0022*
```

```
*      LABEL
C      DIFFEQ FOR ISENTROPE CALCULATION
       SUBROUTINE DIFFEQ (N,X,Y,DY)
       DIMENSION Y(1),DY(1)
       COMMON PZERO
       P=PZERO-X
       IF(P)1,2,2
  1    CALL EXIT
  2    CALL ENT (P,T,Y(1),2)
       CALL FOR RHO (P,T,RHO)
       DY(1)=-1./RHO
       RETURN
       END
                                                                    0013

                                                            TOTAL   0013*
```

```
*     LABEL
      SUBROUTINE PRINT (N,XOUT,Y,DY,J)
C     PRINT FOR ISENTROPE CALCULATION
      DIMENSION XOUT(200),Y(1),DY(1)
      COMMON PZERO,HZERO ,TZERO
      P=PZERO-XOUT(J)
      PRATIO=P/PZERO
      CALL ENT (P,T,Y(1),2)
      TRATIO=T/TZERO
      CALL FORRHO (P,T,RHO)
      CALL FOR RHO (PZERO,TZERO,RHOZER)
      Z=P/(T*RHO*1.8644)
      RRATIO=RHO/RHOZER
      G=(P-PSAVE)*(T+TSAVE)/(T-TSAVE)/(P+PSAVE)
      GAMMA=G/(G-1.)
      GR=Z*GAMMA/(1.-(1.-Z)*GAMMA)
      VEL=0.
      W=2.*(HZERO-Y(1))*1033.*980.7
      IF(W) 6,6,7
 7    VEL=SQRTF(W)
 6    H=Y(1)*.0242048+142.60
      PSAVE=P
      TSAVE=T
      IF (J-1) 2,2,3
 2    PRINT5,PRATIO,TRATIO,RRATIO,P,T,GAMMA,GR,H,Z,VEL
      RETURN
 3    PRINT1,PRATIO,TRATIO,RRATIO,P,T,GAMMA,GR,H,Z,VEL
 5    FORMAT (120H1            P/P0           T/T0      RHO/RHOO                 P
     1       T       GAMMA EFF          GAMMA             H              Z            VEL
     2      ,/36X,84H              ATM          DEG K
     3   CAL/GM                        CM/SEC,//3F12.4,F12.3,F12.1,2F12.4,F12.2,
     4  ,F12.4,F12.1)
 1    FORMAT (3F12.4,F12.3,F12.1,2F12.4,F12.2,F12.4,F12.1)
      RETURN
      END
                                                                                       0035

                                                                            TOTAL      0035*
```

```
*     LABEL
      SUBROUTINE FORRHO (P,T,RHO)
      R=1.8644
      V=R*T/P-(82.5+1.2657*P)/(.01*T)**3.333
      RHO=1./V
      RETURN
      END
                                                                                       0007

                                                                            TOTAL      0007*
```

```
C     P IN ATM T IN DEG K   H IN ATM-CC/GM
      SUBROUTINE ENT (P,T,H,L)
      DIMENSION HZERO(130),TH(130)
      HOFPF(P,T)=4.333*(82.6*P+1.265*P*P)/(.01*T)**3.333
      GO TO (1,2,3,4),L
 4    J=0
 7    J=J+1
C      HZERO IN BTU/LB MOLE   TH IN DEG R
      READ5,HZERO(J),TH(J)
 5    FORMAT (2F10.0)
      TH(J)=TH(J)/1.8
      HZERO(J)=HZERO(J)*.52081
      IF(TH(J))6,6,7
C     NOW HZERO IS IN ATM-CC/GM AND T IS IN DEG K
C     ZERO H AT O DEG   GASEOUS
 6    JEND=J-1
 1    RETURN
 3    DO 33 J=1,JEND
      IF(T-TH(J))32,33,33
 33   CONTINUE
      GO TO 100
 32   IB=J-1
      H=HZERO(IB)+(HZERO(IB+1)-HZERO(IB))/(TH(IB+1)-TH(IB))*(T-TH(IB))
     1  -HOFPF(P,T)
      RETURN
 2    DO 23 J=1,JEND,5
      H1=HZERO(J)-HOFPF(P,TH(J))
      IF(H1-H) 23,25,24
 23   CONTINUE
      J=JEND
 24   JH=J-5
      IF(JH) 100,100,29
 29   DO 27 K=JH,J
      HA=HZERO(K)-HOFPF(P,TH(K))
      IF(HA-H) 27,28,28
 27   HB=HA
      GO TO 100
 28   IB=K-1
      T=TH(IB)+(TH(IB+1)-TH(IB))*(H-HB)/(HA-HB)
      RETURN
 25   T=TH(J)
      RETURN
 100  PRINT101,P,T,H
 101   FORMAT (/42H T OR H IS OUT OF THE RANGE OF HZERO INPUT
     1 ,/ 12X,2H P,12X,2H T,12X,2H H,/3F14.2)
      CALL EXIT
      END
                                                                 0047

                                                      TOTAL      0047*
```

```
C       MAIN TO PUNCH ENTHALPY TABLES
        DIMENSION HH(6)
        CALL ENT(P,T,H,4)
        T1=30.
        DO 2 L=1,4
        T1=T1+60.
            T2 =T1+10.
        PUNCH7,T2
  7     FORMAT (F17.1)
        P=0.
        DO 2 J=1,25
        P=P+.5
        T=T1
        DO 6 K=1,6
        T=T+10.
        CALL ENT (P,T,HH(K),3)
  6     HH(K)=HH(K)*.0242048+142.60
C       H TO BE PUNCHE D TO AGREE WITH DIN I E    IC CAL/GM    O H AT O SOLID
  2     PUNCH3,P,HH
   3    FORMAT (F6.1,6F11.2)
        CALL EXIT
        END
                                                                   0022

                                                          TOTAL    0022*
```

PART 3

```
*       LABEL
        SUBROUTINE DIFFEQ (N,X,Y,DY)
        DIMENSION Y(2),DY(2)
        COMMON PZERO
        S=1.
        P=X
        GO TO (1,2),N
 1      P=PZERO-X
        S=-1.
 2      CALL ENT (P,T,Y(1),2)
        CALL FOR RHO (P,T,RHO)
        DY(1)=S/RHO
        DY(2)=1.
        RETURN
        END
                                                                            0015

                                                                  TOTAL     0015*
```

```
C       MAIN FOR SHOCK CALCULATIONS
        CALL ENT (P,T,H,4)
        PRINT1
 1      FORMAT (120H    TOLL          P01         T01          P1          T1
       1     P2          T2         P02         T02    P02/P01     P1/P02
       2                        ,)
        CALL START(1)
        END
                                                                            0008

                                                                  TOTAL     0008*
```

```
*       LABEL
        SUBROUTINE EQ1(V,REM)
        COMMON PZERO,TZERO,HZERO,TOLL,P2,T2,P1,T1,H1
        CALL FOR RHO (P1,T1,R1)
        U1=SQRTF(2.*(HZERO-H1))
        U2=U1*R1/V
        P2=P1+R1*U1*U1-V*U2*U2
        H2=HZERO-U2*U2*.5
        CALL ENT(P2,T2,H2,2)
        CALL FOR RHO (P2,T2,R2)
        REM=R2-V
        RETURN
        END
                                                                            0013

                                                                  TOTAL     0013*
```

```
*     LABEL
      SUBROUTINE ENT (P,T,H,L)
C     P IN ATM T IN DEG K   H IN ATM-CC/GM
      DIMENSION HZERO(130),TH(130)
      HOFPF(P,T)=4.333*(82.6*P+1.265*P*P)/(.01*T)**3.333
      GO TO (1,2,3,4),L
 4    J=0
 7    J=J+1
C      HZERO IN BTU/LB MOLE   TH IN DEG R
      READ5,HZERO(J),TH(J)
 5    FORMAT (2F10.0)
      TH(J)=TH(J)/1.8
      HZERO(J)=HZERO(J)*.52081
      IF(TH(J))6,6,7
C     NOW HZERO IS IN ATM-CC/GM AND T IS IN DEG K
C     ZERO H AT O DEG    GASEOUS
 6    JEND=J-1
 1    RETURN
 3    DO 33 J=1,JEND
      IF(T-TH(J))32,33,33
 33   CONTINUE
      GO TO 100
 32   IB=J-1
      H=HZERO(IB)+(HZERO(IB+1)-HZERO(IB))/(TH(IB+1)-TH(IB))*(T-TH(IB))
     1  -HOFPF(P,T)
      RETURN
 2    DO 23 J=1,JEND,5
      H1=HZERO(J)-HOFPF(P,TH(J))
      IF(H1-H) 23,25,24
 23   CONTINUE
      J=JEND
 24   JH=J-5
      IF(JH) 100,100,29
 29   DO 27 K=JH,J
      HA=HZERO(K)-HOFPF(P,TH(K))
      IF(HA-H) 27,28,28
 27   HB=HA
      GO TO 100
 28   IB=K-1
      T=TH(IB)+(TH(IB+1)-TH(IB))*(H-HB)/(HA-HB)
      RETURN
 25   T=TH(J)
      RETURN
 100  PRINT101,P,T,H
 101   FORMAT (/42H T OR H IS OUT OF THE RANGE OF HZERO INPUT
     1 ,/ 12X,2H P,12X,2H T,12X,2H H,/3F14.2)
      CALL EXIT
      END
                                                                    0048

                                                       TOTAL        0048*
```

```
      SUBROUTINE PRINT (N,XOUT,Y,DY,J)
      DIMENSION Y(2),DY(2),XOUT(1) ,R(3),REM(3)
      COMMON PZERO,TZERO,HZERO,TOLL,P2,T2,P1,T1,H1
      GO TO (3,4),N
 3    P1=PZERO-XOUT(J)
      CALL ENT (P1,T1,Y(1),2)
      H1=Y(1)
C     FIND FIRST GUESS AT RHO2
      CALL FOR RHO(P1,T1,R(1))
      CALL FOR RHO(PZERO,TZERO,RZERO)
      R(1)=1.01*R(1)
      R(2) = R(1)
          DR=.1*(RZERO-R(1))
      CALL EQ1 (R(1),REM(1))
11    R(2) = R(2) + DR
      CALL EQ1 (R(2),REM(2))
      IF(REM(1)*REM(2)) 10,10,11
 10   R(3)=(R(1)+R(2))*.5
      CALL EQ1 (R(3),REM(3)        )
      L=1
      IF (REM(3)*REM(1)) 12,13,13
 12   L=2
 13   R(L)=R(3)
      IF((R(2)-R(1))*2./R(1)-TOLL) 14,14,10
 14   CONTINUE
      CALL START(2)
 4    IF (Y(1)-HZERO) 5,6,6
 5    XB=Y(2)
      HB=Y(1)
      RETURN
 6    P02=Y(2)-(Y(2)-XB)*(Y(1)-HZERO)/(Y(1)-HB )
      CALL ENT (P02,T02,HZERO,2)
      POUT=P02/PZERO
      POUTA=P1/P02
      PRINT7,TOLL,PZERO,TZERO,P1,T1,P2,T2,P02,T02,POUT,POUTA
 7    FORMAT (F10.6,4(F10.3,F10.1),2F10.5)
      CALL START(1)
      END
                                                                 0038

                                                      TOTAL      0038*
```

```
      SUBROUTINE PRINT (N,XOUT,Y,DY,J)
      DIMENSION Y(2),DY(2),XOUT(1) ,R(3),REM(3)
      COMMON PZERO,TZERO,HZERO,TOLL,P2,T2,P1,T1,H1
      GO TO (3,4),N
 3    P1=PZERO-XOUT(J)
      CALL ENT (P1,T1,Y(1),2)
      H1=Y(1)
C     FIND FIRST GUESS AT RHO2
      CALL FOR RHO(P1,T1,R(1))
      CALL FOR RHO(PZERO,TZERO,RZERO)
      R(1)=1.01*R(1)
      R(2) = R(1)
          DR=.1*(RZERO-R(1))
      CALL EQ1 (R(1),REM(1))
11    R(2) = R(2) + DR
      CALL EQ1 (R(2),REM(2))
      IF(REM(1)*REM(2)) 10,10,11
 10   R(3)=(R(1)+R(2))*.5
      CALL EQ1 (R(3),REM(3)       )
      L=1
      IF (REM(3)*REM(1)) 12,13,13
 12   L=2
 13   R(L)=R(3)
      IF((R(2)-R(1))*2./R(1)-TOLL) 14,14,10
 14   CONTINUE
      CALL START(2)
 4    IF (Y(1)-HZERO) 5,6,6
 5    XB=Y(2)
      HB=Y(1)
      RETURN
 6    P02=Y(2)-(Y(2)-XB)*(Y(1)-HZERO)/(Y(1)-HB )
      CALL ENT (P02,T02,HZERO,2)
      POUT=P02/PZERO
      POUTA=P1/P02
      PRINT7,TOLL,PZERO,TZERO,P1,T1,P2,T2,P02,T02,POUT,POUTA
 7    FORMAT (F10.6,4(F10.3,F10.1),2F10.5)
      CALL START(1)
      END
                                                                   0038

                                                        TOTAL      0038*
```

```
      SUBROUTINE START(N)
      DIMENSION MARK(4),XOUT(200),Y(2),TOL(2),YMIN(2),DY(2)
      COMMON PZERO,TZERO,HZERO, TOLL,P2,T2
      H=.05
      DO 1 J=1,2
      MARK(J)=1
 1    YMIN(J)=20.
      GO TO(100,200),N
 100  READ4, PZERO,TZERO,P1,TOLL
C     SET CONSTANTS FOR RUNGE INTEGRATION DOWN THE ISENTROPE
      X=0.
      TOL(1)=TOLL
      CALL ENT (PZERO,TZERO,Y(1),3)
      HZERO=Y(1)
      MARK(4)=0
 4    FORMAT (4F12.0)
      XOUT(1)=PZERO-P1
      CALL RUNGE (1,X,Y,TOL,YMIN,H,XOUT,MARK)
      CALL EXIT
 200  X=P2
      CALL ENT (P2,T2,Y(1),3)
      MARK(2)=(PZERO-P2)*20.+20.
      TOL(2)=1.
      Y(2)=X
      XOUT(1)=P2
      MAR=MARK(2)
      DO 7 K=2,MAR
 7    XOUT(K)=XOUT(K-1)+.05
      CALL RUNGE (2,X,Y,TOL,YMIN,H,XOUT,MARK)
      CALL EXIT
      END
                                                                    0031

                                                           TOTAL    0031*
```

```
      SUBROUTINE FORRHO (P,T,RHO)
      R=1.8644
      V=R*T/P-(82.5+1.2657*P)/(.01*T)**3.333
      RHO=1./V
      RETURN
      END
                                                                    0006

                                                           TOTAL    0006*
```

PART 4

```
*      LABEL
C      PROGRAM FOR RATE CONTOURS
C      READ SECTION
       DIMENSION R(5), PP(5), FP(3), P(3)
 101   READ1, RHOA,RHOB,SURFA,SURFB,WMOL
 1     FORMAT (5F12.0)
       READ1, TSTART,TEND,DELTAT
       READ40,R
 40    FORMAT (5E12.2)
       PRINT22, RHOA,RHOB,SURFA,SURFB,WMOL,R
 22    FORMAT (14H1RATE CONTOURS,//
      1  6H RHOL=,F8.3, 2H -, F9.6,10H (T DEG C),/
      2 8H SIGMA =,F8.3,2H -,F9.6,10H (T DEG C),/
      3 7H WMOL =,F6.1,//
      4 24H TABLE CONTAINS P IN ATM,//
      5 19X,6H RATE=,E12.3,4E18.3,10H  P INF       ,/
      6 9H T DEG K ,/
      7  5H    =,/ )
       M=(TEND-TSTART)/DELTAT
       T=TSTART-DELTAT
       DO 20 I=1,M
       T=T+DELTAT
C      COMPUTATION
       RHOL=RHOA-RHOB*(T-273.16)
       SIGMA= SURFA-SURFB*(T-273.16)
       CALL PINFIN (T,PINF)
       IF (PINF) 20,20,74
 74    C1=1.01325E6*1.0E16/(1.38*T) *PINF
       C1=LOGF(C1)
       C1=LOGF(       SQRTF(WMOL*2.*SIGMA/(3.1416*6.025E23))/RHOL)+2.*C1
       C2=2.*SIGMA*WMOL/(82.062*1.01325E6*RHOL*T)
       C2=C2*C2*4.188*SIGMA*1.0E16/(1.38*T)
       DO 19 J=1,5
       IF(R(J)) 19,19,21
 21    A=LOGF(R(J))-C1
       B=-2.
       C=C2
C      CHOP FOR P
       P(3)=0.
       FP(1)=C
 11    P(3)=P(3)+3.
       IF(P(3)-55.) 66,66,19
 66    IF(FP(1)*(P(3)*P(3)*(A+B*P(3))+C))2,10,11
 2     P(1)=P(3)-3.
       P(2)=P(3)
 6     P(3)=(P(1)+P(2))*.5
       IF (P(2)-P(1)-.005*P(2)) 10,10,9
 9     L=1
       FP(3)=P(3)*P(3)*(A+B*P(3))+C
       IF (FP(1)*FP(3)) 4,10,5
 4     L=2
 5     P(L)=P(3)
       GO TO 6
 10    IF (P(3)-70.) 18,18,19
 18    PP(J)=EXPF(P(3))*PINF
```

```
19    CONTINUE
20    PRINT 33, T, PP, PINF
33    FORMAT ( F10.2,9X,5E18.3,E11.3 )
      GO TO 101
      END
                                                                      0060

                                                            TOTAL     0060*
```

```
C     MAIN FOR CONDENSATION

      DIMENSION Y(10),TOL(10),YMIN(10),XOUT(100),MARK(5)
      COMMON PZERO, TZERO,WMOL, GAMMA, RHOL,
     1HFG, SURFA, SURFB, XI, ALPHA, AMACH, X, AREA,
     2DADX, P, T, RSTAR, TD, AMASS, AVGR, ASTAR,
     3 SSAT, INTERP,Z ,YDROP,YRATE ,GAMA,GAMB,Y,NPART
     4 ,RTIMES
      INTERP=1
      CALL AREAC(X,AREA,DADX)
100   READ 1, PZERO                                                  ATM
      READ 1, TZERO                                                  DEG. C
      READ 1, WMOL
      READ 1, Z
      READ 1, GAMA
      READ 1, GAMB
      READ 1, RHOL                                                   GM/CC
      READ 1, HFG                                                    BTU/LBM
      READ 1, SURFA                                                  DYNES/CM
      READ 1, SURFB                                                  DYN/CM-C
      READ 1, XI
      READ 1, ALPHA
      READ 1, RTIMES
      READ 1, TOL(4)
      READ 1, TOLL
      READ 1, AMACH
      READ 3, CNTAM                                                  PTS/CM3
      READ 3, RZERO                                                  CM
1     FORMAT (F 20.0)
3     FORMAT (E11.3)
      PRINT2, PZERO, TZERO, WMOL, Z,GAMA,GAMB,RHOL,HFG,SURFA
     1,SURFB, XI, ALPHA, RTIMES, TOL(4), TOLL, AMACH, CNTAM, RZERO
2     FORMAT (25H1 CONDENSATION IN NOZZLES, ///9H PZERO = ,
     1    F10.3,/9H TZERO = , F10.2,/7HWMOL = , F12.2,/5H Z = ,F12.3,/7H
     2 GAMA =,F12.2,/9H GAMB =  ,F12.6,/8H RHOL = ,F12.3,/7H HFG = ,
     3F12.2,/9H SURFA = , F10.2,/9H SURFB = , F11.3,/6H XI = , F16.5,/
     48H ALPHA =,F14.5,/11H RATE*10.**,F8.2,/9H TOL(4) =,F18.8,/7H TOLL
     5=,F18.8,/9H AMACH1 =,F10.2,/8H CNTAM =,E12.3,/8H RZERO =,E12.3,//)
15    PZERO=2115.PZERO
      TZERO=1.8*(TZERO+273.16)
      INTERP=2
      XOUT(1)=1.
      XOUT(2)=AMACH *AMACH
      XOUT(3)=2.*XOUT(2)
      H=0.01
      MARK(1)=1
      MARK(2)=30
      MARK(4)=0
      DO 24 I=5,9
24    TOL(I)=TOLL
      DO 81 I=1,3
81    TOL(I)=0.1
      DO 25 I=1,9
      Y(I)=0.
25     YMIN(I)=0.00001
```

```
      WMOL=WMOL/Z
      Y(1)=25.1327*62.4*CNTAM*       1544.*TZERO/(WMOL*PZERO)
      Y(2)=Y(1)*RZERO
      Y(3)=Y(2)*RZERO/2.
      Y(5)=1.
      Y(6)=1.
      PZERO=PZERO/2115.
      TZERO=TZERO/1.8-273.16
      NPART=1
      X=0.
      N=9
      CALL RUNGE (N, X, Y, TOL, YMIN, H, XOUT, MARK)
      READ 77, L
77    FORMAT(I2)
      IF(L) 101,101,100
101   CALL EXIT
      END
                                                                      0072

                                                              TOTAL   0072*


*     LABEL
C     SUBROUTINF TO COMPUTE NUCLEATION RATE
      SUBROUTINE RATEC(PRESS,TEMP, SIGMA, SSAT, RATE)
      DIMENSION Y(10)
      COMMON PZERO, TZERO,WMOL, GAMMA, RHOL,
     1HFG, SURFA, SURFB, XI, ALPHA, AMACH, X, AREA,
     2DADX, P, T, RSTAR, TD, AMASS, AVGR, ASTAR, SSAT
     3 ,INTERP,Z,YDROP,YRATE,GAMA,GAMB,Y,NPART,RTIMES
      A=RSTAR
      B=10.**16/(1.380*TEMP)
      C=-4.1887*SIGMA*A*A*B
13    D=PRESS*1.01325E6*B
14    E=WMOL/(RHOL*6.025E23)
      EE=2.*SIGMA/(3.1416*WMOL)*6.025E23
      AA=2.*LOGF(D)+ LOGF(E) +.5*LOGF(EE)+ C
      AA=AA+2.303*16.
      IF(AA) 16,16,17
16    RATE=0.0
      GO TO 12
17    CONTINUE
      IF(AA-85.0) 18,18,19
19    AA=85.0
18    RATE=EXPF(AA)
12    RETURN
      END
                                                                      0025

                                                              TOTAL   0025*
```

```
*      LABEL
C      SUBROUTINE TO COMPUTE DERIVATIVES
       SUBROUTINE DIFFEQ (N, X, Y, DY)
       DIMENSION Y(10),DY(10)
       COMMON PZERO, TZERO,WMOL, GAMMA, RHOL,
      1HFG, SURFA, SURFB, XI, ALPHA, AMACH, X, AREA,
      2DADX, P, T, RSTAR, TD, AMASS, AVGR, ASTAR,
      3 SSAT, INTERP,Z ,YDROP,YRATE ,GAMA,GAMB,Y,NPART
 55    TEMP=Y(6)*(TZERO+273.16)
       R=.08478/WMOL
       GAMMA=GAMA-GAMB*(TEMP-273.16)
       FAC=1./(1.+(GAMMA-1.)*(1.-Z))
       GAMMA=GAMMA*FAC
       GO TO (1,2),NPART
 1     DO 3 I=1,9
 3     DY(I)=0.
       DY(5)=-Y(5)/(2./GAMMA+X*(GAMMA-1.)/GAMMA)
       DY(8)=R*TEMP*DY(5)/Y(5)
       DY(6)=Y(6)*(GAMMA-1.)*DY(5)/(GAMMA*Y(5))
       RETURN
 2     CALL PINFIN (TEMP,PINF)
       PRESS=Y(5)*PZERO
       SSAT=PRESS/PINF
       IF (SSAT-1.) 30, 30, 31
30      RATE=0
       RSTAR=0
       DY(9)=0.
       DROPG=0
       GO TO 32
31     SIGMA=SURFA-SURFB*(TEMP-273.16)
       RSTAR=2.*SIGMA*WMOL /(82.062*1.01325E6*RHOL*TEMP*LOGF(SSAT))
       IF (Y(1)-25.1327) 65,65,66
65     AVGR=1.3*RSTAR
       GO TO 67
66     AVGR=SQRTF(2.*Y(3)/Y(1))
67     CALL  RATEC(PRESS, TEMP, SIGMA, SSAT, RATE)
       CALL DROPGC(PRESS, TEMP, SSAT, AVGR, DROPG)
6      DROPG=DROPG/(Y(7)*SQRTF(GAMMA*8.314E7/WMOL*TEMP))
       VEL=SQRTF (-2.*Y(8)*980.7E6)
       DY(9)=1./VEL
32     CALL AREAC(X, AREA, DADX)
       CONLAM=(GAMMA-1.0)/GAMMA*HFG*WMOL/(1544.*1.8*TEMP)*778.
       DY(1)=25.1327* RATE*AREA
       DY(2)=Y(1)*DROPG+DY(1)*RSTAR
       DY(3)=Y(2)*DROPG+12.56637* RATE*AREA*RSTAR*RSTAR
       YDROP=RHOL/AMASS*Y(3)*DROPG
       YRATE=RHOL/AMASS*4.1888*RATE*AREA*RSTAR**3
       DY(4)=YDROP+YRATE
       DO 444 I=1,4
 444   DY(I)=0.
       DY(5)=Y(5)*(((CONLAM-1./(1.-Y(4)))*DY(4)-DADX)/(1. (1.-Y(4))*
      1 ((GAMMA-1.)/GAMMA+1./(GAMMA*Y(7)*Y(7))     )))
       DY(6)=Y(6)*(CONLAM*DY(4)+(GAMMA-1.)/GAMMA*(1.-Y(4))*DY(5)/Y(5))
       DY(7)=Y(7)*(-(1.-Y(4))*DY(5)/(GAMMA*Y(7)*Y(7)*Y(5))-
      1  .5/Y(6)*DY(6)    )
```

```
      DY(8)=R*TEMP*DY(5)/Y(5)
      RETURN
      END
```

```
C     PINFIN FOR CO2      0 TO 240 DEG K
C     BELOW 93  PINF=C*EXPF(-HFG/R/T) WAS USED AND PINF AT 93 USED TO GET C
C     ABOVE 93 AN EQUATION OF THE FORM P=C*EXPF(A/T) WAS USED TO INTERPOLATE
C     BETWEEN DATA POINTS.     DATA TAKEN FROM HAUDBOOK OF PHYSICS AND
C     CHEMISTRY, INTERNATIONAL CRITICAL TABLES, AND MATHESON GAS DATA

      SUBROUTINE PINFIN (T,PINF)
      IF (T-93.)1,1,2
 1    A=6.033
      B=-1263.
      GO TO 10
 2    IF (T-140.) 3,3,4
 3    A=7.492
      B=-1430.
      GO TO 10
 4    IF (T-160.) 5,5,6
 5    A=7.0851
      B=-1373.
      GO TO 10
 6     IF (T-195.) 7,7,8
 7    A=6.8355
      B=-1333.
      GO TO 10
 8    IF (T-216.6) 9,9,11
 9    A=7.028
      B=-1367.
      GO TO 10
 11   A=4.727
      B=-870.1
 10   PINF=10.**(A+B/T)
      RETURN
      END
```

```
*     LABEL
C    SUBROUTINE TO PRINT
      SUBROUTINE PRINT(N, XOUT, YOUT, DY, J)
      DIMENSION XOUT(1), YOUT(7)   ,Y(10) ,DY(1)
      COMMON PZERO, TZERO,WMOL, GAMMA, RHOL,
     1HFG, SURFA, SURFB, XI, ALPHA, AMACH, X, AREA,
     2DADX, P, T, RSTAR, TD, AMASS, AVGR, ASTAR,
     3 SSAT, INTERP,Z ,YDROP,YRATE ,GAMA,GAMB,Y,NPART
      GAMMA=GAMA-GAMB*YOUT(6)*(TZERO+273.16)
      GAMMA=GAMMA/(1.+(GAMMA-1.)*(1.-Z))
      IF (J-2)  21,22,32
 21   AMASS=ASTAR*PZERO*YOUT(5)*2115.*SQRTF(GAMMA*WMOL/(32.2*1544.
     1 *(TZERO+273.16)*YOUT(6)*1.8))
      AMASS=32.2*454.6*AMASS/(30.48*30.48)
      PRINT10
      PSTAR=YOUT(5)
      TSTAR=YOUT(6)
      GSTAR=GAMMA
      RETURN
 22   NPART=2
      DO 26 I=1,9
 26   Y(I)=YOUT(I)
      DO 27 I=1,3
 27   Y(I)=Y(I)*AMASS
      Y(7)=AMACH
      A=PSTAR/(Y(5)*AMACH )*SQRTF(Y(6)*GSTAR/(TSTAR*GAMMA))
      INTERP=3
      AREA=A*ASTAR
      CALL AREAC (X,AREA,DADX )
      INTERP=2
      XOUT(3)=X
      DO 25 I=3,63
 25   XOUT(I+1)=XOUT(I)+.2
32    CALL AREAC(XOUT(J), AREA, DADX)
      AREA=AREA/ASTAR
      TEMP=YOUT(6)*(TZERO+273.16)
      CALL PINFIN (TEMP, PINF)
      PRESS=YOUT(5)*PZERO
      SSAT=PRESS/PINF
      SIGMA=SURFA-SURFB*(TEMP-273.16)
      IF(SSAT-1.) 69,69,67
67    CALL  RATEC(PRESS, TEMP, SIGMA, SSAT, RATE)
      IF(YOUT(1)-25.1327) 69,69,68
68    AVGR= SQRTF(2.*YOUT(3)/YOUT(1))
      CALL DROPGC(PRESS, TEMP, SSAT, AVGR, DROPG)
      DTD=TD-YOUT(6)*(TZERO+273.16)
      PPSF=2115.*PZERO
      TDEGR=1.8*(TZERO+273.16)
      TOTALN=YOUT(1)*WMOL *PPSF/(25.1327*62.4*AMASS*1544.*TDEGR)
 69   PRINT11,XOUT(J),AREA,YOUT(5),YOUT(6),SSAT,YOUT(7),YOUT(4),
     1  YDROP,YRATE,DTD,AVGR,RSTAR,RATE,TOTALN
      RETURN
 10   FORMAT (120H       X      A/A*     P/PO     T/TO     S SAT     MACH    MOIST BY GROWTH
     1Y GROWTH,   NEW PART    TD-T       AVGR       RSTAR       NRATE      TOTALN
     2            ,//)
```

```
11    FORMAT (F7.3,F8.3,2F7.4,F8.3,F7.3,F8.5,2E10.3,F7.2,4E10.3)
      END
                                                                0057

                                                     TOTAL      0057*
```

```
   *      LABEL
          SUBROUTINE DROPGC(PRESS,TEMP, SSAT, AVGR, DROPG)
   C      SUBROUTINE TO COMPUTE DROP GROWTH
          COMMON PZERO, TZERO,WMOLV,GAMMAV,RHOL,
         1HFG, SURFA, SURFB, XI, ALPHA, AMACH, X, AREA,
         2DADX, P, T, RSTAR, TD, AMASS, AVGR, ASTAR,
         3SSAT, INTERP
          J=1
          P=PRESS*1.01325E6
          T=TEMP
          R=AVGR
          L=0
          D(1)=0
          D(2)=0
          TD=T-1.
   1      TD=TD+1.
   5      CALL PINFIN(TD, PINF)
          PD=1.01325E6*PINF*EXPF(RSTAR*T/(TD*R)*LOGF(SSAT))
          GASCON=8.314E7/WMOL
          CONLAM=(GAMMA-1.)/GAMMA*HFG*778./(1544.45*1.8*TEMP)*WMOL
          BETA=P/SQRTF(6.2832*GASCON*T)
          BETAD = PD/SQRTF(6.2832*GASCON*TD)
          DROPG=XI/RHOL*(BETA-BETAD)
                AA  = 1. - BETAD*TD/(BETA*T)
             AAA=.5*(CONLAM-1.)*GAMMA/(GAMMA-1.)*(1.-BETAD/BETA)
          A =         AA+AAA - (1./XI - 1.)    *ALPHA*(TD/T-1.)
          GO TO (8,9),J
    8     J=2
          IF(A) 10,10,9
    10    DROPG=0.
          PRINT11, PD,P,T,A,AA,AAA   ,X,Y(4)
    11     FORMAT(8E12.3)
          RETURN
    9     I=1
          IF(A) 2,2,3
   2      I=2
    3     D(I)=TD
          D3= D(1)*D(2)
          IF(D3) 4,1,4
    4     TD=.5*(D(1)+D(2))
          L=L+1
          IF(L-20) 5,5,60
    60    IF(DROPG) 10,6,6
   6      RETURN
          END
```

```
*     LABEL
C
C          FIRST ORDER DIFF. EQ. ROUTINE--ADJUSTS STEP SIZE
C
      SUBROUTINE  RUNGE(N, X, Y, TOL, YMIN, H, XOUT, MARK)
      DIMENSION  Y(1), YMIN(1), TOL(1), SUB(50), XOUT(1), MARK(1)
      DIMENSION  DY(50), YA(50), FA(50), FB(50), FC(50), YKEEP(50)
      KBTWN = 1
      KBIG = 1
      KLOW = 1
      NCOUNT = 15
      J = MARK(1)
      MAX = MARK(2)
      L = MARK(4)
      IF (L)  210, 210, 220
210   LTEST = 1
      GO TO 230
220   LTEST = 2
      NUM = L
230   DO 250  I = 1, N
250   SUB(I) = TOL(I)/32.0
10    IF (MAX - J)  20, 30, 30
20    RETURN
30    A = XOUT(J) - X
      B = ABSF(1.E-7 * X)
      IF (A + B)  40, 35, 35
35    IF (A - B)  50, 50, 60
40    J = J + 1
      GO TO 10
50    CALL PRINT(N, XOUT, Y, DY, J)
      J = J + 1
      GO TO 10
60    IF (A - 1.5*H)  70, 70, 80
70    H = A
      L = L + 1
      GO TO 1000
80    IF (A - 3.*H)  90, 1000, 1000
90    H = .5*A
C
C          DO RUNGE-KUTTE-MERSON INTEGRATION
C
1000  XA = X + H/3.
      XB = X + .5*H
      CALL DIFFEQ(N, X, Y, DY)
      X = X + H
      DO 1030  I = 1, N
      YKEEP(I) = Y(I)
      FA(I) = H*DY(I)
1030  YA(I) = Y(I) + FA(I)/3.
      CALL DIFFEQ(N, XA, YA, DY)
      DO 1040  I = 1, N
1040  YA(I) = Y(I) + FA(I)/6. + H*DY(I)/6.
      CALL DIFFEQ(N, XA, YA, DY)
      DO 1050  I = 1, N
      FB(I) = H*DY(I)
```

```
1050  YA(I) = Y(I) + .125*FA(I) + .375*FB(I)
      CALL DIFFEQ(N, XB, YA, DY)
      DO 1060  I = 1, N
      FC(I) = H*DY(I)
1060  YA(I) = Y(I) + .5*FA(I) - 1.5*FB(I) + 2.*FC(I)
      CALL DIFFEQ(N, X, YA, DY)
      DO 1130  I = 1, N
      Y(I) = Y(I) + FA(I)/6. + .666666667*FC(I) + H*DY(I)/6.
      U = Y(I)
      IF (ABSF(U) - YMIN(I))  1130, 1090, 1090
1090  KLOW = 2
      E = .2*ABSF(U - YA(I) )
      IF ( E - ABSF(TOL(I)*U) )  1110, 1100, 1100
1100  KBIG = 2
      GO TO 1130
1110  IF ( E - ABSF(SUB(I)*U) )  1130, 1120, 1120
1120  KBTWN = 2
1130  CONTINUE
      GO TO (100, 1135), KLOW
1135  GO TO (1180, 1140), KBIG
1140  NCOUNT = NCOUNT - 1
      IF (NCOUNT) 1150, 1150, 1170
1150  PRINT 1160,  X, H
      PRINT 1165, (I, Y(I), DY(I),  I = 1, N)
      RETURN
1160  FORMAT (58H4STEP SIZE HALVED 15 TIMES CONSECUTIVELY SINCE LAST PRI
     1NT  /29H PROGRAM TERMINATED AT    X =   , E16.8, 8H,    H = , E16.8,
     2//3H  I , 13X, 4HY(I), 16X, 5HDY(I),//)
1165  FORMAT (I3, 7X, 2(E16.8, 4X))
1170  KBIG = 1
      IF (H - B)  1176, 1172, 1172
1172  X = X - H
      H = .5*H
      DO 1174  I = 1, N
1174  Y(I) = YKEEP(I)
      KBTWN = 1
      KLOW = 1
      GO TO 1000
1176  M = 15 - NCOUNT
      PRINT 1178, M, X, H
      PRINT 1165, (I, Y(I), DY(I), I = 1, N)
      RETURN
1178  FORMAT (41H4STEP SIZE BECAME TOO SMALL FOR COMPUTER./20H IT HAS BE
     1EN HALVED , I2, 21H TIMES CONSECUTIVELY./29H PROGRAM TERMINATED AT
     2   X =   , E16.8, 8H,    H = , E16.8,//3H  I, 13X, 4HY(I), 16X,
     35HDY(I),//)
1180  NCOUNT = 15
      GO TO (1190, 1200), KBTWN
1190  H = 2.*H
1200  KBTWN = 1
      KLOW = 1
C
C          CHECK FOR INTERMEDIATE PRINT OUT
C
100   GO TO (10, 110), LTEST
```

```
1050  YA(I) = Y(I) + .125*FA(I) + .375*FB(I)
      CALL DIFFEQ(N, XB, YA, DY)
      DO 1060  I = 1, N
      FC(I) = H*DY(I)
1060  YA(I) = Y(I) + .5*FA(I) - 1.5*FB(I) + 2.*FC(I)
      CALL DIFFEQ(N, X, YA, DY)
      DO 1130  I = 1, N
      Y(I) = Y(I) + FA(I)/6. + .666666667*FC(I) + H*DY(I)/6.
      U = Y(I)
      IF (ABSF(U) - YMIN(I))  1130, 1090, 1090
1090  KLOW = 2
      E = .2*ABSF(U - YA(I) )
      IF ( E - ABSF(TOL(I)*U) )  1110, 1100, 1100
1100  KBIG = 2
      GO TO 1130
1110  IF ( E - ABSF(SUB(I)*U) )  1130, 1120, 1120
1120  KBTWN = 2
1130  CONTINUE
      GO TO (100, 1135), KLOW
1135  GO TO (1180, 1140), KBIG
1140  NCOUNT = NCOUNT - 1
      IF (NCOUNT) 1150, 1150, 1170
1150  PRINT 1160,  X, H
      PRINT 1165, (I, Y(I), DY(I),  I = 1, N)
      RETURN
1160  FORMAT (58H4STEP SIZE HALVED 15 TIMES CONSECUTIVELY SINCE LAST PRI
     1NT  /29H PROGRAM TERMINATED AT    X =   , E16.8, 8H,    H = , E16.8,
     2//3H  I , 13X, 4HY(I), 16X, 5HDY(I),//)
1165  FORMAT (I3, 7X, 2(E16.8, 4X))
1170  KBIG = 1
      IF (H - B)  1176, 1172, 1172
1172  X = X - H
      H = .5*H
      DO 1174  I = 1, N
1174  Y(I) = YKEEP(I)
      KBTWN = 1
      KLOW = 1
      GO TO 1000
1176  M = 15 - NCOUNT
      PRINT 1178, M, X, H
      PRINT 1165, (I, Y(I), DY(I), I = 1, N)
      RETURN
1178  FORMAT (41H4STEP SIZE BECAME TOO SMALL FOR COMPUTER./20H IT HAS BE
     1EN HALVED , I2, 21H TIMES CONSECUTIVELY./29H PROGRAM TERMINATED AT
     2   X =   , E16.8, 8H,    H = , E16.8,//3H  I, 13X, 4HY(I), 16X,
     35HDY(I),//)
1180  NCOUNT = 15
      GO TO (1190, 1200), KBTWN
1190  H = 2.*H
1200  KBTWN = 1
      KLOW = 1
C
C          CHECK FOR INTERMEDIATE PRINT OUT
C
100   GO TO (10, 110), LTEST
```

```
110    IF (L)  120, 120, 150
120    PRINT 130,  X, H
       PRINT 140, (I, Y(I), DY(I),  I = 1, N)
       L = NUM
       GO TO 10
130    FORMAT (5H X = , E16.8, 4X, 4HH = , E16.8, 11X, 1HI, 13X, 4HY(I),
      116X, 5HDY(I)/)
140    FORMAT (55X, I3, 7X, 2(E16.8, 4X))
150    L = L - 1
       GO TO 10
       END
```

```
*     LABEL
C     INTERPOLATION    ROUTINE FOR COMPUTING AREA
C     DADX IS CONTINUOUS
      SUBROUTINE AREAC(XX,AREA,DADX)
      COMMON PZERO, TZERO, WMOL, GAMMA, RHOL,
     1HFG, SURFA, SURFB, XI, ALPHA, AMACH,XX, AREA,
     2DADX,P,T,RSTAR,TD,AMASS,AVGR,ASTAR,
     3SSAT, INTERP
      DIMENSION  DD(50),X(50),A(50),D(50),DA(50)
C
C
C     AREAC  PART 1
C
C
C     INTERP=1, READ  AREA X AND ASTAR
C     SET X,DADX TO CORRESPOND TO ASTAR
C   ASTAR MUST BE IN AREA DATA LIST
      GO TO (1,2,3,4), INTERP
 1    I=0
 11   I=I+1
      READ10, X(I),A(I)
 10   FORMAT(2F15.0)
      IF(A(I)) 11,12,11
 12   READ10, XX,ASTAR
      IEND=I-2
C     IEND = LAST VALUE OF I USED MINUS 1
      AREA=ASTAR
      DADX=0.
C     FIND IZERO
      I=0
 13   I=I+1
      IF(X(I)-XX)  13,14,14
 14   IZERO=I
      D(IZERO)=0.
      DO 15 I=IZERO,IEND
 15   D(I+1) = 2.*(A(I+1)-A(I))/(X(I+1)-X(I))-D(I)
      DO  16 I=2,IZERO
      J=IZERO-I+1
 16   D(J)=2.*(A(J+1)-A(J))/(X(J+1)-X(J))-D(J+1)
      DO 17 I=2,IEND
 17   DD(I) = (D(I)-D(I-1))/(X(I)-X(I-1))
C     PLUG  IA INTO DD
      RETURN
C
C
C     AREAC   PART  2
C
C
C      GIVEN X   OUTPUT IS AREA AND DADX
 2    IF(XX-X(I)) 20,23,22
 20   I=I-1
      IF(XX-X(I))  20,23,23
 23   IB=I
      IA=I+1
      GO TO 24
```

```
 22    I=I+1
       IF(XX-X(I))  25,23,22
 25    IA=I
       IB=I-1
C      FIND AREA AND DADX
 24    AREA=A(IB) + (XX-X(IB))*(DD(IA)
     1  *(XX-X(IB))*.5 + D(IB))
 302   DADX=(DD(IA)*(XX-X(IB))+D(IB))/AREA
       RETURN
C
C
C       AREAC  PART 3
C
C
C      GIVEN AREA FIND X AND DADX
C    IF   MACH IS LESS THAN 1 LOOK BEFORE THROAT
C      IF MACH IS GREATER THAN 1 LOOK AFTER THROAT
 3     I=IZERO
       IF(AMACH-1.) 30,31,31
 30    I=I-1
       IF (AREA-A(I))  32,32,30
 32    IB=I
       IA=I+1
       GO TO 34
 31    I=I+1
       IF(AREA-A(I))  35,32,31
 35    IA=I
       IB=I-1
C    FIND X AND DADX
 34     IF( D(IA)-D(IB)) 36,37,36
 36    SIGN=1.
 301   XX= (-D(IB)+SIGN* SQRTF(D(IB)*D(IB) -2.*DD(IA)*(A(IB)-AREA)))
     1 /DD(IA) + X(IB)
       IF(XX-X(IB))  38,39,39
 38    SIGN=-1.
       GO TO 301
 39    IF(XX-X(IA)) 302,302,38
 37    XX=(AREA-A(IB))/D(IB) + X(IB)
       DADX=D(IB)/AREA
 4     RETURN
       END
```

```
      SUBROUTINE AREAC (X,AREA,DADX)
      COMMON PZERO,TZERO,WMOL,GAMMA,RHOL,HFG,SURFA,SURFB,XI,AL,AM,XX,AREA
     1A,DADX,P,T,RSTAR,TD,AMASS,AVGR,ASTAR,SSAT,INTERP
      GO TO (1,2,3),INTERP
 1    CONTINUE
      ASTAR=1.
      X=.55
      RETURN
C     NOZZLE TWO B
 2    IF (X-1.45)10,11,11
 10   AREA=1.+.00889*(X-.55)
      DADX=.00889/AREA
      RETURN
 11   IF (X-4.85)12,13,13
 12   AREA=1.008+.0218*(X-1.45)
      DADX=.0218/AREA
      RETURN
 13   AREA=1.082+.0133*(X-4.85)
      DADX=.0133/AREA
      RETURN
 3    IF (AREA-1.008) 30,30,31
 30   X=(AREA-1.)*112.5+.55
      DADX=.00889/AREA
      RETURN
 31   X=(AREA-1.008)/.0218+1.45
      DADX=.0218/AREA
      RETURN
      END
                                                                   0028

                                                     TOTAL         0028*
```

APPENDIX I

ESTIMATION OF EXPERIMENTAL ERROR

TEMPERATURE MEASUREMENTS

Estimated error (difference between measured and actual temperature) on temperature readings except where otherwise noted is + 0.5°, - 1.5°F. This was determined after the following measurements and observations.

1) Temperature of various portions of the ice bath of the reference junction were found to vary by as much as 1°F from the freezing point, 32.2°F, despite its containment in an insulated thermos.

2) A calibration of the potentiometer (Wheatstone bridge type) used for measurements, compared exactly with those readings of the standard copper-constantan conversion tables at each end (32°F and 212°F) of the calibration and showed a maximum variation of + 1.0°F between.

3) The time constant of the thermocouple was measured with the aid of a Sanborn Recorder capable of recording a 50 cps signal with no distortion. Subjecting the thermocouple to various step changes in temperature, it was found that for still water τ = .15 sec, for still air, τ = 1.4 sec, and for response to the variation of human breath, τ = .6 sec. The measured time constant of the potentiometer was .9 sec ± .2 sec.

Based on these observations, a reference temperature of 32.2°F was *assumed* for all measurements and the variation in ice bath temperature allowed for in the estimated larger possible negative error.

Assuming a linear temperature transient over a 1 minute period, a variation from 190°F to - 50°F would result in a rate change of - 4.0°F/sec. Hence, for the non-condensing curves, this effect alone could contribute an error of about 5°F, in the thermocouple (τ = .6) and potentiometer circuit (τ = .9 sec). Hence, in the non-condensing curves, an error of + 4.5°F, - 1.5°F is estimated. In measurements involving condensation, care was taken to let temperature readings reach a relatively constant level before data (photos) were taken. No transient effects are estimated for those cases.

~~TEMPERATURE~~ PRESSURE MEASUREMENTS

Pressure readings taken by the mercury manometer board are estimated accurate within ± .1" Hg, this would amount to ± 1.25% error in the pressure ratios near station 18 on the figures for Nozzle I.

Minimum pressure readings for Nozzle II were in the vicinity of 28" Hg, well beyond the region of condensation. Hence, pressure ratios in this vicinity are estimated accurate to within .5%.

In the region of condensation (station 10) pressure levels range near 80" Hg. Hence, error in pressure ratios in this region is estimated at ± .125%, two orders of magnitude less than the pressure variation caused by condensation at this point.

Error has been introduced into the values of stagnation pressure wherever they have not been directly measured by the manometer board owing to the high pressure level, or the stagnation tank pressure gauge, as occurred several times for Nozzle I. General observations of the behavior of the pressure ratio at the throat have shown that although its value remained remarkably close to .535 for all pressure levels, it had a slight tendency to decrease with increasing pressure. Based on these observations (and others with air, where average p/p_o measured .523 and the same tendency was noted) it is estimated that the pressure ratio at the throat could have been lowered to a minimum value of .525 at the highest pressure levels. Hence, calculated stagnation pressures are estimated to have an error of + 1%, - 2%.

Measurements in Nozzle II used the stagnation pressure gauge for all determinations of stagnation pressure after the gauge was calibrated and found to be accurate to within 1/2 psi at all pressures within the range of experimentation. Consequently, all stagnation pressure readings for Nozzle II are estimated accurate to within 1/2 psi and static pressure readings within .1" Hg.

DENSITY

Distance between optical glass side walls in the interferometric measurements was .956 inches. At the wall the boundary layer was about .006" at the throat and somewhat larger downstream (See Figure 12). Within the boundary layer densities are lower than in the mainstream, due to temperature recovery effects. This will cause a small error in the measured interferometric fringe shift data when applied to determination of density in the midstream. An upper limit on error in density measurements was estimated by assuming a thickness of the order of the displacement thickness (also given an upper limit of $\delta^* = 1/3\ \delta$) to be of temperature equal to the stagnation temperature.

Near the throat, assuming $\delta^* = .002''$

$$2\delta^* = .004'' \qquad l = .956'' \simeq 1.0''$$

$$\frac{T_{stream}}{T_\delta} = .8 \qquad \therefore \frac{\rho_\delta}{\rho_{stream}} = .8$$

Hence,

$$\rho_s - \rho_\delta \simeq .2\rho_s \qquad \text{also,} \quad \rho_o - \rho_s \simeq .6\rho_s$$

The fringe shift due to difference in density over length ℓ is

$$S = \frac{\ell G}{\lambda}(\rho_1 - \rho_2)$$

Hence,

$$\frac{S_\delta}{S} = \frac{\delta^*(\rho_s - \rho_\delta)}{l(\rho_o - \rho_s)} = \frac{.004}{.96}\frac{(.2\rho_s)}{(.6\rho_s)} \simeq .13\%$$

Similar estimates further downstream indicated that maximum error in density measurements probably do not exceed .2%.

thesD7836
Non-equilibrium condensation of carbon d
3 2768 001 89533 7
DUDLEY KNOX LIBRARY